
– CONTINENTAL EXTENSIONAL TECTONICS –

THE PAPAROA METAMORPHIC CORE COMPLEX OF WESTLAND, NEW ZEALAND.

A THESIS SUBMITTED IN PARTIAL

FULFILLMENT OF THE REQUIREMENTS FOR

THE DEGREE OF

MASTER OF SCIENCE IN GEOLOGY

AT THE

UNIVERSITY OF CANTERBURY

BY

MICHELLE ERICA JUNE HERD

UNIVERSITY OF CANTERBURY

2007

Frontispiece:

– Ductile deformation associated with the Pike Detachment Fault –
ultra-mylonite outcropping at Morrisey Creek, north of Fox River Mouth.

TABLE OF CONTENTS

LIST OF FIGURES

LIST OF TABLES

ACKNOWLEDGEMENTS

I would like to thank my supervisors Dr. Uwe Ring and Associate Professor John Bradshaw for their enthusiasm and assistance in this project.

Many thanks to Dr. Robert Bolhar for his help in geochemical work while in Australia and advice in the department.

Thanks also to Dr. J. Michael Palin from the University of Otago for his involvement in the LA-ICP-MS work in Canberra.

Thanks to Mr. Rob Spiers and Mr. Stephen Brown for their technical support, and to Dr. David Shelley for his help with optical mineralogy.

Financial support from the Mason Trust Fund.

To Julia Hofmann, who travelled from Germany to join me in the adventure of field work on the West Coast of New Zealand.

And finally, to my family and friends, who provided me with ongoing support and encouragement.

ABSTRACT

Cretaceous continental extension was accommodated by the development of the Paparoa Metamorphic Core Complex, resulting in the separation of New Zealand from Gondwana. High grade (Lower Plate) and low grade (Upper Plate) rocks are separated by the Ohika and Pike Detachment Faults. The two detachment faults have distinctly different histories, with greater exhumation along the Pike Detachment Fault. The onset of crustal extension is proposed to have commenced along the Pike Detachment Fault at 116.2 ± 5.9 Ma (Rb/Sr dating). Both geochemical and geochronological approaches are adopted for this thesis, through the *in situ* analysis of oxygen and hafnium isotope ratios, trace metals and U-Pb content. Chemical changes are tracked during the petrogenesis of the Buckland Granite, with mafic replenishment observed in the later stages of crystallisation. Crystallisation temperatures of the Buckland Granite are calculated using zircon saturation thermometry, with an average Ti-in-zircon temperature of 697°C (upper-amphibolite facies). Inherited zircons in Lower Plate rocks show distinct age peaks at c. 1000, 600 and 300 Ma, illustrating the incorporation of heterogeneous local crust (Greenland Group and Karamea Batholith). Model ages (T_{DM}) are calculated for inherited zircons of the Lower Plate rocks, which record the time at which magma bodies (zircon host rocks) were extracted from the mantle. Maximum and minimum model ages for the Buckland Granite average at 3410 Ma and 2969 Ma, with the maximum T_{DM} value of 3410 Ma coinciding with the proposed major crustal formation event of the Gondwana supercontinent at c. 3.4-3.5 Ga. Two distinct U-Pb zircon age peaks are observed in the Buckland Granite at 102.4 ± 0.7 and 110.3 ± 0.9 Ma. The 110.3 ± 0.9 Ma age is interpreted as the crystallisation age of the pluton, while the 102.4 ± 0.7 is proposed to represent a younger thermal (magmatic?) event associated with the 101-102 Ma Stitts Tuff.

CHAPTER 1: INTRODUCTION

The development of metamorphic core complexes takes place in areas in which regional extension follows a period of contraction, which resulted in the over-thickening of the continental crust. Relationships between Upper and Lower Plate rocks, and the role of detachment faulting still continue to bemuse geologists, with opposing views on the growth of ductile shear zones, and conflict over the role of plutonism and igneous underplating on isostatic uplift.

1.1. Metamorphic core complexes

Early investigations into the development of mountain systems saw the description of central ‘axial core zones’, within which ductile flow was believed to take place (Eskola 1949). Observations of the associated metamorphism of crustal rocks resulted in such structures being classified as gneissic domes. The juxtaposition of deformed material against relatively undeformed cover rocks was noted in the gneissic dome structures, and referred to as ‘infrastructure’ and ‘suprastructure’ domains, respectively. These domains were seen to be sharply separated by regional-scale ‘decollements’, along which steep metamorphic gradients and structural discontinuities exist (Eskola 1949, Misch 1960).

The tectonic relationship between these distinctly different domains was first addressed by Price and Mountjoy (1970), who illustrated that the uplift of ‘infrastructure’ rocks and coeval lateral movement were intimately linked. The gravitationally-driven movement away from the uplifting block was also proposed to be the driving force of adjacent foreland fold and thrust belt development.

Armstrong (1972) extended upon this tectonic interpretation by stating that ‘decollements’ were low-angle ‘denudation’ faults, along which significant displacement took place at the regional-scale.

Many of the early investigations focussed on either the presence of contractional or extensional structures only, and failed to note that the two opposing tectonic regimes are both of importance (Coney and Harms 1984). The post-plate tectonics interpretation of metamorphic terranes along the major mountain ranges of the North American Cordillera, along with revised interpretations of gneissic dome structures, led to the eventual development of the metamorphic core complex theory (Coney 1980). Nomenclature earlier suggested for gneissic dome structures were replaced by more appropriate terms, with ‘infrastructure’, ‘suprastructure’ and ‘decollements’ renamed as Lower Plate, Upper Plate and detachment faults, respectively. The Lower Plate is positioned below detachment faults in the foot wall, while the Upper Plate rests above detachment faults in the hanging wall (Coney 1980). This revised nomenclature has since become widely used in the scientific community.

The Lower Plate consists of ductilely deformed rocks of the lower crust, which have experienced upper-amphibolite to middle-greenschist facies metamorphism under the extensional regime. Lower Plate rocks are often referred to as the ‘basement rocks’ of metamorphic core complexes, and commonly contain plutonic rocks emplaced into mid-crustal levels. Upper Plate rocks, on the other hand, have not experienced ductile deformation during extension, and often consist of both sedimentary and volcanic units of the upper crust. The Upper Plate forms the cover sequence of metamorphic core

complexes, with multiple stages of brittle deformation recorded in the variety of faults present within the upper crust (Lister and Davis 1989). It is important to note that variations in both the composition and age of units in both the Lower and Upper Plates of metamorphic core complexes may be considered to be irrelevant with respect to the nature of extension (Coney 1980).

The development of metamorphic core complexes commonly post-dates a period of contraction, in response to the over-thickening of the continental crust. Contraction often encourages plutonism at depth, resulting in further strain being added to the crust. Granitoid plutons emplaced within Lower Plate domains during extension are frequently found to have a garnet-bearing, two-mica type mineralogy, which develops in response to the melting of over-thickened crustal material at depth. The link between granitoid mineralogy and the structural nature of metamorphic core complexes has been suggested to provide insight into both the petrogenetic history and tectonic evolution of such systems (Coney 1980).

Thermal relaxation of the continental crust follows after the cessation of contraction, in response to the ending of convergent tectonics (Brun et al. 1994). The pre-thickening and subsequent thermal relaxation of the crust leads to the development of detachment faults, to accommodate regional-scale extension. The juxtaposition of highly deformed rocks against relatively undeformed rocks occurs along these detachment faults, allowing the Lower and Upper Plate rocks to rest in tectonic contact. The dragging of the Lower Plate from beneath the Upper Plate results in the alteration and brittle deformation of rocks

adjacent to the active detachment faults. Chloritisation, cataclasis and brecciation of Lower Plate rocks develops in response to their exhumation into shallower crustal depths, resulting in a quartz-sericite assemblage (Coney 1980, Davis et al. 1983, Davis et al. 1986, Tulloch and Palmer 1990).

The evolution of faulting within metamorphic core complexes has been addressed by many authors, resulting in a variety of models being suggested to address the mechanism of crustal extension.

The development of metamorphic core complexes was initially proposed to take place under simple shear regimes, in which a single detachment fault would exist through time, in an ‘evolving shear zone’ situation. In this model, the detachment fault was considered to represent the brittle-ductile transition zone (continental stress guide), with brittle deformation being restricted to the Upper Plate, and ductile deformation within the Lower Plate only (Wernicke 1981a, Wernicke 1981b, Miller et al. 1983, Wernicke 1983, Wernicke 1985).

This model does not account for igneous activity commonly associated with metamorphic core complexes, and does not acknowledge magmatism as a direct consequence of continental crustal extension. This model has been discarded on several grounds, with evidence against the suggestion that brittle and ductile deformation must take place at the same period within the Upper and Lower Plates, respectively. In this model, mylonitisation of rocks may only occur during the faulting of a single detachment, which does not account for the observed overprinting of both brittle and ductile structures in metamorphic core complexes (Lister and Davis 1989).

Two other models of interest both acknowledge the growth of several large-scale shear zones within the crust through time, with the development of these detachment faults through the exploitation of older normal faults associated with the earlier stages of extension. The overprinting of ductile and brittle structures commonly observed is thus accounted for, through the multiple generations of detachment faults within individual metamorphic core complexes. The difference between the two models is based on the angle at which the older normal faults lie.

The development of detachment faults from initially low-angle normal faults was proposed by Davis and co workers (1980), to account for the low-angle listric nature of ductile shear zones. This model is not widely accepted, as several low-angle normal faults at close intervals would be required to promote extension, which is considered to be mechanically unlikely (Lister and Davis 1989).

The alternate model suggests the development of detachment faults from high-angle normal faults, at angles between 30-60˚. Block rotation accommodates extension through the rotation of high-angle faults, resulting in the development of low-angle listric detachment faults (Buck 1988, Wernicke and Axen 1988, Lister and Davis 1989, Brun et al. 1994, Wjins et al. 2005). This model is considered to be structurally feasible, with detachment faults representing the upper equivalents of ductile shear zones at depth (Davis et al. 1983, Lister et al. 1984, Lister and Snoke 1984, Reynolds and Spencer 1985, Wernicke 1985, Davis et al. 1986, Lister and Davis 1989).

The development of multiple detachment faults within an individual metamorphic core complex takes place, through the splaying of shear zones from a primary master fault at

depth, beneath an extending upper plate. Primary master faults are thought to develop along the brittle-ductile transition (continental stress guide), as regional-scale structures able to govern structural responses within both the brittle and ductile crust (Lister and Davis 1989). Splaying of detachment faults from the primary master fault may occur in response to stresses associated with the isostatic uplift of the Lower Plate, in attempt to maintain ductile flow. Continued isostatic uplift through continued extension of the continental crust, results in the formation of multiple generations of detachment faults through time. As the isostatic uplift continues, previously active detachment faults become inactive, to be replaced by new detachment faults. The cessation in activity of detachment faults results from their warping during isostatic uplift, causing the detachment faults to lie at different orientations to the regional extensional direction. New detachment faults therefore splay off the primary master fault, with low-angle listric geometries to accommodate extension. Inactive shear zones remain preserved within the Lower Plate of metamorphic core complexes, with characteristic bow-like geometries. The bowing up of old shear zones into shallower crustal levels experiencing active detachment faulting results in the exposure of the mylonitic front, through the horizontal back-rotation of the mylonitic rocks (Figure 1.1; Lister and Davis 1989, Reynolds and Lister 1990).

Heterogeneous strain softening of the continental crust is required for the accommodation of regional-scale strain under an extensional regime. The development of shear zones through strain softening allows the ductile flow of material at depth, which is not possible through bulk deformation of the surrounding country rock. Strain softening

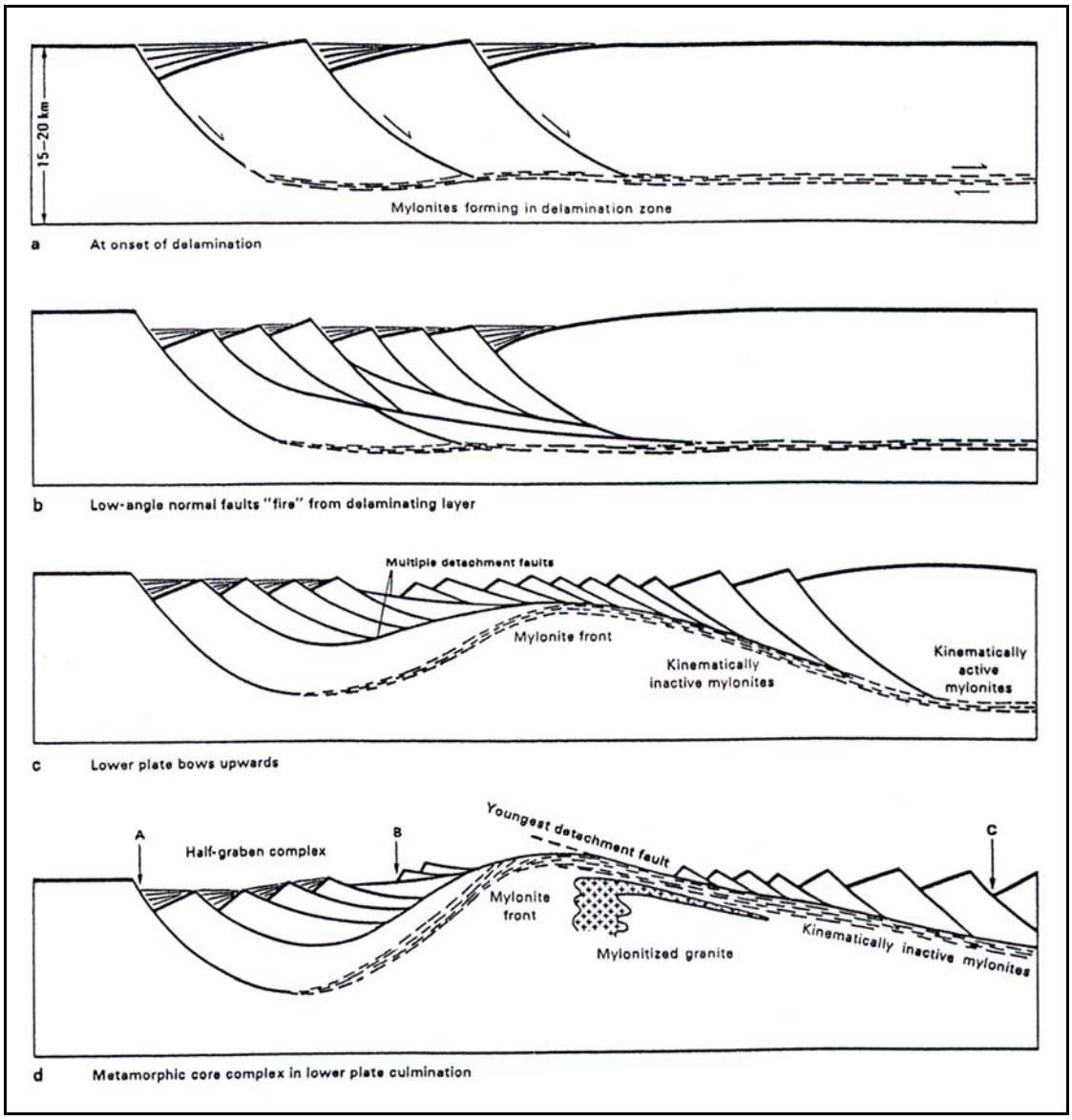

Figure 1.1: Model of metamorphic core complex formation, from the onset of delamination (a), development of low angle faults (b), isostatic uplift of the Lower Plate (c), to exposure of the mylonitic front in the final stages of continental extension (d). Note the dragging of mylonitised granite along the youngest detachment fault, during its emplacement into the Lower Plate (Lister and Davis 1989).

may take place through the decrease of stress at a constant strain rate, through the increase in strain rate at constant stress, or through the involvement of both mechanisms (White et al. 1980). Cataclasis along detachment faults promotes continued strain softening, which may also be accelerated through the incorporation of water sourced from crystallising granitoid plutons (if present) in the Lower Plate (Lister and Davis 1989).

Minerals within mylonitised polymineralic rocks respond differently to deformation, with harder minerals being able to withstand strain and remain as porphyroclasts, and the softer minerals of the matrix undergoing recrystallisation. Mylonitic rocks developed through the extreme ductile deformation of quartzo-feldspathic rocks will therefore consist of feldspar porphyroclasts, with a quartz-dominated recrystallised matrix (White et al. 1980). The plastic deformation of plagioclase feldspar and alkali feldspar may occur in mylonites which have experienced amphibolite to granulite facies metamorphism (Goode 1978). Granitoid plutons commonly emplaced in the Lower Plate are subject to such deformation, with the degree of metamorphism directly correlating to the position from the shear zone.

The role of ductile flow in metamorphic core complexes has been the subject of debate, with varying views on the depth at which this style of deformation occurs. Ductile flow within the mid- and lower-crust has been suggested as the main mechanism encouraging regional-scale extension (Block and Royden 1990, Bertotti et al. 2000), rather than simply flow strictly within the asthenosphere (Spencer 1984).

In the model with flow occurring strictly within the asthenosphere, detachment faulting removes hanging wall material through extension and/or erosion, therefore reducing the vertical load of the continental crust. The subsequent development of a horizontal pressure gradient at depth encourages the lateral flow of material towards the central region of a developing metamorphic core complex. Ductile flow of material within the asthenosphere is proposed to be the main mechanism driving the extension, through the isostatic uplift of the Moho at the regional-scale (Figure 1.2; Spencer 1984, Block and Royden 1990). Mid-crustal rocks undergoing extension, however, do not support this theory, as many may become ductile at temperatures as low as 280˚C, through the deformation and recrystallisation of quartz.

Ductile flow of material within the mid-crust is considered to be a more likely mechanism responsible for regional-scale extension. Isostatic uplift and subsequent thinning of the continental crust is shown to take place without the isostatic uplift of the Moho, through the upwelling of the weakened lower crust only (Figure 1.2; Block and Royden 1990).

The symmetry or asymmetry of metamorphic core complexes at the regional scale depends on the style of detachment faulting, as shown by numerical modelling (Lister et al. 1991). The rheology of the crust strongly influences the structural geometry of metamorphic core complexes, with symmetric extension commonly taking place in hot, weakened crust, and asymmetric extension in cold, stiff crust (Ranalli and Murphy 1987, Bertotti et al. 2000, Wjins et al. 2005). The extension of the crust may take place through a

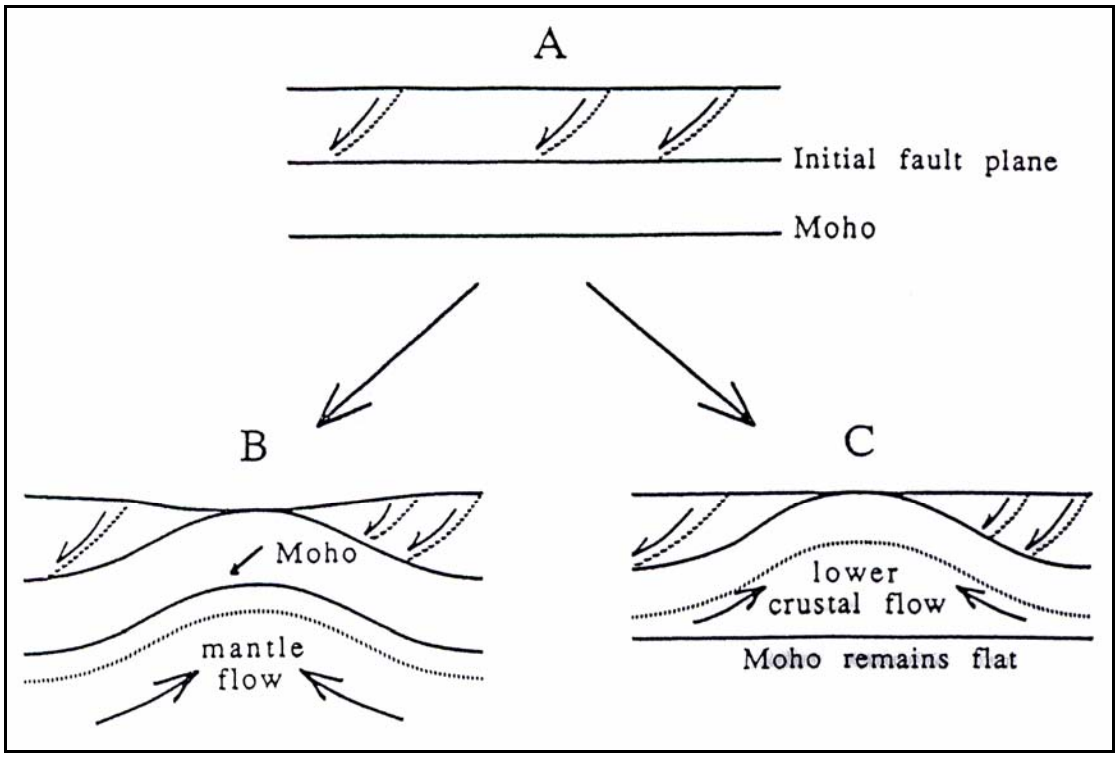

Figure 1.2: Diagram illustrating the proposed behaviour of the Moho during continental extension and associated isostatic uplift of the Lower Plate in metamorphic core complexes. The Moho is considered to be initially horizontal (a), and may either become uplifted by mantle flow (b), or remain flat with ductile flow being accommodated in the lower crust (c) (Block and Royden 1990).

variety of mechanisms, with extension being accommodated by large detachment faults (Figure 1.3). Symmetric metamorphic core complexes involve two detachment faults, positioned on either side of the uplifting Lower Plate. Asymmetric metamorphic core complexes, on the other hand, involve only one detachment fault, along which the Lower Plate is dragged from underneath the Upper Plate.

Lower Plate rocks of symmetric metamorphic core complexes may be intruded by vapour-present ('wet') plutonic rocks, in which monazite and zircon are common. The degree of dissolution of monazite is increased by the presence of vapour, with plutons characteristically showing elevated levels of light-Rare Earth Elements (LREE's) and heavy-Rare Earth Elements (HREE's). Asymmetric metamorphic core complexes commonly involve the intrusion of vapour-undersaturated ('dry') plutonic rocks, with monazite, zircon ± garnet present in the residual melt. LREE's and HREE's are anomalously low in concentration, while positive Eu spikes are commonly observed (Watt and Harley 1993).

The chemistry of vapour-present ('wet') plutonic rocks is commonly observed in S-type granitoid rocks, emplaced into previously over-thickened continental crust during extension at the regional-scale (Watt and Harley 1993).

The development of metamorphic core complexes, regardless of mechanism, requires the isostatic uplift of (at least) the continental crust at the regional-scale. Lower Plate rocks dragged out from beneath the Upper Plate become uplifted to elevations above sea level, to produce the characteristic dome-like profile (Coney 1980, Lister and Davis 1989, Waight et al. 1998b). Metamorphic unroofing of the Lower Plate encourages the erosion and transportation of clastic material along active detachment faults, to become

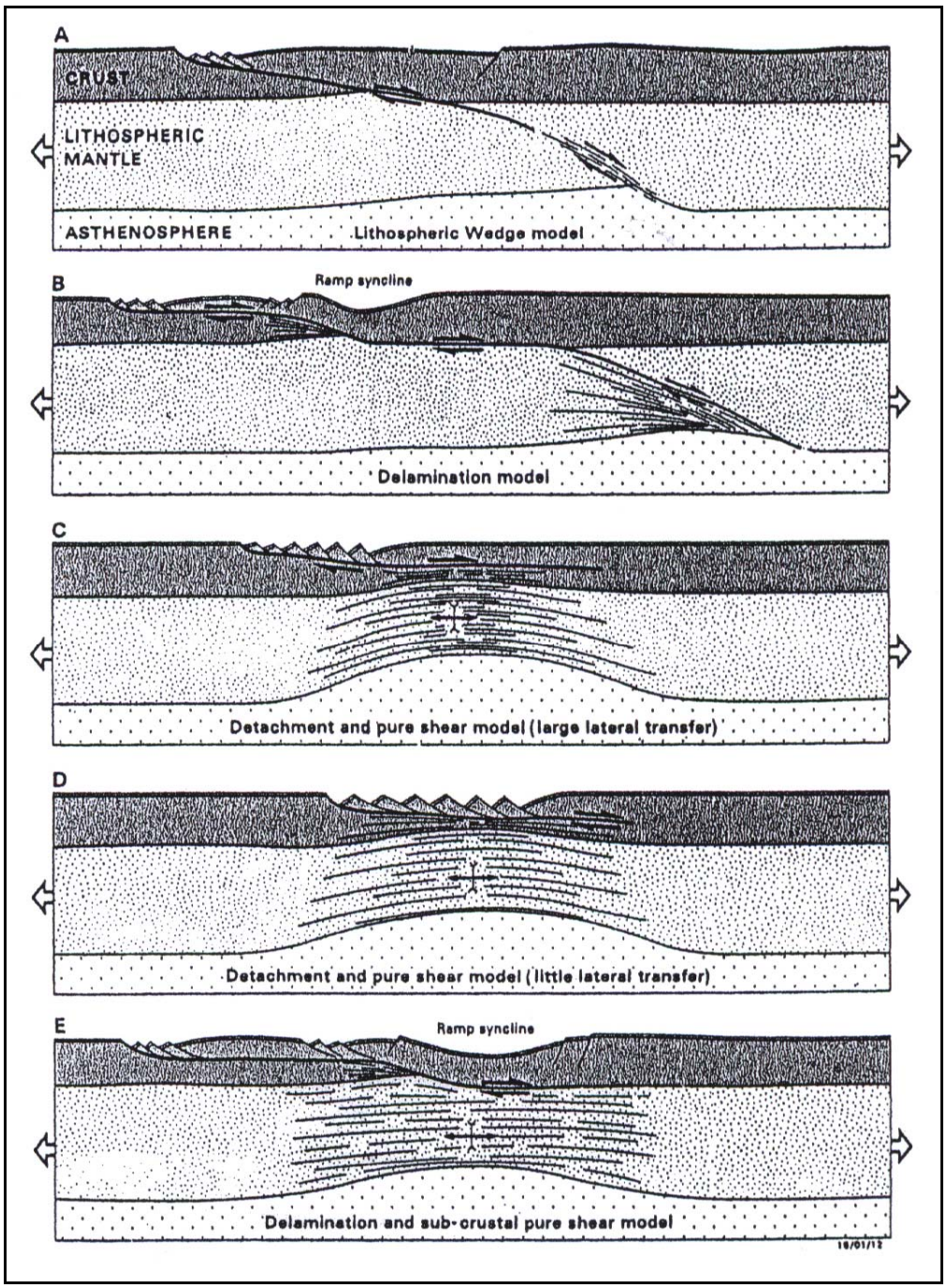

Figure 1.3: Five schematic diagrams of crustal extension associated with detachment faulting, including: a single through-going detachment (A), a detachment with ramps and flats (B), stretching of the lithosphere by pure shear without influencing the adjacent rift basins (C), stretching of the lithosphere by pure shear directly beneath the detachment (D), and a combination of ramps and flats with ductile stretching beneath the detachment (E) (Lister et al. 1991).

deposited in non-marine basins along outer margins of metamorphic core complexes (Coney 1980, Brun et al. 1994, Bertotti et al. 2000).

This phase of extension is characterised by the ductile flow of material towards the central region, with subsidence of the hanging walls and uplift of the footwalls along detachment faults (Bertotti et al. 2000). The mylonitisation of rocks continues under the ductile regime, and persists until accommodation of the extension is reached through the development of detachment faults (White et al. 1980). Gravitational instability associated with the domal geometry leads to horizontal spreading and crustal extension, further accelerating isostatic uplift.

Mylonitic rocks exposed at the surface of ancient metamorphic core complexes represent older phases of ductile deformation, which become uplifted by younger phases of detachment faulting, which develop as individual splays to accommodate extension.

The mechanism responsible for isostatic uplift is subject to debate, with opposing views on the role of plutonism and igneous underplating in metamorphic core complexes. Plutonism and igneous underplating of the Lower Plate may continue for an extended period of time, until the reservoir becomes expended. The role of rheology of the continental crust, however, is proposed to be the dominant driving force of isostatic uplift, with plutonism and igneous underplating considered to be of secondary importance (Brun et al. 1994, Wjins et al. 2005).

Variations in rheology results in the division of the continental crust into two layers through mechanical stratification during thermal relaxation (Ranalli and Murphy 1987, Brun et al. 1994, Wjins et al. 2005), with the upper crust consisting of strong, cold rocks

(Lister and Davis 1989), and the lower crust of hot, weak rocks (Gans 1987, Block and Royden 1990). Clearly rheological layering influences responses of the crust to tectonic activity, with brittle failure in the upper crust, and ductile deformation taking place in the lower crust.

Both vertical and lateral contrasts in the rheology of the crust may exist in response to tectonic denudation of the continental crust, with lateral variations considered to be subordinate to the vertical rheology during continental extension. Vertical contrasts in rheology are considered the controlling mechanism during metamorphic core complex formation, supported by both analogue and numerical modelling of crustal extension (Brun et al. 1994, Wjins et al. 2005). Brun and co workers (1994) propose that plutonism and/or igneous underplating of the Lower Plate is required for the weakening of the lower crust, to allow metamorphic core complex formation. Numerical modelling by Wjins and co workers (2005), however, illustrates that this is not necessary, provided there is a uniformly weak zone within the lower crust through basic contrasts in rheology.

The eventual death of metamorphic core complexes follows the loss of isostatic uplift, with the shift from dominantly ductile to the more brittle style of deformation and associated subsidence in both foot- and hanging walls of the detachment faults (Lister et al. 1991, Bertotti et al. 2000). This shift is facilitated by the cessation of ductile flow at depth, through rheological changes in the crust. Large strength ratios responsible for the exhumation of the weak lower crust change to small strength ratios, resulting in the strengthening of the lower crust. The isostatic uplift of the Lower Plate may no longer

continue, as the lower crust becomes more rigid in shallower crustal levels and inhibits ductile flow (Wjins et al. 2005).

Normal faulting of the upper crust develops perpendicular to the older ductile structures, parallel to stretching lineation directions (Davis et al. 1980). Brittle faults become superimposed upon the older ductile structures, along structurally weakened zones (Coney 1980, Lister et al. 1991). Rotation of crustal blocks takes place during the tilting of the high-angle normal faults to accommodate continued extension in the upper crust, resulting in the development of younger low-angle listric detachment faults (Lister and Davis 1989, Rosenbaum et al. 2005).

Rigid block faulting and rotation of crustal blocks in metamorphic core complexes is believed to represent the final stages of extension prior to the eventual separation of continental crust, and formation of oceanic crust (Coney 1980, Reynolds and Spencer 1985, Lister and Davis 1989, Rosenbaum et al. 2005). The axis of brittle extension commonly develops within basement rocks of the Lower Plate, where isostatic uplift was at its greatest during the earlier ductile phase of extension (Falvey and Mutter 1981). Brittle faulting associated with newly forming oceanic crust often show direct geometrical relationships with the older ductile features, with spreading ridges commonly forming normal to the older extensional direction (Coney 1980, Lister et al. 1991). Continental margins previously joined prior to extension commonly display differences, in both structural features and uplift-subsidence patterns on either side of the spreading ridge (Lister et al. 1991).

1.2.Regional geology

A terrane approach has been adopted in New Zealand for the correlation of rock units older than 100 million years in age. The South Island consists of around ten major terranes which have been grouped into the Median Tectonic Zone, the Eastern Province, and the Western Province (Figure 1.4; Bradshaw 1989, Bradshaw 1993). It is important to note that each terrane is an incomplete section, which must be taken into consideration when piecing together the geological record. Rocks of the South Island have also experienced 480 km of lateral displacement along the Miocene to Recent Alpine Fault, with an associated overprinting of previous tectonic structures by the Cenozoic movement (Landis and Coombs 1967).

The Median Tectonic Zone consists of a complex elongate section of plutonic, volcanic and volcanically-derived sediments formed along magmatic arc(s) during the Carboniferous to Cretaceous period (Bradshaw 1993, Kimbrough et al. 1993, Muir et al. 1998, Mortimer et al. 1999). Plutonism occurred in a convergent tectonic regime, due to convergence of the Phoenix and Pacific Plates and over-thickening of the continental crust during this period

The Eastern Province is dominated by Permian to early Cretaceous volcanics and accretionary material, deposited along the eastern margin of Gondwana. Material from both the Median Tectonic Zone and the Eastern Province prior to the Early Cretaceous developed under a convergent tectonic regime.

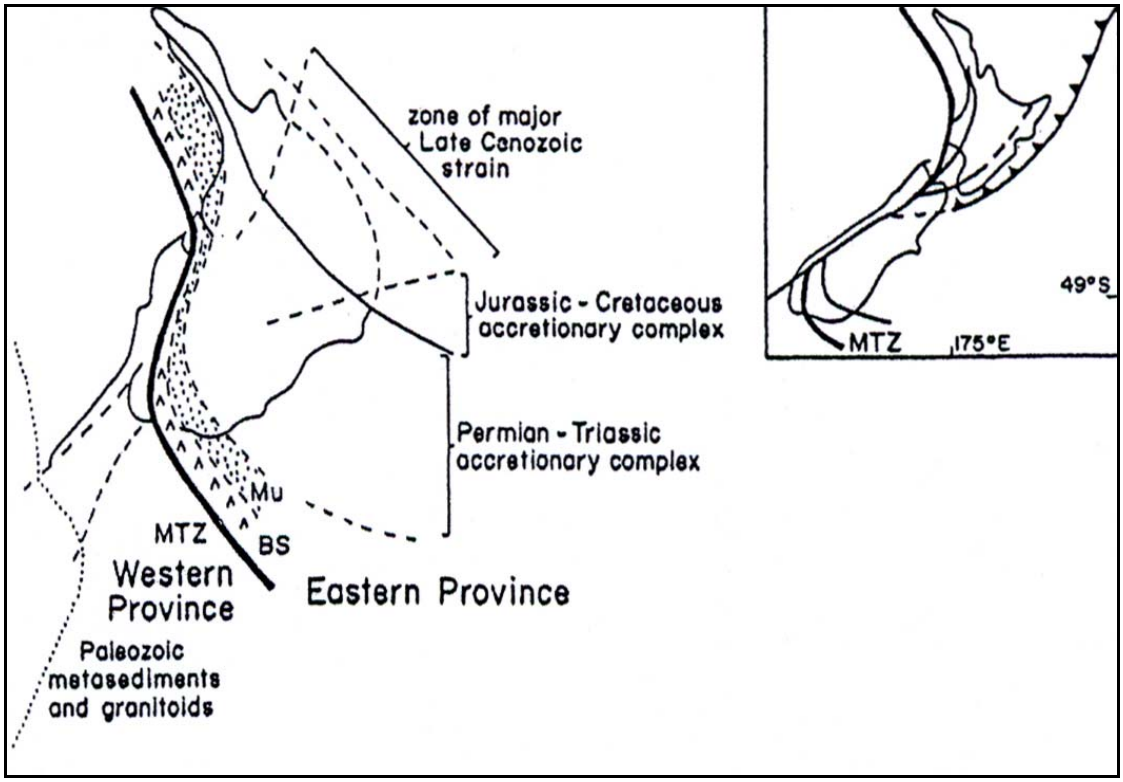

Figure 1.4: Schematic diagram illustrating the configuration of the Median Tectonic Zone and the Eastern and Western Provinces of New Zealand, prior to the late-Cenozoic displacement associated with the onset of the Alpine Fault plate boundary (Bradshaw 1993).

The oblique collision of the Phoenix and Pacific Plates with the eastern margin of Gondwana during the Early Cretaceous resulted in an almost immediate switch from contractional to extensional tectonics (Laird 1981, Bradshaw 1989), and initiated further emplacement of granitoid rocks into the volcanic arc. Such Cretaceous granitoids are found in both the Median Tectonic Zone, as discussed above, and the Western Province.

The Western Province has been divided into the Takaka and Buller Terranes, which are separated by the Anatoki Fault (Bradshaw 1989).

The Takaka Terrane consists of clastic material, limestones, quartzites and volcanics ranging from Cambrian to Devonian in age. Mafic rocks and granitoids were then emplaced into the Terrane during the Devonian and Cretaceous, respectively.

The majority of the Buller Terrane consists of the Greenland Group which was deposited during the Cambrian to Ordovician period, and makes up the 'basement' of this terrane. The Greenland Group is a quartz-rich metamorphosed flysch unit, non-calcareous and unfossiliferous in nature, with a minimum Rb-Sr age of 495 ± 11 Ma (Adams 1975, Hume 1977, Kimbrough and Tulloch 1989).

The Buller Terrane consists largely of Paleozoic metasediments peppered with various granitoid rocks intruded during the Devonian, Carboniferous and Early Cretaceous (Figure 1.5; Muir et al. 1994, Muir et al. 1995, Muir et al. 1998, Waight et al. 1998b). These granitoid rocks have been divided into three suites by Tulloch (1988) on the basis of variations in both age and geochemistry. The Karamea Suite is dominated by S-type granitoids ranging in age from the Devonian to the Carboniferous. The Separation Point Suite is Cretaceous in age, and consists of I-type granitoids, including the Separation Point Granite. The final group is referred to as the Rahu Suite, which contains transitional

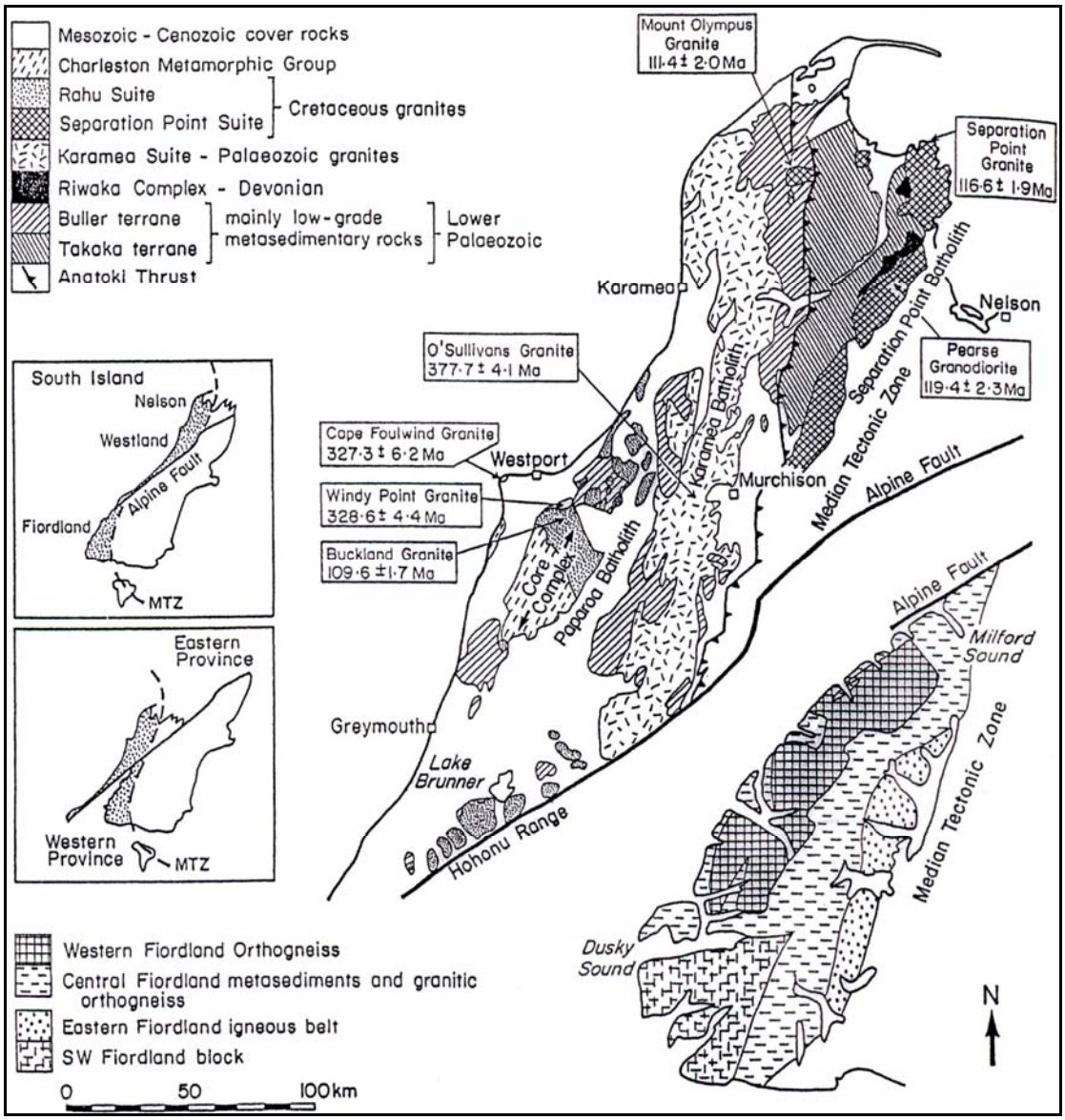

Figure 1.5: Geological map outlining the basement terranes of the NW Nelson-Westland and correlatives in the Fiordland area, with granitoid outcrop locations and emplacement ages in the Buller and Takaka Terranes. The location of Western Province rocks is shown in the inset, both before and after the onset of the Alpine Fault (Muir et al. 1994).

I/S-type granitoids, alkali-lamprophyre dikes and the Charleston Metamorphic Group (Nathan 1975, Tulloch and Kimbrough 1989). The Hohonu Suite to the south is the correlative of the Rahu Suite due to similarities in age and petrology (Tulloch 1988, Waight et al. 1997, Waight et al. 1998b).

The majority of granitoids within the Rahu Suite are biotite granites and granodiorites, with some muscovite-bearing granitoids. The Buckland Granite is included in the Rahu Suite, and is of particular interest to this thesis in regards to the development of the Paparoa Metamorphic Core Complex in the Western Province.

The Western Province was then disturbed by the emplacement of Cretaceous calc-alkaline Rahu Suite granitoids (Buckland Granite), and experienced extreme deformation during the development of the Paparoa Metamorphic Core Complex under an extensional regime (Tulloch and Kimbrough 1989, Waight et al. 1998b).

The Paparoa Metamorphic Core Complex is bound by two master detachments, the Ohika and Pike Detachment Faults to the north and the south of the Paparoa Range, respectively (Figure 1.6). The Ohika Detachment Fault dips to the NNE with a ‘top-to-the-NNE’ shear sense, while the Pike Detachment dips to the SSW with a ‘top-to-the-SSW’ sense of shear (Tulloch and Kimbrough 1989).

Sedimentary basins developed rapidly in response to the initiation of crustal extension, in both grabens and half-grabens. The non-marine Mid Cretaceous Pororari Group was deposited in basins NE and SW of the Paparoa Range (Figure 1.6), with beds generally dipping to the SW in the north-eastern basins, and NW in the south-eastern basins. The

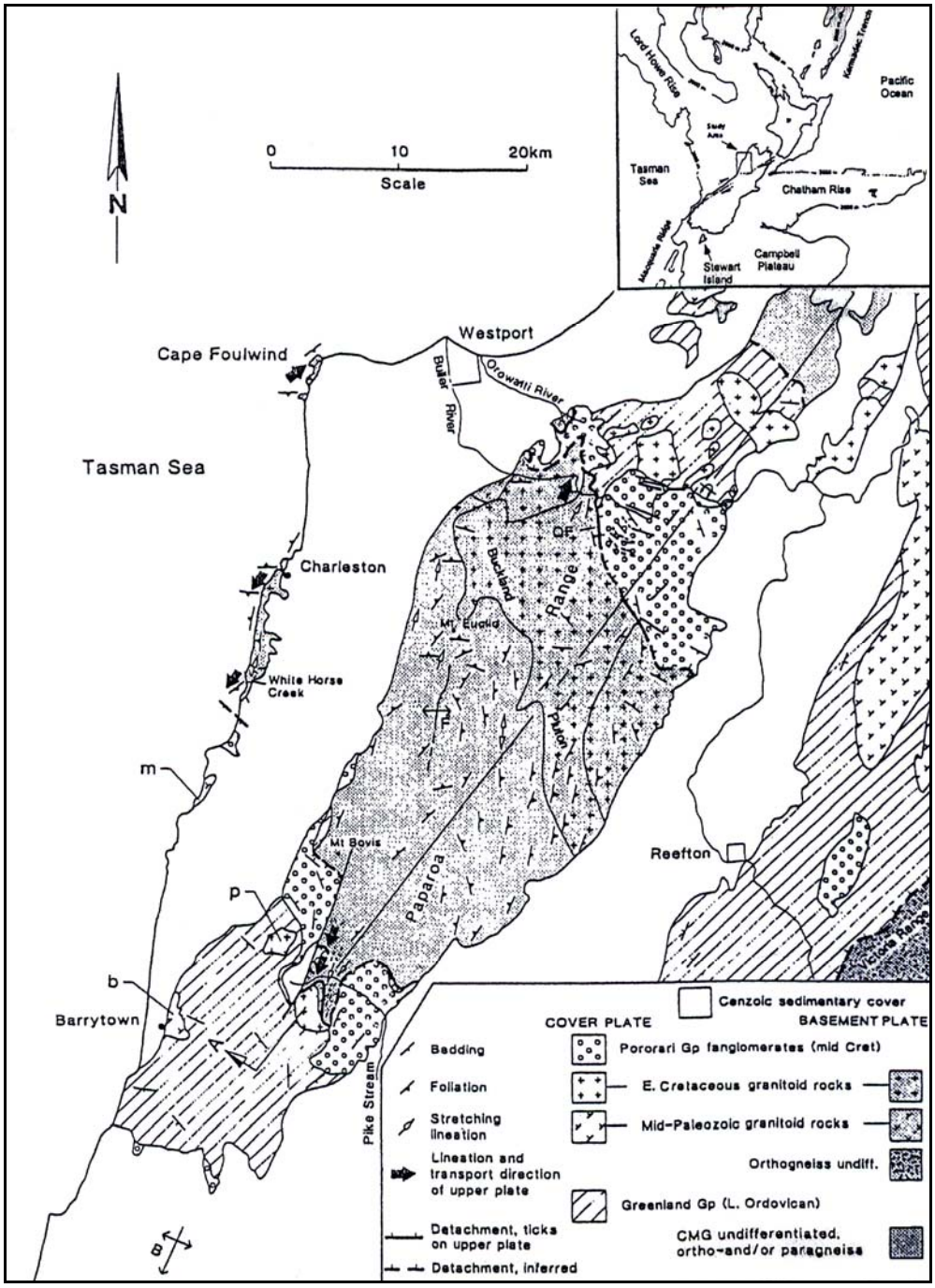

Figure 1.6: Geological map of the Paparoa Metamorphic Core Complex, with the Ohika and Pike Detachment Faults located to the north and south of the Paparoa Range, respectively. Upper Plate (cover plate) and Lower Plate (basement plate) rocks are shown, along with the bedding and foliation measurements of various units (Tulloch and Kimbrough 1989). Inset of study location from Spell et al. (2000).

Pororari Group comprises of a basal non-marine mudstone, the 101-102 Ma vitric Stitts Tuff, and sandstone overlain by the coarse Hawks Crag Breccia (Tulloch and Kimbrough 1989, Muir et al. 1997). The Stitts Tuff was initially proposed to be the volcanic equivalent of the nearby Berlins Porphyry pluton (Bowen 1964). Dates for both the Stitts Tuff and the Berlins Porphyry were later found to be c. 101-102 and 110 Ma, respectively, which disproves an igneous link between the two groups (Muir et al. 1997).

Rotation of the Hawks Crag Breccia accommodated continued extension of the brittle upper crust during the final stages of detachment faulting. Movement along the Pike Detachment Fault is suggested to have continued for some time after the Ohika Detachment Fault, with exhumation of the Lower Plate until c. 98 Ma along the Ohika Detachment Fault, and c. 85 Ma along the Pike Detachment Fault (Tulloch and Palmer 1990). The c. 30 Ma of activity along the detachment faults is considered to be too long, with a life span of c. 10 Ma thought to be more likely (e.g. Ring et al. 2007).

NNE-SSW extension led to the eventual separation of the New Zealand section from Gondwana, through the development of the NNW-SSE Tasman Basin spreading margin by c. 84 Ma (Figure 1.7; Laird 1981, Grindley and Davey 1982, Bradshaw 1989, Tulloch and Kimbrough 1989, Muir et al. 1992, Laird 1993, Waight et al. 1998b, Spell et al. 2000, Laird and Bradshaw 2004). Emplacement of the alkaline A-type French Creek Granite, and the associated alkaline-basalt Hohonu dike swarm at 81.7 ± 1.8 Ma in a dominantly WNW orientation, corresponds with the onset of sea floor spreading (Tulloch and Kimbrough 1989, Tulloch et al. 1994, Waight 1994, Waight et al. 1997, Waight et al. 1998a).

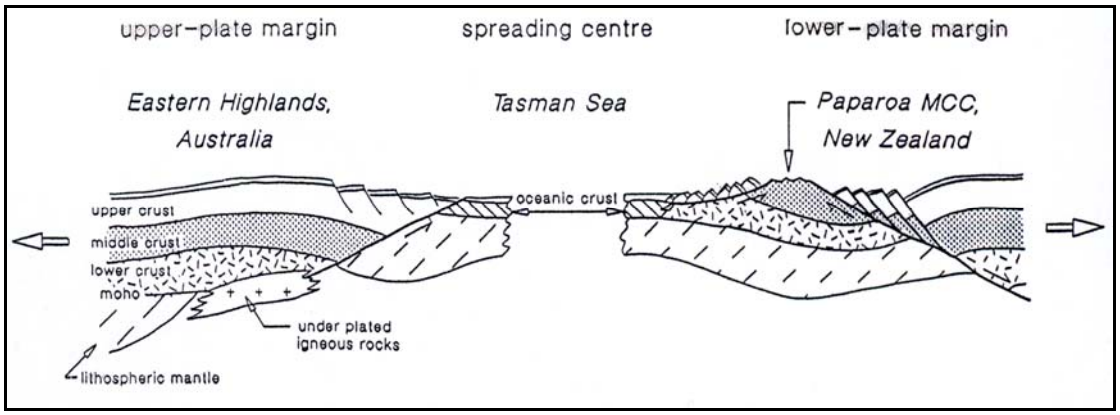

Figure 1.7: Schematic crosssection showing the asymmetric passive margins of the Tasman Sea Basin, which developed in the final stages of rifting after the development of the Paparoa Metamorphic Core Complex (Tulloch and Kimbrough, 1989).

Marine transgressions during the Mid Tertiary resulted in the blanketing of the Charleston Metamorphic Group and Pororari Group rocks (Tulloch and Kimbrough 1989). Subsequent erosion, transportation and deposition of material over time resulted in the present day exposure level of the West Coast.

1.3. Thesis objectives

Observations in the geology of South Island terranes over the years have provided a multitude of information related to the evolution of New Zealand, and its relationship with the Gondwana supercontinent during the Paleozoic and Mesozoic eras. The model of the Paparoa Metamorphic Core Complex proposed by Tulloch and Kimbrough in 1989 is relatively simplistic, and has led to several questions. This thesis brings together observations and interpretations made by previous workers on the initiation, development and cessation of the Paparoa Metamorphic Core Complex, and attempts to extend upon

such data with structural, geochemical and geochronological approaches. Objectives for this particular thesis are outlined below.

1. Carry out a detailed review of the behaviour of metamorphic core complexes in general, and compare with current knowledge of the Paparoa Metamorphic Core Complex.
2. Determine whether the degree of deformation in Lower Plate rocks corresponds to their position in respect to the adjacent detachment faults.
3. Interpret deformational structures and textures of a variety of rocks from the complex, at both the hand specimen and thin section scale.
4. Carry out detailed geochemical and geochronological investigations using both the *in situ* sampling of individual zircon minerals, and the 'whole rock' approach of hand specimens from the complex. Sample various elements and trace metals to achieve greater understanding of the petrogenesis and metamorphism of rocks from the complex, to build on and compare with geochemical findings by previous studies.
5. Calculate the crystallisation temperatures reached during the period of crustal extension, and attempt to constrain the timing of detachment faulting through the dating of the mylonitisation at either ends of the complex. Directly correlate the timing (U-Pb dating) of crystallisation with calculated temperatures (based on Ti content), by the detailed *in situ* sampling of individual zircon grains.
6. Attempt to better constrain the timing of crystallisation of the Buckland Granite.

7. Establish the role of detachment faulting in the emplacement of the Buckland Granite. Determine whether the pluton is likely to have been syn-tectonic or late tectonic in nature, and whether the Pike Detachment Fault became more dominant than the Ohika Detachment Fault during extension. If so, what effect did this dominance in movement to the south have on the pluton?
8. Address the issue of inheritance through detailed geochemical and geochronological investigations into the provenance of a variety of rocks from the complex.
9. Calculate the timing at which the zircon-host rocks were initially extracted from the mantle, and link to major crustal formation events in the early stages of Earth's history.
10. List potential questions for future research in the Paparoa Metamorphic Core Complex.

1.4. Location of study

The Paparoa Metamorphic Core Complex is located in the Western Province on the West Coast of the South Island, New Zealand. It is important to note that the West Coast of the South Island is dominated by dense rainforest, with limited exposure. Outcrops are considerably difficult to find, with steep terrain further limiting access to certain areas.

Areas of interest include the Lower Buller Gorge near Westport, a section along the coastline south of Charleston, and the Pike Stream area in the Paparoa Range near Greymouth. Outcrops in the Lower Buller Gorge area are accessible along both rail and road side cuttings, and within the major river systems. The coastline south of Charleston

provides a more accessible sequence of outcrop, from Morrissey Creek to the Fox River Mouth. The Pike Stream, on the other hand, has limited outcrops found within nearby river systems.

1.5. Methodology

In order to gain a greater understanding of the mechanisms involved in continental extensional tectonics, and the nature of the Paparoa Metamorphic Core Complex, a variety of approaches must be taken.

1.5.1. Field work

Four weeks of intensive field work was undertaken in the Lower Buller Gorge area, the coastal section from Charleston to the Fox River Mouth, and the Pike Stream area in the Paparoa Range. Foliations and stretching lineations were recorded during the structural mapping of these areas, in an attempt to show any regional pattern of deformation associated with the development of the core complex.

The degree of deformation of the core complex-related rocks was addressed through the development of a ‘basement deformation classification’ system, based on field observations and thin section analysis. Five levels of deformation were qualitatively established, as follows:

(I) Undeformed granitoid,

(II) Deformed granitoid,

(III) Orthogneiss (strongly deformed granitoid),

(IV) Mylonite, and

(V) Ultramylonite

This classification system was used in attempt to illustrate the relationship between the degree of deformation of the Paparoa Metamorphic Core Complex rocks and their location with respect to the adjacent detachment faults.

The collection of oriented hand specimens provided material for geochemical analysis, and allowed the degree of ductile deformation to be observed at the thin section scale.

1.5.2. Geochemical work: CL imaging, SIMS and LA-ICP-MS

Four samples from the Paparoa Metamorphic Core Complex were both sourced from PETLAB (UC08368, UC05592 and RNZ119) and collected during field work (PCC06-01), for both the *in situ* sampling of individual zircon minerals, and whole rock geochemical sampling. These two approaches were adopted in attempt to further constrain the chemical makeup and history of the core complex, and to determine whether the sampling methods carried out in this thesis (documented core vs. rim analyses of individual zircon grains) provide more detailed findings than previous investigations.

PETLAB samples were sourced from the following locations:

1. UC08368 – Lat/Long 41.83683˚S; 171.66402˚E (NZGD49),
2. UC05592 – Lat/Long 41.84829˚S; 171.70589˚E (NZGD49), and
3. RNZ119 – Lat/Long 41.84909˚S; 171.7158˚E (NZGD49).

Zircon separation was carried out through the crushing of hand specimens with a hydraulic press, and the sieving of material for particles between 50 and 350µm. Zircon grains were then extracted using standard heavy liquid and magnetic techniques, using a Frantz separator. Individual zircons were handpicked under a binocular microscope, mounted in epoxy resin and then polished to expose the interior sections of grains.

Zircons from each of the four samples were then digitally imaged using cathodoluminescence (CL) by Dr. Robert Bolhar at the University of Otago. CL imaging was undertaken prior to sampling for labelling and publication purposes, as analysis by *in situ* Laser Ablation-Inductively Coupled Plasma-Mass Spectrometry (LA-ICP-MS) and Multi-Collector-Inductively Coupled Plasma-Mass Spectrometry (MC-IPC-MS) is destructive. The nature of individual zircons, such as growth patterns, lattice defects, and overgrowth structures, are made visible through CL imaging, enabling accurate *in situ* geochemical sampling of specific sites of interest within individual grains.

Oxygen isotopes were analysed for each of the four samples by Dr. Robert Bolhar and Dr. Martin Whitehouse in the NordSIMS facility at the Swedish Museum of Natural History using the Secondary Ion Mass Spectrometry (SIMS) technique, following the procedures outlined in Nemchin and co workers (2006a), Nemchin and co workers (2006b) and Schuhmacher and co workers (1994). Each mount was polished to expose any xenocrystic cores present, and coated in approximately 30nm of gold in preparation for the analysis.

LA-ICP-MS was carried out at the Australian National University in Canberra, and at the University of Melbourne, Australia. Procedures followed those described by Ballard and co workers (2001) and Woodhead and co workers (2004).

The four samples from the Paparoa Metamorphic Core Complex were analysed using the pulsed Lambda Physik LPX 120I UV ArF excimer laser in the Research School of Earth Sciences at the Australian National University. The excimer laser operates at 70mJ and 5Hz to allow spot sizes of 24µm or 32µm, with penetration depths of around 20µm. Mixed He-Ar gas transported ablated material from the sample cell and flow homogeniser to the Aglient 7500 Quadrupole ICP-MS.

The *in situ* analysis of hafnium was carried out in the School of Earth Sciences at the University of Melbourne, using the Nu Plasma MC-ICP-MS coupled to a 193-nm ArF excimer laser, with a spot size of 30-40µm operating at 60mJ and total intensity of 1-2V.

Each analysis commenced with 20 seconds of background data collection, followed by 40 seconds of laser ablation, in which trace metals and elemental ratios were recorded. A period of 30 to 60 seconds without ablation between each sample, often referred to as a ‘gas blank’ period, allowed the stabilisation of background levels to ensure consistency within the data.

Data reduction involved the removal of outliers and background levels collected during spot analysis. Exclusion of the first 10 scans in each spot analysis reduced the effect of instrumental mass bias, by removing unsteady ion counts. Correction for the inter-element fractionation of Pb, Th, and U involved the averaging of known values from

standard zircons Temora and 91500, and the silicate glass NIST SRM 610 (Wiedenbeck et al. 1995, Pearce et al. 1997, Black et al. 2003).

1.5.3. Geochemical work: whole rock analysis (XRF)

Ten samples from the Paparoa Metamorphic Core Complex were used for whole rock analysis, including the four samples also used for trace metal/U-Pb dating, as outlined above. The remaining six samples were collected along an East-West profile through the Lower Buller Gorge area.

Whole rock samples were crushed using the hydraulic press, until broken into smaller clasts, and then run through the Ring Mill until the samples were of a floury consistency. Samples were then analysed using the X-Ray Fluorescence (XRF) process after Norrish and Hutton (1969), modified by Harvey and co workers (1973) and Norrish and Chappell (1977) for major and trace elements, respectively.

The classification of rocks from the Paparoa Metamorphic Core Complex allows direct comparisons to be made between samples, and provides information on the composition of these samples for additional geochemical work.

CHAPTER 2: STRUCTURAL GEOLOGY

The Paparoa Metamorphic Core Complex displays many characteristic features of Cordilleran-type metamorphic core complexes, with similarities in both the structural geology and mineralogy of associated rocks.

2.1. Previous work

The observed juxtaposition of relatively undeformed rocks above high grade metamorphic rocks in the Paparoa Range has recently been interpreted as an ancient metamorphic core complex, associated with the separation of the New Zealand section from Gondwana during the Cretaceous (Tulloch and Kimbrough 1989).

Development of the symmetric Paparoa Metamorphic Core Complex accommodated the regional-scale extension through the development of two detachment faults north and south of the Paparoa Range, referred to as the Ohika and Pike Detachment Faults, respectively (Figure 2.1). The Ohika Detachment Fault dips to the NNE, with a 'top-to-the-NNE' sense of shear, while the Pike Detachment dips to the SSW with 'top-to-the-SSW' shear sense. Regional extension of the continental crust took place in a NNE-SSW orientation, in both the Upper and Lower Plates on either side of the detachment faults (Kimbrough and Tulloch 1989). Previous authors investigating structural relationships in the Paparoa Range noted the opposing shear sense patterns, which remains consistent with the metamorphic core complex model (Laird 1967, Hume 1977). The opposing sense of shear is recorded within the S-C fabrics of mylonitic rocks, and illustrates the bivergent style of continental extension during this period (Tulloch and Kimbrough 1989, Spell et al. 2000).

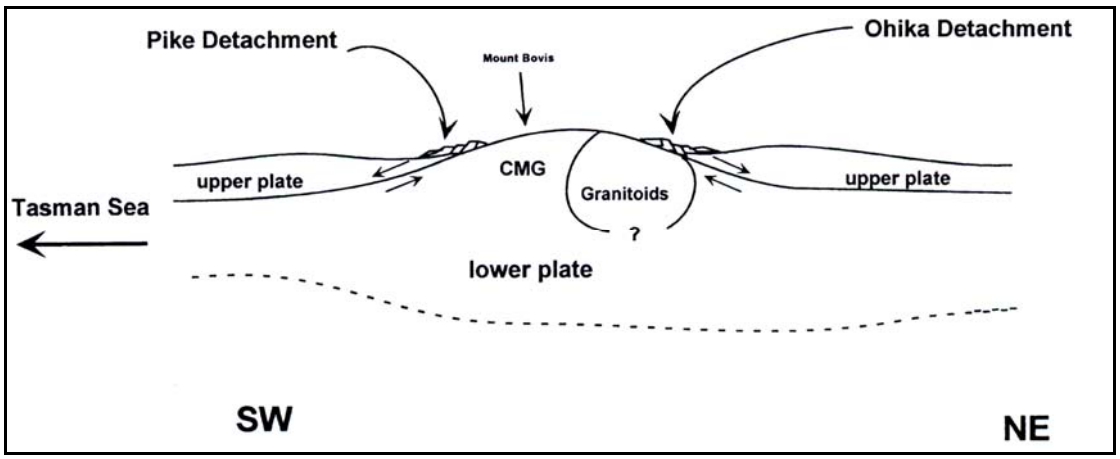

Figure 2.1: Schematic crosssection showing the basic structure of the Paparoa Metamorphic Core Complex, with the Ohika and Pike Detachment Faults located on the north-eastern and south-western sides of the isostatically uplifting Lower Plate. The deformed Charleston Metamorphic Group (CMG) rocks and granitoids are shown in the Lower Plate, with the Pororari Group sediments adjacent to both detachment faults in the Upper Plate (Spell et al. 2000).

The onset of ductile deformation in the Paparoa Metamorphic Core Complex is recorded at 114 ± 18 Ma in the Charleston Metamorphic Group orthogneiss (Kimbrough and Tulloch 1989), and at 116.2 ± 5.9 Ma in the ultramylonite at Morrisey Creek (Ring et al. 2006). Ductile deformation took place under upper-amphibolite facies metamorphic conditions, as recorded in deformed feldspars within mylonitic rocks of the Lower Plate (Hutton et al. 1990, White 1994).
Continental extension was facilitated by this ductile regime, through the mechanism of ductile flow at depth, resulting in the isostatic uplift of the Lower Plate through detachment faulting. Isostatic uplift may have been further accelerated by the coeval emplacement of the Buckland Granite.

The Buckland Granite was emplaced into the Lower Plate at 109.6 ± 1.7 Ma (Muir et al. 1992), covering an area of approximately 180 km². However, there is only one

single U-Pb age known for the Buckland Granite and the question is whether this age is actually representative for the intrusion age of the huge pluton.

The biotite-muscovite + garnet granite displays the characteristic mineralogy expected for plutons emplaced under an extensional regime, with approximately 1km² of the pluton being garnet bearing (Coney 1980, Graham and White 1990). Sedimentary material became incorporated into the Buckland Granite magma during its emplacement, resulting in the inheritance of pre-existing zircons from a variety of sources. The presence of sedimentary input into the Buckland Granite allows the pluton to be classified as a S-type granite, with low temperature S-type melts generally becoming more felsic as they evolve through the crust (Chappell and White 1974, Chappell and White 1992, Clemens 2003, Chappell et al. 2004).

The last stages of ductile shearing within the Paparoa Range are recorded within the Buckland Granite, which suffered from varying degrees of ductile deformation during emplacement (Muir et al. 1992, Waight et al. 1998b, Spell et al. 2000). Emplacement of the Buckland Granite post-dated the timing of upper amphibolite-facies metamorphism of the Charleston Metamorphic Group orthogneisses, as reflected in the metamorphic mineralogy of the pluton (Tulloch and Kimbrough 1989, White 1994).

The presence of an undeformed lamprophyre dike in the Lower Buller Gorge area provides relative timing on the cessation of ductile deformation at that location, with an age of c. 80 to 86 Ma (Tulloch and Kimbrough 1989).

The onset of upper crustal extension is believed to post-date the ductile regime by 5 to 10 Ma (Tulloch and Kimbrough 1989, Laird 1993, Muir et al. 1997). However,

strain-compatibility arguments make this inference questionable because upper and lower crust have to undergo the same amount of extension at the same time.

Extension within the upper crust was accommodated by the development of high-angle normal faults striking approximately 120˚, which tilted to form low-angle detachment faults through the rotation of crustal blocks of the Upper Plate (Tulloch and Kimbrough 1989).

The detachment faults at either end of the complex became footwalls to the newly forming, asymmetric non-marine basins. The coeval metamorphic unroofing of the Lower Plate fed clastic material into the basins adjacent to the Ohika Detachment Fault from c. 102 to 90 Ma, to form the Hawks Crag Breccia of the Pororari Group (Tulloch and Palmer 1990, Muir et al. 1992, Spell et al. 2000). Clast compositions record changes in source material during metamorphic unroofing, with an upward change from clasts of the Greenland Group metasediments, to the incorporation of granitoid clasts (Nathan 1978, Tulloch and Palmer 1990). The timing of deposition of the Hawks Crag Breccia in basins adjacent to the Pike Detachment Fault, however, is not well constrained due to a lack of a dateable horizon. It is possible that the breccia older in the southern basins may be c. 15 Ma older than the northern deposits.

Extension is suggested to have initially been controlled by exhumation along the Ohika Detachment Fault, and is proposed to predate the Pike Detachment Fault (Tulloch and Palmer 1990, Spell et al. 2000). Deposition of c. 102 Ma Hawks Crag Breccia in the northern basins is proposed to have taken place during this early stage of metamorphic unroofing, along the transport direction of the Ohika Detachment Fault (Tulloch and Kimbrough 1989). Exhumation along the Ohika Detachment Fault encouraged the emplacement of the c. 109 Ma Buckland Granite into the thinning

Lower Plate adjacent to the shear zone. However, the timing of deposition of the Hawks Crag Breccia and of emplacement of the Buckland Granite does not fit, as the Hawks Crag Breccia (containing Buckland Granite clasts) is considerably younger than the pluton. If the Ohika detachment moved already by 109 Ma and the Buckland granite was synkinematic to the detachment, then the critical question would be as to where the upper crustal extension has been accommodated between 109 and 102 Ma.

Thermal relaxation of the crust followed, causing the locking up of the Ohika Detachment Fault and subsequent shift in exhumation along the newly forming Pike Detachment Fault (Spell et al. 2000).

Movement along the Pike Detachment Fault resulted in the dragging of the syntectonic Buckland Granite to the south at depth during emplacement, accelerating the cooling and metamorphic unroofing of the pluton (Hutton et al. 1990, Waight et al. 1998b, Spell et al. 2000). The dominance of Buckland Granite clasts within the Hawks Crag Breccia in the southern basins can be accounted for by the dragging of the pluton and the then adjacent Hawks Crag Breccia deposits to the south (Graham and White 1990, Spell et al. 2000).

Beds within the Hawks Crag Breccia, deposited parallel to the adjacent detachment faults during exhumation, became rotated towards the centre of the metamorphic core complex under the brittle regime – resulting in the tilting of beds towards the uplifted Paparoa Range (Tulloch and Kimbrough 1989, Spell et al. 2000). The tilting of the Hawks Crag Breccia continued after deposition ceased, through continued exhumation along the detachment faults, very soon after the breccia started to be deposited at c. 101-102 Ma (Tulloch and Kimbrough 1989).

The second stage of extension involved the complete separation of the New Zealand section from the Gondwana supercontinent, through the development of oceanic crust by c. 84 Ma (Grindley and Davey 1982). The NNW-SSE Tasman Sea spreading ridge developed perpendicular to the previous extension direction responsible for the Paparoa Metamorphic Core Complex, as expected in Cordilleran-style metamorphic core complexes (Figure 1.7; Coney 1980, Tulloch and Kimbrough 1989). The injection of dikes parallel to the newly forming spreading ridge reflects the change of extension direction, with dikes exploiting previously weakened upper crustal rocks (Tulloch and Kimbrough 1989, Waight 1994, Waight 1995).

The Pike Detachment Fault has been proposed to have continued to be active until c. 85 Ma, based on K-Ar sericite dating, with the Pike Detachment Fault suggested to play a great role in the eventual separation of the New Zealand section from Gondwana through the development of the Tasman Sea Basin (Tulloch and Palmer 1990). The timing of extension, however, is more likely to have ceased earlier, at c. 90 Ma, with ~10-15 Ma of relative quiescence before the complete separation of New Zealand from Gondwana at c. 84 Ma.

2.2. The Paparoa Metamorphic Core Complex

The structure of the Paparoa Metamorphic Core Complex has been investigated by previous authors, with the locations of the Ohika and Pike Detachment Faults being inferred by the tectonic contact seen between Lower and Upper Plate rocks. It is important to note the difficultly in pinpointing the location of detachment faults due to the limited access to outcrops on the West Coast.

The Ohika Detachment Fault outcrops along State Highway 6 in the Lower Buller Gorge, and separates the Greenland Group, Pororari Group and Berlins Porphyry of

the Upper Plate from the Buckland Granite, Railway Quartz Diorite and the Windy Point Granite of the Lower Plate (Figure 2.2; Nathan 1978). No exposure of the Ohika Detachment Fault has been observed, but has been inferred on the basis of brecciated

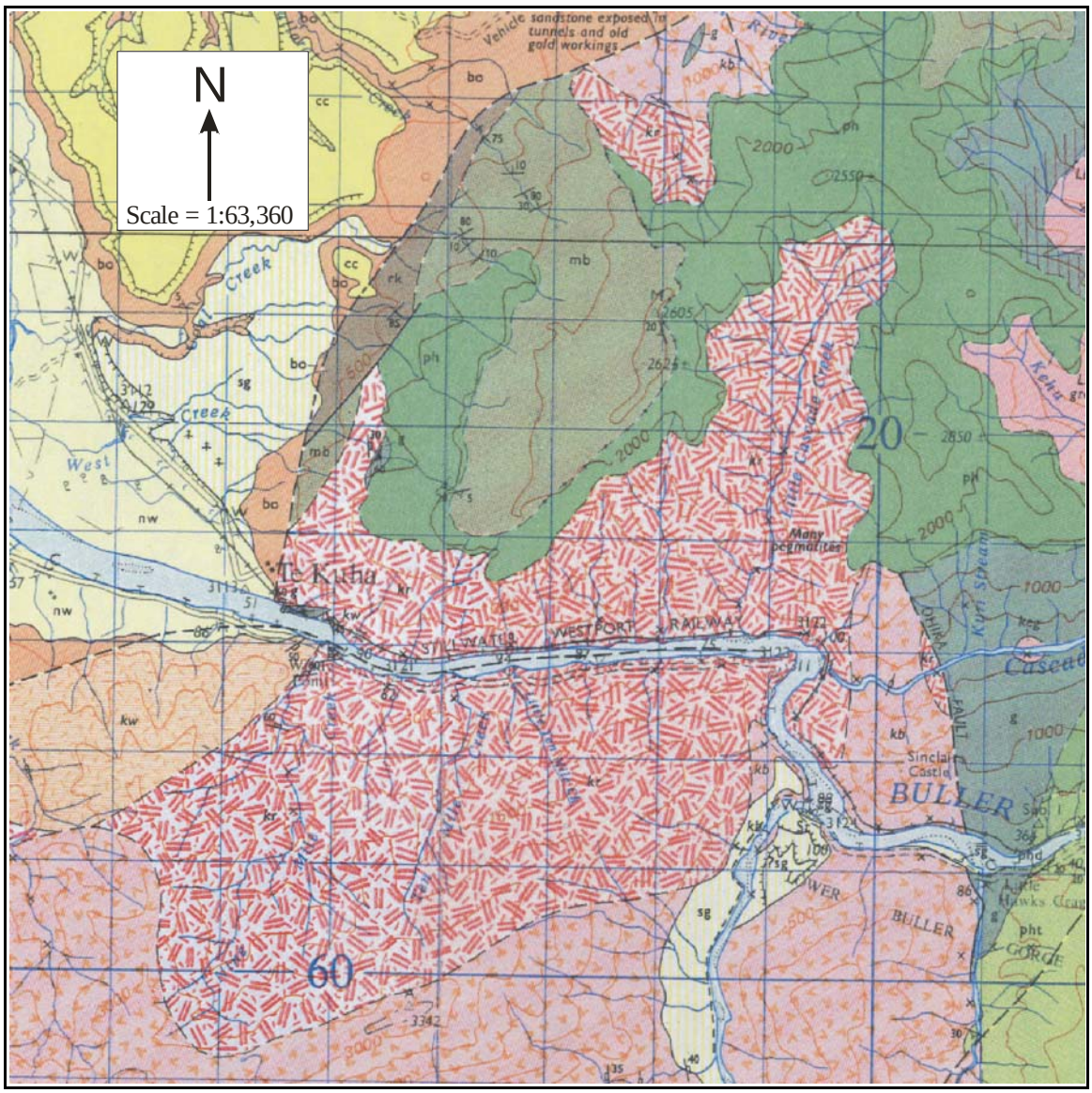

Figure 2.2: Geological map of the Lower Buller Gorge area on the West Coast of New Zealand (Nathan 1978).

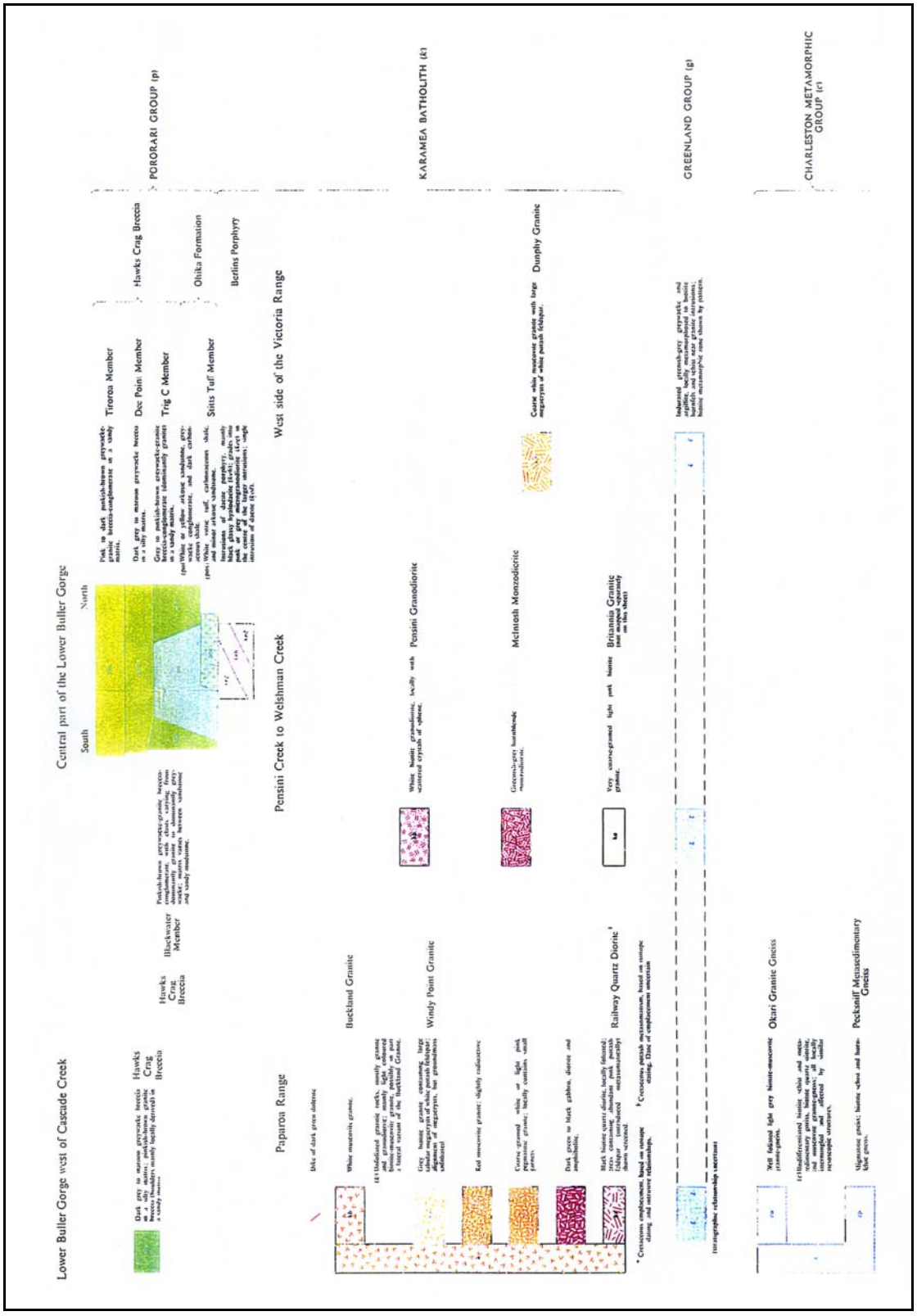

Figure 2.2 (continued): Legend for the geological map of the Lower Buller Gorge area on the West Coast of New Zealand (Nathan 1978).

mylonitic rocks found within the upper reaches of the Orowaiti Rivers (Tulloch and Kimbrough 1989).

The Pike Detachment Fault is located at the southern end of the Paparoa Range in the Pike Stream area (Figure 2.3), extending to the highly deformed rocks exposed along the coastline north of the Fox River Mouth (Figure 2.4; Nathan 1975). Upper Plate rocks in the Pike Stream area are extensively silicified at the top of the range, with large quartz veins running through the Greenland Group metasediments. The silicification of material is thought to represent alteration of rocks adjacent to the shear zone, which may be used to infer the ESE trending contact southwest of Mount Bovis (Tulloch and Kimbrough 1989). The nearby White Knight Stream contains a quartz-rich contact (Nathan 1978), which may represent the continuation of the Pike Detachment Fault to the south. The detachment fault is proposed to have been located a few hundred metres above the current topography in the Pike Stream area, with only the deep crustal equivalent rocks being exposed at present (Tulloch and Kimbrough 1989).

Several models have been proposed for mechanisms responsible for the development of metamorphic core complexes, based on the sense of shear along detachment faults. The uniform-simple model proposed by Wernicke (1985) and Lister and Davis (1989) requires a uniform sense of shear across the whole metamorphic core complex.

The Paparoa Metamorphic Core Complex does not strictly match this model, with opposing sense of shear at either end of the Paparoa Range, associated with movement along the Ohika and Pike Detachment Faults. Opposing shear sense is recorded in the Upper Plate cover rocks, with the tilted Pororari Group units dipping towards the central region of the Paparoa Range (Tulloch and Kimbrough 1989).

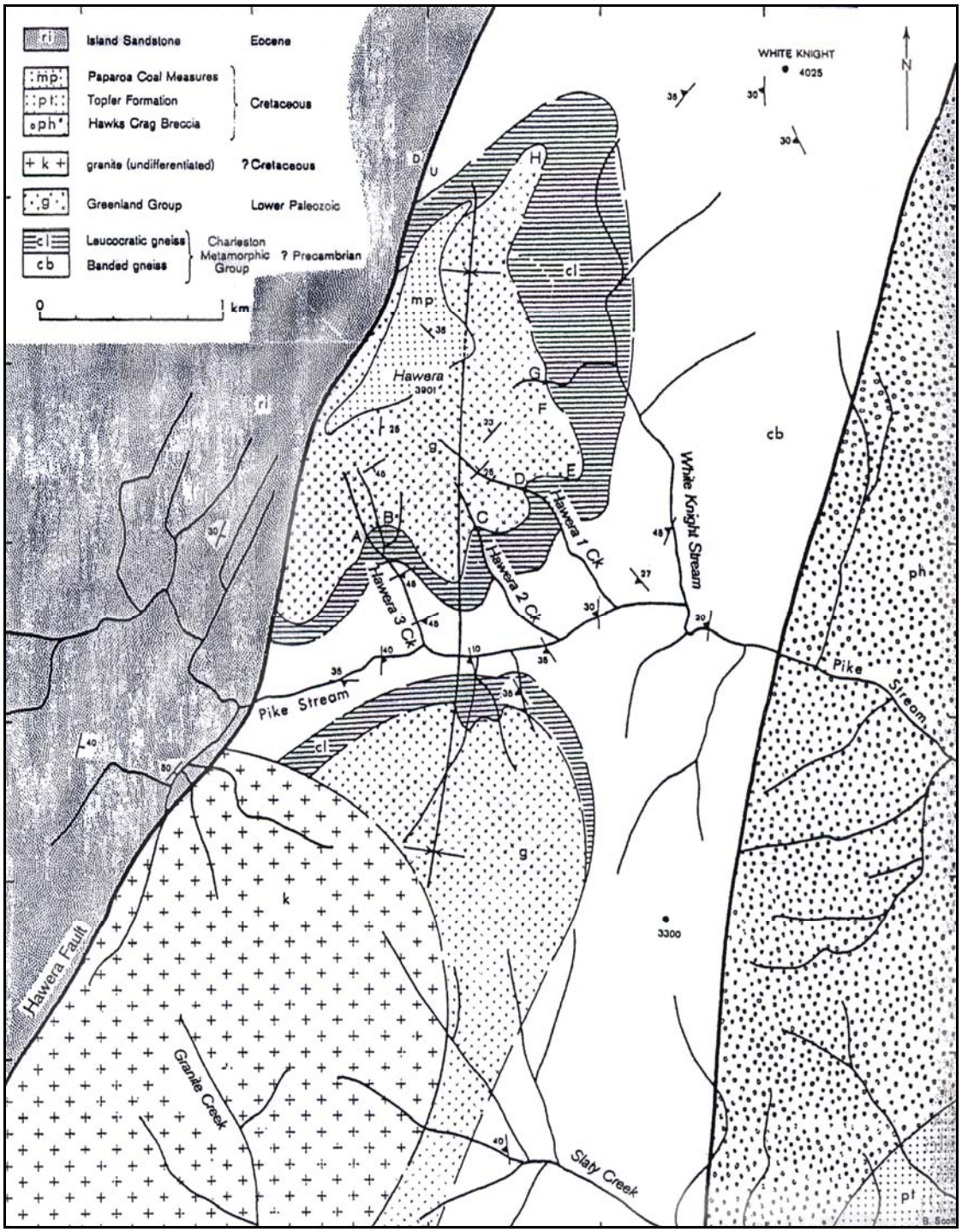

Figure 2.3: Geological map of the Pike Stream area in the Paparoa Range, West Coast, New Zealand (Hume 1977).

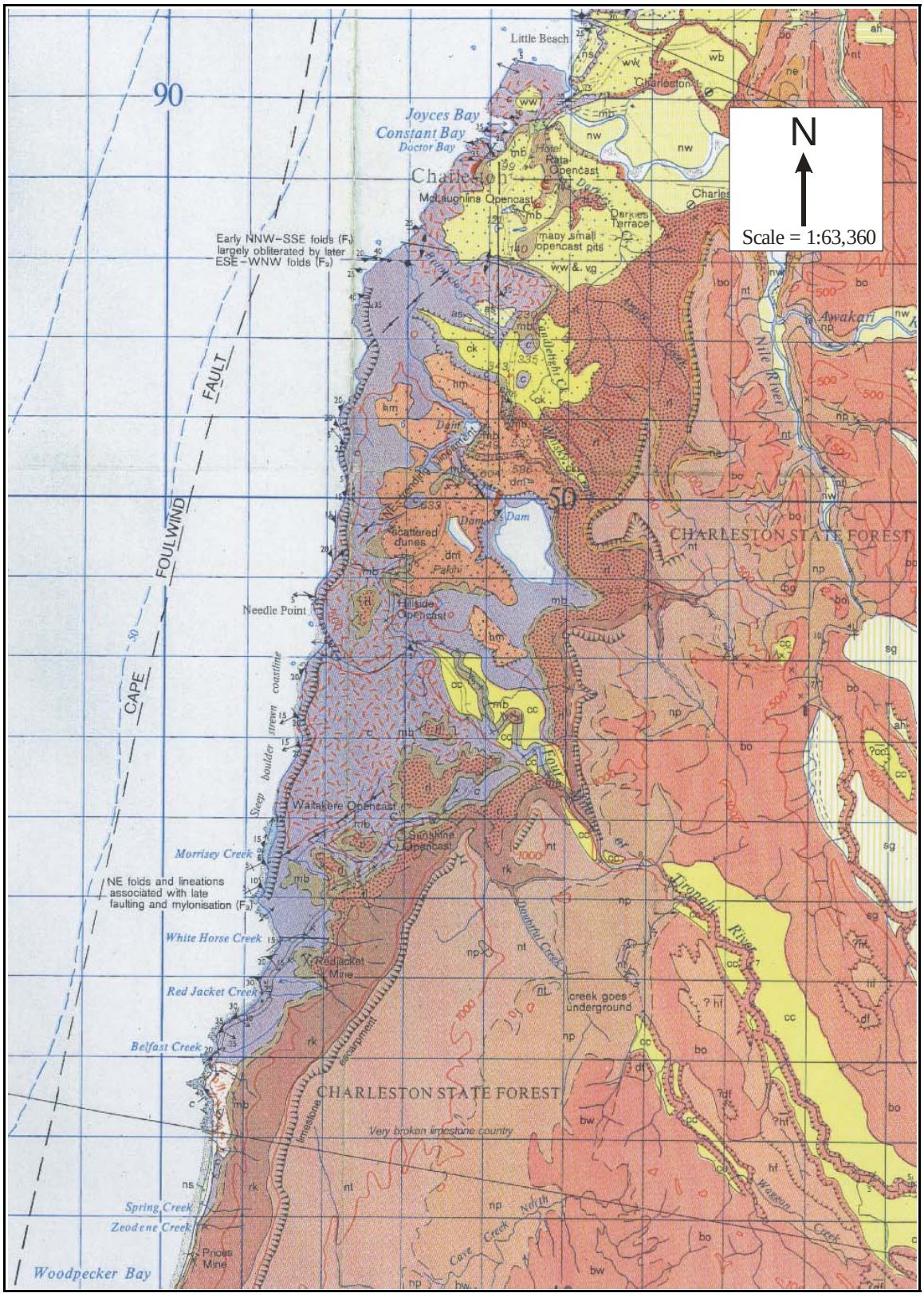

Figure 2.4: Geological map of the Foulwind-Charleston area on the West Coast of New Zealand (Nathan 1975).

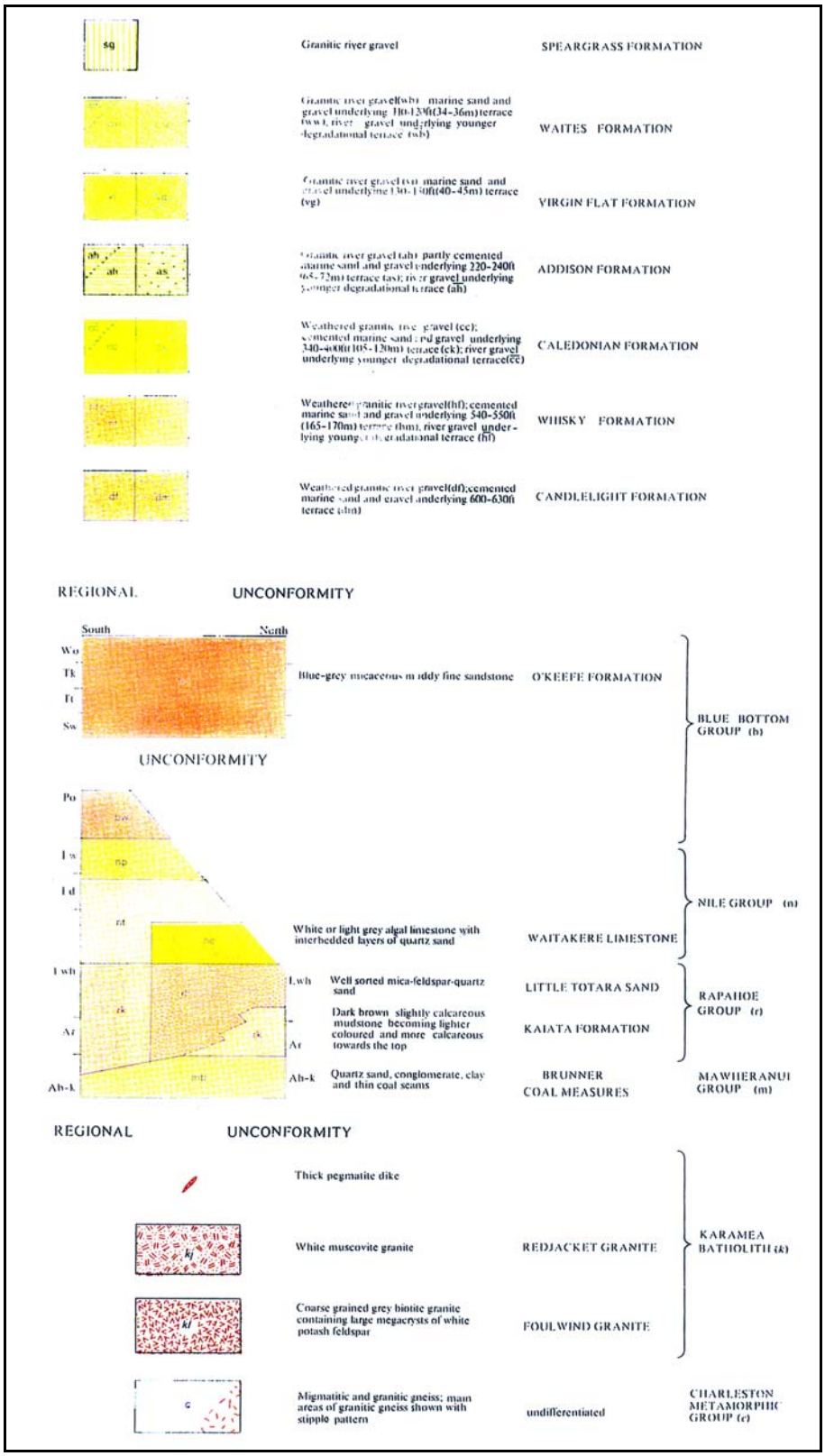

Figure 2.4 (continued): Legend for the geological map of the Foulwind-Charleston area on the West Coast of New Zealand (Nathan 1975).

Exhumation and slip rates have been calculated for the Paparoa Metamorphic Core Complex detachment faults, based on a variety of techniques. Exhumation rates reflect a vertical component of movement, while slip rates refer to movement along a fault plane at any particular angle.

Tulloch and Palmer (1990) calculated a minimum slip rate of 1.1-1.4 mm/yr from depths of c. 25km, from Buckland and Blackwater Granite clasts in the Hawks Crag Breccia deposits adjacent to the Ohika Detachment Fault in the Lower Buller Gorge. The slip rate along the Pike Detachment Fault was calculated to be 0.6-1.0mm/yr – a slower rate than that proposed by Tulloch and Palmer (1990). Pressure and temperature estimates for the Charleston Metamorphic Group rocks adjacent to the Pike Detachment Fault were calculated at 4 ±1 kbar and 600 ± 50˚C, respectively (White 1994). Based on the P-T estimates, a geothermal gradient of c. 50-90˚C/km for the Paparoa Metamorphic Core Complex was calculated by White (1994).

The proposed geothermal gradients of White (1994) were used in a later paper by Spell and co workers (2000), for the calculation of cooling rates for exhumed rocks within the Paparoa Metamorphic Core Complex. A cooling rate of c. 110˚C/Ma was proposed for the c. 330˚C cooling of rocks from c. 500-170˚C, with 4-7km of exhumation along the Pike Detachment Fault at a slip rate of 1-2mm/yr.

2.3. Own observations

Additional observations were made during the period of field work, with the adoption of a basement deformation classification scheme in areas adjacent to both the Ohika and Pike Detachment Faults to determine whether the degree of ductile deformation increases towards the shear zones as expected.

The deformation of Lower Plate rocks in the Lower Buller Gorge was found to follow a progressive increase towards the inferred Ohika Detachment Fault, ranging from outcropping undeformed granitoid rocks through to orthogneiss (Figure 2.5). No mylonite was directly observed during the period of field work, but mylonitic float sourced from the upper reaches of the Little Cascade Creek has been noted by earlier investigations (Ledlie 1989-1990). The increased deformation of rocks adjacent to the Ohika Detachment Fault follows the expected pattern of metamorphic gradients. However, deformation directly below the Ohika Detachment Fault is entirely cataclastic in nature, and resulted in a several hundred metres thick cataclastically deformed zone in the footwall of the Ohika Detachment Fault.

Contact metamorphism of the Greenland Group metasediments resulted in the development of andalusite, probably in response to the emplacement of the Buckland Granite into the Lower Plate. The andalusite present within the cataclastic Upper Plate rocks is immediately juxtaposed against the Buckland Granite, suggesting the offset along the Ohika Detachment Fault was relatively limited.

Rocks of the Pike Stream area experienced a high degree of exhumation, with mylonitic deformation observed. Deformation becomes cataclastic towards the inferred Pike Detachment Fault, with the overall nature of deformation being heterogeneous (Figure 2.6). The heterogeneous pattern of deformation is also observed in the coastal section north of the Fox River Mouth. Lower Plate rocks exposed at the coastline show a progressive decrease in metamorphic grade towards the shear zone, with undeformed granitoid rocks and cataclastic rocks outcropping near the inferred detachment fault. Ductile deformation becomes increasingly stronger

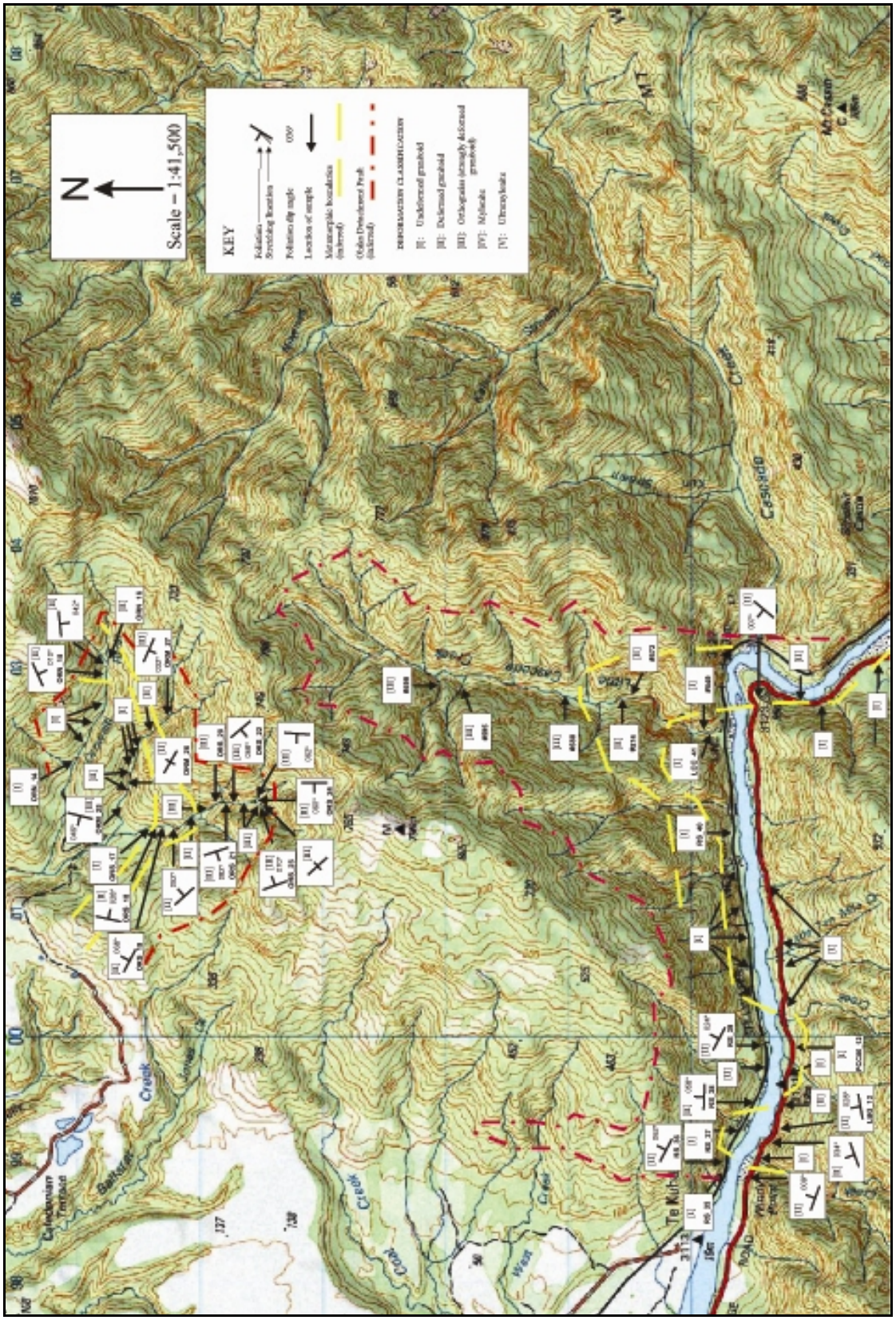

Figure 2.5: Geological map of own observations in the Lower Buller Gorge area, with granitoid rocks being classified under the adopted basement deformation scheme (from I to III). Locations of samples for geochemical analyses are shown (RS-35 to RS-40), with foliation and lineation measurements shown for deformed granitoids. The inferred location of the Ohika Detachment Fault is shown. Scale = 1:41,500

Figure 2.6: Geological map of own observations in the Pike Stream area of the Paparoa Range, with granitoid rocks being classified under the adopted basement deformation scheme (from II to IV). Scale = 1:33,300.

to the north, through deformed granitoid rocks to the mylonites and ultramylonites of Morrisey Creek (Figure 2.7).

Greater exhumation took place along the Pike Detachment Fault compared to the Ohika Detachment Fault, with greater offset occurring along the Pike Detachment Fault to allow the exhumation of the mylonites and ultramylonites of Morrisey Creek. The ductile deformation of basement rocks along the coastline section does not follow the expected pattern, with respect to the inferred location of the Pike Detachment Fault. Deformation is observed to be heterogeneous, where mylonitisation took place at depth and became cataclastically overprinted towards the detachment. This rapid transition from ultramylonites (c. 350-500˚C) to cataclasite (c. 150-250˚C) is exposed over a distance of c. 500m along the coastline. Using this 350-500˚C temperature difference and the geothermal gradient of 50-90˚C/km (White 1994), an estimated 4-10km of material is cut out over the distance of c. 500m. Mylonites of the Paparoa Metamorphic Core Complex record NNE stretching lineations plunging to both the north and south of the Paparoa Range, which is regionally consistent with the transport directions of Upper Plate rocks during exhumation (Tulloch and Kimbrough 1989). The majority of deformed rocks at Morrisey Creek have NE trending stretching lineations, with NE-SW oriented foliations (Figure 2.7). Stretching lineations in the Lower Plate rocks are oriented sub-parallel to the earlier subduction zone along the eastern margin of Gondwana, and perpendicular to the later Tasman Sea spreading centre (Tulloch and Kimbrough 1989, Tulloch and Palmer 1990).

2.4 Hand specimens

Hand specimens were collected from the Lower Buller Gorge area (samples RS-35 to RS-40) and the coastline north of Fox River Mouth (sample PCC06-01).

Figure 2.7: Geological map of own observations along the coastal section north of Fox River Mouth (inset), with granitoid rocks being classified under the adopted basement deformation scheme (from II to V). Location of samples for geochemical analyses are shown (PCC06-01 and PCC06-02), with foliation and lineation measurements shown for deformed granitoids. The inferred location of the Pike Detachment Fault is shown. Scale of inset = 1:33,300; scale of coastline = 1:50,000.

River Mouth (Figures 2.5 and 2.7). The Lower Plate rocks collected within the Lower Buller Gorge (hand specimens RS-35 to RS-40) all display variation in the degree of deformation, from relatively undeformed to slightly deformed in nature. The mylonite hand specimen (PCC06-01), sourced north of the Fox River Mouth, displays a distinct mylonitic fabric, with smeared feldspar phenocrysts housed within a sheared matrix. The alignment of micas produces the strong mylonitic foliation, with lenses of recrystallised quartz running sub-parallel to this.

2.5 Thin section work

The use of optical mineralogy aids interpretations into the nature of deformation within the Paparoa Metamorphic Core Complex, through the study of microstructures. Observations and interpretations into the 'microtectonics' of rocks at the thin section-scale are made in reference to the work by Passchier and Trouw (1996).

Intracrystalline deformation is suggested by the presence of undulose extinction, which develops in response to dislocations in the crystal lattice during deformation. Deformation of feldspar twins may also occur during metamorphism, resulting in the bending and/or fracturing of twin planes.

Thin sections were cut from hand specimens RS-35 to RS-40 and PCC06-01, with sections being cut perpendicular to foliation (if present). Estimated percentages of mineralogy are listed in Table 2.1, with observations from each sample being discussed below.

RS-35		RS-36		RS-37	
Chlorite:	30%	Quartz:	40%	Quartz:	30%
Quartz:	25%	Chlorite:	10%	Chlorite:	30%
Alk. Feldspar:	15%	Biotite:	20%	Alk. Feldspar:	25%
Plag. Feldspar:	15%	Alk. Feldspar:	10%	Plag. Feldspar:	10%
Biotite:	<5%	Plag. Feldspar:	10%	Muscovite:	<5%
Zircon:	<5%	Muscovite:	<5%	Biotite:	<1%
Muscovite:	<5%	Zircon:	<5%	Magnetite:	<1%
Magnetite:	<1%	Magnetite:	<1%	Zircon:	<1%

RS-38		RS-39		RS-40	
Quartz:	25%	Quartz:	30%	Quartz:	40%
Chlorite:	20%	Alk. Feldspar:	25%	Alk. Feldspar:	20%
Alk. Feldspar:	25%	Plag. Feldspar:	20%	Plag. Feldspar:	15%
Plag. Feldspar:	10%	Biotite:	10%	Chlorite:	10%
Muscovite:	10%	Muscovite:	10%	Muscovite:	10%
Biotite:	<5%	Chlorite:	<5%	Biotite:	<5%
Magnetite:	<5%	Magnetite:	<1%	Zircon:	<1%
Zircon:	<1%	Zircon:	<1%		

PCC06-01	
Quartz:	30%
Biotite:	30%
Plag. Feldspar:	15%
Alk. Feldspar:	10%
Muscovite:	10%
Zircon:	<5%
Magnetite:	<1%

Table 2.1: Percentage estimates of thin sections for hand specimens RS-35 to RS-40 from the Lower Buller Gorge area and hand specimen PCC06-01 from the coastal section north of Fox River Mouth.

Sample RS-35 (Figure 2.8a and 2.8b):

Chlorite comprises a large percentage of the total minerals present, resulting from the alteration of biotite. Chlorite grains are subhedral in shape.

Quartz minerals have experienced dynamic recrystallisation, and display both undulose extinction and fluid inclusion trails. Quartz grains are anhedral in shape.

Feldspar minerals present include alkali- and plagioclase feldspar, with both albite and pericline twins observed. Some feldspar grains exhibit undulose extinction and fluid inclusion trails, however, no deformation of twinning is observed. Feldspar grains are subhedral to anhedral in shape.

Minor amounts of biotite and muscovite are present, which are both anhedral in shape. A small percentage of magnetite and zircon grains are present.

This specimen is largely undeformed at the thin section scale, with an overall seriate-interlobate grain distribution pattern (I in the deformation classification scheme).

Sample RS-36 (Figures 2.8c and 2.8d):

Quartz grains are equigranular to anhedral in shape, with undulose extinction and fluid inclusion trails present. Obvious dynamic recrystallisation has occurred.

Chlorite grains are acicular in shape, and have developed in response to the alteration of biotite. Acicular grains of biotite are reddy-brown in appearance, and are aligned in an obvious foliation.

Feldspars present include alkali- and plagioclase feldspar, which are anhedral in shape. Feldspar minerals are very fine grained in response to extensive dynamic recrystallisation. Anhedral muscovite grains are accompanied by a small number of zircon and magnetite minerals.

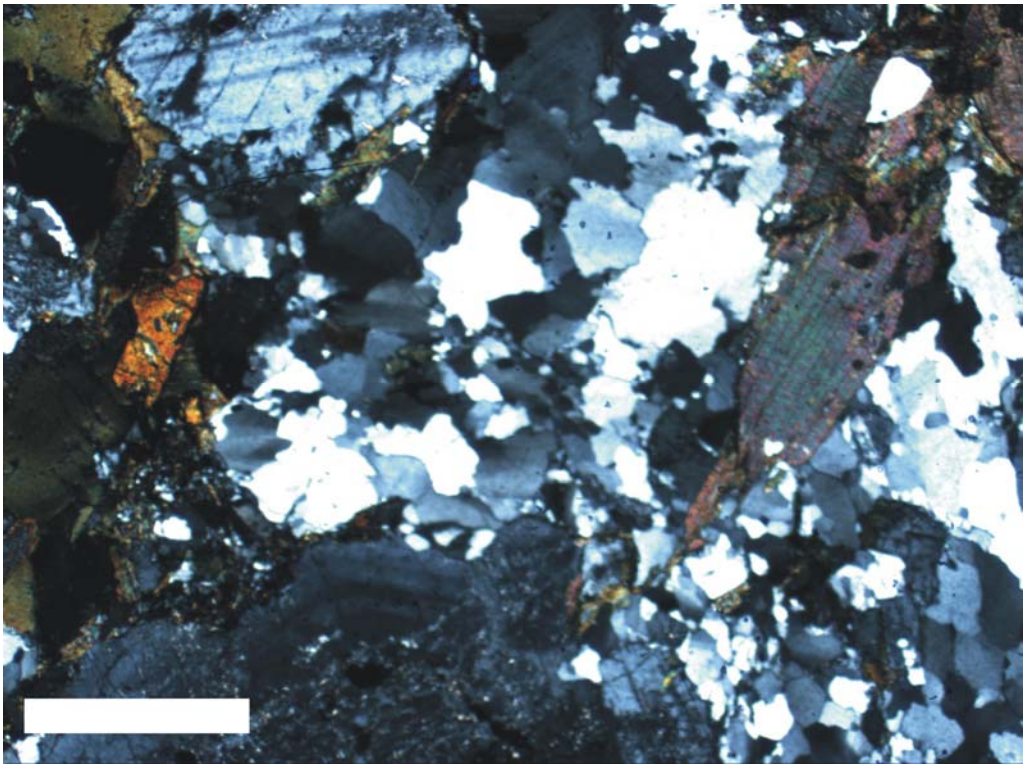

Figure 2.8a: Thin section image of RS-35 at 2.5x mag. Scale bar: 1cm. CPL. Note the limited deformation (dynamic recrystallisation of quartz grains).

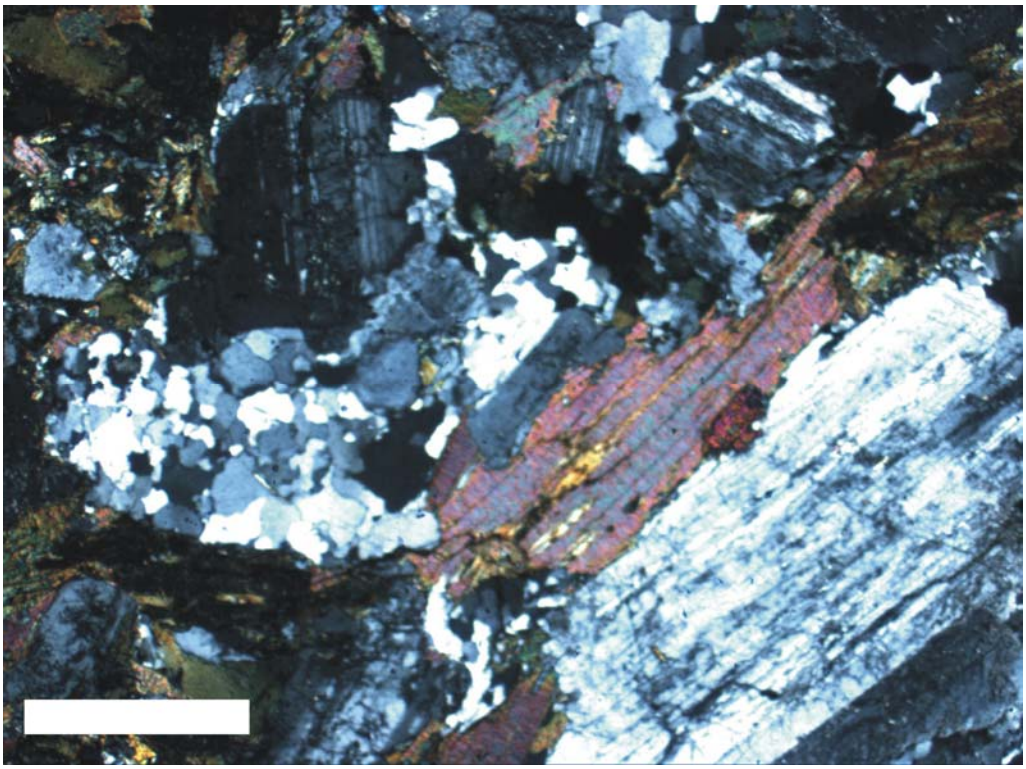

Figure 2.8b: Thin section image of RS-35 at 2.5x mag. Scale bar: 1cm. CPL. Note the limited deformation (dynamic recrystallisation of quartz grains).

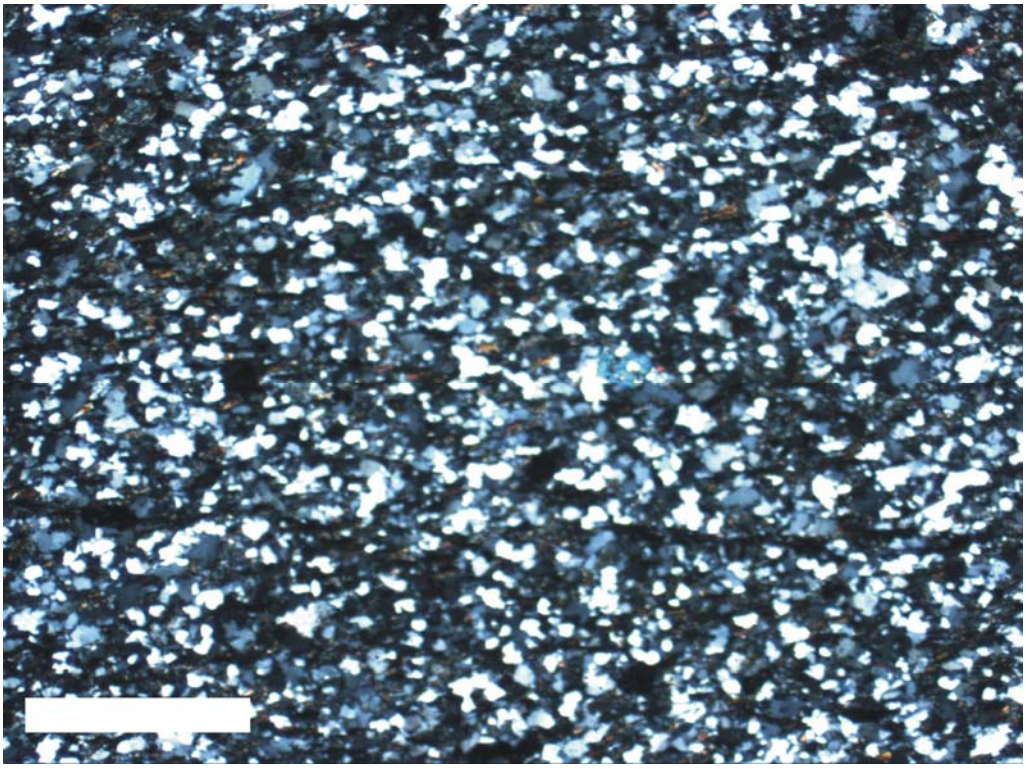

Figure 2.8c: Thin section image of RS-36 at 2.5x mag. Scale bar: 1cm. CPL. Note the dynamic recrystallisation of quartz and feldspar and the beginnings of foliation development

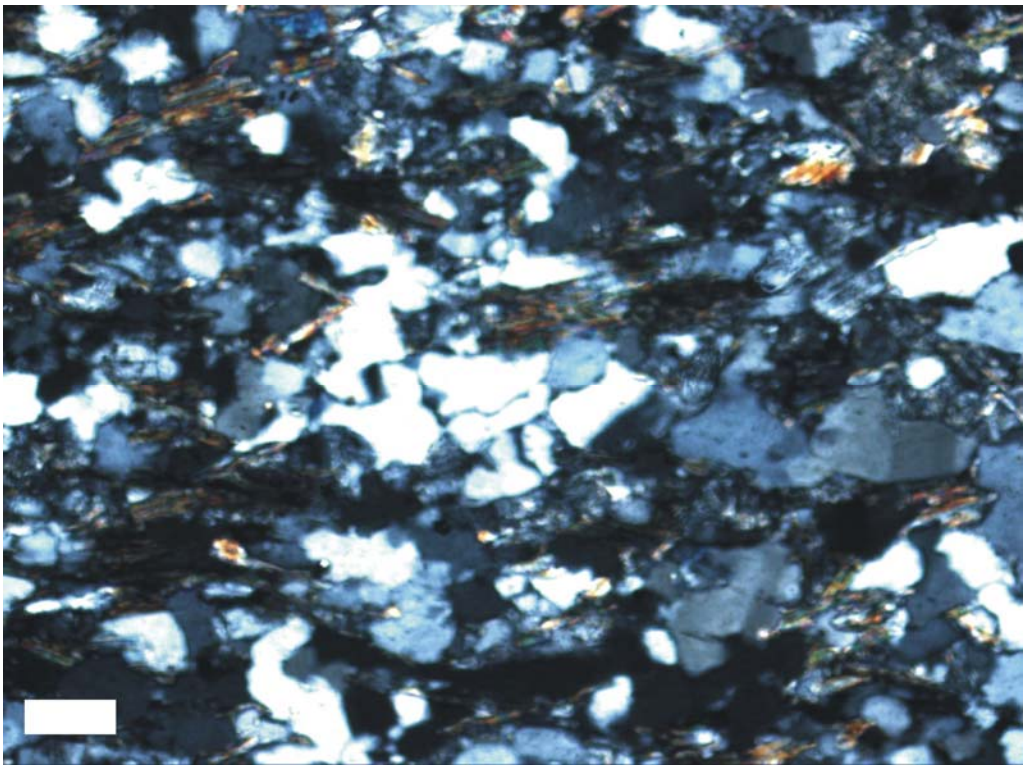

Figure 2.8d: Thin section image of RS-36 at 10x mag. Scale bar: 1cm. CPL.

This specimen appears to have experienced a small degree of deformation, resulting in the inequigranular, fine grained appearance of the sample, and the beginnings of foliation development (II in the deformation classification scheme).

Sample RS-37 (Figures 2.8e and 2.8f):

Quartz grains are anhedral in shape, with undulose extinction, fluid inclusion trails, and evidence of dynamic recrystallisation.

Alkali- and plagioclase feldspar minerals show both undulose extinction and fluid inclusion trails, with a subhedral grain shape. The larger relic grains show evidence of recrystallisation, and overprinting and/or replacement by rods of muscovite in a myrmekitic fashion. Albite and pericline twinning present, with no obvious deformation of twins.

Chlorite grains are subhedral to anhedral in shape, with undulose extinction. Mica grains show subhedral to anhedral patterns, with the biotite having a reddy-brown appearance. Minor amounts of magnetite and zircon are present.

This specimen is seriate-interlobate in nature, and is considered to be relatively undeformed (I in the deformation classification scheme).

Sample RS-38 (Figures 2.8g and 2.8h):

Quartz grains show evidence for dynamic recrystallisation, with undulose extinction, fluid inclusion trails and quartz ribbons present. Grains are anhedral in shape.

Chlorite and biotite minerals make up the foliation, and are closely associated due to the process of alteration. Grain shapes range from subhedral to acicular in appearance.

Muscovite grains are acicular in shape, aligned parallel to the foliation.

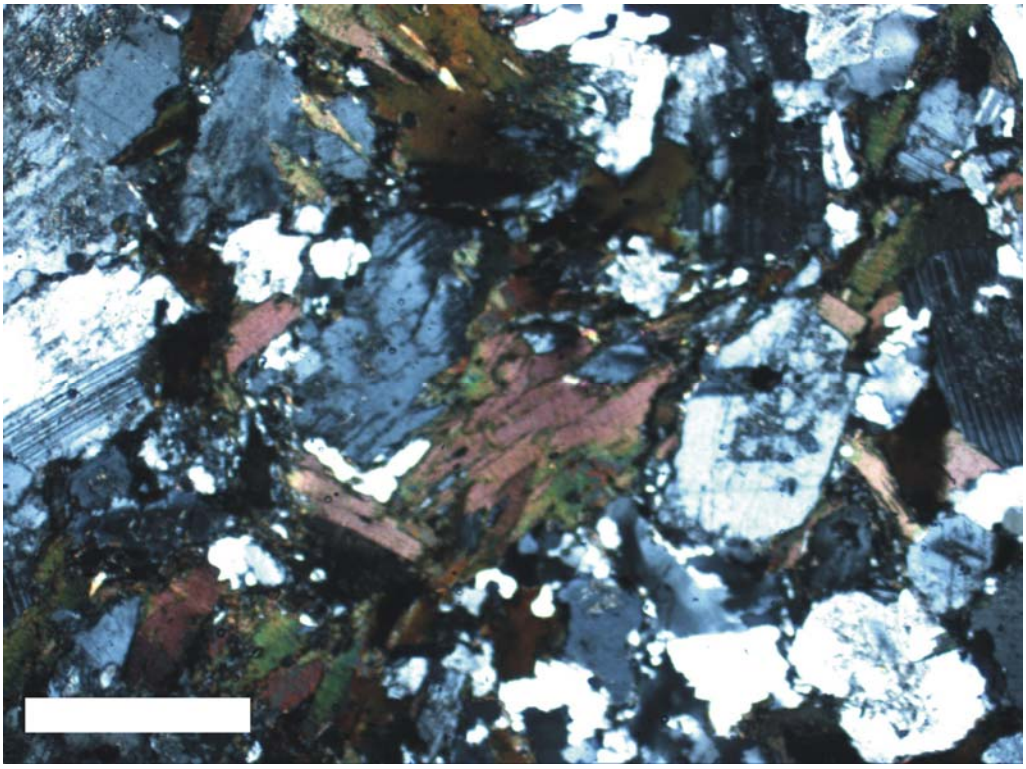

Figure 2.8e: Thin section image of RS-37 at 2.5x mag. Scale bar: 1cm. CPL. Note dynamic recrystallisation of quartz, and overprinting and/or replacement by rods of muscovite in a myrmekitic fashion.

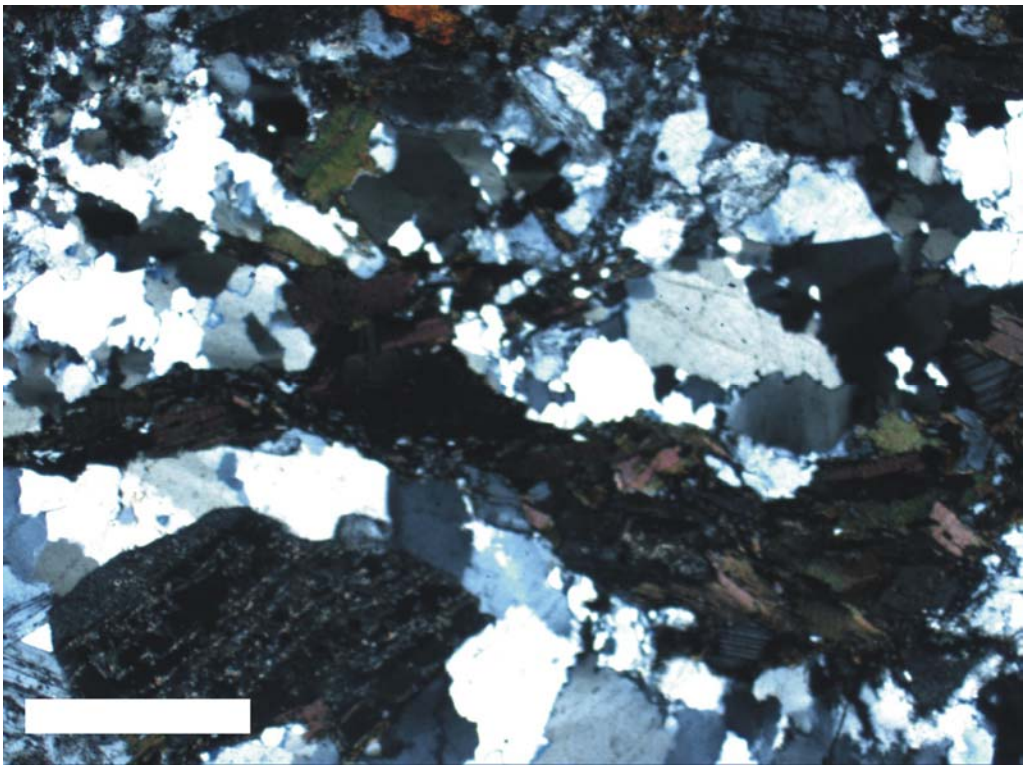

Figure 2.8f: Thin section image of RS-37 at 2.5x mag. Scale bar: 1cm. CPL. Note dynamic recrystallisation of quartz and development of quartz ribbons.

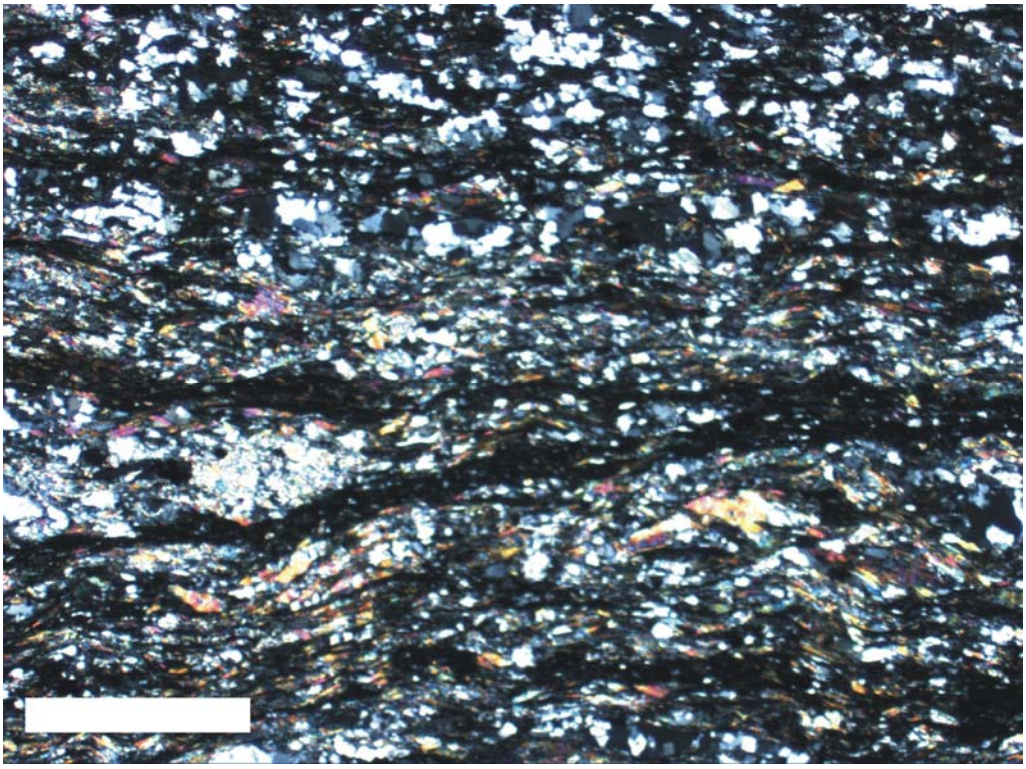

Figure 2.8g: Thin section image of RS-38 at 2.5x mag. Scale bar: 1cm. CPL. Note the distinct foliation, dynamic recrystallisation of quartz and feldspar grains and the development of quartz ribbons.

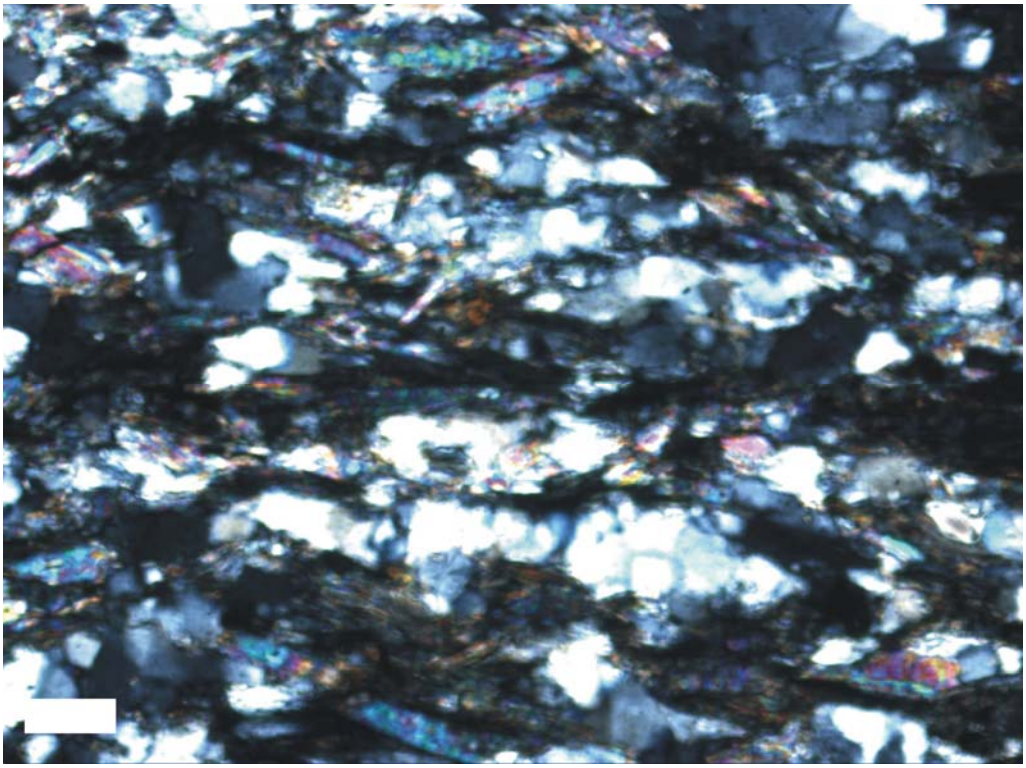

Figure 2.8h: Thin section image of RS-38 at 10x mag. Scale bar: 1cm. CPL.

Feldspar minerals are very fine in grain size, due to the influence of dynamic recrystallisation. No twinning is observed due to the fine grain size.

Small percentages of magnetite and zircon grains are present.

This specimen shows a substantial amount of recrystallisation, with the development of an obvious foliation in an inequigranular fashion (II in the deformation classification scheme).

Sample RS-39 (Figures 2.8i and 2.8j):

Quartz minerals are observed to consist of fine grained areas in which dynamic recrystallisation has occurred, and in the larger, less deformed quartz ribbons. Grains are largely anhedral in shape, with undulose extinction and fluid inclusion trails present.

Feldspar minerals include both alkali- and plagioclase feldspar, which are subhedral to anhedral in shape. The feldspars also show fine grained areas associated with dynamic recrystallisation, and larger relic grains with less extensive deformation. Plagioclase minerals display myrmekitic textures by the inclusion of thin rods of quartz within the relic grains. No deformation of twins observed.

Biotite grains are subhedral to anhedral in shape, and have a reddy-brown appearance. Muscovite grains have subhedral to acicular patterns, with the beginnings of mica fish development.

Chlorite is relatively sparse in this sample, as little observable alteration has taken place. Grains are subhedral to acicular in shape. Minor amounts of magnetite and zircon are present.

This specimen shows some degree of deformation, with dynamic recrystallisation and undulose extinction observed in most minerals present. The overall pattern of

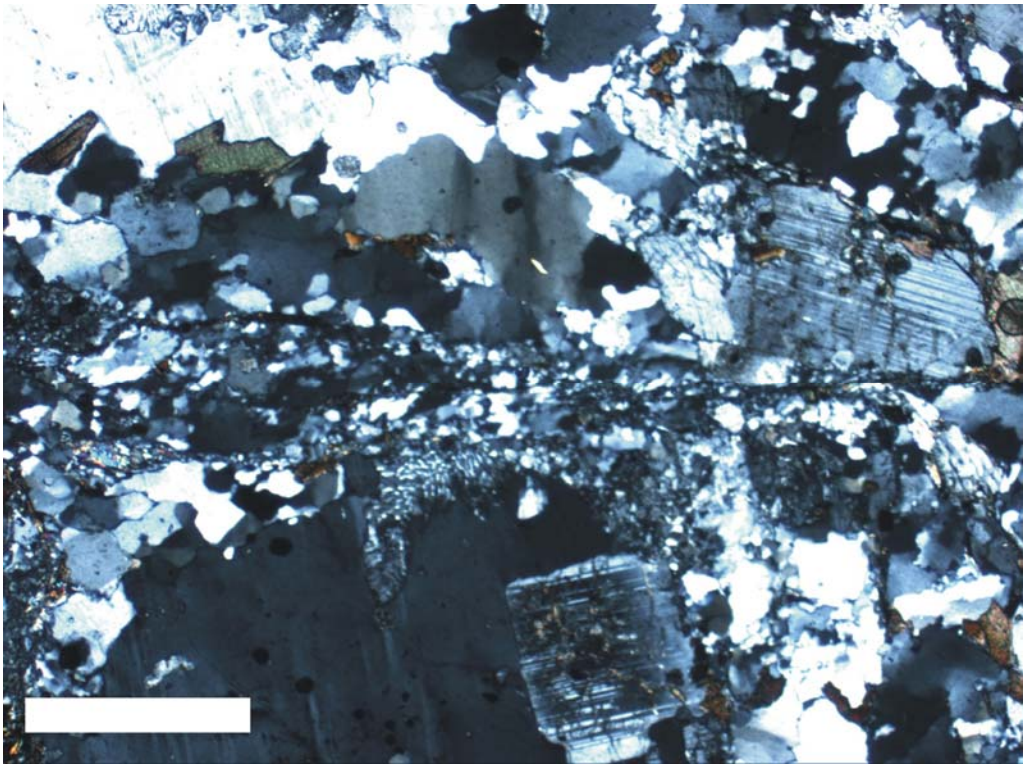

Figure 2.8i: Thin section image of RS-39 at 2.5x mag. Scale bar: 1cm. CPL. Note the dynamic recrystallisation of quartz and feldspar, development of quartz ribbons, and the myrmekitic texture of the feldspar due to the inclusion of quartz rods.

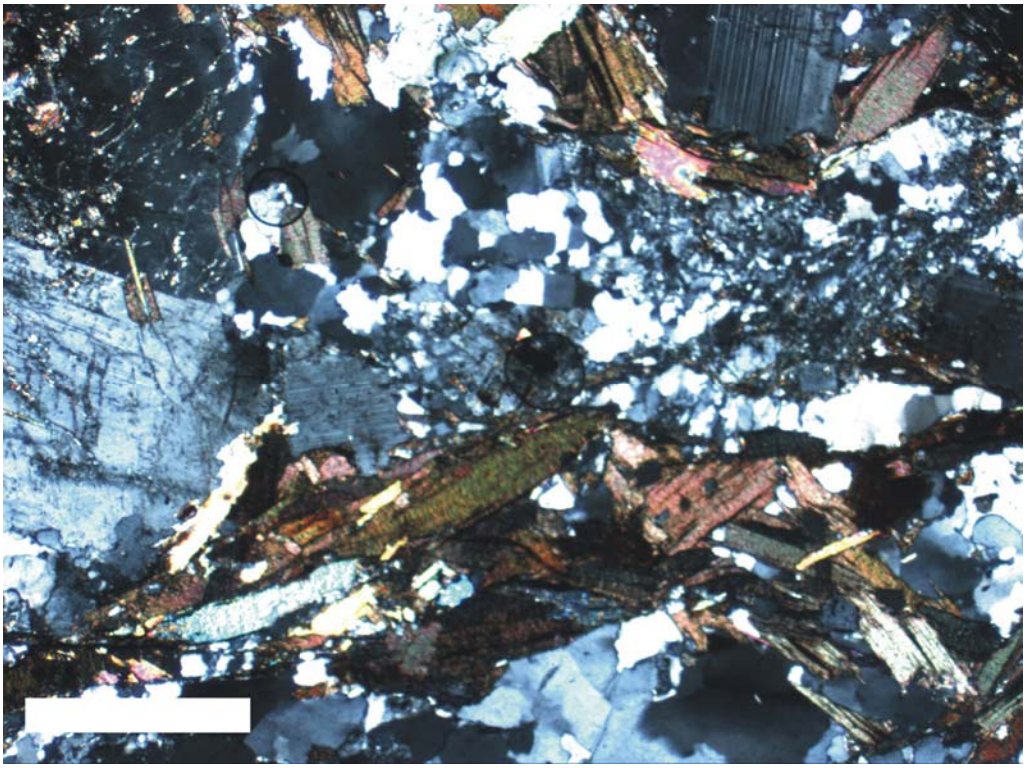

Figure 2.8j: Thin section image of RS-39 at 2.5x mag. Scale bar: 1cm. CPL.

grain shapes is seriate-interlobate in nature (II in the deformation classification scheme).

Sample RS-40 (Figures 2.8k and 2.8l):

Quartz grains are anhedral in shape, with elongate subgrains and fluid inclusion trails present. Dynamic recrystallisation and undulose extinction present.

Feldspar minerals show undulose extinction, dynamic recrystallisation and fluid inclusion trails. Both alkali- and plagioclase feldspar minerals are present, with anhedral grain shapes. Deformed albite and pericline twins are observed, with flame shaped albite lamellae common.

Chlorite grains are subhedral to anhedral in shape. Large muscovite grains are acicular in shape, with the beginnings of mica fish. Biotite grains present are anhedral in shape; however, the majority of grains have been altered to chlorite. Minor amounts of zircon, with no opaques observed.

This specimen is seriate-interlobate in nature, and is considered to have experienced some degree of deformation. Dynamic recrystallisation and undulose extinction is observed in most minerals, with flame shaped albite lamellae and the initiation of mica fish growth also illustrating the degree of deformation (II in the deformation classification scheme).

Sample PCC06-01 (Figures 2.8m and 2.8n):

Quartz minerals display undulose extinction, fluid inclusion trails and evidence for dynamic recrystallisation. Grains are anhedral in shape, with quartz also existing in ribbons.

Reddy-brown biotite grains are subhedral to acicular in shape, aligned in a foliation.

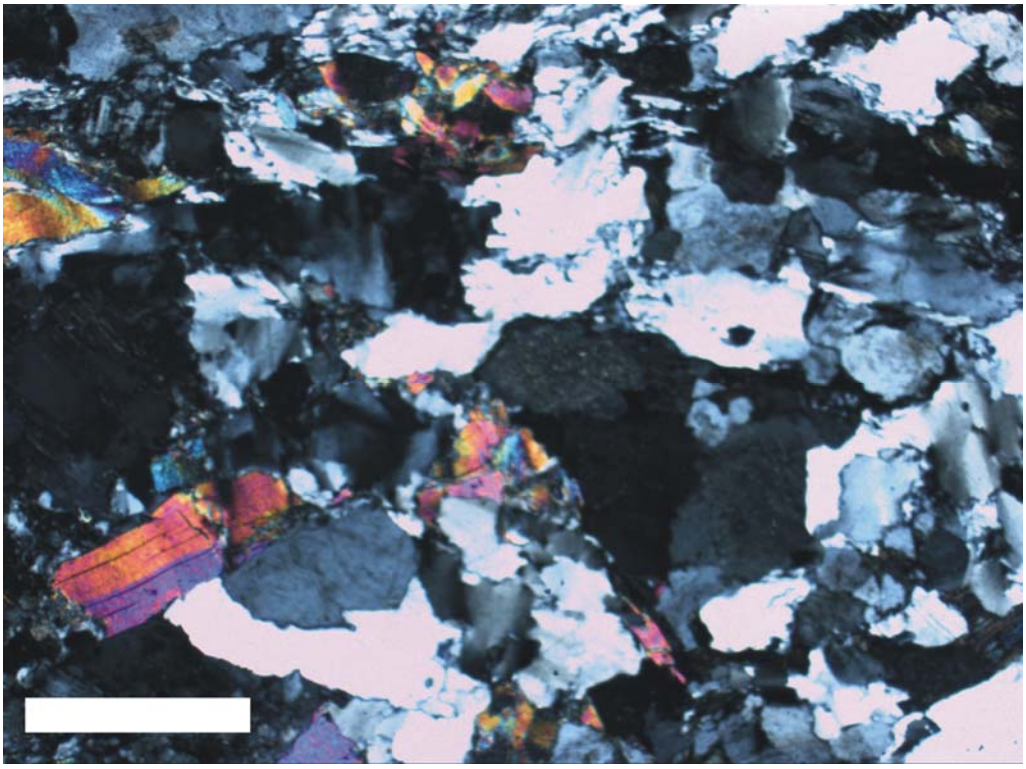

Figure 2.8k: Thin section image of RS-40 at 2.5x mag. Scale bar: 1cm. CPL. Note the dynamic recrystallisation of quartz and feldspar, the deformation of both albite and pericline twins and the beginnings of mica fish.

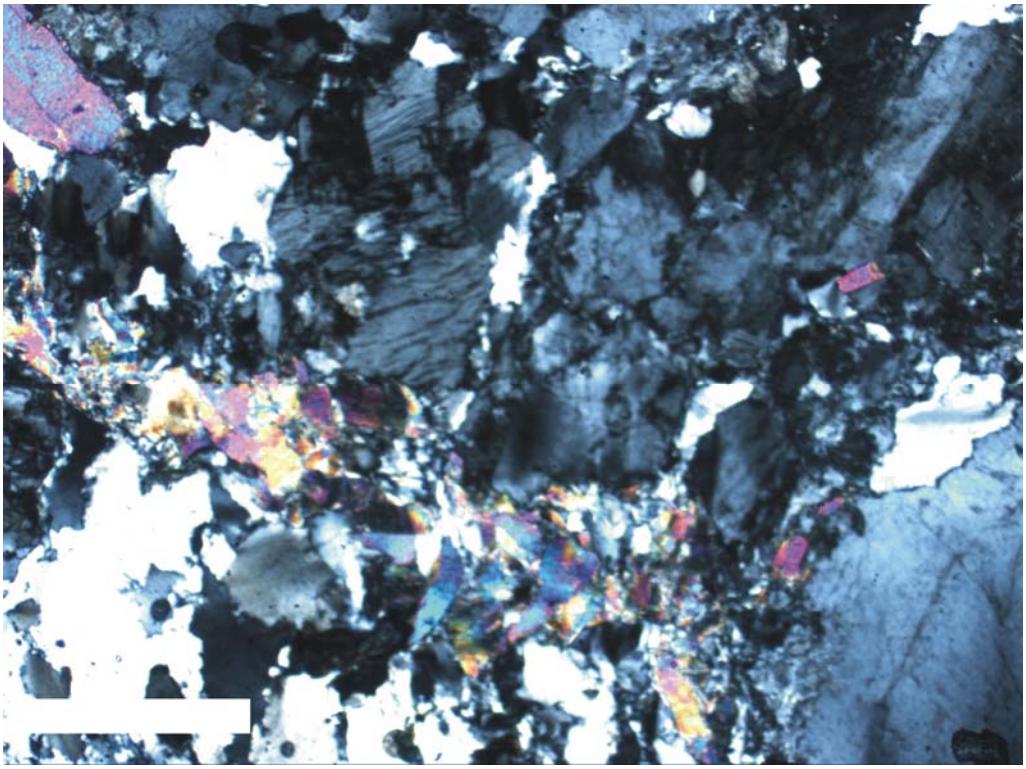

Figure 2.8l: Thin section image of RS-40 at 2.5x mag. Scale bar: 1cm. CPL. Note the presence of flamed shaped lamellae in the feldspar grains and the extensive dynamic recrystallisation of quartz and feldspar.

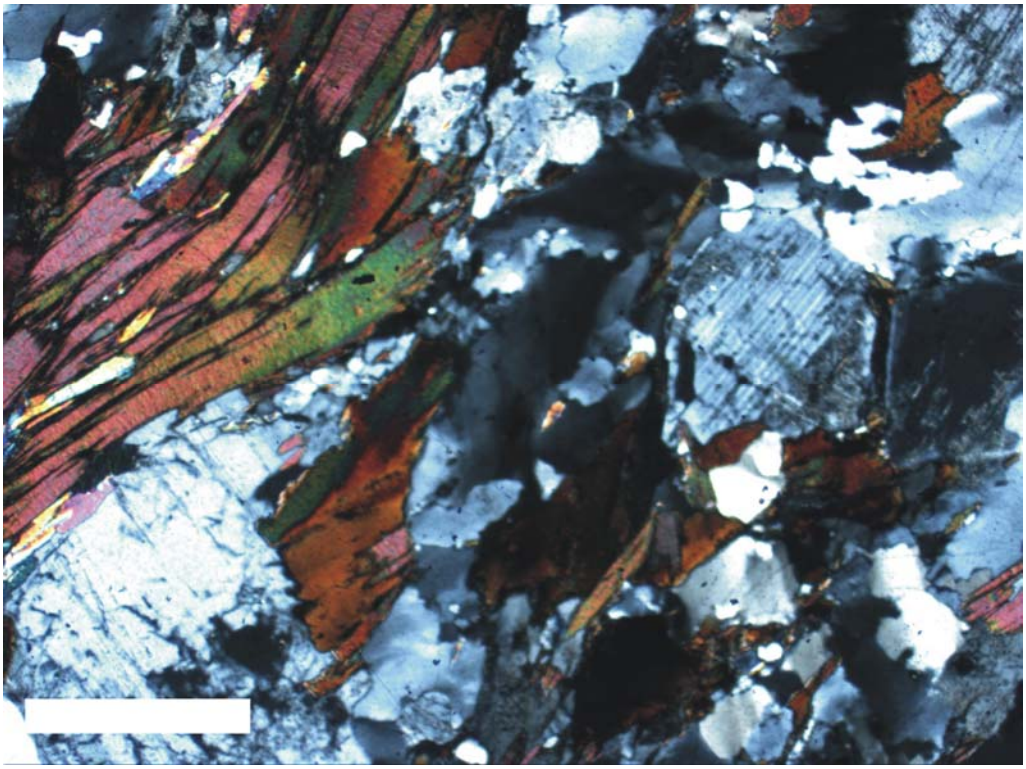

Figure 2.8m: Thin section image of PCC06-01 at 2.5x mag. Scale bar: 1cm. CPL. Note the extensive dynamic recrystallisation of quartz and feldspar, the growth of muscovite ribbons and mica fish.

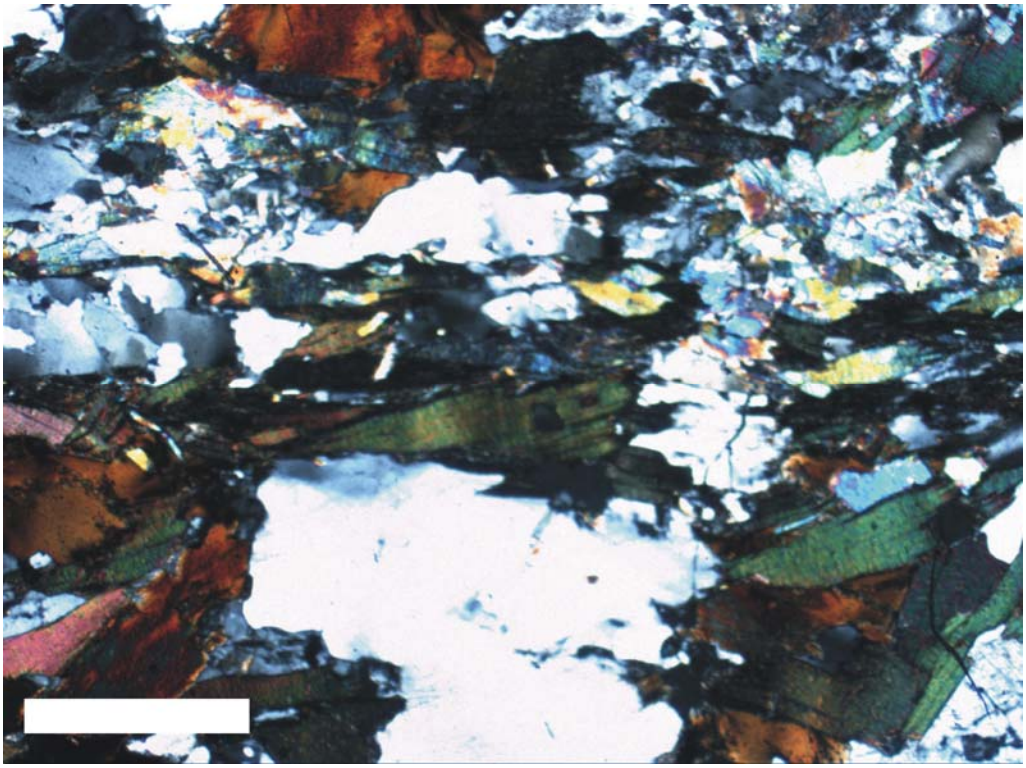

Figure 2.8n: Thin section image of PCC06-01 at 2.5x mag. Scale bar: 1cm. CPL.

Feldspars include both alkali- and plagioclase feldspar, which are anhedral in shape. Both albite and microcline twins present, with evidence of deformation by the bending of twins. Muscovite grains are acicular in shape, and are present in ribbons parallel to the foliation and as mica fish. Minor amounts of zircon and magnetite present, with no observable chlorite due to a lack of alteration.

Quartz grains commonly deform plastically in mylonitic rocks, with recrystallised quartz squeezing between the more robust feldspar grains. Feldspars often deform in a brittle fashion in mylonitic rocks, with the disintegration of sharp grain boundaries and fracturing of grains being common (Tulloch and Kimbrough 1989). This behaviour is observed both in previous studies on the Paparoa Metamorphic Core Complex, and in this sample (PCC06-01).

This specimen is seriate-interlobate in nature, and is considered to have experienced a high degree of deformation associated with mylonitisation (IV in the deformation classification scheme).

Lower Plate rocks adjacent to the Ohika Detachment Fault (samples RS-35 to RS-40) experienced limited recrystallisation of quartz, with deformation predominantly cataclastic in nature.

The Lower Plate rock adjacent to the Pike Detachment Fault (sample PCC06-01), however, shows greater levels of ductile deformation, with the recrystallisation of quartz and development of mica fish.

CHAPTER 3: ZIRCONOLOGY

3.1. Use of zircon in geochronology

Petrogenetic studies have recently shifted from the whole rock approach, in favour of analysing individual mineral groups. The advantages and disadvantages for each approach have been summarised by Amelin and co workers (2000), as shown in Table 3.1.

Zircon minerals are a valuable tool in petrogenetic investigations, through textures recorded within the minerals, and the overall morphology of the grains within samples. Zircon ($ZrSiO_4$) consists of various elements which are of interest in geochemical studies, including U, Pb, Th, Hf, P, Y, and the Rare Earth Elements (REE's). A solid solution series exists between $ZrSiO_4$ and $HfSiO_4$, with (Hf, Zr)SiO4 with more than 90 mol.-% hafnium component being referred to as hafnon (Neves et al. 1974). The chemical structure of zircon is discussed in detail by Finch and Hanchar (2003) and references therein.

The development of crustal material from the mantle may be investigated through the interpretation of Hf isotopes, while oxygen isotopes highlight the presence or absence of a sedimentary source (Hawkesworth and Kemp 2006, Kemp et al. 2006).

Titanium has recently become an important tool in the calculation of zircon crystallisation temperatures during magmatic and/or metamorphic events (Valley 2003, Watson and Harrison 2005), with temperature and melt composition influencing the solubility of titanium (Hayden and Watson 2007). By using titanium content as a proxy

	Mineral grains and grain fragments	Whole rocks
Complexity of geochemical systems	Variable. Small size allows better chances of finding simple systems	Very complex. Assembly of multiple phases with various ages and evolution paths
Diagnostics of components with various ages and origins	U-Pb dating using microbeam techniques or crystal fragments; Imaging	Indirect evidence from geological relationships
Dating options	Direct precise dating with U-Pb	Isochron dating – relatively imprecise and involves assumptions difficult to verify
Closed versus open systems: Geochemical check	Monitoring closed system behaviour of the U-Pb. Extrapolation to other systems assumes slow diffusion of elements	Closed system assumption is as good as the isochron fit (if the other conditions of isochron model are satisfied). Comparison between different isotopic systems is possible but may not be straightforward
Closed verses open systems: Additional ways of checking	Imaging: CL, BSE, optical microscopy of etched surface, etc.	Several lines of indirect evidence: deformation textures, presence of secondary minerals, changes in rock chemistry
Sample preparation	Complex, time-consuming, and requires substantial experience	Relatively simple and straightforward
Difficulties	Mainly analytical (handing and precise analysis of very small mineral grains and fragments)	Mainly geochemical (related to the complexity of the system)
Prospect for the data improvement with the advancement of analytical techniques	Increasing sensitivity of isotopic analysis and better methods for cutting mineral grains can greatly enhance the data quality	Improving analytical precision would be useful. Sensitivity is relatively less important for most rocks

Table 3.1: Comparisons between the use of individual minerals and whole rocks in geochemical investigations (Amelin et al. 2000).

for temperature, links between metamorphic facies, geochemistry and geochronology may be made.

The resilience of zircon is reflected in its ability to endure magmatic and metamorphic events, and withstand the processes of erosion and chemical alteration. It is due to this resilience that older xenocrystic cores may be inherited into younger rock units, thus providing clues to the provenance of the rock unit (Black et al. 1986, Compston and Pidgeon et al. 1986, Corfu et al. 2003).

3.2. Zircon morphology

Zircons can be classified on the basis of observations relating to their crystal shape, inherited make-up and origin (e.g. metamorphic, igneous, hydrothermal or inherited). Observations of variations (or absences) in crystal shape, growth zoning, alteration and metamorphism may be made through using cathodoluminescence (CL) or back-scattered-electron (BSE) imaging, inferred through U-Pb geochronology.

3.2.1. Crystal shape

Simple observations of zircon crystals using CL or BSE images provide clues to the evolution of individual grains within rock units, and therefore an appreciation of its geological history and provenance.

The external nature of zircons often reflects the conditions in which it has existed. Rounded grains may be indicative of shearing associated with metamorphism, erosion or resorption, while more angular grains often reflect primary crystal growth which has not experienced much disturbance (Hoskin and Schaltegger 2003). An overall decrease in

grain size is commonly observed in zircons that have experienced high levels of strain, such as those contained in mylonitic shear zones (Wayne and Sinha 1988).

3.2.2. Primary oscillatory growth zoning

Internal features, especially the nature of their contacts, also aid investigations into geochronology. Growth zones are made visible through CL and BSE imaging, with band thicknesses (measured in μm), inherited xenocrystic cores and younger overgrowth rims being highlighted by such imaging techniques. Zoning patterns develop in response to variations in the concentrations of Zr, Hf, P, Y, REE's, U and Th, due to the low diffusion rates and relative immobility of such elements (Belousova et al. 2006). Mattinson and co workers (1996) suggest growth zones develop through the interaction of crystal growth, diffusion rate, the relationship between the solid-liquid interface, and the extent of supersaturation of the melt. Primary oscillatory growth zoning can therefore be used as a proxy for intracrystalline diffusion, and may also record the relative degree of zircon-saturation of a melt. Zircon grains with widely spaced zoning patterns suffering from dissolution commonly characterize melts undersaturated in zircon, while the more narrowly spaced zoning patterns with little to no dissolution commonly develop in zircon-saturated melts (Vavra 1990).

Different periods of zircon growth often vary chemically, and therefore emit different colours in both CL and BSE imaging techniques. In general, dark zones in CL (light in BSE) represent U- and Th-rich sections; whereas light zones in CL (dark in BSE) generally represent U-poor and REE-rich sections (Corfu et al. 2003).

Contacts between inherited xenocrystic cores and overgrowth rims may be truncated in various fashions, and ‘ghost’ textures may develop through the preservation of primary oscillatory growth zoning during later metamorphism. The presence of ‘ghost’ growth zones in zircon illustrates the minerals ability to retain chemical histories, despite suffering from partial recrystallisation (Hoskin and Black 2000).

3.2.3. Alteration and metamorphism

The destruction of primary oscillatory zoning patterns in grains is thought to take place during recrystallisation of zircon under solid state conditions, through increased strain within the mineral lattices at low temperatures (Köppel and Sommerauer 1974, Hoskin and Black 2000). Brittle deformation of individual grains, and subsequent alteration and/or Pb-loss, may take place at temperatures beneath the 600-650°C annealing temperature of zircon (Mezger and Krogstad 1997).

Solid-state recrystallisation may result in a number of deformation textures, including blurred primary zoning, convoluted zoning, and ‘ghost’ textures through transgressive recrystallisation (Hoskin and Schaltegger 2003 and references therein).

Zircon minerals may also become altered through the resorption of original growth zones, which may represent phases of zircon undersaturation in the melt. Once resorbed, zircon may recrystallise, often resulting in the truncation and overlapping of any remaining primary textures. Multiple discontinuities may develop in response to a number of processes, such as the incorporation of several xenocrystic cores, resorption of both primary and secondary structures, or several episodes of resorption during a single magmatic event (Corfu et al. 2003).

3.2.4. Pb-loss

The loss of Pb in zircons is thought to develop through the mobilisation of Pb during metamictization (Mezger and Krogstad 1997, Hoskin and Black 2000). Metamictization involves the complete destruction of mineral lattices as a result of the radioactive decay of U and Th, to produce metamict material (Woodhead et al. 1991). The external morphology of such material remains undamaged, while the internal lattice commonly experiences volume expansion and associated fracturing. Fracturing allows fluid to move through the metamict material, thus promoting further damage to the mineral lattice (Hoskin and Schaltegger 2003).

Volume expansion of xenocrystic cores occurs through the radioactive decay of U, resulting in radial cracking and the fracturing of brittle low-U rims. Conversely, zircons with low-U xenocrystic cores are unlikely to experience expansion-related fracturing, leaving high-U rims to darken (in CL) relative to the xenocrystic cores. This method of alteration results in the hydration of zircon, with a general increase in Fe and Ca and reduction in Pb (Wayne and Sinha 1988).

Processes involved in the loss of Pb from zircons have been discussed by Mezger and Krogstad (1997), who propose four main methods:

1. recrystallisation of metamict zircon, resulting in the mobilisation of Pb,
2. Pb diffusion in metamict zircon without the process of recrystallisation,
3. leaching of Pb from metamict zircon via fluids, and
4. diffusion of Pb in pristine zircon.

Diffusion of pristine zircon, however, does not develop under most crustal conditions, as it does not involve the process of metamictization. Diffusion in metamict zircon is

considered the most likely method of Pb-loss, as mineral lattices with high levels of radiation-related damage encourage high rates of diffusion (Cherniak et al. 1991). Pb-loss associated with the crystallisation of new zircon, or recrystallisation of existing grains, generally takes place under amphibolite- to granulite-facies metamorphic conditions (Hoskin and Black 2000). Non-metamict zircon may potentially experience Pb-loss by volume diffusion via fractures within the mineral lattice, under similar metamorphic conditions (Ashwal et al. 1999). Significant levels of Pb-loss by volume diffusion, however, are considered to be highly unlikely due to the extremely slow rate of diffusion in non-metamict zircons shown in laboratory simulations (Cherniak and Watson 2003). Metamict zircons are more likely to suffer from Pb-loss through diffusion, due to increased diffusion rates through radioactively-damaged mineral lattices (Cherniak et al. 1991).

Any evidence of alteration obtained from CL imaging is clearly of great importance, as geochemical analyses from such grains would be considered unreliable for interpretation (Corfu et al. 2003).

3.3. Morphology of zircons from the PMCC

The morphology of zircons from samples RNZ119, UC08368, UC05592 and PCC06-01 are shown in Figures 3.1a, 3.1b, 3.1c and 3.1d, and discussed below. Uranium content has been used to link the geochemistry of zircons with CL imaging, and is described as either ‘high’ or ‘low’ in content. For the purpose of this thesis, high-uranium content includes all concentrations greater than 1000ppm, while low-uranium content refers to values lower than 100ppm (Tables 3.2a, 3.2b, 3.2c and 3.2d; Mezger and Krogstad 1997).

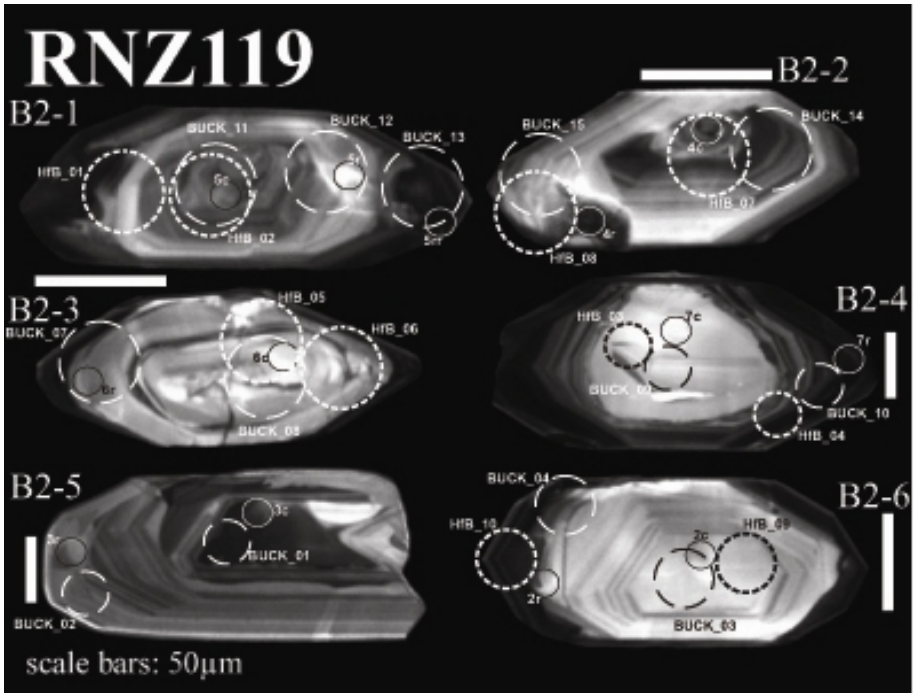

Figure 3.1a: Cathodoluminescence images of individual zircon grains from sample RNZ119. Grains from left to right: B2-1, B2-2, B2-3, B2-4, B2-5 and B2-6. Scale bars: 50 µm in length. Geochemical sampling locations shown as circles for oxygen (solid lines), hafnium (short dashes) and U-Pb + trace elements (long dashes).

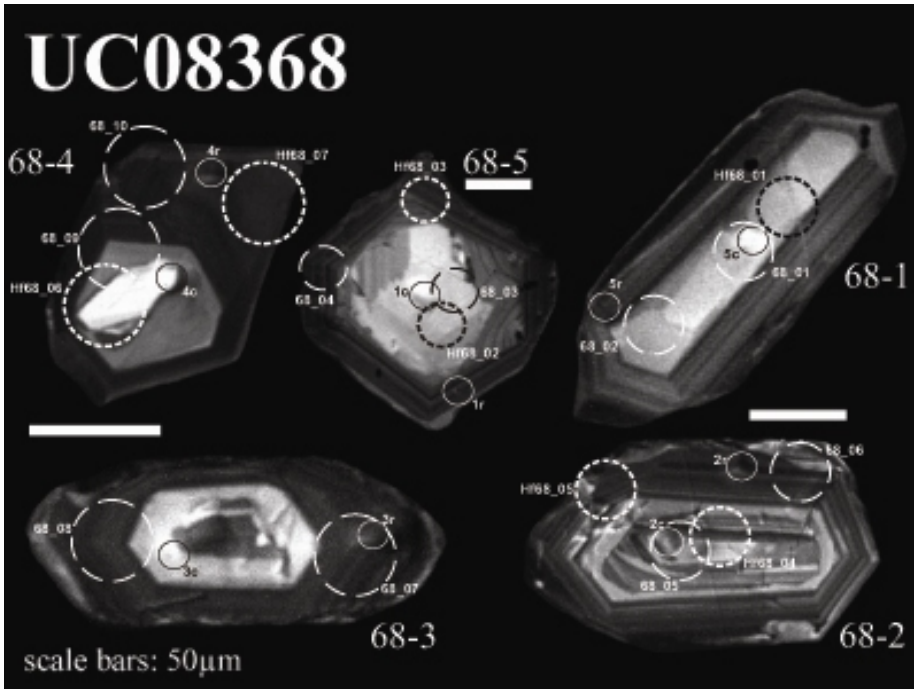

Figure 3.1b: Cathodoluminescence images of individual zircon grains from sample UC08368. Grains from left to right: 68-4, 68-5, 68-1, 68-3 and 68-2. Scale bars: 50 µm in length. Geochemical sampling locations shown as circles for oxygen (solid lines), hafnium (short dashes) and U-Pb + trace elements (long dashes).

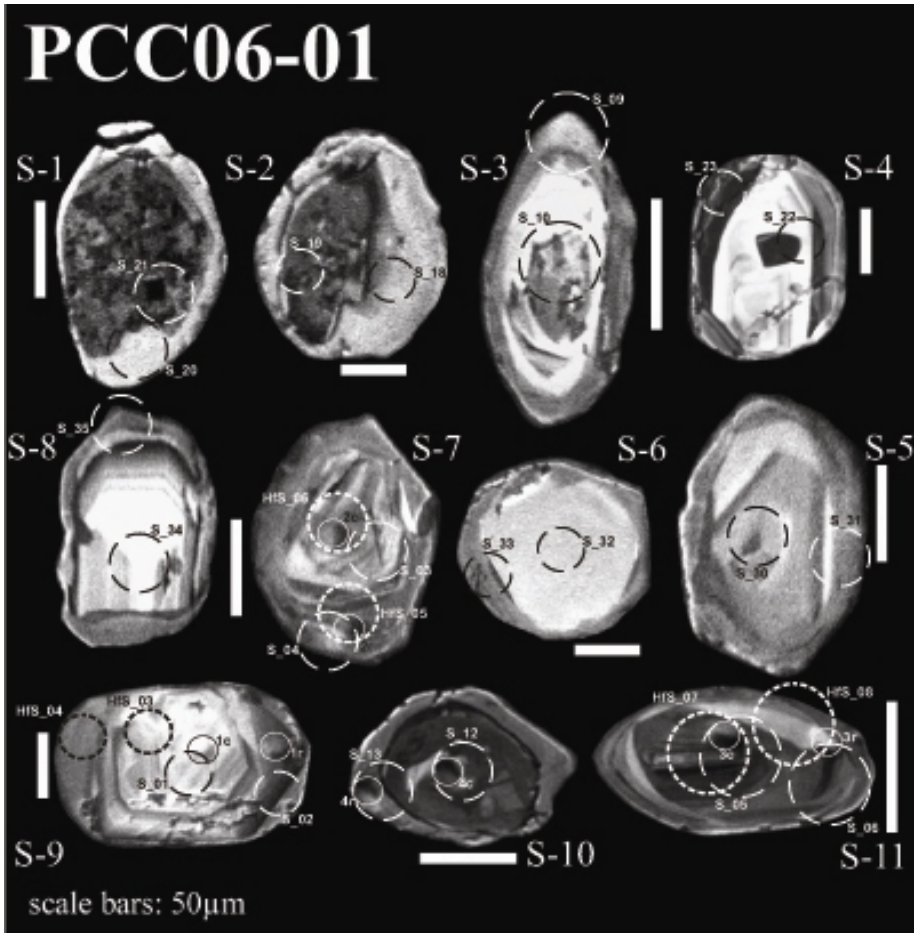

Figure 3.1c: Cathodoluminescence images of individual zircon grains from sample PCC06-01. Grains from left to right: S-1, S-2, S-3, S-4, S-8, S-7, S-6, S-5, S-9, S-10 and S-11. Scale bars: 50 µm in length. Geochemical sampling locations shown as circles for oxygen (solid lines), hafnium (short dashes) and U-Pb + trace elements (long dashes).

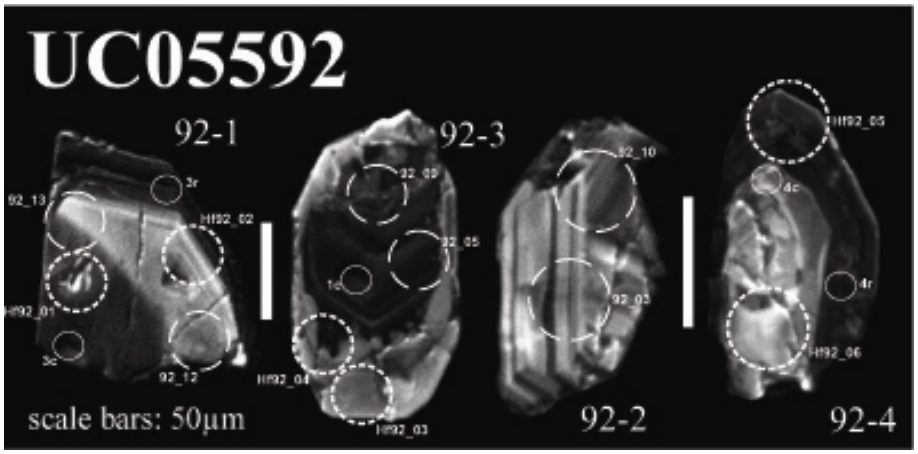

Figure 3.1d: Cathodoluminescence images of individual zircon grains from sample UC05592. Grains from left to right: 92-1, 92-3, 92-2 and 92-4. Scale bars: 50 µm in length. Geochemical sampling locations shown as circles for oxygen (solid lines), hafnium (short dashes) and U-Pb + trace elements (long dashes).

Analysis	C vs. R	^{208}Pb corr'd ^{206}Pb/^{238}U age (Ma)	observed ±1s.e.	U (ppm)	±	Th (ppm)	±	Th/U
BUCK_01	**C**	**373.71906**	**1.88504915**	**775**	**44.6**	**68.1**	**4**	**0.09**
BUCK_02	**R**	**111.1498235**	**0.451633494**	**542.3**	**2.9**	**72.4**	**0.5**	**0.13**
BUCK_03	C	112.5138063	0.718688839	314.1	4.7	118.7	2.3	0.38
BUCK_04	R	135.4818137	1.05858967	158.3	1.4	72.5	0.7	0.46
BUCK_05	**C**	**110.4814407**	**0.901695887**	**248.7**	**4**	**267.2**	**5.8**	**1.07**
BUCK_06	**R**	**103.4311859**	**0.637038014**	**1486.1**	**41.7**	**223.5**	**9**	**0.15**
BUCK_07	R	562.5694685	14.85492491	939.9	46.4	28.8	1.6	0.03
BUCK_08	C	1604.237201	29.27925056	330.6	13.1	116.7	7.1	0.35
BUCK_09	**C**	**636.0121967**	**5.858756696**	**252.4**	**7.6**	**46.3**	**1.7**	**0.18**
BUCK_10	**R**	**101.3314408**	**0.479427994**	**3492.2**	**25.3**	**87.1**	**1**	**0.02**
BUCK_11	C	314.6349783	17.57113524	318.3	5.6	71.5	1.6	0.22
BUCK_12	C	116.3241816	1.712684739	93.3	5.2	28.2	1.7	0.3
BUCK_13	R	103.2511763	0.519606292	2117.3	79.7	154.5	14.7	0.07
BUCK_14	**C**	**102.7025288**	**0.415364854**	**976.9**	**7.8**	**223.9**	**2.8**	**0.23**
BUCK_15	**R**	**109.3607797**	**0.63347052**	**696.4**	**31.4**	**94.7**	**5.6**	**0.14**
BUCK_16	C	109.4416091	0.457400445	439.1	4.3	137.9	1.4	0.31
BUCK_17	R	110.6759035	0.678463122	457.5	8.5	109.1	3.7	0.24
BUCK_18	*C*	*111.7369862*	*0.735415838*	*145.5*	*1.1*	*94.7*	*0.8*	*0.65*
BUCK_19	*R*	*108.060718*	*0.958843766*	*188.3*	*5.3*	*135.6*	*4.3*	*0.72*
BUCK_20	*R*	*122.695243*	*1.321720263*	*1229.9*	*24.5*	*109*	*2.7*	*0.09*
BUCK_21	**R**	**118.7945414**	**1.280689392**	**144**	**7.3**	**98.8**	**5.1**	**0.69**
BUCK_22	**C**	**550.1788569**	**7.688484969**	**202.6**	**1.9**	**84.8**	**2**	**0.42**
BUCK_23	C	470.4739599	3.90259659	1164.2	34.6	613.9	19.2	0.53
BUCK_24	R	108.9868464	1.032028442	1820.6	41.8	116.6	3.2	0.06
BUCK_25	**C**	**1071.627117**	**4.752595087**	**94.6**	**0.9**	**54**	**0.7**	**0.57**
BUCK_26	**R**	**1083.140186**	**4.679171728**	**154.9**	**1.7**	**57.6**	**0.8**	**0.37**
BUCK_27	R	101.7708905	0.493086322	824.8	7.2	122.8	1.3	0.15
BUCK_28	C	276.8368327	5.100204643	188.2	4.6	42.6	1.2	0.23
BUCK_29	*C*	*228.5945607*	*1.848285917*	*391.7*	*9.7*	*325.8*	*9.7*	*0.83*
BUCK_30	**R**	**77.27770481**	**0.770636644**	**5484.4**	**89.8**	**1567.4**	**29.4**	**0.29**
BUCK_31	**C**	**239.1498642**	**2.945583965**	**2872**	**80.8**	**496.2**	**21.9**	**0.17**
BUCK_32	R	301.3601198	2.972386859	2942	75	153.2	7.2	0.05
BUCK_33	C	520.7914135	18.42075521	1121.8	29.6	74.7	4.7	0.07
BUCK_34	**C**	**103.3208177**	**1.51073136**	**3219.4**	**37.6**	**1102.5**	**14.6**	**0.34**
BUCK_35	**R**	**101.74642**	**0.747147447**	**1339**	**32.6**	**296.1**	**7.6**	**0.22**

Table 3.2a: U, Th and Th/U ratios of zircon grains with ^{208}Pb corrected ^{206}Pb/^{238}U ages from sample RNZ119. Alternating font style (bold vs. regular) show analyses common to individual zircon grains. Analyses in italics are sample spots which were not able to be distinguished as cores or rims.

Analysis	Cores vs. rims	^{208}Pb corr'd ^{206}Pb/^{238}U age	observed ±1s.e.	U (ppm)	±	Th (ppm)	±	Th/U
68_01	**C**	**0.07608141**	**0.0012919**	**506.4**	**31.6**	**94.3**	**7.3**	**0.19**
68_02	**R**	**0.06297728**	**0.0006158**	**318.9**	**11.1**	**90.1**	**3.5**	**0.28**
68_03	C	0.17666481	0.00173279	131.4	2.9	70.1	1.7	0.53
68_04	R	0.16617933	0.00189755	220.1	2.9	136.4	3	0.62
68_05	**C**	**0.0798396**	**0.00089678**	**1141.4**	**19.1**	**377.9**	**12.8**	**0.33**
68_06	**R**	**0.07119915**	**0.00076679**	**1376.1**	**30**	**341.4**	**12.3**	**0.25**
68_07	R	0.2062262	0.00348624	603.8	8.9	194.8	6.6	0.32
68_08	R	0.0741271	0.0016922	1445.7	78.8	107.6	6.1	0.07
68_09	**C**	**0.12545889**	**0.00327354**	**326.3**	**10.7**	**61.7**	**3.4**	**0.19**
68_10	**R**	**0.05230716**	**0.00064004**	**1239.2**	**51.2**	**44.1**	**1.9**	**0.04**
68_11	C	0.17352587	0.00284299	372.5	13.5	86	3.6	0.23
68_12	R	0.15833916	0.00196004	832.3	25.8	146.8	5.5	0.18
68_13	*C*	*0.05740094*	*0.0002753*	*194.5*	*2.8*	*97*	*2.1*	*0.5*
68_14	*?*	*0.06517195*	*0.00156919*	*2028.1*	*98.6*	*66.8*	*6.7*	*0.03*
68_15	*?*	*0.081862*	*0.00089336*	*1113.9*	*34*	*57.4*	*2.5*	*0.05*
68_16	*?*	*0.04756201*	*0.00047228*	*1699.7*	*12.7*	*26.2*	*0.3*	*0.02*
68_17	**C**	**0.19215437**	**0.00105178**	**375**	**2.7**	**224.5**	**1.8**	**0.6**
68_18	**R**	**0.16091985**	**0.00299038**	**352.9**	**2.4**	**38.7**	**0.7**	**0.11**
68_19	C	0.21546371	0.00772619	287.6	7.3	111.2	3.9	0.39
68_20	R	0.05335202	0.00033827	1398.1	35.1	100.9	2.8	0.07
68_21	**C**	**0.10709415**	**0.00364908**	**612.9**	**32.9**	**128.4**	**11.5**	**0.21**
68_22	**R**	**0.15350531**	**0.00149673**	**180**	**6.2**	**89.2**	**4.2**	**0.5**
68_23	*?*	*0.16727636*	*0.00120705*	*336.8*	*7.3*	*154.5*	*4.4*	*0.46*
68_24	*?*	*0.08179109*	*0.00090845*	*1238.1*	*21.1*	*36*	*1.3*	*0.03*
68_25	*?*	*0.05836476*	*0.00046647*	*314.2*	*16.2*	*109.7*	*6.9*	*0.35*
68_26	*?*	*0.05435531*	*0.00025136*	*555.9*	*32.8*	*113.3*	*8.2*	*0.2*
68_27	*?*	*0.06342026*	*0.00041078*	*402.1*	*19.3*	*121.8*	*5.9*	*0.3*
68_28	*?*	*0.0508367*	*0.00019292*	*2225.1*	*24.6*	*99.2*	*4.5*	*0.04*
68_29	*?*	*0.08962102*	*0.00266691*	*981*	*47.2*	*177.1*	*13.3*	*0.18*
68_30	*?*	*0.05067122*	*0.00039926*	*2031.5*	*28.8*	*59.5*	*1.8*	*0.03*

Table 3.2b: U, Th and Th/U ratios of zircon grains with ^{208}Pb corrected ^{206}Pb/^{238}U ages from sample UC08368. Alternating font style (bold vs. regular) show analyses common to individual zircon grains. Analyses in italics ("?") are sample spots which were not able to be distinguished as cores or rims.

Analysis	Cores vs. rims	^{208}Pb corr'd ^{206}Pb/^{238}U age	observed ±1s.e.	U (ppm)	±	Th (ppm)	±	Th/U
S_01	**C**	**1473.462613**	**6.627419359**	**238**	**3**	**106.2**	**1.8**	**0.45**
S_02	**R**	**1413.899969**	**6.78040733**	**1120.6**	**23.5**	**285.7**	**7.1**	**0.25**
S_03	C	1378.486856	9.219342881	544.3	11	93.3	3.9	0.17
S_04	R	1203.748023	15.5701138	825.8	9.6	62.9	4.5	0.08
S_05	**C**	**596.4776804**	**3.502823746**	**834.3**	**14.4**	**334.6**	**6.9**	**0.4**
S_06	**R**	**592.8904502**	**1.983523096**	**528.4**	**6.8**	**154.6**	**2**	**0.29**
S_07	R	352.904914	1.687624792	658.3	11.3	8.9	0.2	0.01
S_08	*R*	*610.3007943*	*13.47716906*	*384.9*	*9.5*	*59.6*	*3.7*	*0.15*
S_09	**R**	**338.6017125**	**1.404528002**	**636.5**	**2.8**	**5.5**	**0.2**	**0.01**
S_10	**C**	**1000.848893**	**3.72274997**	**328.4**	**3.3**	**225.8**	**2.5**	**0.69**
S_11	C	1170.802297	33.13401823	96.5	4.3	52.5	3.3	0.54
S_12	**C**	**995.0984611**	**7.524167576**	**1837.7**	**26.5**	**116.4**	**5.9**	**0.06**
S_13	**R**	**659.88117**	**4.272457158**	**1085.5**	**18**	**93.5**	**2.4**	**0.09**
S_15	*R*	*762.1101741*	*10.96420316*	*584.9*	*9.6*	*223.1*	*8.4*	*0.38*
S_16	C	905.0466005	5.031039359	640.2	3.9	278.5	2.8	0.44
S_17	R	529.705269	4.204342851	575.1	9.1	43.2	1	0.08
S_18	**R**	**782.9927549**	**30.01356276**	**2936.5**	**117.9**	**367.3**	**40.4**	**0.13**
S_19	**C**	**697.1386036**	**9.95563885**	**1190.1**	**57.4**	**148**	**15.8**	**0.12**
S_20	R	462.0378448	3.231204731	731.1	16.4	29.6	0.8	0.04
S_21	C	529.9996739	2.838762267	2033.4	31.9	142	2.7	0.07
S_22	**C**	**865.339485**	**14.69212228**	**333.2**	**22**	**56.4**	**4.7**	**0.17**
S_23	**R**	**562.758152**	**3.194642802**	**1208.7**	**8.5**	**32.8**	**0.4**	**0.03**
S_24	C	595.0140087	4.861365097	180.2	2.6	45	2.7	0.25
S_25	R	381.0645092	3.749285606	409.2	14.4	17.2	1	0.04
S_26	**C**	**919.9552513**	**3.791293593**	**551.9**	**6.8**	**362.3**	**4.8**	**0.66**
S_27	**R**	**442.6680036**	**2.40193608**	**507.9**	**8.3**	**33**	**1.5**	**0.06**
S_28	C	621.3486368	3.077654289	1894.2	31.4	109.8	3.2	0.06
S_29	R	486.1675665	5.777617644	364.1	11.3	158.8	9.2	0.44
S_30	**C**	**1954.576378**	**8.222018884**	**359.8**	**5.8**	**315.7**	**6.6**	**0.88**
S_31	**R**	**674.4936096**	**13.86225464**	**513.2**	**5.9**	**15.3**	**0.8**	**0.03**
S_32	C	550.1452145	3.289844363	130.1	1.3	53.7	0.6	0.41
S_33	R	329.0483789	1.771434217	626.9	3.9	5.8	0.4	0.01
S_34	**C**	**924.6954943**	**6.204854501**	**120.4**	**2.9**	**30.4**	**0.8**	**0.25**
S_35	**R**	**770.8304771**	**8.300412506**	**753.4**	**25.9**	**30.5**	**1.8**	**0.04**

Table 3.2c: U, Th and Th/U ratios of zircon grains with ^{208}Pb corrected ^{206}Pb/^{238}U ages from sample PCC06-01. Alternating font style (bold vs. regular) show analyses common to individual zircon grains. Analyses in italics ("?") are sample spots which were not able to be distinguished as cores or rims.

Analysis	Cores vs. rims	^{208}Pb corr'd $^{206}Pb/^{238}U$ age	observed ±1s.e.	U (ppm)	±	Th (ppm)	±	Th/U
92_01	*?*	*297.4303486*	*3.991886304*	*860.6*	*7.8*	*217.1*	*3*	*0.25*
92_02	*?*	*239.5477162*	*3.886700438*	*1168*	*32.7*	*200.6*	*7.4*	*0.17*
92_03	**C**	**336.0306656**	**2.080477828**	**629.7**	**15**	**281.9**	**13.6**	**0.45**
92_04	*?*	*761.1094961*	*9.247204587*	*3334.7*	*44.2*	*221.3*	*3.2*	*0.06*
92_05	C	1015.456051	4.461412297	3345.5	69.9	269.4	5.7	0.08
92_06	**R**	**160.9600057**	**6.355173783**	**2589.3**	**94.6**	**193.5**	**8.6**	**0.07**
92_07	**R**	**249.3183688**	**13.86488785**	**1711.9**	**167.1**	**169.2**	**18.8**	**0.1**
92_08	**C**	**665.0654357**	**5.522177547**	**623.9**	**5.7**	**180.2**	**1.9**	**0.29**
92_09	R	781.3093172	6.247766846	3728.8	70	266.9	7.6	0.07
92_10	**R**	**293.3765261**	**1.784479247**	**595.6**	**10.5**	**529.2**	**10.8**	**0.89**
92_11	*C*	*295.2686703*	*2.537155842*	*747.9*	*8.1*	*678.2*	*13.7*	*0.91*
92_12	R	329.0550824	5.364985881	914.6	11.7	245.9	8.8	0.27
92_13	C	86.64086097	1.312660606	6814.6	152.8	201.3	14.6	0.03

Table 3.2d: U, Th and Th/U ratios of zircon grains with ^{208}Pb corrected $^{206}Pb/^{238}U$ ages from sample UC05592. Alternating font style (bold vs. regular) show analyses common to individual zircon grains. Analyses in italics ("?") are sample spots which were not able to be distinguished as cores or rims.

Aspect ratios of all zircon grains are listed in Table 3.3, with average aspect ratios shown in Table 3.4.

3.3.1. RNZ119

Zircon grains from this sample are dominantly euhedral in shape, with aspect ratios ranging from 1.6:1 to 3:1, with a mean of 2.5:1 (Table 3.4).

CL imaging shows a general trend of decreasing luminosity towards the crystal margins, with 'dark' and 'light' growth zoning bands ranging between 5 to 10 μm in thickness.

Sample name	Zircon grain	Long/short axis (μm)	Aspect ratio
PCC06-01	S_01	140/75	1.9:1
	S_02	175/150	1.2:1
	S_03	120/60	2:01
	S_04	75/60	1.25:1
	S_05	150/100	1.5:1
	S_06	150/125	1.2:1
	S_07	125/100	1.25:1
	S_08	125/75	1.7:1
	S_09	175/110	1.6:1
	S_10	110/75	1.5:1
	S_11	100/50	2:01
UC05592	92_01	150/100	1.5:1
	92_02	110/75	1.5:1
	92_03	150/75	2:01
	92_04	110/60	1.8:1
RNZ119	B_01	150/50	3:01
	B_02	150/50	3:01
	B_03	150/50	3:01
	B_04	300/125	2.4:1
	B_05	275/125	2.2:1
	B_06	200/125	1.6:1
UC08368	68_01	225/80	2.8:1
	68_02	175/125	1.4:1
	68_03	150/60	2.5:1
	68_04	125/80	1.6:1
	68_05	200/200	1:01

Table 3.3: Long/short axis and aspect ratios for zircons from the four samples from the Paparoa Metamorphic Core Complex.

Sample	Zircon length range (μm)	Minimum aspect ratio	Maximum aspect ratio	Mean aspect ratio
RNZ119	150-300	1.6:1	3:01	2.5:1
UC08368	125-220	1:01	2.8:1	1.8:1
UC05592	100-150	1.5:1	2:01	1.7:1
PCC06-01	100-300	1.2:1	2:01	1.6:1

Table 3.4: Aspect ratios from samples RNZ119, UC08368, UC05592 and PCC06-01 from the Paparoa Metamorphic Core Complex. The range of zircon grain lengths (in μm), minimum, maximum and mean aspect ratios are shown.

The nature of zoning varies between grains, with angular terminations in B2-1, B2-2, B2-5 and B2-6, and rounded in nature in B2-3 and B2-4.

The uranium content and luminosity of zircon grains in CL images follow the expected pattern in most cases, with ‘light’ zones having low-uranium and ‘dark’ zones containing high-uranium (Figures 3.1a and Table 3.2a). The exception within this sample is zircon grain B2-6, which shows a ‘light’ xenocrystic core and ‘dark’ rim with higher uranium within the central zone. The variation in uranium content between the xenocrystic core and rim of this grain, however, is minimal.

Alteration of zircon grains within this sample includes cracking (B2-3 and B2-6) and corrosion (B2-1, B2-2 and B2-4), as shown in Figure 3.2a.

3.3.2. UC08368

Zircon grains within this sample are euhedral and stubby in nature, with aspect ratios ranging from 1:1 to 2.8:1, with a mean of 1.8:1 (Table 3.4).

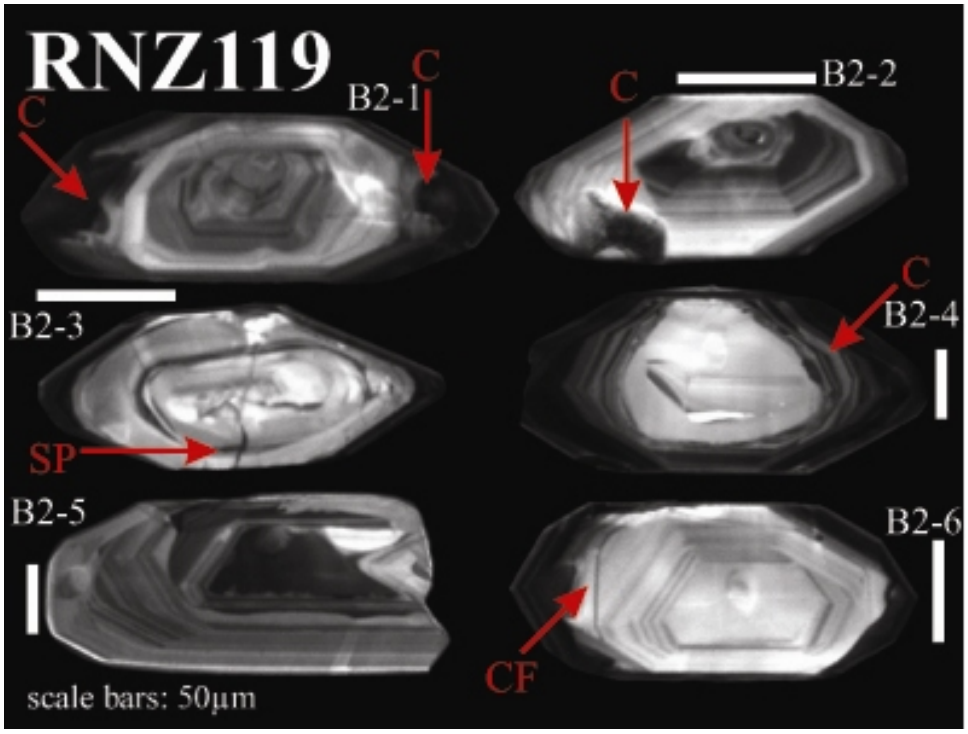

Figure 3.2a: Cathodoluminescence images of zircons from sample RNZ119 from the Paparoa Metamorphic Core Complex. Various morphologic features are shown, as follows: ‘C’ for corrosion; ‘CF’ for concentric fracturing and ‘SP’ for damage associated with sample processing.

The use of CL imaging highlights different zones of growth with average thicknesses of 5 to 10 µm under CL. Zircons from this sample show an overall reduction in luminosity towards crystal edges.

Most zoning patterns present show truncations of central zones by subsequent growth bands, as seen in grains 68-2 and 68-5. The preservation of oscillatory zoning patterns in grains which have suffered solid-state recrystallisation produces ‘ghost textures’, as seen in grain 68-5. Corrosion of grains may have taken place in grains 68-1 and 68-2 (Figure 3.2b).

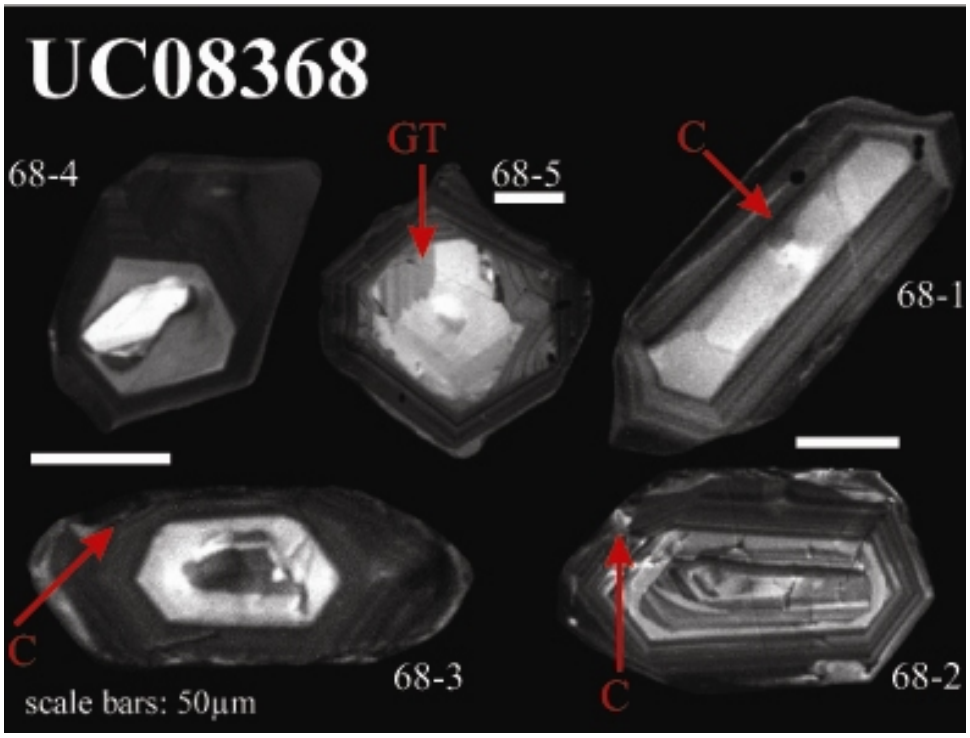

Figure 3.2b: Cathodoluminescence images of zircons from sample UC08368 from the Paparoa Metamorphic Core Complex. Morphologic features are shown as follows: 'C' for corrosion and 'GT' for 'ghost' textures.

The uranium content and luminosity patterns in CL images correlate well in most grains from this sample, with high-uranium content being associated with 'dark' zones and low-uranium with 'light' zones (Figures 3.1b and Table 3.2b). Grains with high-uranium rims and low-uranium xenocrystic cores include 68-2, 68-4 and 68-5, while 68-1 has low-uranium rims (xenocrystic core not sampled) and 68-3 has low-uranium rims and a high-uranium xenocrystic core.

3.3.3. PCC06-01

Zircon grains from this sample are subhedral and sub-rounded, in contrast to the more elongate euhedral zircons from RNZ119, UC08368 and UC05592. Crystal edges are

somewhat irregular, and stubby in nature, with aspect ratios ranging from 1.2:1 to 2:1, and a mean of 1.6:1 (Table 3.4).

The relationship between uranium-content and degree of luminosity is consistent throughout the sample, with high-uranium sections appearing ‘dark’, and low-uranium sections ‘light’, in CL images. Grains with high-uranium xenocrystic cores and low-uranium rims include S-1, S-10 and S-11, while the remainder show low-uranium xenocrystic cores and high-uranium rims (Figure 3.1c).

Growth zones average between 5 to 10 μm in thickness, with bands seen in grains S-3, S-4, S-7, S-8, S-10 and S-11. Angular terminations between banding and xenocrystic core-rim divisions are common within this sample, which may be associated with dissolution and/or corrosion. Dissolution textures are commonly observed in S-type granitoid rocks, and develop through the shift from crystallisation in an initially zircon-undersaturated melt to a zircon-saturated melt (Hoskin and Schaltegger 2003 and references therein). Some grains show evidence of metamictization, by a ‘mottled’ or ‘crumbly’ appearance in CL images, as evident in the ‘dark’, uranium-rich xenocrystic cores of S-1 and S-2 (Figure 3.2c).

3.3.4. UC05592

The crystal shape of zircons from this sample are euhedral and stubby with aspect ratios ranging from 1.5:1 to 2:1, with a mean of 1.7:1 (Table 3.4).

An overall decrease in luminosity is observed from the centre to the edges of most grains, with growth zones averaging between 5 to 10 μm in thickness. Growth zoning is preserved in most grains, as seen in the xenocrystic core of 92-3, and the rims of 92-1 and

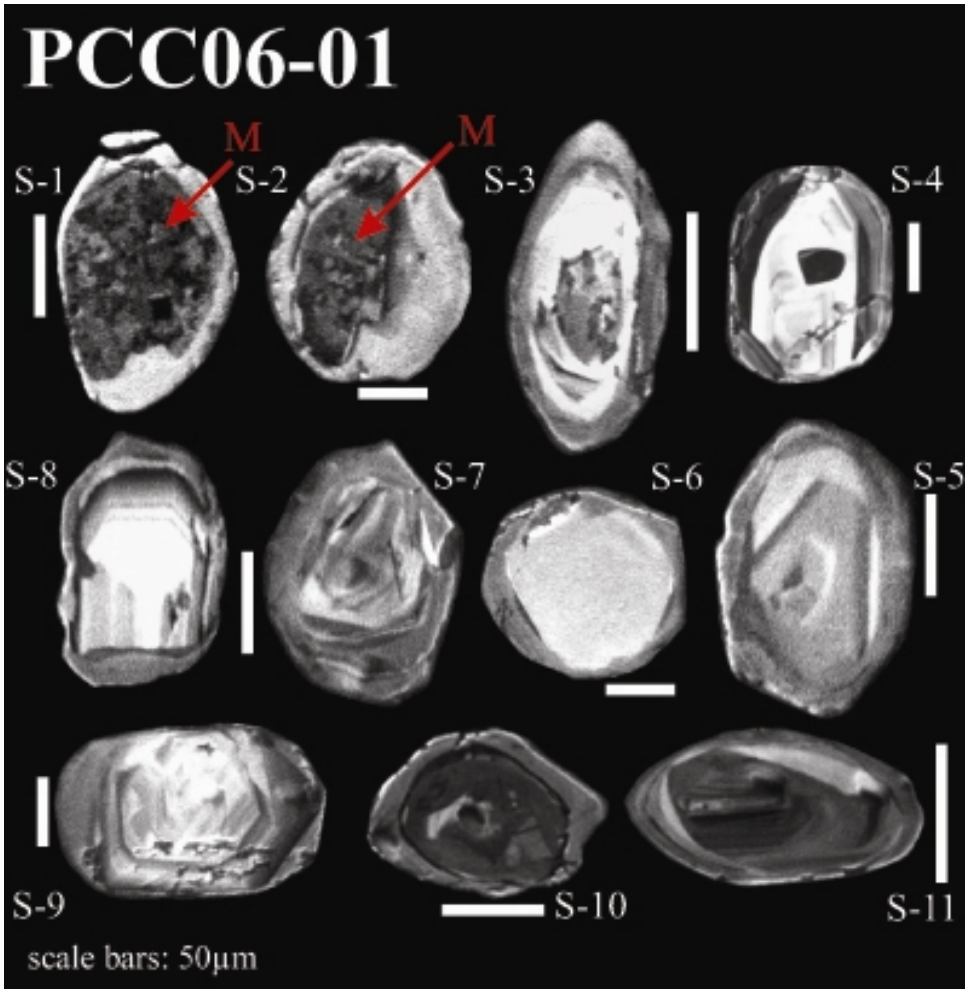

Figure 3.2c: Cathodoluminescence images of zircons from sample PCC06-01 from the Paparoa Metamorphic Core Complex. Morphologic feature shown: 'M' for metamictization.

92-2. Overgrowth rims are clearly separate from the xenocrystic cores of grains in this sample, by differences in luminosity in CL images and chemical compositions.

Uranium content and luminosity of grains follow the expected pattern, of 'dark' zones consistent with high-uranium, and 'light' with low-uranium content. The majority of grains are relatively uranium-rich in both the xenocrystic cores and rims, and show both

high-uranium rims (92-1) and high-uranium xenocrystic cores (92-2 and 92-3) (Figure 3.1d and Table 3.2d).

Three out of the four grains shown are fragmented and cracked, with at least one grain (92-1) suffering from surficial damage associated with sample processing (Figure 3.2d).

3.4. Discussion of PMCC zircon morphology

Interpretations of the morphology of zircon are based on information deduced from a combination of CL images and chemical sampling.

Observations in zircon crystal shapes allow interpretations to be made about the overall setting in which grains were produced. The growth of stubby and equant euhedral zircon crystals is generally associated with slow-cooling of zircon-saturated intrusions at depth (Corfu et al. 2003, Hoskin and Schaltegger 2003).

Zircon grains from the Buckland Granite (sample RNZ119) are dominantly euhedral in shape, reflecting their slow crystallisation out of the melt during cooling of the pluton. Zircon crystals from samples UC08368, UC05592 and PCC06-01 are dominantly stubby in shape, which suggests the growth of such grains within deep seated plutonic rocks. The rounding of zircon grains, as seen in sample PCC06-01, is thought to have resulted from the sedimentary transport of crystals associated with the recycling of crustal material since their initial growth in the parent rock(s). Metamorphic processes such as the dissolution of growth terminations and shearing during active detachment faulting may have also resulted in the rounding of grains.

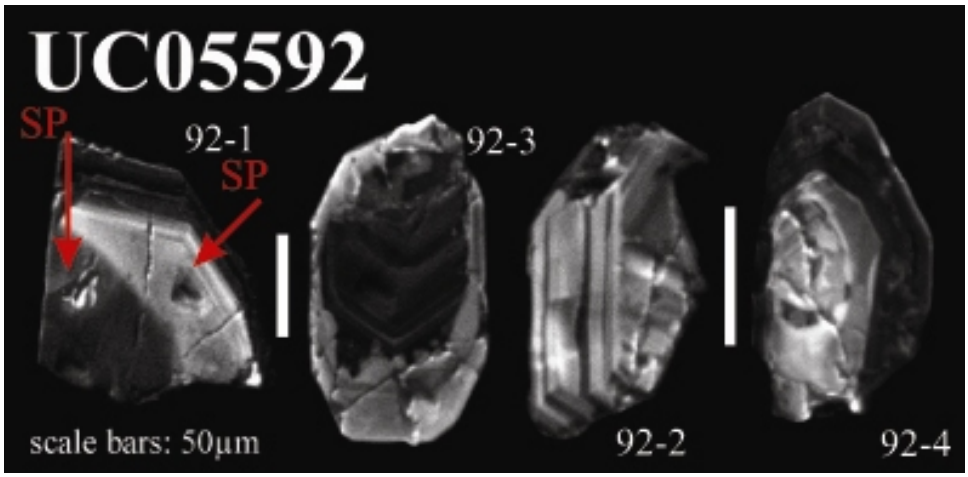

Figure 3.2d: Cathodoluminescence images of zircons from sample UC05592 from the Paparoa Metamorphic Core Complex. Various morphologic features are shown, as follows: ‘C’ for corrosion; ‘CF’ for concentric fracturing; ‘GT’ for ‘ghost’ textures; ‘M’ for metamictization and ‘SP’ for damage associated with sample processing.

Aspect ratios involve the measurement of long and short axes of individual grains, and allow quick comparisons of grain shapes to be made. The use of aspect ratios complements observations in crystal shapes, to aid interpretations of crystallisation conditions, as discussed above. Research into the response of zircons to increased strain shows a systematic reduction in the grain size and aspect ratios of affected crystals (Sinha and Glover 1978). Zircons from the Paparoa Metamorphic Core Complex display a similar behaviour, with the smallest mean aspect ratio belonging to the sample PCC06-01, collected from the Pike Detachment shear zone (Table 3.4).

Variations in the luminescence of zircon grains in CL images correspond with the geochemical data, with ‘dark’ and ‘light’ zones commonly representing high- and low-uranium contents, respectively. The distinction between xenocrystic cores and rims is based on the morphology of individual grains, and interpretations of geochemical and geochronological data.

The location of xenocrystic core-rim divisions is based upon variations in the luminescence of grains in the CL images, which is clearly subject to interpretation.

'Ghost textures' in zircon grains develop through the preservation of growth zoning during the process of resorption. Grain 68-5 of UC08368 is thought to display these textures, and thus record the recrystallisation of zircon in the solid-state (Figure 3.2b).

The metamictization of zircon minerals involves the destruction of mineral lattices by radioactive decay, resulting in a 'mottled' or 'crumbly' appearance in CL images. Zircon grains S-1 and S-2 from sample PCC06-01 show evidence for metamictization, as shown in Figure 3.2c. Fracturing of metamictized zircon may take place in response to differences in the properties of uranium-rich and uranium-poor zones within individual grains. Concentric fractures may develop along such boundaries, as seen in grain B2-6 of sample RNZ119.

Volume expansion of uranium-rich zones in metamictized zircons may result in the cracking of adjacent uranium-poor zones, allowing potential alteration within grains by metamorphic fluids to take place. Grain B2-3 from the sample RNZ119 shows cracking patterns, which could result from either volume expansion or damage associated with sample processing. This grain has a high-uranium xenocrystic core and low-uranium rims, however, which does not support the idea of volume expansion-related damage. Fracturing of the grain B2-3 is therefore more likely to be due to damage associated with sample processing.

Corrosion is evident in grains B2-1, B2-2 and B2-4 of sample RNZ119, and 68-1, 68-2 and 68-3 of sample UC08368, caused by the oxidisation of zircon. Pits seen on the

surface of grain 92-1 (of UC05592), and fragmentation of grains B2-5 (of RNZ119) and 92-1, 92-2 and 92-4 (of UC05592) is attributed to damage associated with the removal and preparation of crystals for geochemical analysis.

The morphological features of zircon grains are complemented by both geochemical and geochronological data, which allows greater interpretations into the petrogenesis of igneous and metamorphic rocks to be made.

CHAPTER 4: GEOCHEMISTRY AND GEOCHRONOLOGY

4.1. Geochemical investigations

The use of zircon in the interpretation of granitoid petrogenesis is extended through the use of geochemistry. Initial geochemical sampling often involves whole rock analysis, through X-ray fluorescence (XRF).

Oxygen isotopes and hafnium constrain the role of crustal contamination, allowing interpretations into the petrogenesis of the Buckland Granite during its emplacement into the Paparoa Metamorphic Core Complex. Caution is required when using hafnium as an indicator of crustal contamination, as the crystallisation of zircons in a melt may mix with inherited zircons from other sources, which separated from the mantle at a different time in the evolution of the crust (Hawkesworth and Kemp 2006). A combined geochemical approach is clearly of great importance, with the use of oxygen isotopes providing greater confidence in establishing the role of crustal contamination in granitoid petrogenesis.

The concentration of titanium in zircon grains allows the calculation of crystallisation temperatures, with the zircon saturation thermometry technique. Rare Earth Elements (REE's) help to further constrain the petrogenetic nature of rocks from the Paparoa Metamorphic Core Complex.

4.1.1. Whole rock analysis (XRF)

Major and trace element concentrations of crushed hand specimens are measured through the process of XRF. Data for major elements, trace elements or a combination of both may be illustrated using bivariate diagrams. One of the most commonly used types of bivariate diagrams today are Harker Diagrams, which usually have silica plotted as the abscissa against major and trace elements. Patterns and trends in the

chemical makeup of individual samples are clearly shown in such diagrams, allowing initial interpretations to be made.

Samples from the Paparoa Metamorphic Core Complex were analysed by XRF, for both major and trace element concentrations. UC05592, PCC06-01, UC08368, and RS-35 to RS-40 were crushed and analysed at the University of Canterbury in 2006 (Tables 4.1a and 4.1b). The XRF data for RNZ119 was obtained from earlier whole rock analysis at the University of Canterbury for Muir and co workers (1997), with all data listed in Tables 4.1c and 4.1d).

Bivariate diagrams for samples UC05592, PCC06-01, UC08368, RS-35 to RS-40 and RNZ119 are plotted with SiO_2 vs. TiO_2, Al_2O_3, Fe_2O_3, MnO, MgO, CaO, Na_2O, K_2O and P_2O_5 (Figure 4.1). These samples from the Paparoa Metamorphic Core Complex show a relative decrease with increasing SiO_2 for TiO_2, MnO, Al_2O_3, MgO, Fe_2O_3, CaO and P_2O_5, and a relative increase with increasing SiO_2 for Na_2O and K_2O.

The use of whole rock analysis, however, is relatively limited in regards to provenance studies as only the 'end result' of an evolved body of rock is accessible. Clearly, the *in situ* sampling of individual minerals is the more favourable method for obtaining information on the petrogenesis of a rock unit.

4.1.2. Oxygen isotopes

Oxygen isotopes are a useful geochemical tool for looking at potential crustal contamination within magmas, and the influence of mantle-derived material in magmatic systems. The sluggish diffusion rates of oxygen isotopes make them especially useful in the interpretation of chemical changes within a body of rock over time.

Sample	SiO_2 (%)	TiO_2(%)	Al_2O_3 (%)	Fe_2O_3T (%)	MnO (%)	MgO (%)	CaO (%)	Na_2O (%)	K_2O (%)	P_2O_5 (%)	LOI	Total
UC05592	73.31	0.1	15	1.01	0.02	0.22	0.93	4.25	4.34	0.08	0.76	100.01
PCC06-01	69.05	0.7	14.54	5.23	0.05	2.24	1.21	2.09	3.44	0.16	1.77	100.47
UC08368	72	0.37	14.28	2.15	0.02	0.75	0.33	2.62	5.64	0.15	2.02	100.33
RS_35	59.22	0.93	17.32	6.4	0.08	3.44	3.98	3.25	2.56	0.31	2.58	100.06
RS_36	70.29	0.63	13.5	5.15	0.04	2.41	0.48	1.66	2.7	0.17	3.06	100.09
RS_37	63.45	0.81	16.59	5.4	0.08	3.05	3.52	3.27	2.97	0.25	1.09	100.46
RS_38	66.26	0.74	16.36	6.12	0.05	3.01	0.33	0.91	3.49	0.15	2.97	100.39
RS_39	69.38	0.48	15.46	3.35	0.04	0.92	1.85	3.06	4.55	0.31	1.06	100.46
RS_40	73.46	0.24	14.08	1.72	0.04	0.71	1.17	3.02	5.35	0.1	0.53	100.41

Table 4.1a: XRF results of major elements from samples UC05592, PCC06-01, UC08368, and RS-35 to RS-40.

Sample	V (ppm)	Cr (ppm)	Ni (ppm)	Zn (ppm)	Zr (ppm)	Nb (ppm)	Ba (ppm)	La (ppm)	Ce (ppm)	Nd (ppm)	Ga (ppm)	Pb (ppm)	Rb (ppm)	Sr (ppm)	Th (ppm)	Y (ppm)
UC05592	7	<3	3	32	62	8	693	20	38	18	19	35	192	291	7	18
PCC06-01	95	86	34	97	184	15	357	23	71	36	20	24	232	85	14	22
UC08368	25	14	10	47	185	14	456	50	130	73	19	37	256	74	37	23
RS_35	136	114	36	97	220	10	720	22	68	29	22	11	132	545	8	28
RS_36	115	78	29	61	163	12	264	26	72	42	17	20	169	53	10	36
RS_37	117	88	30	84	180	7	770	15	67	25	20	13	134	510	3	13
RS_38	118	109	40	105	175	13	646	28	75	41	21	24	125	53	11	33
RS_39	37	14	9	71	153	26	367	23	74	34	23	32	365	96	15	29
RS_40	26	12	7	46	131	9	622	38	81	40	18	39	228	295	19	10

Table 4.1b: XRF results of trace elements from samples UC05592, PCC06-01, UC08368, and RS-35 to RS-40.

Sample	SiO_2 (%)	TiO_2(%)	Al_2O_3 (%)	Fe_2O_3T (%)	MnO (%)	MgO (%)	CaO (%)	Na_2O (%)	K_2O (%)	P_2O_5 (%)	LOI	Total
RNZ119	73.29	0.11	15.12	1.23	0.03	0.14	0.95	4.25	4.05	0.07	0.56	99.8

Table 4.1c: XRF results of major elements within the sample RNZ119, carried out at the University of Canterbury, Christchurch, New Zealand (Muir et al., 1997).

Sample	V (ppm)	Cr (ppm)	Ni (ppm)	Zn (ppm)	Zr (ppm)	Nb (ppm)	Ba (ppm)	La (ppm)	Ce (ppm)	Nd (ppm)	Ga (ppm)	Pb (ppm)	Rb (ppm)	Sr (ppm)	Th (ppm)	Y (ppm)
RNZ119	13	7	3	46	95	7	1054	27	47	20	19	28	166	453	12	16

Sample	Sc (ppm)	Co (ppm)	Cs (ppm)	Sm (ppm)	Eu (ppm)	Gd (ppm)	Tb (ppm)	Tm (ppm)	Yb (ppm)	Lu (ppm)	Hf (ppm)	Ta (ppm)	U (ppm)
RNZ119	2.4	32	9.7	4.22	0.78	3.2	0.4	0.17	1.03	0.16	2.8	1.54	4

Table 4.1d: XRF results of trace elements within the sample RNZ119, carried out at the University of Canterbury, Christchurch, New Zealand (Muir et al., 1997).

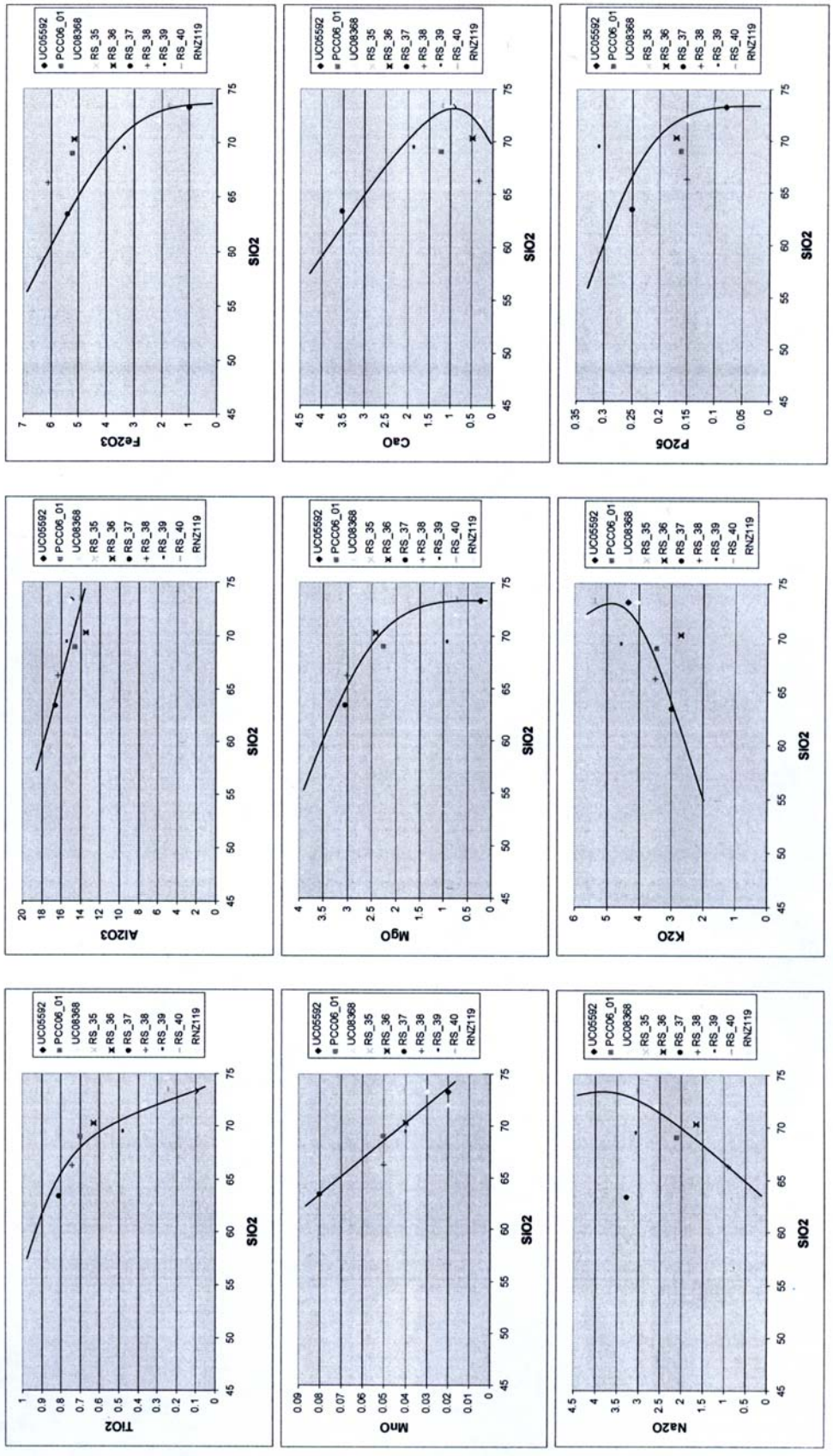

Figure 4.1: Bivariate plots of SiO_2 vs. TiO_2, Al_2O_3, Fe_2O_3, MnO, MgO, CaO, Na_2O, K_2O and P_2O_5 for samples UC05592, PCC06-01, UC08368, RS-35 to RS-40 and RNZ119, from the Paparoa Metamorphic Core Complex.

The oxygen system involves the three stable isotopes ^{16}O, ^{17}O and ^{18}O, with the $^{18}O/^{16}O$ ratio measured with respect to SMOW (Standard Mean Ocean Water). SMOW is the most commonly accepted international standard used in oxygen isotope work, and was originally defined by Craig in 1961 using the National Bureau of Standards sample NBS-1 by the following equation:

$$(^{18}O/^{16}O)_{SMOW} = 1.008\ (^{18}O/^{16}O)_{NBS\text{-}1}$$

The current formula commonly in use for oxygen isotope work is as follows:

$$\delta\ (^{18}O/^{16}O) = \frac{(^{18}O/^{16}O)_{sample} - (^{18}O/^{16}O)_{SMOW}}{(^{18}O/^{16}O)_{SMOW}}$$

$\delta^{18}O$ values calculated with this formula are expressed per mil (‰), with $\delta^{18}O$ values >6.5‰ representative of ^{18}O-enriched material, and $\delta^{18}O$ values <6.5‰ of material depleted in ^{18}O (Faure 1986). In general, mantle rocks have $\delta^{18}O$ values of +5 to +6‰, while the continental crust lies between +10 to >+25‰. Igneous rocks commonly lie between +5 to +15‰, with values >6.5‰ involving the incorporation of supra-crustal, recycled components in the melt (Winter 2001, Valley 2003, Kemp et al. 2006). The $\delta^{18}O$ value of 5.3 ± 0.3‰ represents the peridotitic mantle, with values greater than this having a distinct sedimentary signature (Eiler 2001, Valley 2003, Valley et al. 2005, Kemp et al. 2006). The nature of oxygen at the time of zircon crystallisation is recorded in $\delta^{18}O$ values, in grains that have not experienced metamictization. $\delta^{18}O$ values may be therefore linked to U-Pb ages, Hf and Ti, for each individual rock sample (Valley 2003).

Oxygen isotope data were sampled *in situ* from specimens RNZ119 [n2056], PCC06-01 [n2064], UC05592 [n2065] and UC08368 [n2068], using the SIMS technique (Table 4.2). The standard $\delta^{18}O$ value used was 9.86‰, which lies within error of the accepted SMOW value of 9.58‰ (Winter 2001). Average $\delta^{18}O$ values for each sample were calculated, +/- per mil to 2dp (Table 4.3). $\delta^{18}O$ values yield good positive averages for each sample, illustrating the relative enrichment of ^{18}O to SMOW.

RNZ119 [n2056] has the greatest margin of error for both xenocrystic cores and rims (8.34 ± 0.36 and 8.47 ± 0.36, respectively); with PCC06-01 [n2064] having the highest $\delta^{18}O$ values for xenocrystic cores (9.66 ± 0.15), and UC08368 [n2068] for rims (10.46 ± 0.16).

No outliers are considered to exist in the data, as all $\delta^{18}O$ values lie between the +5 and +15‰ characteristic of most igneous rocks (Winter 2001), with error margins of ± 0.15 to 0.36 per mil. No anomalous features were observed in CL where sampling took place, as any zircon grains containing visible inclusions or cracks were avoided to reduce potential outliers in the data set (Figures 3.1a, 3.1b, 31c and 3.1d).

4.1.3. Titanium

Titanium is a major element in zircon which has recently become a useful geochemical tool in the calculation of crystallisation temperatures of zircon-bearing igneous rocks. Zircon saturation thermometry has developed in the last few decades, with two main approaches.

Sample	Analysis	$\delta^{18}O$	± per mil	Sample	Analysis	$\delta^{18}O$	± per mil
RNZ119	n2056_ox_1c	8.81	0.37	PCC06-01	n2064_ox_1c	8.69	0.16
	n2056_ox_1r	7.96	0.37		n2064_ox_1r	8.73	0.15
	n2056_ox_2c	8.78	0.36		n2064_ox_2c	7.55	0.17
	n2056_ox_2r	8.03	0.37		n2064_ox_2r	9.3	0.14
	n2056_ox_3c	8.49	0.36		n2064_ox_3r	8.83	0.16
	n2056_ox_3r	10.06	0.36		n2064_ox_3c	7.96	0.15
	n2056_ox_4c	10.26	0.36		n2064_ox_4c	11.21	0.15
	n2056_ox_4r	7.97	0.36		n2064_ox_4r	11.78	0.16
	n2056_ox_5c	7.5	0.36				
	n2056_ox_5r	7.75	0.36	UC08368	n2068_ox_1c	7.21	0.19
	n2056_ox_5rr	7.69	0.36		n2068_ox_1r	10.43	0.16
	n2056_ox_6c	8.68	0.36		n2068_ox_2c	7.05	0.14
	n2056_ox_6r	9.45	0.36		n2068_ox_2r	10.37	0.15
	n2056_ox_7c	5.85	0.36		n2068_ox_3c	8.84	0.14
	n2056_ox_7r	8.87	0.36		n2068_ox_3r	10.02	0.16
					n2068_ox_4c	10.33	0.17
UC05592	n2065_ox_1c	8.72	0.16		n2068_ox_4r	9.62	0.16
	n2065_ox_2r	8.74	0.17		n2068_ox_5c	11.39	0.17
	n2065_ox_3c	8.51	0.16		n2068_ox_5r	11.87	0.18
	n2065_ox_3r	9.29	0.14				
	n2065_ox_4c	9.05	0.16				
	n2065_ox_4r	6.34	0.16				

Table 4.2: Oxygen isotope data for samples RNZ119 (n2056), PCC06-01 (n2064), UC05592 (n2065) and UC08368 (n2068) from the Paparoa Metamorphic Core Complex.

Sample [analysis number]	Average δ18O (cores)	± per mil (2dp)	Average δ18O (rims)	± per mil (2dp)	Average δ18O (total)	± per mil (2dp)
RNZ119 [n2056]	8.34	0.36	8.47	0.36	8.41	0.36
PCC06-01	8.85	0.16	9.66	0.15	9.26	0.16
UC05592 [n2065]	8.76	0.16	8.12	0.16	8.44	0.16
UC08368 [n2068]	8.96	0.16	10.46	0.16	9.71	0.16

Table 4.3: Average $\delta^{18}O$ data with +/- per mil (2dp) for RNZ119 (n2056), PCC06-01 (n2064), UC05592 (n2065) and UC08368 (n2068).

The ‘old’ approach to zircon saturation thermometry involves the use of major element concentrations by ‘whole rock’ analyses, based on hydrothermal experiments between 750 and 1020˚C (Hanchar and Watson 2003 and references therein).

Compositional data of melts and their associated crystallised zircons are used in the solubility model, which was introduced by Watson and Harrison in 1983 with the following equation:

$$\ln D_{Zr}^{zircon/melt} = (-3.80 - [0.85\ (M - 1)]) + 12900/T$$

Where $D_{Zr}^{zircon/melt}$ represents the ratio of zirconium in the solid to zirconium in the melt; M represents the cation ratio: $(Na + K + 2{*}Ca)/(Al{*}Si)$; and T is temperature (Kelvin).

The ‘new’ approach to zircon saturation thermometry involves the *in situ* sampling of titanium from individual zircon grains, in order to calculate crystallisation temperatures (Watson et al. 2006). Titanium is a well constrained trace element in zircon which is relatively unaffected by changes in pressure, and records temperature changes over time by variations in its concentration under Ti-saturated conditions.

Crystallisation temperatures are calculated with the following formula, and usually have error margins of less than ± 10˚C within the 400-1000˚C range (Watson et al. 2006):

$$T\ (°C)_{zircon} = \frac{5080 \pm 30}{(6.01 \pm 0.03) - \log (Ti)} - 273$$

This method of calculating temperatures is considerably more efficient than the 'whole rock' approach, and is becoming widely adopted in the scientific community.

Titanium content of zircon grains in samples RNZ119, UC08368, UC05592 and PCC06-01 were analysed by LA-ICP-MS at the Australian National University Research School of Earth Sciences in Canberra. Raw titanium data from LA-ICP-MS are listed in Table 4.4.

Crystallisation temperatures have been calculated for the Buckland Granite (RNZ119) with the 'new' zircon saturation thermometry approach, to estimate temperature conditions during its emplacement into the Paparoa Metamorphic Core Complex (Table 4.5a). The other three samples (UC08368, UC05592 and PCC06-01) are not able to provide any information on crystallisation temperatures during the Cretaceous, due to their emplacement pre-dating the onset of the regional-scale extension of the continental crust.

The average crystallisation temperature of the Buckland Granite (RNZ119) was calculated using all 35 analyses (including both xenocrystic cores and rims), at 697°C (3sf), with a standard deviation of 54.6 (3sf).

Xenocrystic cores and rims of zircon grains were analysed separately for the Buckland Granite sample (RNZ119), in attempt to determine differences in age and temperature during crystal growth. δT (°C) was calculated by subtracting the estimated temperatures of rims from the estimated temperatures of xenocrystic cores, for each grain that was sampled (Table 4.5a). Positive δT values are indicative of grains with older xenocrystic

Analysis	C/R	^{49}Ti (ppm)	Analysis	C/R	^{49}Ti (ppm)	Analysis	C/R	^{49}Ti (ppm)	Analysis	C/R	^{49}Ti (ppm)
BUCK_01	**C**	**12.4505762**	**S_01**	**C**	**6.13279773**	**68_01**	**C**	**7.2751621**	*92_01*	*?*	*5.19045061*
BUCK_02	**R**	**5.46449378**	**S_02**	**R**	**3.58149235**	**68_02**	**R**	**6.9718059**	*92_02*	*?*	*6.32271604*
BUCK_03	C	7.34289163	S_03	C	116.823362	68_03	C	15.4403668	**92_03**	**C**	**10.1351718**
BUCK_04	R	4.91487438	S_04	R	4.447368	68_04	R	10.309374	*92_04*	*?*	*6.12474064*
BUCK_05	**C**	**16.9924246**	**S_05**	**C**	**4.55021644**	**68_05**	**C**	**3.02027338**	92_05	C	8.53398422
BUCK_06	**R**	**30.3653469**	**S_06**	**R**	**4.53062354**	**68_06**	**R**	**3.45456618**	**92_06**	**R**	**16.176449**
BUCK_07	R	3.37231522	S_07	R	2.96656859	68_07	R	4.51691887	**92_07**	**R**	**5.03999167**
BUCK_08	C	7.58597952	*S_08*	*R*	*10.8926193*	68_08	R	3.35837087	**92_08**	**C**	**4.7169596**
BUCK_09	**C**	**12.4386343**	**S_09**	**R**	**2.40664106**	**68_09**	**C**	**5.7392717**	92_09	R	9.27295862
BUCK_10	**R**	**4.19160108**	**S_10**	**C**	**10.6204462**	**68_10**	**R**	**3.64127513**	**92_10**	**R**	**27.6782022**
BUCK_11	*C*	*6.63844782*	S_11	C	11.0773172	68_11	C	6.44492435	*92_11*	*C*	*6.84313387*
BUCK_12	C	5.76247482	**S_12**	**C**	**8.45227391**	68_12	R	19.3850417	92_12	R	5.40506217
BUCK_13	R	2.46354315	**S_13**	**R**	**5.12374529**	*68_13*	*C*	*13.7176361*	92_13	C	34.3898434
BUCK_14	**C**	**8.82482737**	*S_15*	*R*	*4.30121848*	*68_14*	*?*	*2.794775*			
BUCK_15	**R**	**6.81697016**	S_16	C	5.25663973	*68_15*	*?*	*7.45304616*			
BUCK_16	C	6.13070206	S_17	R	4.17381941	*68_16*	*?*	*4.16316984*			
BUCK_17	R	15.0398032	**S_18**	**R**	**17.1927495**	**68_17**	**C**	**9.37381595**			
BUCK_18	*C*	8.20092837	**S_19**	**C**	**338.482517**	**68_18**	**R**	**2.32423607**			
BUCK_19	*R*	*15.5382059*	S_20	R	3.88436996	68_19	C	5.00670847			
BUCK_20	*R*	*4.31481643*	S_21	C	117.194074	68_20	R	5.3922307			
BUCK_21	**R**	**8.08909817**	**S_22**	**C**	**3.62803598**	**68_21**	**C**	**3.68821368**			
BUCK_22	**C**	**4.13408424**	**S_23**	**R**	**4.27311604**	**68_22**	**R**	**17.5831998**			
BUCK_23	C	4.49786203	S_24	C	13.1278789	*68_23*	*?*	*29.7943473*			
BUCK_24	R	4.48319055	S_25	R	3.63314014	68_24	?	bdl			
BUCK_25	**C**	**16.7101318**	**S_26**	**C**	**9.25974963**	*68_25*	*?*	*6.24947728*			
BUCK_26	**R**	**12.2827945**	**S_27**	**R**	**3.23339699**	*68_26*	*?*	*484.410963*			
BUCK_27	R	5.09853367	S_28	C	7.94891407	*68_27*	*?*	*4.25543931*			
BUCK_28	C	5.44973055	S_29	R	6.05693557	68_28	?	bdl			
BUCK_29	*C*	*9.03373213*	**S_30**	**C**	**5.40372423**	*68_29*	*?*	*20.7464822*			
BUCK_30	**R**	**33.3480631**	**S_31**	**R**	**3.86650967**	*68_30*	*?*	*4.74840605*			
BUCK_31	**C**	**14.33371**	S_32	C	21.7017824						
BUCK_32	R	14.6704514	S_33	R	57.4859607						
BUCK_33	C	3.07919183	**S_34**	**C**	**8.73303043**						
BUCK_34	**C**	**6.23715787**	**S_35**	**R**	**4.61315236**						
BUCK_35	**R**	**3.94952321**									

Table 4.4: Titanium contents of RNZ119 (Buck), PCC06-01 (S), UC08368 (68) and UC05592 (92). Alternating font style (bold vs. regular) shows analyses common to individual zircon grains. Analyses in italics are samples spots which are not common to individual grains. '?' = analyses which may not be distinguished between cores or rims; bdl = below detection level.

Analysis	C vs. R	^{207}Pb corr'd ^{206}Pb/^{238}U age (Ma)	observed ±1s.e.	^{49}Ti (ppm)	Ti-in-zircon T (°C)	δT (°C) (C - R)
BUCK_01	**C**	**373.43**	**1.9**	**12.450576**	**760.6105429**	**70.111612**
BUCK_02	**R**	**110.98**	**0.5**	**5.4644938**	**690.4989309**	
BUCK_03	C	112.43	0.7	7.3428916	714.5328101	32.3740501
BUCK_04	R	135.25	1.1	4.9148744	682.15876	
BUCK_05	**C**	**109.21**	**0.8**	**16.992425**	**789.8182829**	**-59.1835709**
BUCK_06	**R**	**103.14**	**0.6**	**30.365347**	**849.0018538**	
BUCK_07	R	537.44	14.2	3.3723152	653.6569557	63.5987075
BUCK_08	C	1580.18	28.6	7.5859795	717.2556632	
BUCK_09	**C**	**634.64**	**5.8**	**12.438634**	**760.5229054**	**90.6204834**
BUCK_10	**R**	**101.45**	**0.5**	**4.1916011**	**669.902422**	
BUCK_11	C	313.79	17.4	6.6384478	706.1952894	
BUCK_12	C	110.82	1.7	5.7624748	694.731312	63.565715
BUCK_13	R	103.08	0.5	2.4635432	631.165597	
BUCK_14	**C**	**102.36**	**0.4**	**8.8248274**	**730.101364**	**21.725977**
BUCK_15	**R**	**108.83**	**0.6**	**6.8169702**	**708.375387**	
BUCK_16	C	108.85	0.5	6.1307021	699.7161191	-78.4435213
BUCK_17	R	110.2	0.7	15.039803	778.1596404	
BUCK_18	*C*	*111.15*	*0.7*	*8.200928*	*723.8334875*	
BUCK_19	*R*	*107.22*	*0.9*	*15.53821*	*781.2483127*	
BUCK_20	*R*	*122.74*	*1.3*	*4.314816*	*672.1096543*	
BUCK_21	**R**	**118.46**	**1.2**	**8.0890982**	**722.6684709**	**-53.8150661**
BUCK_22	**C**	**557.18**	**7.7**	**4.1340842**	**668.8534048**	
BUCK_23	C	470.32	3.8	4.497862	675.2930395	0.2511122
BUCK_24	R	108.78	1	4.4831906	675.0419273	
BUCK_25	**C**	**1066.92**	**4.7**	**16.710132**	**788.2029755**	**28.8301231**
BUCK_26	**R**	**1080.67**	**4.6**	**12.282795**	**759.3728524**	
BUCK_27	R	101.55	0.5	5.0985337	685.0287766	5.2554973
BUCK_28	C	275.69	5.1	5.4497306	690.2842739	
BUCK_29	*C*	*227.41*	*1.7*	*9.033732*	*732.1180311*	
BUCK_30	**R**	**76.11**	**0.8**	**33.348063**	**859.1773898**	**-85.5405257**
BUCK_31	**C**	**233.38**	**2.9**	**14.33371**	**773.6368641**	
BUCK_32	R	300.95	3	14.670451	775.8160871	-128.7867827
BUCK_33	C	510.91	18.2	3.0791918	647.0293044	
BUCK_34	**C**	**103.09**	**1.5**	**6.2371579**	**701.1106577**	**35.7081605**
BUCK_35	**R**	**101.26**	**0.7**	**3.9495232**	**665.4024972**	

Table 4.5a: Zircon saturation thermometry of the Buckland Granite (RNZ119) using titanium content, based on the method outlined in Watson et al., 2006. Alternating font style (bold vs. regular) shows analyses common to individual zircon grains. Analyses in italics are samples spots which are not common to individual grains, and are not included in the δT (°C) calculations.

cores and younger rims, while negative δT values represent grains which have ‘younger’ xenocrystic cores with ‘older’ rims.

Both positive and negative δT values are found in the Buckland Granite sample (RNZ119), with negative δT values resulting from either Pb-loss or the *in situ* sampling technique. Pb-loss is considered to be unlikely, as no substantial evidence of metamictization was observed in CL for RNZ119 zircons. The inversion of ages within individual grains is suggested to have resulted from the presence of shallow cores, which appeared to be large in the CL images. The *in situ* sampling technique may have drilled through the shallow core material, into progressively younger zircon growth rims. The averaging out of ‘core’ age data would lead to the core appearing younger than the outer rim, and thus cause the inversion of ages. This is considered to be the most likely suggestion of the two, and is proposed for the five zircon grains with analysis numbers BUCK-05 and 06, BUCK-16 and 17, BUCK-21 and 22, BUCK-30 and 31 and BUCK-32 and 33.

Crystallisation temperatures of both zircon cores and rims within the Buckland Granite (RNZ119) are listed in Tables 4.5b and 4.5c, respectively. The average crystallisation temperature of xenocrystic cores from sample RNZ119 is 723°C (3sf), with a standard deviation of 40.9 (3sf). The average crystallisation temperature of zircon rims from sample RNZ119 is 730°C (3sf), with a standard deviation of 67.8 (3sf). The difference in average temperatures between xenocrystic cores and rims of sample RNZ119 is considered to be negligible.

Granitoids rich in inherited zircons are considered to be ‘cold temperature’, with temperatures less than 800˚C. Inheritance-poor granitoids contain few to no zircons,

Analysis	Cores only	^{207}Pb corr'd $^{206}Pb/^{238}U$ age (Ma)	observed ±1s.e.	^{49}Ti (ppm)	Ti-in-zircon T (°C)
BUCK_01	C	373.43	1.9	12.450576	760.6105429
BUCK_03	C	112.43	0.7	7.3428916	714.5328101
BUCK_05	C	109.21	0.8	16.992425	789.8182829
BUCK_08	C	1580.18	28.6	7.5859795	717.2556632
BUCK_09	C	634.64	5.8	12.438634	760.5229054
BUCK_11	C	313.79	17.4	6.6384478	706.1952894
BUCK_12	C	110.82	1.7	5.7624748	694.731312
BUCK_14	C	102.36	0.4	8.8248274	730.101364
BUCK_16	C	108.85	0.5	6.1307021	699.7161191
BUCK_18	C	111.15	0.7	8.2009284	723.8334875
BUCK_22	C	557.18	7.7	4.1340842	668.8534048
BUCK_23	C	470.32	3.8	4.497862	675.2930395
BUCK_25	C	1066.92	4.7	16.710132	788.2029755
BUCK_28	C	275.69	5.1	5.4497306	690.2842739
BUCK_29	C	227.41	1.7	9.0337321	732.1180311
BUCK_31	C	233.38	2.9	14.33371	773.6368641
BUCK_33	C	510.91	18.2	3.0791918	647.0293044
BUCK_34	C	103.09	1.5	6.2371579	701.1106577

Table 4.5b: Zircon saturation thermometry of zircon xenocrystic cores from sample RNZ119 based on the method outlined in Watson et al. (2006).

Analysis	Rims only	^{207}Pb corr'd $^{206}Pb/^{238}U$ age (Ma)	observed ±1s.e.	^{49}Ti (ppm)	Ti-in-zircon T (°C)
BUCK_02	R	110.98	0.5	5.4644938	690.4989309
BUCK_04	R	135.25	1.1	4.9148744	682.15876
BUCK_06	R	103.14	0.6	30.365347	849.0018538
BUCK_07	R	537.44	14.2	3.3723152	653.6569557
BUCK_10	R	101.45	0.5	4.1916011	669.902422
BUCK_13	R	103.08	0.5	2.4635432	631.165597
BUCK_15	R	108.83	0.6	6.8169702	708.375387
BUCK_17	R	110.2	0.7	15.039803	778.1596404
BUCK_19	R	107.22	0.9	15.538206	781.2483127
BUCK_20	R	122.74	1.3	4.3148164	672.1096543
BUCK_21	R	118.46	1.2	8.0890982	722.6684709
BUCK_24	R	108.78	1	4.4831906	675.0419273
BUCK_26	R	1080.67	4.6	12.282795	759.3728524
BUCK_27	R	101.55	0.5	5.0985337	685.0287766
BUCK_30	R	76.11	0.8	33.348063	859.1773898
BUCK_32	R	300.95	3	14.670451	775.8160871
BUCK_35	R	101.26	0.7	3.9495232	665.4024972

Table 4.5c: Zircon saturation thermometry of zircon rims from sample RNZ119 based on the method outlined in Watson et al. (2006).

and are referred to as ‘hot temperature’ systems, with temperatures greater than 800˚C (Miller et al. 2003, Hanchar and Watson 2003). Temperatures calculated using zircon saturation thermometry are maximum and minimum estimates for the ‘cold’ and ‘hot’ temperature granitoids, respectively (Kemp et al. 2005a). The presence of both inherited and igneous zircon in the Buckland Granite suggests the pluton was ‘cold’ in temperature, under this classification.

Crystallisation temperatures of the Buckland Granite range from 697°C to 730°C, which lies within the upper-amphibolite facies.

The ultramylonite outcropping along the coastline north of the Fox River mouth was sampled at White Horse Creek (sample PCC06-02; Figure 2.7) for the isotopic dating by Rb/Sr analysis of the fine-grained matrix, feldspar and muscovite grains present. A Rb/Sr age of 116.2 ± 5.9 Ma with 2σ error was calculated for this sample, and is proposed to represent a pre-ultramylonitic early stage of deformation (Figure 4.2; Ring et al. 2006). The recrystallisation of feldspars within sample PCC06-02 indicates that deformation was well within the amphibolite facies range at 116.2 ± 5.9 Ma – further supporting the upper-amphibolite facies metamorphism of the Buckland Granite during the Cretaceous.

4.1.4. Hafnium

Hafnium is a major element within zircon, with average HfO_2 concentrations of 0.5-2.0 wt% (Hoskin and Schaltegger 2003). The incompatible, highly immobile element resists alteration due to its robust nature (Kemp et al. 2005b), and exhibits almost identical geochemical behaviour as zircon (Claiborne et al. 2006), making it an excellent tool for petrogenetic studies.

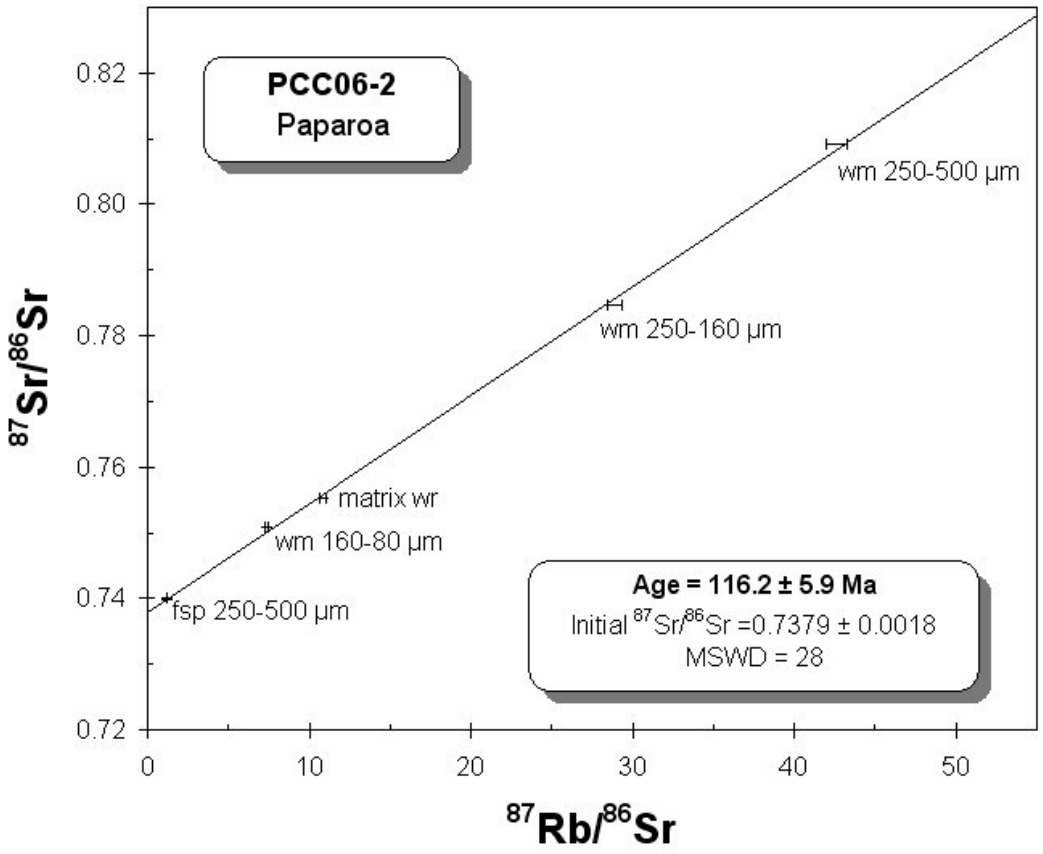

Figure 4.2: Plot of $^{87}Sr/^{86}Sr$ vs. $^{87}Rb/^{86}Sr$ of a mylonite (sample PCC06-02) from White Horse Creek at the southern end of the Paparoa Metamorphic Core Complex. A maximum age of ductile deformation is calculated as 116.2 ± 5.9 Ma (Ring et al. 2006).

Lutetium and hafnium are linked by the branched isobaric decay of ^{176}Lu to ^{176}Hf, while ^{177}Hf remains as a stable isotope (Dickin 2005, Belousova et al. 2006). Corrections for *in situ* radiogenic growth are not required, due to the low concentration of Lu-Hf ratios, and the high concentration of Hf within zircon (Yang et al. 2007).

Lu-Hf isotopes provide the means to trace chemical changes within a body of rock over time, with $^{176}Hf/^{177}Hf$ being calculated from the $^{176}Lu/^{177}Hf$ measured during sampling (Griffin et al. 2000). Initial $^{176}Hf/^{177}Hf$ ratios represent the composition of

hafnium during the crystallisation of zircon, with the *in situ* decay of ^{176}Lu considered to be insignificant (Kinny and Maas 2003). The initial $^{176}Hf/^{177}Hf$ ratio remains relatively unchanged during the evolution of a melt, allowing initial $^{176}Hf/^{177}Hf$ ratios to be directly linked to crystallisation ages calculated from the *in situ* sampling of U-Pb by laser ablation (Kinny and Maas 2003, Harrison et al. 2005).

Initial $^{176}Hf/^{177}Hf$ ratios of samples may be calculated using the Lu-Hf ratio, which involves the use of the following formula, where t = elapsed time and λ = the ^{176}Lu β-decay constant (Blichert-Toft and Albarède 1997):

$$(^{176}Hf/^{177}Hf)_t = (^{176}Hf/^{177}Hf)_{initial} + (^{176}Lu/^{177}Hf)_t \cdot (e^{\lambda t} - 1)$$

Elapsed time since the crystallisation of the Buckland Granite from the Paparoa Metamorphic Core Complex is calculated as 109.6 ± 1.7 Ma (Muir et al. 1992). The value of the ^{176}Lu β- decay constant is currently under revision, with 1.86×10^{-11} y^{-1} considered to be the most accurate estimate to date (Scherer et al. 2001, Kinny and Maas 2003). Hf deviations from CHUR (chondritic uniform reservoir) are described in parts per ten thousand as ε_{Hf} (initial Hf isotope ratios) with the following formula, where t = elapsed time (Kinny and Maas 2003):

$$\varepsilon_{Hf} = [(^{176}Hf/^{177}Hf)_t/(^{176}Hf/^{177}Hf)_{chondrites} - 1] \times 10^4$$

Any differences observed between measured $^{176}Hf/^{177}Hf$ values and calculated $(^{176}Hf/^{177}Hf)_{initial}$ values are considered to be negligible.

ε_{Hf} values may be either positive or negative with respect to chondritic $^{176}Hf/^{177}Hf$ ($\varepsilon_{Hf} = 0$), with positive values ($\varepsilon_{Hf} > 0$) indicating a mantle influence, while negative

values ($\varepsilon_{Hf} < 0$) infer the involvement of crustal material within the igneous system (Belousova et al. 2006, Hawkesworth and Kemp 2006).

Model ages may be calculated using Hf isotope ratios and $^{207}Pb/^{206}Pb$ ages, to calculate the time at which magma bodies (zircon host rocks) were extracted from a reference reservoir due to its robustness during alteration (Amelin et al. 1999, Nebel-Jacobsen et al. 2005, Nebel et al. 2007). The use of $^{176}Lu/^{177}Hf$ and $^{176}Hf/^{176}Hf$ values from Vervoort and Blichert-Toft (1999), along with U-Pb zircon ages allows a two-stage model age (T_{DM}) to be calculated. Reference reservoirs may either be the depleted mantle (DM) or the chondritic uniform reservoir (CHUR). The isotopic composition of a melt at the model age (T_{DM}) can therefore be assumed to be the same as the depleted mantle (Nebel et al. 2007). The depleted mantle is assumed to have an average Hf isotope value (εHf_{DM}) of 15.9, based on the values 0.038 and 0.283223 for $^{176}Lu/^{177}Hf$ and $^{176}Hf/^{176}Hf$, respectively (Vervoort and Blichert-Toft 1999).

Felsic and mafic T_{DM} values may be calculated for a magma to establish the minimum and maximum timing of extraction from the mantle, respectively (Nebel et al. 2007). Model ages allow the correlation of igneous rocks to major crustal-building and/or orogenic events during the history of the Earth, with the Early Proterozoic to Late Archean considered to be a period of accelerated crustal formation (Taylor and McLennan 1985).

Hafnium concentrations were sampled by the *in situ* LA-ICP-MS method, for samples RNZ119, UC08368, UC05592 and PCC06-01 from the Paparoa Metamorphic Core Complex (Table 4.6a), with hafnium data for the standards used being listed in Table 4.6b. Locations of analyses for each sample are shown in the

cathodoluminescence images (Figures 3.1a, 3.1b, 3.1c and 3.1d), which do not show any evidence of cracking or inclusions that result in anomalous values.

ε_{Hf} values have been calculated for zircons for sample RNZ119, following the method outlined in Nebel and co workers (2007) in which U-Pb zircon ages are correlated with Hf values of individual zircon grains.

Calculated ε_{Hf} values (including maximum and minimum ε_{Hf}) and T_{DM} of all analyses are listed in Table 4.7. ε_{Hf} values ranged from 14.4 to -22.2, with an average value of -1.7 and a standard deviation of 8.0. Maximum ε_{Hf} (uncorrected) values have an average of 1.8, with a standard deviation of 8.2. Minimum ε_{Hf} (uncorrected) values have an average of -4.7, with a standard deviation of 7.8.

T_{DM} mafic and T_{DM} felsic values for sample RNZ119 average at 3410 Ma and 2969 Ma, respectively, with the mafic T_{DM} value of 3410 Ma coinciding with the proposed major crustal formation event of the Gondwana supercontinent at c. 3.4-3.5 Ga (Kemp et al. 2006).

ε_{Hf} values were also calculated separately for zircon xenocrystic cores and rims for the sample RNZ119 (Tables 4.8a and 4.8b). Xenocrystic cores had an average ε_{Hf} value of -0.1, with a standard deviation of 11.1. Maximum ε_{Hf} (uncorrected) values for xenocrystic cores have an average of 3.3, with a standard deviation of 2.3. Minimum ε_{Hf} (uncorrected) values for xenocrystic cores have an average of -3.0, with a standard deviation of 1.7. Zircon rims had an average ε_{Hf} value of 0.0, with a standard deviation of 13.5.

Analysis	C vs. R	Volts	$^{176}Hf/^{177}Hf$	2σ error	$^{176}Lu/^{177}Hf$	corrected $^{176}Lu/^{177}Hf$
RNZ119						
HfB_01	**R**	**1.11**	**0.282997**	**0.000308**	**0.00239**	**0.00227**
HfB_02	**C**	**1.9**	**0.282671**	**0.000088**	**0.00025**	**0.00024**
HfB_03	C	2.12	0.282339	0.000074	0.0005	0.00047
HfB_04	R	3.44	0.282702	0.000067	0.00119	0.00113
HfB_05	**C**	**2.16**	**0.281748**	**0.000093**	**0.00082**	**0.00078**
HfB_06	**R**	**2.21**	**0.281804**	**0.00009**	**0.0009**	**0.00085**
HfB_07	C	2.36	0.282711	0.000088	0.00031	0.0003
HfB_08	R	1.87	0.282837	0.000157	0.00106	0.00101
HfB_09	**C**	**1.7**	**0.282804**	**0.0001**	**0.00055**	**0.00053**
HfB_10	**R**	**4.44**	**0.282785**	**0.000074**	**0.00169**	**0.00161**
UC08368						
Hf68_01	*C*	*2.44*	*0.282532*	*0.000077*	*0.00092*	*0.00088*
Hf68_02	C	1.63	0.282164	0.000093	0.00051	0.00049
Hf68_03	R	2.43	0.28252	0.000074	0.00049	0.00047
Hf68_04	**C**	**1.73**	**0.282423**	**0.0001**	**0.00148**	**0.00141**
Hf68_05	**R**	**2.26**	**0.282504**	**0.000083**	**0.00152**	**0.00145**
Hf68_06	C	1.78	0.282082	0.000101	0.00042	0.0004
Hf68_07	R	1.4	0.282136	0.000105	0.00088	0.00084
UC05592						
Hf92_01	**C**	**1.79**	**0.282646**	**0.000095**	**0.00197**	**0.00188**
Hf92_02	**R**	**1.99**	**0.282828**	**0.000092**	**0.0021**	**0.002**
Hf92_03	R	2.91	0.282545	0.000073	0.0002	0.00019
Hf92_04	R	2.41	0.282369	0.000085	0.00105	0.001
Hf92_05	**R**	**3.08**	**0.282843**	**0.000101**	**0.00276**	**0.00263**
Hf92_06	**C**	**1.33**	**0.283096**	**0.000249**	**0.00153**	**0.00146**
PCC06-01						
HfS_01	R	1.9	0.282167	0.000097	0.00064	0.00061
HfS_02	C	1.41	0.282135	0.000123	0.00137	0.0013
HfS_03	**C**	**1.74**	**0.281889**	**0.000094**	**0.00089**	**0.00085**
HfS_04	**R**	**2.36**	**0.281901**	**0.000085**	**0.00106**	**0.00101**
HfS_05	R	1.71	0.282072	0.000088	0.00117	0.00112
HfS_06	C	1.42	0.282145	0.000108	0.00127	0.00121
HfS_07	**C**	**1.51**	**0.282482**	**0.000116**	**0.00048**	**0.00046**
HfS_08	**R**	**2.42**	**0.282525**	**0.000076**	**0.00048**	**0.00046**

Table 4.6a: Hafnium data for samples RNZ119, UC08368, UC5592 and PCC06-01. Alternating font style (bold vs. regular) shows analyses common to individual zircon grains. Analyses in italics are samples spots which are not common to individual grains, and are not included in the Hf calculations.

Analysis	Volts	$^{176}Hf/^{177}Hf$	2σ error	$^{176}Lu/^{177}Hf$	measured-accepted
266_01	1.05	0.281646	0.000125	0.000222	1.60E-05
266_02	1.06	0.281594	0.000142	0.000219	-3.60E-05
266_03	1.07	0.281613	0.000152	0.000219	-1.70E-05

Table 4.6b: Hafnium data for standards used for the samples UC08368, UC5592 and PCC06-01.

Analysis	C vs. R	$^{176}Hf/^{177}Hf$	2σ error	Lu/Hf (corrected)	U-Pb age (Ma)	± 1 se	Hf age (corrected)	Hf CHUR at T
HfB_01	R	0.282997	0.000308	0.00227	314.6349783	17.57113524	0.282984	0.282577
HfB_02	C	0.282671	0.000088	0.00024	116.3241816	1.712684739	0.28267	0.2827
HfB_03	C	0.282339	0.000074	0.00047	636.0121967	5.858756696	0.282333	0.282376
HfB_04	R	0.282702	0.000067	0.00113	101.3314408	0.479427994	0.2827	0.282709
HfB_05	C	0.281748	0.000093	0.00078	1604.237201	29.27925056	0.28174	0.282422
HfB_06	R	0.281804	0.00009	0.00085	562.5694685	14.85492491	0.281778	0.281763
HfB_07	C	0.282711	0.000088	0.0003	102.7025288	0.415364854	0.28271	0.282708
HfB_08	R	0.282837	0.000157	0.00101	109.3607797	0.63347052	0.282835	0.282704
HfB_09	C	0.282804	0.0001	0.00053	112.5138063	0.718688839	0.282803	0.282702
HfB_10	R	0.282785	0.000074	0.00161	135.4818137	1.05858967	0.282781	0.282688
Average	-	0.2825398	0.0001139	0.000919	379.5168395	7.2582294	0.2825398	0.0001139

Analysis	C vs. R	εHf	εHf max (uncorrected)	εHf min (uncorrected)	Hf_{DM} at T	calculated T_{DM}	T_{DM} mafic	T_{DM} felsic
HfB_01	R	14.4	25.8	4	0.282999	344	3410	2969
HfB_02	C	-1	2.1	-4.1	0.28314	987	3410	2969
HfB_03	C	-1.5	1.3	-3.9	0.282769	1444	3410	2969
HfB_04	R	-0.3	2.1	-2.6	0.283151	937	3410	2969
HfB_05	C	-1.4	2.8	-3.8	0.282068	2243	3410	2969
HfB_06	R	-22.2	-18.7	-25.1	0.282822	2447	3410	2969
HfB_07	C	0.1	3.2	-3	0.28315	918	3410	2969
HfB_08	R	4.6	10.3	-0.9	0.283145	686	3410	2969
HfB_09	C	3.6	7.1	0.1	0.283143	744	3410	2969
HfB_10	R	3.3	6.1	0.8	0.283127	778	3410	2969
Average	-	-1.7	1.8	-4.7	0.282952	1243	3410	2969
Std dev	-	8	8.2	7.8	0	664.3	-	-

Table 4.7: Combined LA-ICP-MS data for sample RNZ119, with calculated values for εHf and T_{DM} for all analyses. The calculation of εHf follows the method used by Nebel et al. (2007), with U-Pb ages sourced from individual zircon grains. Averages and standard deviations are shown for εHf, εHf max (uncorrected), εHf min (uncorrected), Hf_{DM} at T and calculated T_{DM}.

Analysis	C vs. R	$^{176}Hf/^{177}Hf$	2σ error	Lu/Hf	U-Pb age (Ma)	± 1 se	Hf age	Hf CHUR at T
HfB_02	C	0.282671	0.000088	0.00024	116.32418	1.7126847	0.28267	0.2827
HfB_03	C	0.282339	0.000074	0.00047	636.0122	5.8587567	0.282333	0.282376
HfB_05	C	0.281748	0.000093	0.00078	562.56947	14.854925	0.28174	0.282422
HfB_07	C	0.282711	0.000088	0.0003	102.70253	0.4153649	0.28271	0.282708
HfB_09	C	0.282804	0.0001	0.00053	112.51381	0.7186888	0.282803	0.282702
Average	-	0.2824546	8.86E-05	0.000464	306.02444	4.712084	0.2824546	8.86E-05

Analysis	C vs. R	εHf	εHf max	εHf min	Hf_{DM} at T	calculated T_{DM}	T_{DM} mafic	T_{DM} felsic
HfB_02	C	-1	2.1	-4.1	0.28314	987	3410	2969
HfB_03	C	-1.5	1.3	-3.9	0.282769	1444	3410	2969
HfB_05	C	-24.1	-20.6	-27.1	0.282822	2546	3410	2969
HfB_07	C	0.1	3.2	-3	0.28315	918	3410	2969
HfB_09	C	3.6	7.1	0.1	0.283143	744	3410	2969
Average	-	-4.6	-1.4	-7.6	0.283005	1328	3410	2969
Std dev	-	11.1	11	11	0	728.7	-	-

Table 4.8a: Combined LA-ICP-MS data for sample RNZ119, with calculated values for εHf and T_{DM} for zircon xenocrystic cores only. The calculation of εHf follows the method used by Nebel et al. (2007), with U-Pb ages sourced from individual zircon grains. Averages and standard deviations are shown for εHf, εHf max (uncorrected), εHf min (uncorrected), Hf_{DM} at T and calculated T_{DM}.

Analysis	C vs. R	$^{176}Hf/^{177}Hf$	2σ error	Lu/Hf	U-Pb age (Ma)	± 1 se	Hf age	Hf CHUR at T
HfB_01	R	0.282997	0.000308	0.00227	314.63498	17.571135	0.282984	0.282577
HfB_04	R	0.282702	0.000067	0.00113	101.33144	0.479428	0.2827	0.282709
HfB_06	R	0.281804	0.00009	0.00085	1604.2372	29.279251	0.281778	0.281763
HfB_08	R	0.282837	0.000157	0.00101	109.36078	0.6334705	0.282835	0.282704
HfB_10	R	0.282785	0.000074	0.00161	135.48181	1.0585897	0.282781	0.282688
Average	-	0.282625	0.000139	0.001374	453.00924	9.8043748	0.282625	0.000139

Analysis	C vs. R	εHf	εHf max	εHf min	Hf_{DM} at T	calculated T_{DM}	T_{DM} mafic	T_{DM} felsic
HfB_01	R	14.4	25.8	4	0.282999	344	3410	2969
HfB_04	R	-0.3	2.1	-2.6	0.283151	937	3410	2969
HfB_06	R	0.5	4.6	-1.7	0.282068	2143	3410	2969
HfB_08	R	4.6	10.3	-0.9	0.283145	686	3410	2969
HfB_10	R	3.3	6.1	0.8	0.283127	778	3410	2969
Average	-	4.5	9.8	-0.1	0.282898	978	3410	2969
Std dev	-	5.9	9.4	2.6	0	687	-	-

Table 4.8b: Combined LA-ICP-MS data for sample RNZ119, with calculated values for εHf and T_{DM} for zircon rims only. The calculation of εHf follows the method used by Nebel et al. (2007), with U-Pb ages sourced from individual zircon grains. Averages and standard deviations are shown for εHf, εHf max (uncorrected), εHf min (uncorrected), Hf_{DM} at T and calculated T_{DM}.

Maximum ε_{Hf} (uncorrected) values for zircon rims have an average of 5.1, with a standard deviation of 16.0. Minimum ε_{Hf} (uncorrected) values for zircon rims have an average of -4.7, with a standard deviation of 11.6.

ε_{Hf} values of zircons from sample RNZ119 are both negative and positive, with an average negative value of -1.7. The presence of negative ε_{Hf} values indicates crustal involvement during the crystallisation of zircon, as expected for the S-type nature of the Buckland Granite.

4.1.5. REE's

The REE's are a group of trivalent cation elements, which successfully record geochemical processes taking place during the petrogenesis of igneous and metamorphic rocks (Wark and Miller 1993, Cherniak and Watson 2003). Elements commonly included within the REE group are yttrium, lanthanum and the lanthanides, from cerium to lutetium (Henderson 1996), which is adopted for this thesis.

REE's are considered to be incompatible in silicate magmatic systems, and reside in the melt during crystallisation of magma. REE's become incorporated into minerals with larger cations, including zircon, titanite, apatite, epidote and garnet (Henderson 1996). REE's are subdivided into the light REE's (LREE's), which range from lanthanum to samarium, and the heavy REE's (HREE's), from gadolinium to lutetium (Henderson 1996).

Zircon is an excellent tool in geochemical investigations into the petrogenesis of igneous and metamorphic rocks, and is commonly sampled by *in situ* techniques including SIMS and LA-ICP-MS. Unaltered zircons characteristically show a reduction in LREE's and an increase in HREE's, with positive Ce and negative Eu anomalies (Hoskin and Schaltegger 2003). Zircons which have not suffered alteration

generally have very low concentrations of L, Be, B, F, Na, Mg, Al, P, Ca, Sc, Ti, V, Cr, Mn, Fe, Sr, Nb, Ba and Ta (Hoskin and Schaltegger 2003). Zircons which have experienced alteration often display a relative increase in LREE's and reduction in HREE's, through the leaching of the highly mobile elements during hydrothermal fluid movement through the crust (Tulloch and Christie 2000). The role of fluid flow on the behaviour of REE's in the continental crust is of importance, as REE's are considered mobile in aqueous systems. Hydrothermal fluids encourage the leaching and transport of REE's along faults or fractures in the upper crust (Henderson 1996).

Previous geochemical work has been undertaken in the Paparoa Metamorphic Core Complex, with the sampling of REE concentrations in rocks adjacent to the Ohika and Pike Detachment Faults of the Paparoa Metamorphic Core Complex (Figure 4.3a; Christie et al. 1998, Tulloch and Christie 2000). Depleted concentrations of REE's were observed in granitoid rocks of the Lower Plate, while elevated concentrations were found in the Greenland Group metasediments and Hawks Crag Breccia units of the Upper Plate. Depletions and elevations of REE concentrations are relative to 'background rocks', which include geochemical data from unaltered samples of the Buckland and Charleston Granites (Tulloch and Christie 2000). The reduction of REE's in Lower Plate rocks is proposed to have taken place through the leaching of elements by hydrothermal fluids during the rapid exhumation of the Lower Plate granitoid rocks during extension. Fluids are suggested to have transported the mobile REE's into the Upper Plate, to become concentrated within the water-saturated cover rocks of the metamorphic core complex (Tulloch 1995). This REE analysis showed a negative trend with an enrichment of LREE's and depletion of HREE's (Figure 4.3b;

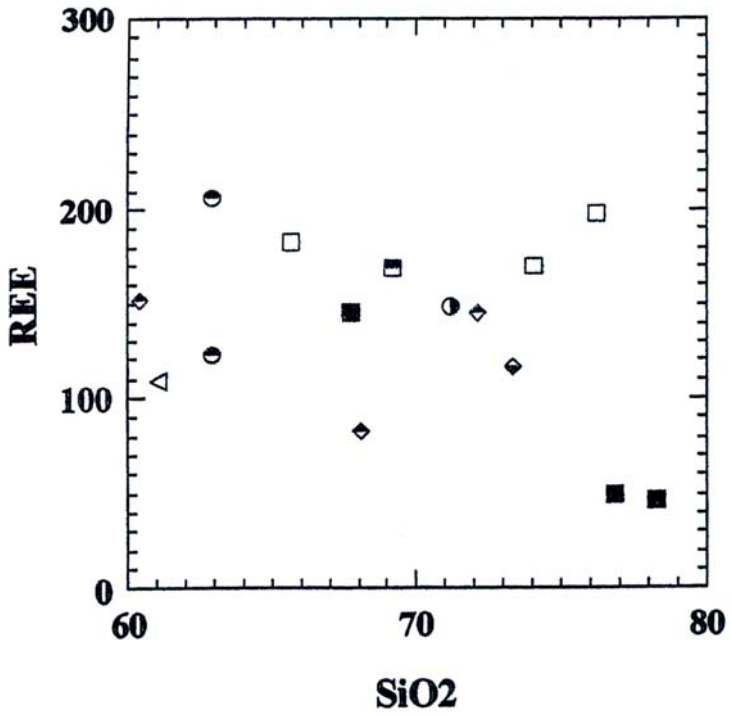

Figure 4.3a: Plot of SiO_2 vs. REE's of rocks adjacent to the Pike and Ohika Detachment Faults of the Paparoa Metamorphic Core Complex (Tulloch and Christie 2000).

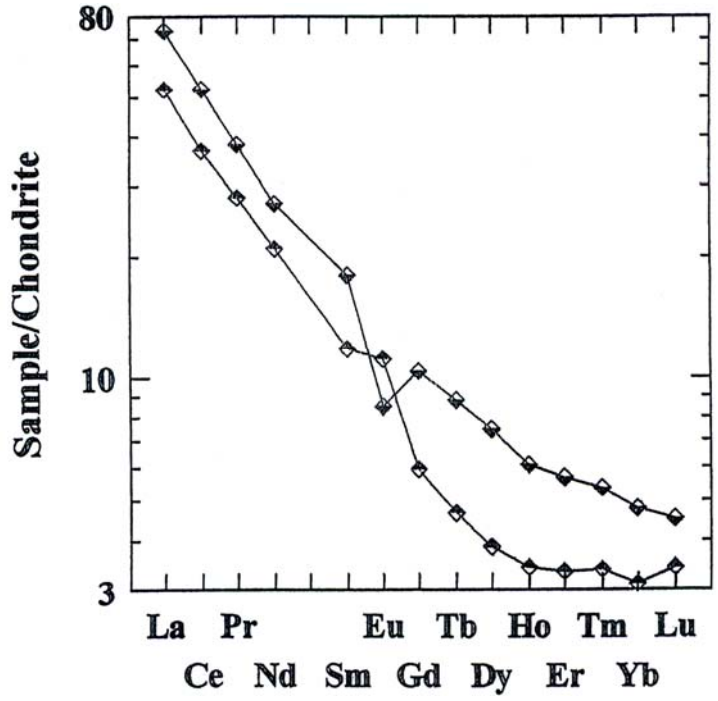

Figure 4.3b: Plot of chondrite-normalised REE's of unaltered granitoids of the Paparoa Metamorphic Core Complex (Tulloch and Christie 2000).

Tulloch and Christie 2000). It is important to note that the proposed role of hydrothermal fluids on REE concentrations within the Lower Buller Gorge area is based on very few samples, and may only reflect a localised geochemical process (Tulloch and Christie 2000).

Further geochemical investigations have been carried out, with the sampling of REE's of rocks associated with both the Ohika and Pike Detachment Faults of the Paparoa Metamorphic Core Complex. The concentrations of REE's ^{139}La, ^{140}Ce, ^{147}Sm, ^{153}Eu, ^{163}Dy and ^{175}Lu, along with ^{89}Y, were measured during the *in situ* LA-ICP-MS analyses of zircons from samples UC05592, UC08368, RNZ119 and PCC06-01 (Tables 4.9a, 4.9b, 4.9c and 4.9d). Remaining REE's were interpolated from these values, and plotted in chondrite-normalised REE diagrams. Xenocrystic cores and rims are plotted separately, to allow comparisons to be made both within and between samples. The break of trends in the following chondrite-normalised REE diagrams exists due to the exclusion of Pm values.

Ce and Eu anomalies within the data followed the expected positive and negative trends, respectively for unaltered igneous zircon. The presence of anomalously high levels of P and La in some analyses is considered to represent the sampling of mineral inclusions, such as monazite and apatite, within individual zircon grains. These analyses are therefore considered to be outliers, and have not been included in the chondrite-normalised REE diagrams.

<u>UC05592</u>

The REE concentrations of xenocrystic zircon cores are shown in Figure 4.4a, with analyses 92-03, 92-05, 92-08 and 92-11. REE patterns of zircon rims are plotted

Analysis	U (ppm)	±	Th (ppm)	±	Th/U	P (ppm)	±	HfO_2 (wt%)	^{208}Pb corr'd $^{206}Pb/^{238}U$ age	observed ±1s.e.	calculated MSWD	expected MSWD
92_01	860.6	7.8	217.1	3	0.25	618.9	6	1.2	297.4303486	3.991886304	5	1.43643578
92_02	1168	32.7	200.6	7.4	0.17	716.4	4	1.3	239.5477162	3.886700438	152.8075412	1.333333333
92_03	629.7	15	281.9	13.6	0.45	871.2	17.9	1.2	336.0306656	2.080477828	9.473423558	1.333333333
92_04	3334.7	44.2	221.3	3.2	0.06	1042.1	20.6	1.7	761.1094961	9.247204587	803.3213859	1.333333333
92_05	3345.5	69.9	269.4	5.7	0.08	1614.2	20.3	1.9	1015.456051	4.461412297	119.8832065	1.333333333
92_06	2589.3	94.6	193.5	8.6	0.07	741.3	15.1	1.5	160.9600057	6.355173783	517.7242367	1.353553391
92_07	1711.9	167.1	169.2	18.8	0.1	663.2	37.4	1.4	249.3183688	13.86488785	5	1.34554737
92_08	623.9	5.7	180.2	1.9	0.29	177.7	1.1	1.1	665.0654357	5.522177547	60.00929658	1.333333333
92_09	3728.8	70	266.9	7.6	0.07	1518.3	20.6	1.7	781.3093172	6.247766846	302.2228965	1.333333333
92_10	595.6	10.5	529.2	10.8	0.89	451.7	3.1	0.9	293.3765261	1.784479247	11.62403015	1.333333333
92_11	747.9	8.1	678.2	13.7	0.91	720.2	5.7	1.1	295.2686703	2.537155842	16.63493576	1.396059017
92_12	914.6	11.7	245.9	8.8	0.27	1295.2	38	1.2	329.0550824	5.364985881	18.39309442	1.333333333
92_13	6814.6	152.8	201.3	14.6	0.03	1480.4	14	1.9	86.64086097	1.312660606	87.79967131	1.478091444

Analysis	^{139}La (ppm)	^{140}Ce (ppm)	^{147}Sm (ppm)	^{153}Eu (ppm)	^{163}Dy (ppm)	^{175}Lu (ppm)	^{89}Y (ppm)	^{49}Ti (ppm)
92_01	0.47570434	7.49130251	3.75167754	0.27510323	141.066834	90.6590186	799.997253	5.19045061
92_02	1.2385237	8.74418374	5.88348366	1.50120944	169.324199	107.806052	963.218442	6.32271604
92_03	0.06678214	9.73908861	5.74662396	0.26812464	223.976896	139.350776	1293.95621	10.1351718
92_04	7.08186636	8.08434736	11.9641149	1.96617462	252.462256	195.773296	1343.82783	6.12474064
92_05	0.95862041	3.83612537	5.25443728	0.51734065	325.350738	275.502049	1910.43546	8.53398422
92_06	5.24033636	25.4310669	23.2866859	10.0504853	276.279911	125.716239	1305.58304	16.176449
92_07	2.29319763	6.55300502	4.9946358	1.00625184	191.887374	110.180503	1048.19722	5.03999167
92_08	1.64036425	14.9680122	3.83682013	0.74659946	70.8164675	49.7045213	406.583134	4.7169596
92_09	43.3290393	72.7002631	38.0816225	9.93158674	388.911008	254.111672	2075.40588	9.27295862
92_10	0.55665141	24.3686256	9.02298675	0.61598326	220.440653	106.016148	1180.84025	27.6782022
92_11	1.62655351	24.968973	9.81230007	1.224361	260.792109	125.891791	1426.50612	6.84313387
92_12	2.43587319	11.2586028	6.08266613	1.13033753	210.021299	130.872529	1238.12156	5.40506217
92_13	32.402713	64.2886503	79.1710769	26.4260736	774.593158	295.808391	3257.70474	34.3898434

Table 4.9a: LA-ICP-MS results for sample UC05592, where bdl: below detection level.

Analysis	U (ppm)	±	Th (ppm)	±	Th/U	P (ppm)	±	HfO_2 (wt%)	^{208}Pb corr'd $^{206}Pb/^{238}U$ age	observed ±1s.e.	calculated MSWD	expected MSWD
68_01	506.4	31.6	94.3	7.3	0.19	406.3	6.5	1.5	0.07608141	0.0012919	116.1578264	1.333333333
68_02	318.9	11.1	90.1	3.5	0.28	365	5.1	1.2	0.06297728	0.0006158	11.71830583	1.333333333
68_03	131.4	2.9	70.1	1.7	0.53	289.9	1.9	1.1	0.17666481	0.00173279	22.75100419	1.388514345
68_04	220.1	2.9	136.4	3	0.62	214	2.2	1.2	0.16617933	0.00189755	61.99061316	1.350823208
68_05	1141.4	19.1	377.9	12.8	0.33	610.7	41	1.3	0.0798396	0.00089678	139.4833375	1.335672543
68_06	1376.1	30	341.4	12.3	0.25	535.5	37	1.3	0.07119915	0.00076679	133.2402302	1.333333333
68_07	603.8	8.9	194.8	6.6	0.32	480.1	7.1	1.1	0.2062262	0.00348624	353.0931365	1.368229847
68_08	1445.7	78.8	107.6	6.1	0.07	1102.3	39.1	1.4	0.0741271	0.0016922		3.828427125
68_09	326.3	10.7	61.7	3.4	0.19	187.8	3	1.1	0.12545889	0.00327354	290.6561264	1.34554737
68_10	1239.2	51.2	44.1	1.9	0.04	758.6	27.8	1.4	0.05230716	0.00064004	48.83806808	1.43643578
68_11	372.5	13.5	86	3.6	0.23	563.2	11.1	1.2	0.17352587	0.00284299	176.4189644	1.333333333
68_12	832.3	25.8	146.8	5.5	0.18	7444.4	583.5	1.3	0.15833916	0.00196004	197.8094162	1.333333333
68_13	194.5	2.8	97	2.1	0.5	610.4	5.3	1	0.05740094	0.0002753	2.512312171	1.335672543
68_14	2028.1	98.6	66.8	6.7	0.03	567.7	18.7	1.5	0.06517195	0.00156919	303.5846307	1.516397779
68_15	1113.9	34	57.4	2.5	0.05	338.8	5.6	1.5	0.081862	0.00089336	109.8190828	1.333333333
68_16	1699.7	12.7	26.2	0.3	0.02	11265.4	1139.6	1.6	0.04756201	0.00047228	23.36627952	1.471404521
68_17	375	2.7	224.5	1.8	0.6	438.4	3.5	0.9	0.19215437	0.00105178	10.57191364	1.478091444
68_18	352.9	2.4	38.7	0.7	0.11	91.8	3.6	1.3	0.16091985	0.00299038	261.8578685	1.335672543
68_19	287.6	7.3	111.2	3.9	0.39	309.3	8.6	1.1	0.21546371	0.00772619	500.6073312	1.371390676
68_20	1398.1	35.1	100.9	2.8	0.07	948.6	21.7	1.4	0.05335202	0.00033827	28.06228211	1.333333333
68_21	612.9	32.9	128.4	11.5	0.21	377.7	13.8	1.4	0.10709415	0.00364908	755.2797601	1.333333333
68_22	180	6.2	89.2	4.2	0.5	253.9	6.4	1.1	0.15350531	0.00149673	10.6720748	1.478091444
68_23	336.8	7.3	154.5	4.4	0.46	439.1	2.9	1	0.16727636	0.00120705	17.88406087	1.441726104
68_24	1238.1	21.1	36	1.3	0.03	269	11.6	1.4	0.08179109	0.00090845	54.71455943	1.508000508
68_25	314.2	16.2	109.7	6.9	0.35	560.6	18.6	1.1	0.05836476	0.00046647	11.01820751	1.338061702
68_26	555.9	32.8	113.3	8.2	0.2	477.4	12.4	1.3	0.05435531	0.00025136	5.329991165	1.338061702
68_27	402.1	19.3	121.8	5.9	0.3	424.4	5.9	1.2	0.06342026	0.00041078	7.090854152	1.40824829
68_28	2225.1	24.6	99.2	4.5	0.04	724.1	19.9	1.6	0.0508367	0.00019292	17.80485794	1.333333333
68_29	981	47.2	177.1	13.3	0.18	481.5	17.7	1.4	0.08962102	0.00266691	509.9625242	1.356348323
68_30	2031.5	28.8	59.5	1.8	0.03	651.6	4.6	1.5	0.05067122	0.00039926	43.8369768	1.417028828

Table 4.9b: LA-ICP-MS results for sample UC08368, where bdl: below detection level.

Analysis	^{139}La (ppm)	^{140}Ce (ppm)	^{147}Sm (ppm)	^{153}Eu (ppm)	^{163}Dy (ppm)	^{175}Lu (ppm)	^{89}Y (ppm)	^{49}Ti (ppm)
68_01	bdl	2.80581379	3.7246978	0.14910712	90.7540103	56.5191697	476.834277	7.2751621
68_02	bdl	2.28476949	5.4439662	0.1878542	90.9569033	16.256701	366.590111	6.9718059
68_03	0.0336273	9.26777764	4.88978258	0.58911961	78.2177948	34.7529252	404.116214	15.4403668
68_04	bdl	12.1597321	5.33840384	0.5690099	100.431253	40.413456	526.971184	10.309374
68_05	1.55616383	12.5677761	5.44478829	0.54141964	134.190212	91.1669749	816.660916	3.02027338
68_06	71.8255326	154.437139	17.4923422	0.64881751	160.202404	92.5363498	921.118888	3.45456618
68_07	0.42221099	9.2693531	5.87023748	1.73594176	101.040977	85.0177345	618.532797	4.51691887
68_08	bdl	1.13579907	3.66379434	0.16654676	181.987386	103.116854	1092.00711	3.35837087
68_09	bdl	3.82624257	2.5790648	0.44237088	62.8002721	37.2484828	338.02898	5.7392717
68_10	0.05876913	0.64393832	2.44813473	0.1425128	123.309997	88.5371385	790.590314	3.64127513
68_11	bdl	2.00270951	3.97951737	0.14881723	104.748414	61.8580419	586.322468	6.44492435
68_12	19.3466632	61.2788924	24.867306	0.95614028	147.373499	75.7370115	741.848163	19.3850417
68_13	0.05129359	2.85523338	8.00766672	0.53410589	156.790928	76.7684365	839.290956	13.7176361
68_14	bdl	2.2334935	1.84365456	0.17391933	108.16896	103.988924	716.43157	2.794775
68_15	0.02715874	1.03416723	4.25064652	0.06448785	61.9488266	36.4984173	307.886574	7.45304616
68_16	11.6085834	22.4436813	12.1869529	0.86539667	134.301383	89.4470477	906.826208	4.16316984
68_17	0.05409918	13.4429181	13.9315843	3.77685196	367.802517	193.057357	2058.5756	9.37381595
68_18	bdl	1.81221771	0.57551656	0.18883838	15.7152566	21.0652187	103.208835	2.32423607
68_19	bdl	5.78946177	4.59035061	0.40773931	109.82779	65.2640123	624.509983	5.00670847
68_20	0.41164836	1.51746681	4.63385543	0.17442883	166.1911	80.9717119	963.970769	5.3922307
68_21	bdl	14.2157965	2.82863443	0.23202953	90.4591498	74.702286	540.400362	3.68821368
68_22	0.05538655	25.5398444	2.47456541	0.44554625	67.1150709	54.1050027	383.359675	17.5831998
68_23	0.04719652	2.73789168	10.1753435	0.4061461	229.904879	102.460891	1214.01122	29.7943473
68_24	bdl	0.81203576	0.74161711	0.09279152	41.4125178	42.5366	264.657088	bdl
68_25	bdl	4.20953602	4.78970629	0.48096786	108.101349	48.1659054	563.454038	6.24947728
68_26	0.29490558	3.09470484	3.69914348	0.21325702	113.584343	52.278702	643.599897	484.410963
68_27	bdl	2.93026771	5.58177462	0.27583494	117.060778	35.8686764	570.12811	4.25543931
68_28	0.19736607	1.96665821	3.11562653	0.15618732	132.134641	125.404887	851.079339	bdl
68_29	0.10089548	5.89480242	4.63863647	0.21082513	154.15602	90.4689235	900.105077	20.7464822
68_30	0.05602852	0.70429162	2.56954044	0.12329184	84.8115406	100.342896	582.682079	4.74840605

Table 4.9b (continued): LA-ICP-MS results for sample UC08368, where bdl: below detection level.

Analysis	U (ppm)	±	Th (ppm)	±	Th/U	P (ppm)	±	HfO_2 (wt%)	^{208}Pb corr'd $^{206}Pb/^{238}U$ age	observed ±1s.e.	calculated MSWD	expected MSWD
BUCK_01	775	44.6	68.1	4	0.09	878.2	21.7	1.4	373.71906	1.88504915	9.536319402	1.331042355
BUCK_02	542.3	2.9	72.4	0.5	0.13	383.1	3.1	1.3	111.1498235	0.451633494	5	1.333333333
BUCK_03	314.1	4.7	118.7	2.3	0.38	313.8	4.8	1.1	112.5138063	0.718688839	5	1.335672543
BUCK_04	158.3	1.4	72.5	0.7	0.46	157.1	1.5	1	135.4818137	1.05858967	1.465020447	1.447213595
BUCK_05	248.7	4	267.2	5.8	1.07	294.4	2	0.9	110.4814407	0.901695887	2.624205708	1.331042355
BUCK_06	1486.1	41.7	223.5	9	0.15	832.3	13.9	1.2	103.4311859	0.637038014	5	1.333333333
BUCK_07	939.9	46.4	28.8	1.6	0.03	982.6	10	1.5	562.5694685	14.85492491	1026.788457	1.331042355
BUCK_08	330.6	13.1	116.7	7.1	0.35	273.7	7.9	1.2	1604.237201	29.27925056	316.3974393	1.331042355
BUCK_09	252.4	7.6	46.3	1.7	0.18	371.4	5	1.3	636.0121967	5.858756696	26.71174895	1.331042355
BUCK_10	3492.2	25.3	87.1	1	0.02	1312.2	9.9	1.7	101.3314408	0.479427994	13.69291182	1.340502612
BUCK_11	318.3	5.6	71.5	1.6	0.22	289.6	2.6	1.2	314.6349783	17.57113524	5	1.816496581
BUCK_12	93.3	5.2	28.2	1.7	0.3			1	116.3241816	1.712684739	5	1.4
BUCK_13	2117.3	79.7	154.5	14.7	0.07	852	12.7	1.6	103.2511763	0.519606292	6.989626798	1.331042355
BUCK_14	976.9	7.8	223.9	2.8	0.23	524.6	5	1.2	102.7025288	0.415364854	2.920392212	1.335672543
BUCK_15	696.4	31.4	94.7	5.6	0.14	422.8	10.6	1.3	109.3607797	0.63347052	5	1.335672543
BUCK_16	439.1	4.3	137.9	1.4	0.31	395.9	3	1.3	109.4416091	0.457400445	1.665647195	1.331042355
BUCK_17	457.5	8.5	109.1	3.7	0.24	394.1	8	1.2	110.6759035	0.678463122	3.282758145	1.348155312
BUCK_18	145.5	1.1	94.7	0.8	0.65	149.4	1.1	1.1	111.7369862	0.735415838	1.48994729	1.333333333
BUCK_19	188.3	5.3	135.6	4.3	0.72	13283.8	1441.5	0.9	108.060718	0.958843766	2.500086982	1.335672543
BUCK_20	1229.9	24.5	109	2.7	0.09	508	5	1.3	122.695243	1.321720263	27.71909054	1.331042355
BUCK_21	144	7.3	98.8	5.1	0.69	273.2	5	1	118.7945414	1.280689392	2.104008669	1.338061702
BUCK_22	202.6	1.9	84.8	2	0.42	265.3	3.8	1.1	550.1788569	7.688484969	45.48266991	1.331042355
BUCK_23	1164.2	34.6	613.9	19.2	0.53	850.7	19.2	0.9	470.4739599	3.90259659	76.55273469	1.331042355
BUCK_24	1820.6	41.8	116.6	3.2	0.06	691.6	11.8	1.3	108.9868464	1.032028442	22.20336632	1.331042355
BUCK_25	94.6	0.9	54	0.7	0.57	547.8	3.7	1.2	1071.627117	4.752595087	3.811244511	1.331042355
BUCK_26	154.9	1.7	57.6	0.8	0.37	452.3	2.7	1.3	1083.140186	4.679171728	5.482796578	1.333333333
BUCK_27	824.8	7.2	122.8	1.3	0.15	583.6	4.6	1.4	101.7708905	0.493086322	3.349183688	1.331042355
BUCK_28	188.2	4.6	42.6	1.2	0.23	164.7	3.3	1.1	276.8368327	5.100204643	25.7587374	1.331042355
BUCK_29	391.7	9.7	325.8	9.7	0.83	218.8	2	1.1	228.5945607	1.848285917	8.032224636	1.331042355
BUCK_30	5484.4	89.8	1567.4	29.4	0.29	1876.1	29.9	1.5	77.27770481	0.770636644	52.87146902	1.331042355
BUCK_31	2872	80.8	496.2	21.9	0.17	882.5	13.4	1.7	239.1498642	2.945583965	341.7543145	1.331042355
BUCK_32	2942	75	153.2	7.2	0.05	1685.1	14.8	1.4	301.3601198	2.972386859	83.52580698	1.464990555
BUCK_33	1121.8	29.6	74.7	4.7	0.07	818.7	25.4	1.3	520.7914135	18.42075521	628.8510225	1.516397779
BUCK_34	3219.4	37.6	1102.5	14.6	0.34	424	10.5	1.1	103.3208177	1.51073136	93.17082499	1.43643578
BUCK_35	1339	32.6	296.1	7.6	0.22	639.9	8.2	1.4	101.74642	0.747147447	12.44027929	1.331042355

Table 4.9c: LA-ICP-MS results for sample RNZ119, where bdl: below detection level.

Analysis	^{139}La (ppm)	^{140}Ce (ppm)	^{147}Sm (ppm)	^{153}Eu (ppm)	^{163}Dy (ppm)	^{175}Lu (ppm)	^{89}Y (ppm)	^{49}Ti (ppm)
BUCK_01	bdl	1.26298466	2.00400941	0.0961079	148.21612	138.98341	1951.67836	12.4505762
BUCK_02	bdl	1.9260517	4.32003419	0.63208206	106.42534	20.7674773	861.478995	5.46449378
BUCK_03	0.03477289	5.88007328	5.41628822	1.24382732	82.5291037	32.8549165	734.379314	7.34289163
BUCK_04	bdl	7.66482985	2.51228598	0.80333707	31.8704424	13.1797863	288.00197	4.91487438
BUCK_05	0.17760706	32.2759722	7.95479619	3.79468043	130.234806	48.5110771	1220.68315	16.9924246
BUCK_06	0.3222416	24.0999731	6.47095406	2.41915728	231.582403	136.96128	2620.20788	30.3653469
BUCK_07	bdl	1.00958298	1.9847203	0.26492578	111.41215	84.9348632	1371.77557	3.37231522
BUCK_08	0.07508612	5.92149772	3.27122947	0.18175728	80.3233592	54.5334385	894.148916	7.58597952
BUCK_09	0.02915521	1.29430948	2.42026233	0.07794054	79.0109708	37.8758439	822.66457	12.4386343
BUCK_10	3.12739346	6.8623307	7.97847349	1.35265721	335.445864	155.349801	3408.80281	4.19160108
BUCK_11	0.03831667		3.82419358	0.5940348	80.995328		788.10112	6.63844782
BUCK_12	0.02908224	4.23877613	1.24227902	0.48508734	22.3240771			5.76247482
BUCK_13	0.37363	9.40503222	4.14684891	1.38107816	158.948848	127.355022	1974.6816	2.46354315
BUCK_14	bdl	4.11038081	11.6310052	1.63583898	175.007774	21.7060994	1241.86504	8.82482737
BUCK_15	bdl	5.55210887	4.10238986	0.94996216	89.2752656	63.3638287	911.182577	6.81697016
BUCK_16	bdl	3.67242994	5.29646865	0.7683258	100.921159	37.3704255	939.001788	6.13070206
BUCK_17	0.79345709	8.95817006	4.9918272	1.27263413	91.5253922	45.5969299	978.70146	15.0398032
BUCK_18	bdl	15.6793608	3.5350909	1.26726114	23.2430213	6.06986352	178.513809	8.20092837
BUCK_19	29.8015204	102.059111	32.4095151	5.8255659	124.661781	31.8302787	1009.58585	15.5382059
BUCK_20	bdl	2.36647758	4.47886172	0.63830446	108.73833	21.245988	806.231095	4.31481643
BUCK_21	bdl	18.9094894	2.65700022	0.90926153	62.3650431	42.2137351	713.544177	8.08909817
BUCK_22	0.03150806	7.03416166	4.33097673	0.6544593	98.5462618	67.0428115	1068.24743	4.13408424
BUCK_23	bdl	35.6950658	15.5930641	1.6756475	390.955229	190.617927	4143.76665	4.49786203
BUCK_24	bdl	2.55390101	5.13508599	0.7412309	155.141451	40.6843138	1362.56466	4.48319055
BUCK_25	bdl	3.90384528	10.0814316	0.48173491	164.965727	66.8690165	1620.59347	16.7101318
BUCK_26	bdl	4.09086843	2.85188995	0.08682458	89.5465852	52.4911318	971.738517	12.2827945
BUCK_27	0.05656819	4.20520974	5.39934497	1.01889069	157.158849	61.2684492	1526.01729	5.09853367
BUCK_28	0.08049318	2.09213606	1.66729644	0.28650117	30.9270061	13.8675286	275.081102	5.44973055
BUCK_29	bdl	22.0778845	4.35222286	0.92055525	81.0476407	56.1393724	949.874165	9.03373213
BUCK_30	21.7975033	138.338346	128.23057	45.798112	919.995942	250.206785	8017.2712	33.3480631
BUCK_31	13.1730879	31.7265746	39.2036897	10.6310428	270.038915	130.964489	2425.44109	14.33371
BUCK_32	53.6919833	108.424639	22.5906306	3.34568143	261.932387	160.384076	3162.56422	14.6704514
BUCK_33	42.4897335	91.8790402	6.68515172	0.17608236	71.166653	73.4429904	906.054677	3.07919183
BUCK_34	4.31308832	74.4498425	22.0171464	5.13672449	241.278692	175.063837	2919.79562	6.23715787
BUCK_35	0.88712306	23.6174707	7.04335544	1.80544073	140.947677	128.186206	1758.5691	3.94952321

Table 4.9c (continued): LA-ICP-MS results for sample RNZ119, where bdl: below detection level.

Analysis	U (ppm)	±	Th (ppm)	±	Th/U	P (ppm)	±	HfO_2 (wt%)	^{208}Pb corr'd $^{206}Pb/^{238}U$ age	observed ±1s.e.	calculated MSWD	expected MSWD
S_01	238	3	106.2	1.8	0.45	400.8	2.2	1.3	1473.462613	6.627419359	5	1.340502612
S_02	1120.6	23.5	285.7	7.1	0.25	353.6	2.5	1.5	1413.899969	6.78040733	75.94601558	1.333333333
S_03	544.3	11	93.3	3.9	0.17	682.1	78.1	1.4	1378.486856	9.219342881	54.07748004	1.333333333
S_04	825.8	9.6	62.9	4.5	0.08	157.4	3.9	1.5	1203.748023	15.5701138	372.1240543	1.333333333
S_05	834.3	14.4	334.6	6.9	0.4	172.4	2.3	1.3	596.4776804	3.502823746	30.13173429	1.333333333
S_06	528.4	6.8	154.6	2	0.29	68.5	0.8	1.3	592.8904502	1.983523096	6.195894986	1.333333333
S_07	658.3	11.3	8.9	0.2	0.01	602.6	3	1.3	352.904914	1.687624792	9.517111939	1.333333333
S_08	384.9	9.5	59.6	3.7	0.15	536.4	35.2	1.3	610.3007943	13.47716906	152.5888114	1.333333333
S_09	636.5	2.8	5.5	0.2	0.01	597.8	5	1.4	338.6017125	1.404528002	7.166703794	1.333333333
S_10	328.4	3.3	225.8	2.5	0.69	339.6	2.6	0.8	1000.848893	3.72274997	9.792179646	1.333333333
S_11	96.5	4.3	52.5	3.3	0.54	330.3	9.1	0.9	1170.802297	33.13401823	5	1.350823208
S_12	1837.7	26.5	116.4	5.9	0.06	889.9	48.3	1.3	995.0984611	7.524167576	202.8888731	1.333333333
S_13	1085.5	18	93.5	2.4	0.09	368.8	5.6	1.4	659.88117	4.272457158	47.15318281	1.333333333
S_15	584.9	9.6	223.1	8.4	0.38	233	6.9	1.3	762.1101741	10.96420316	160.9280363	1.333333333
S_16	640.2	3.9	278.5	2.8	0.44	433.7	2.4	1.1	905.0466005	5.031039359	37.6187951	1.333333333
S_17	575.1	9.1	43.2	1	0.08	352.2	5.9	1.3	529.705269	4.204342851	40.87300437	1.333333333
S_18	2936.5	117.9	367.3	40.4	0.13	975.6	34.4	2	782.9927549	30.01356276	5	1.348155312
S_19	1190.1	57.4	148	15.8	0.12	710.9	21.5	1.3	697.1386036	9.95563885	152.7886798	1.368229847
S_20	731.1	16.4	29.6	0.8	0.04	490.2	2.2	1.5	462.0378448	3.231204731	5	1.340502612
S_21	2033.4	31.9	142	2.7	0.07	571.6	9.2	1.8	529.9996739	2.838762267	34.22874823	1.377964473
S_22	333.2	22	56.4	4.7	0.17	298.9	4.3	1.4	865.339485	14.69212228	5	1.340502612
S_23	1208.7	8.5	32.8	0.4	0.03	486.8	4.6	1.7	562.758152	3.194642802	40.3309504	1.333333333
S_24	180.2	2.6	45	2.7	0.25	368.1	25.8	1.2	595.0140087	4.861365097	12.1775386	1.34299717
S_25	409.2	14.4	17.2	1	0.04	362.2	11.4	1.2	381.0645092	3.749285606	23.74269252	1.333333333
S_26	551.9	6.8	362.3	4.8	0.66	615.6	19	0.9	919.9552513	3.791293593	16.44255454	1.333333333
S_27	507.9	8.3	33	1.5	0.06	396.9	5.2	1.2	442.6680036	2.40193608	10.41634067	1.333333333
S_28	1894.2	31.4	109.8	3.2	0.06	620.9	6.3	1.5	621.3486368	3.077654289	46.39961635	1.333333333
S_29	364.1	11.3	158.8	9.2	0.44	356.6	1.8	1.4	486.1675665	5.777617644	35.25185059	1.333333333
S_30	359.8	5.8	315.7	6.6	0.88	316.1	6.8	1.1	1954.576378	8.222018884	21.61165129	1.333333333
S_31	513.2	5.9	15.3	0.8	0.03	392.7	3.3	1.3	674.4936096	13.86225464	295.0443365	1.333333333
S_32	130.1	1.3	53.7	0.6	0.41	132.9	1.6	1.2	550.1452145	3.289844363	4.657897075	1.335672543
S_33	626.9	3.9	5.8	0.4	0.01	603.5	3	1.4	329.0483789	1.771434217	10.38366575	1.333333333
S_34	120.4	2.9	30.4	0.8	0.25	729.3	9.1	1	924.6954943	6.204854501	8.537962331	1.333333333
S_35	753.4	25.9	30.5	1.8	0.04	414.2	11.4	1.6	770.8304771	8.300412506	34.97411172	1.365148372

Table 4.9d: LA-ICP-MS results for sample PCC06-01, where bdl: below detection level.

Analysis	^{139}La (ppm)	^{140}Ce (ppm)	^{147}Sm (ppm)	^{153}Eu (ppm)	^{163}Dy (ppm)	^{175}Lu (ppm)	^{89}Y (ppm)	^{49}Ti (ppm)
S_01	0.02851514	8.02103288	2.17168192	0.17946254	81.2029569	64.0840456	960.06343	6.13279773
S_02	0.02893233	13.5521443	2.23333833	0.10413731	92.2921869	92.2373835	1187.82799	3.58149235
S_03	0.77506447	15.2027136	1.09829075	0.25837394	25.2524869	52.7960832	395.893781	116.823362
S_04	0.0349698	7.6653366	0.41698124	0.15214427	28.7102008	50.6207219	428.362894	4.447368
S_05	0.04942055	31.9954154	6.39467379	1.31743489	69.30474	27.8488866	618.838723	4.55021644
S_06	bdl	23.1195499	0.90297542	0.20951425	16.0255196	11.3201313	176.348231	4.53062354
S_07	bdl	1.01422014	0.60992697	0.11651671	68.7841891	97.6344272	1008.9598	2.96656859
S_08	bdl	1.28204678	6.16913492	0.16073341	116.858632	37.6128166	1057.75393	10.8926193
S_09	bdl	0.22302388	0.60003675	0.12767159	68.3077348	91.7909086	1009.14104	2.40664106
S_10	bdl	12.8228918	8.42609689	1.43521615	170.664936	91.1355488	1857.54629	10.6204462
S_11	bdl	13.4568152	6.30782325	0.8642218	120.22964	67.6007277	1266.71789	11.0773172
S_12	bdl	0.86202403	3.27986199	0.12156156	117.786342	125.40734	1584.71971	8.45227391
S_13	0.05034041	0.83939262	1.69130693	0.1398594	45.117808	38.6407378	569.243186	5.12374529
S_15	bdl	20.1579407	0.99441229	0.23833846	39.225164	58.481655	549.434155	4.30121848
S_16	0.04593721	17.1132098	13.3901438	0.24877397	224.813107	87.6308636	2221.61324	5.25663973
S_17	0.0294698	3.78301407	1.12796929	0.07471669	57.546075	66.5792781	760.445973	4.17381941
S_18	4.05856229	28.6567691	32.9142844	15.0983114	273.166026	244.535746	2366.4446	17.1927495
S_19	1.70371908	11.8288145	14.7426542	8.06358641	115.24854	93.8506994	869.956354	338.482517
S_20	0.03584247	0.47897001	0.67739809	0.1139064	56.3154254	80.6655513	807.1713	3.88436996
S_21	1.3694693	8.29606717	7.99846822	9.28798351	110.557057	182.616006	1859.84012	117.194074
S_22	bdl	3.57135666	1.28076288	0.09119551	62.0863016	52.1854348	769.157137	3.62803598
S_23	bdl	2.1894544	0.71527237	0.11109096	68.4964748	107.386032	1090.98887	4.27311604
S_24	0.03296219	1.69035446	3.76753168	0.23696577	85.6995187	31.6772052	842.446974	13.1278789
S_25	0.02748634	1.22049846	0.69959466	0.11046505	40.3966839	34.8929076	543.227439	3.63314014
S_26	0.42030538	21.5110629	20.7300741	3.07965245	283.553235	106.984403	2770.10536	9.25974963
S_27	bdl	1.75080754	1.08660297	0.16603866	48.0561489	53.3862438	661.454979	3.23339699
S_28	0.02570989	1.99266098	3.07680965	0.08844466	125.499583	39.4366078	1311.69728	7.94891407
S_29	0.06500357	4.16695441	3.43893442	0.23321312	76.8676717	22.1232001	725.060056	6.05693557
S_30	0.04216345	21.050884	6.71358511	0.87016625	96.7183692	43.5254105	966.485671	5.40372423
S_31	bdl	1.74878046	1.02853869	0.28584619	52.8749778	47.6581129	692.59121	3.86650967
S_32	bdl	2.37051002	4.13870497	0.13185223	13.1715854	1.80047948	86.3251542	21.7017824
S_33	0.05493741	0.30789068	0.77404362	0.29404621	59.2083096	85.682512	925.4626	57.4859607
S_34	bdl	1.15899916	4.60520907	0.26033032	126.902716	76.5733397	1464.9185	8.73303043
S_35	bdl	0.61388546	1.78970877	0.12914631	73.9117656	35.0274371	801.121328	4.61315236

Table 4.9d (continued): LA-ICP-MS results for sample PCC06-01, where bdl: below detection level

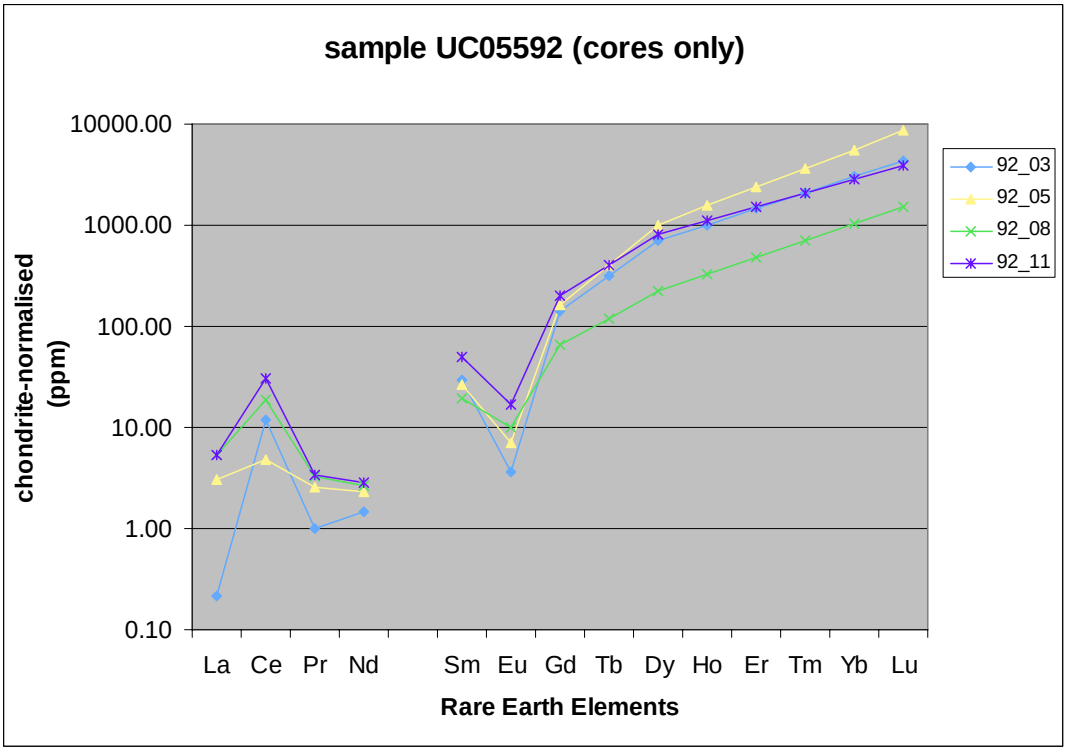

Figure 4.4a: REE chondrite-normalised diagram showing values of zircon xenocrystic cores from sample UC05592.

separately in Figure 4.4b, with analyses 92-06, 92-07- 92-10 and 92-12. Element concentrations for each analysis are listed in Table 4.9a. Analyses 92-09 and 92-13 were considered to be outliers, and were removed from the data set. Analysis 92-09 exhibited anomalously high levels of both P and Lu, which is suggested to represent the sampling of a mineral inclusion present within the zircon grain. Analysis 92-13 was removed due to its variation from the general positive trend within the data set.

Distinctive anomalies are observed in both the 'cores only' and 'rims only' plots, with Ce and Eu having positive and negative anomalies, respectively.

The average REE values of xenocrystic cores and rims are plotted together, with obvious positive and negative anomalies for Ce and Eu, respectively (Figure 4.4c).

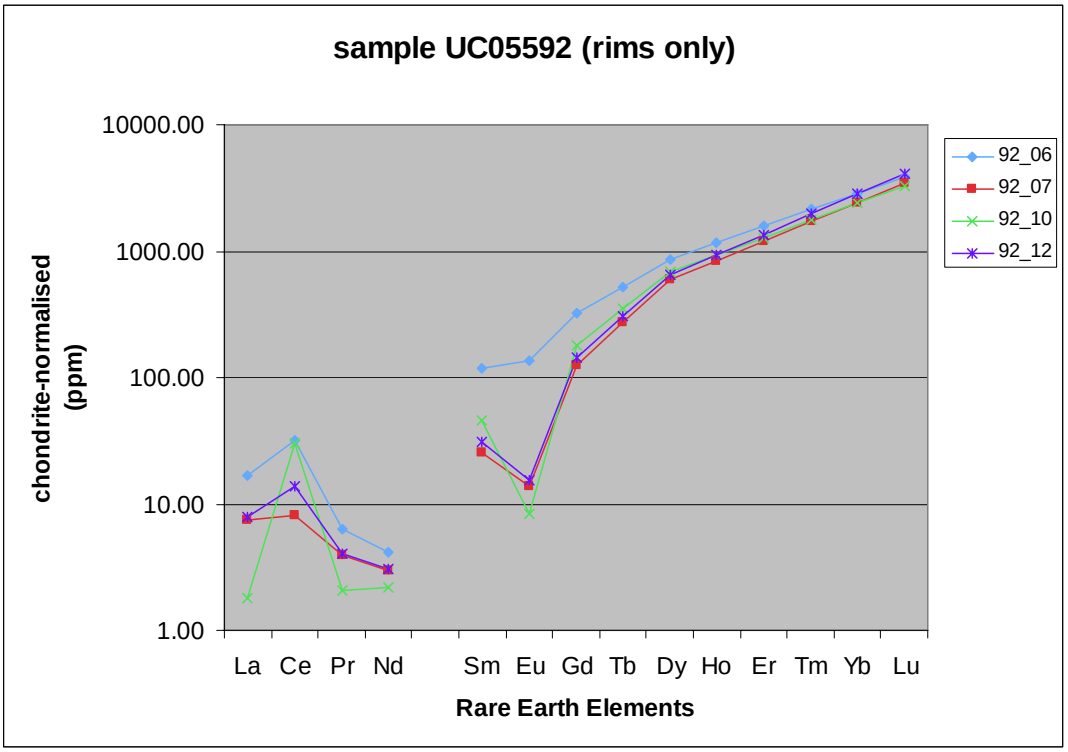

Figure 4.4b: REE chondrite-normalised diagram showing values of zircon rims from sample UC05592.

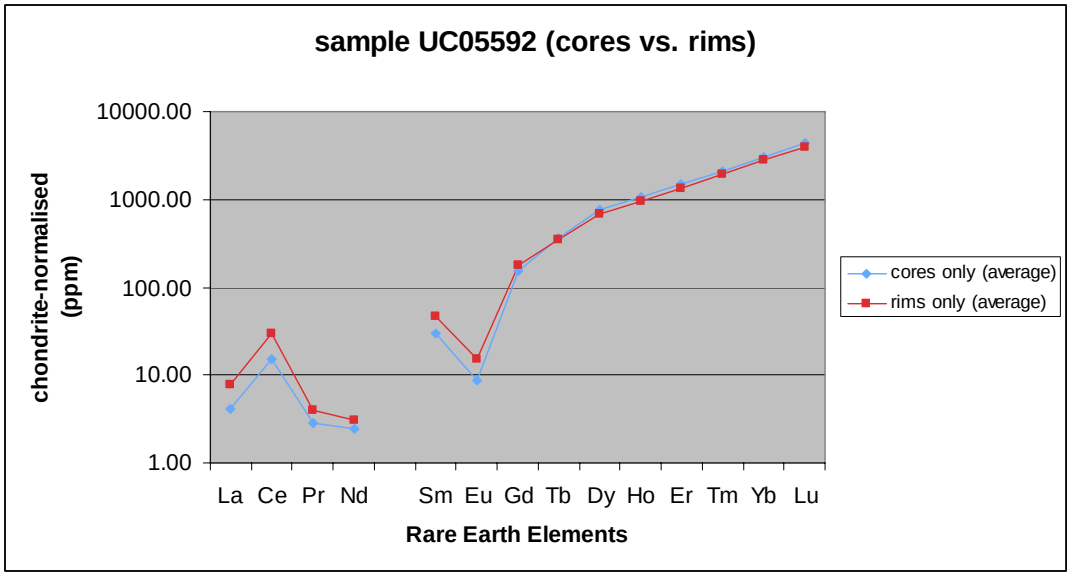

Figure 4.4c: REE chondrite-normalised diagram showing average REE values of xenocrystic cores and rims of zircons from sample UC05592.

UC08368

The REE concentrations of xenocrystic zircon cores are shown in Figure 4.4d, with analyses 68-01, 68-03, 68-05, 68-09, 68-11, 68-13, 68-19 and 68-21. REE patterns of zircon rims are plotted separately in Figure 4.4e, with analyses 68-02, 68-04, 68-07, 68-08, 68-10, 68-20 and 68-22. Element concentrations for each analysis are listed in Table 4.9b.

Analyses 68-06, 68-12 and 68-18 were considered to be outliers, and were removed from the data set. Analysis 68-06 exhibited anomalously high levels of both P and Lu, which is suggested to represent the sampling of a mineral inclusion present within the zircon grain. Analyses 68-12 and 68-18 were removed due to their variation from the general positive trend within the data set.

Distinctive anomalies are observed in both the ‘cores only’ and ‘rims only’ plots, with Ce and Eu having positive and negative anomalies, respectively.

The average REE values of xenocrystic cores and rims are plotted together, with an obvious negative Eu anomaly (Figure 4.4f). No trend is shown for elements La to Nd, and therefore no anomaly is shown for Ce, due to the limited La values required for the interpolation of Pr and Nd values.

RNZ119

The REE concentrations of xenocrystic zircon cores are shown in Figure 4.4g, with analyses BUCK-01, BUCK-03, BUCK-05, BUCK-08, BUCK-09, BUCK-11, BUCK-12, BUCK-14, BUCK-16, BUCK-18, BUCK-22, BUCK-23, BUCK-25, BUCK-28, BUCK-29 and BUCK-34. REE patterns of zircon rims are plotted separately in Figure 4.4h, with analyses BUCK-02, BUCK-04, BUCK-06, BUCK-07, BUCK-13, BUCK-

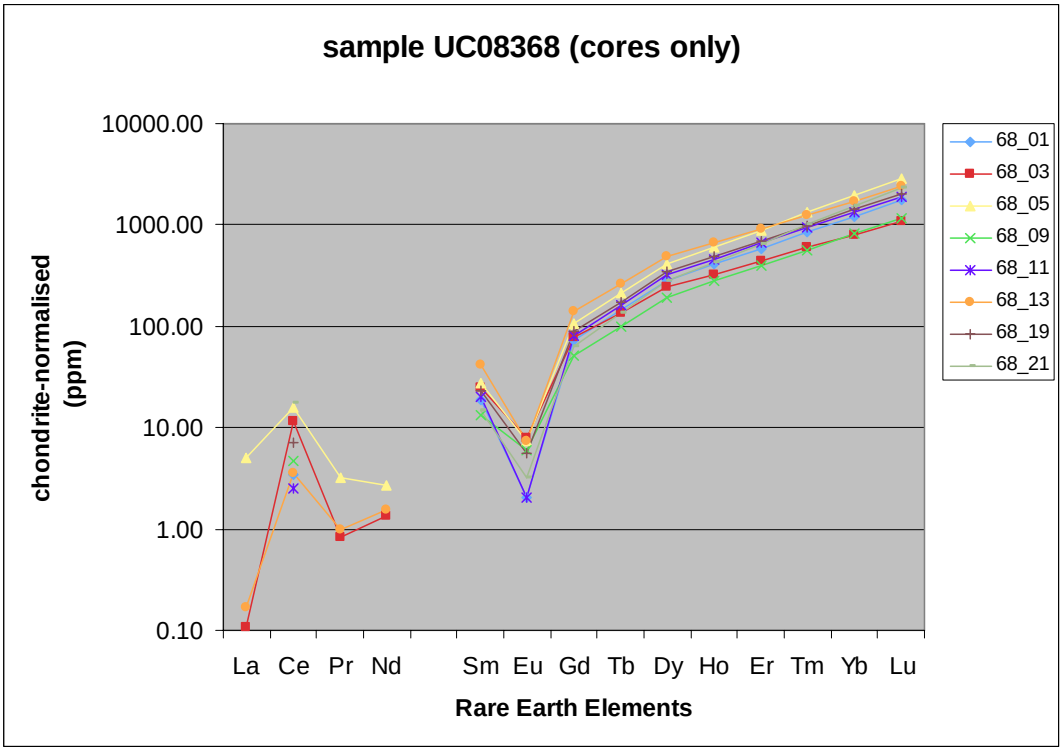

Figure 4.4d: REE chondrite-normalised diagram showing values of zircon xenocrystic cores from sample UC08368.

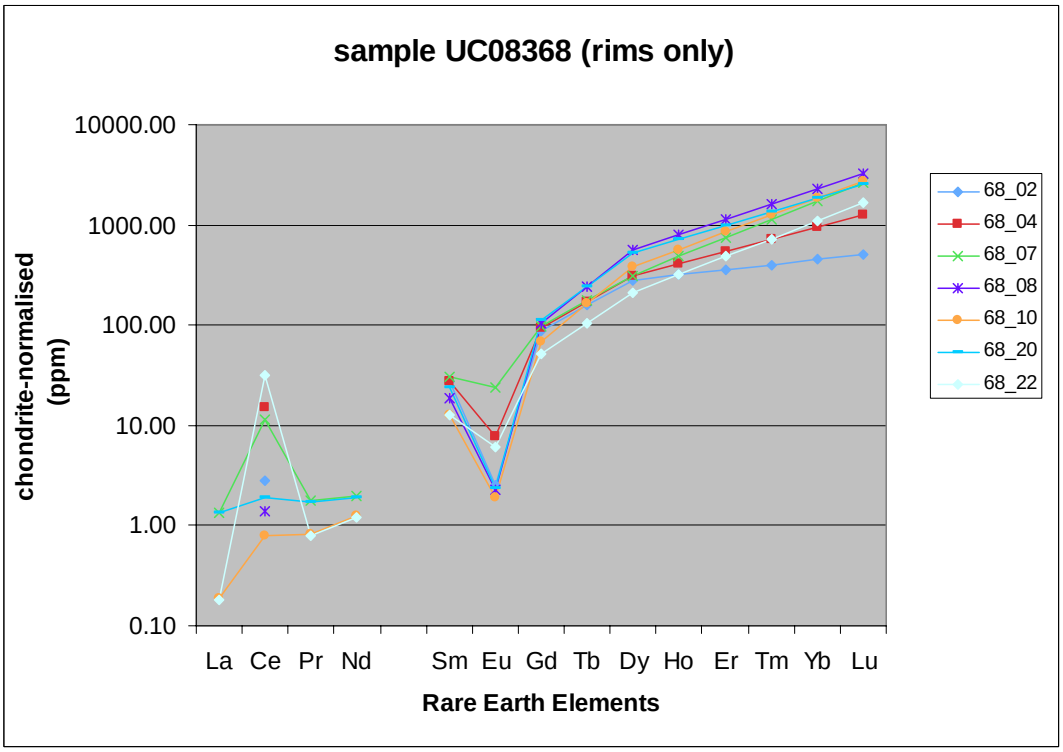

Figure 4.4e: REE chondrite-normalised diagram showing values of zircon rims from sample UC08368.

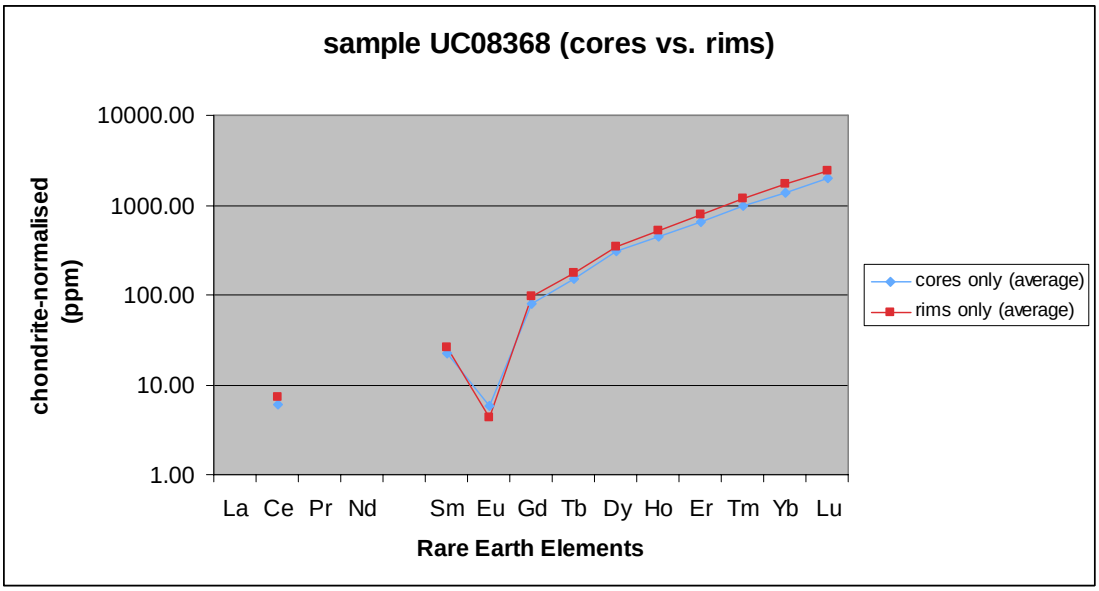

Figure 4.4f: REE chondrite-normalised diagram showing average REE values of xenocrystic cores and rims of zircons from sample UC08368.

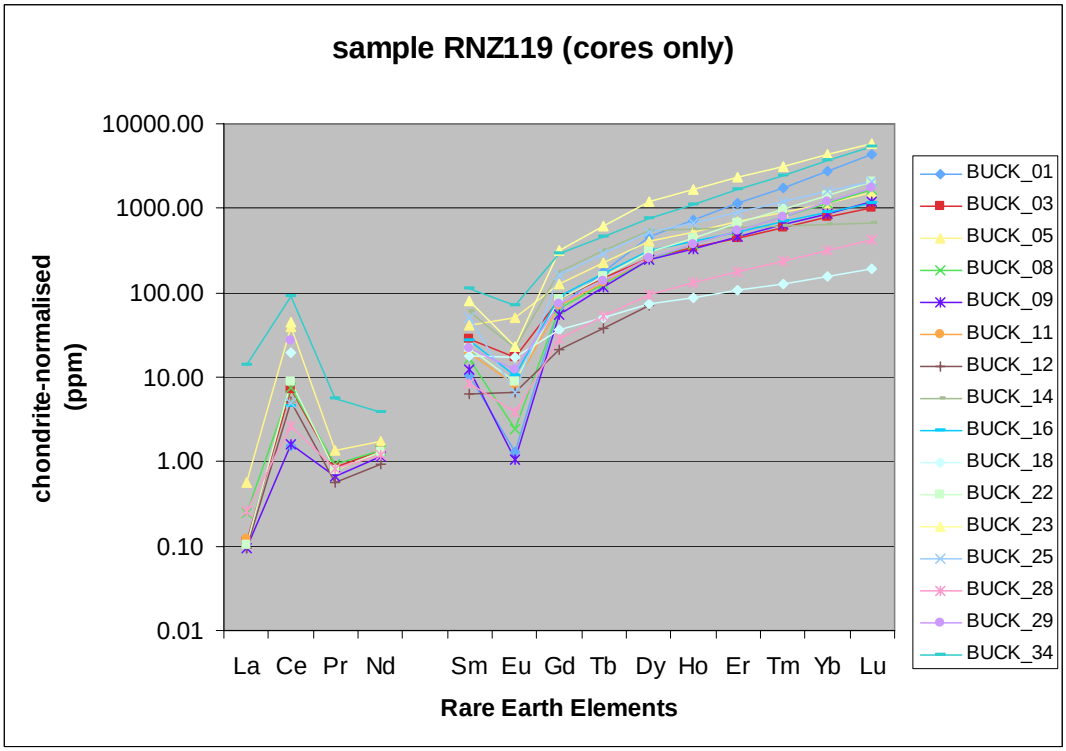

Figure 4.4g: REE chondrite-normalised diagram showing values of zircon xenocrystic cores from sample RNZ119.

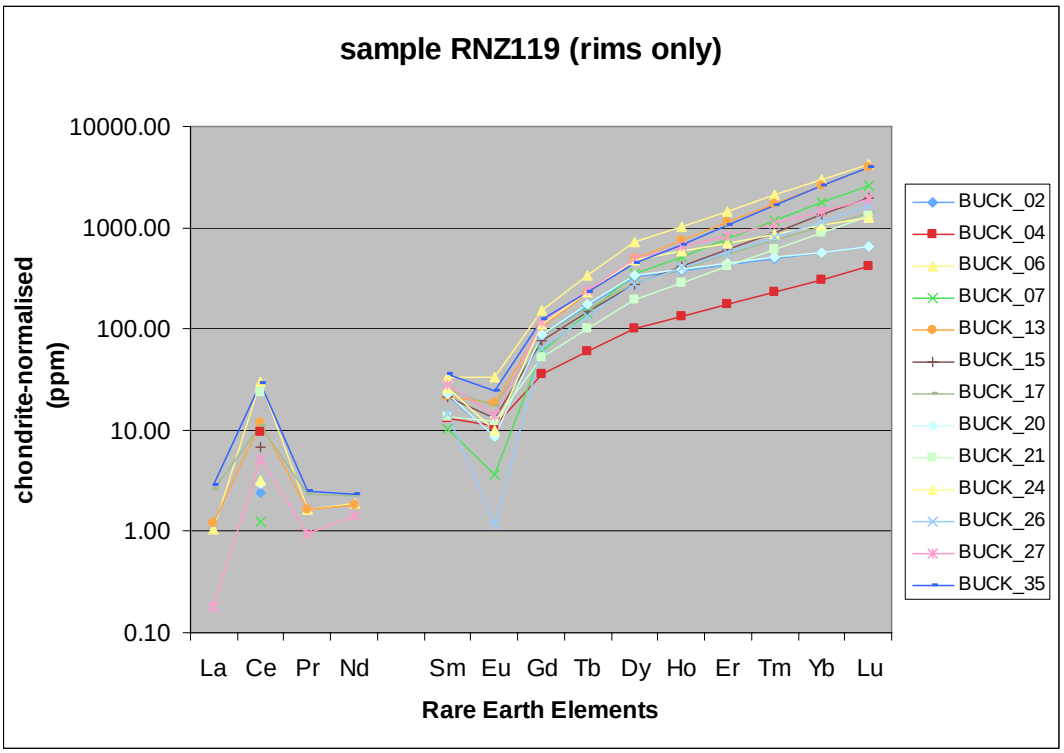

Figure 4.4h: REE chondrite-normalised diagram showing values of zircon rims from sample RNZ119.

15, BUCK-17, BUCK-20, BUCK-21, BUCK-24, BUCK-26, BUCK-27 and BUCK-35. Element concentrations for each analysis are listed in Table 4.9c.

Analyses BUCK-10, BUCK-19, BUCK-30, BUCK-31, BUCK-32 and BUCK-33 were considered to be outliers, and were removed from the data set. Analyses BUCK-19, BUCK-30 and BUCK-32 exhibited anomalously high levels of both P and Lu, which is suggested to represent the sampling of a mineral inclusion present within the zircon grain. Analyses BUCK-10, BUCK-31 and BUCK-33 were removed due to their variation from the general positive trend within the data set.

Distinctive anomalies are observed in both the ‘cores only’ and ‘rims only’ plots, with Ce and Eu having positive and negative anomalies, respectively.

The average REE values of xenocrystic cores and rims are plotted together, with an obvious negative Eu anomaly (Figure 4.4i). No trend is shown for elements La to Nd, and therefore no anomaly is shown for Ce, due to the limited La values required for the interpolation of Pr and Nd values.

PCC06-01

The REE concentrations of xenocrystic zircon cores are shown in Figure 4.4j, with analyses S-01, S-03, S-05, S-10, S-12, S-16, S-19, S-21, S-22, S-24, S-26, S-28, S-30 and S-34. REE patterns of zircon rims are plotted separately in Figure 4.4k, with analyses S-02, S-04, S-06, S-08, S-09, S-11, S-13, S-15, S-17, S-20, S-23, S-25, S-27, S-29, S-31, S-33 and S-35. Element concentrations for each analysis are listed in Table 4.9d.

Analyses S-18 and S-32 were considered to be outliers, and were removed from the data set. Analysis S-18 exhibited anomalously high levels of both P and Lu, which is suggested to represent the sampling of a mineral inclusion present within the zircon grain. Analysis S-32 was removed due to its variation from the general positive trend within the data set.

Distinctive anomalies are observed in both the ‘cores only’ and ‘rims only’ plots, with Ce and Eu having positive and negative anomalies, respectively.

The average REE values of xenocrystic cores and rims are plotted together, with an obvious negative Eu anomaly (Figure 4.4l). No trend is shown for elements La to Nd, and therefore no anomaly is shown for Ce, due to the limited La values required for the interpolation of Pr and Nd values.

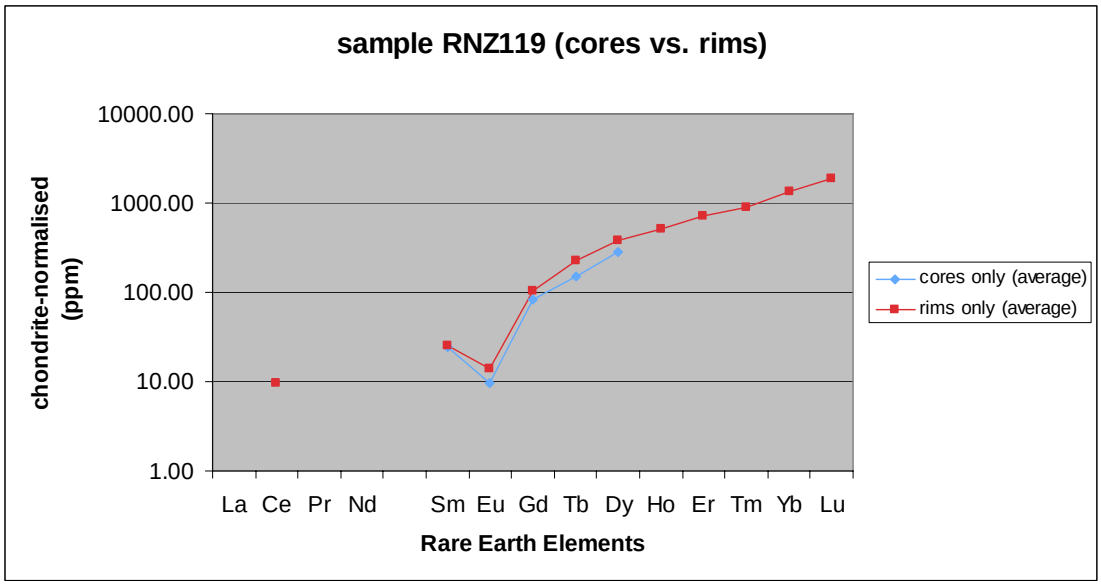

Figure 4.4i: REE chondrite-normalised diagram showing average REE values of xenocrystic cores and rims of zircons from sample RNZ119.

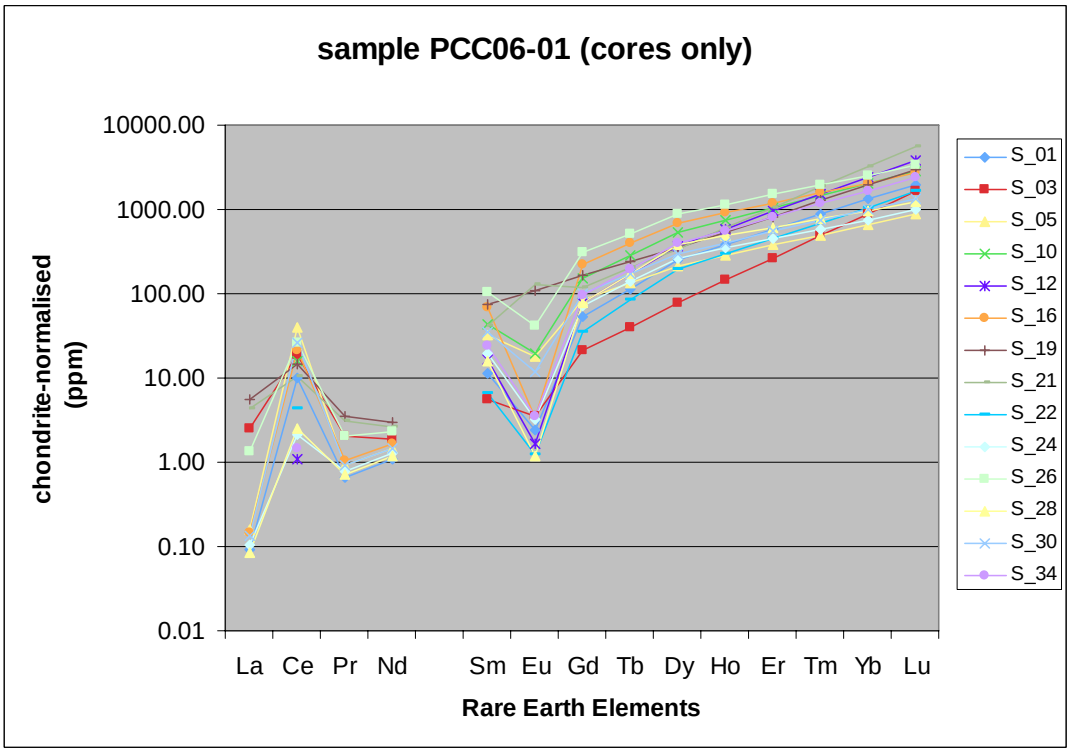

Figure 4.4j: REE chondrite-normalised diagram showing values of zircon xenocrystic cores from sample PCC06-01.

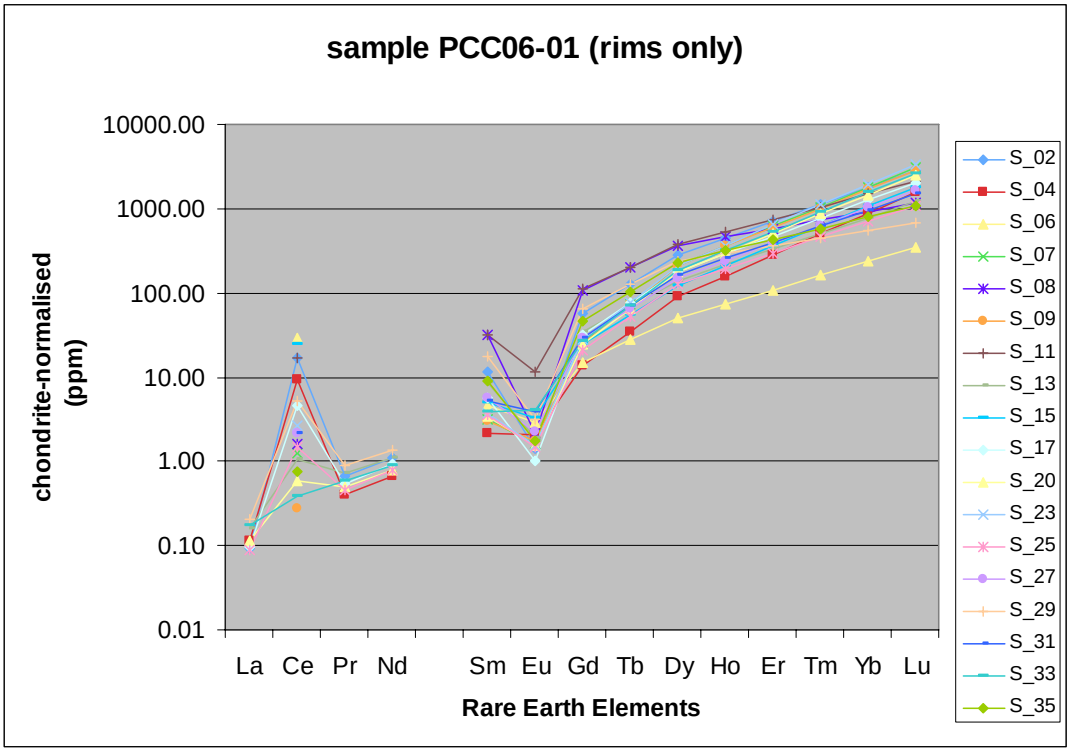

Figure 4.4k: REE chondrite-normalised diagram showing values of zircon rims from sample PCC06-01.

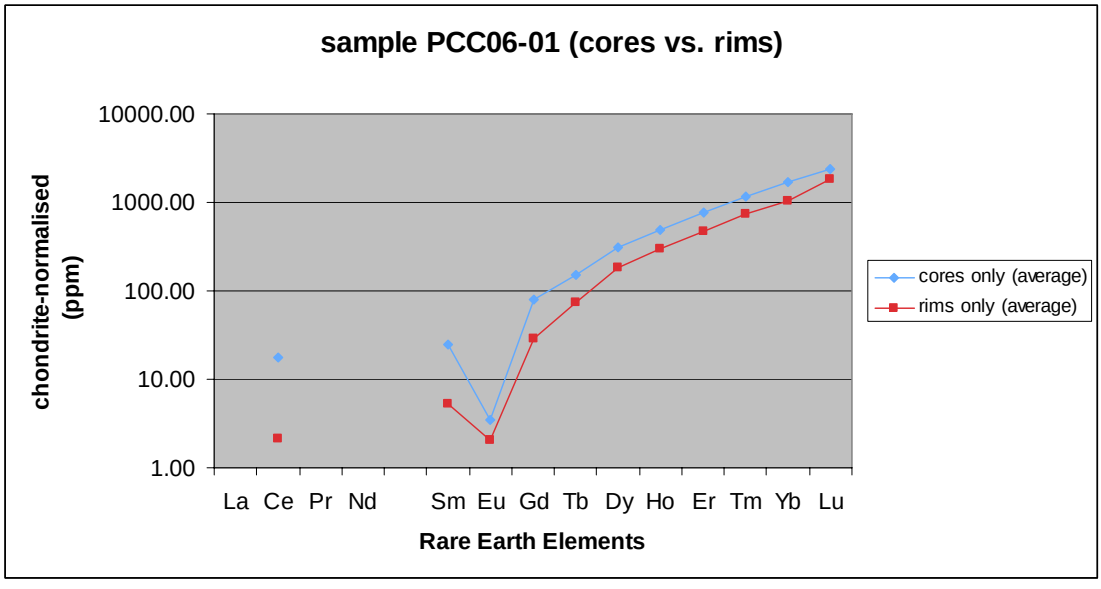

Figure 4.4l: REE chondrite-normalised diagram showing average REE values of xenocrystic cores and rims of zircons from sample PCC06-01.

The REE patterns for UC05592, UC08368, RNZ119 and PCC06-01 all show positive trends with a relative enrichment of HREE's and depletion of LREE's, as expected for zircon-bearing rocks which have not suffered extensive alteration. These findings contrast with those of Tulloch and Christie (2000), where alteration led to the (at least) localised leaching of the HREE's of Lower Plate rocks adjacent to the Ohika Detachment Fault in the Lower Buller Gorge area, to produce the negative slope in the chondrite-normalised REE diagram (Figure 4.3b).

Sample PCC06-01, sourced just north of the inferred Pike Detachment Fault, does not display any evidence for the leaching of REE's by hydrothermal fluid movement along the fault plane during extension.

4.2. Geochronological investigations

The use of geochronology in igneous and metamorphic petrogenetic studies provides information on the timing of crystallisation and metamorphism within an individual rock unit. *In situ* sampling of U-Th-Pb concentrations in individual zircon grains allows U-Pb dates to be calculated, with greater accuracy than using the whole rock approach.

4.2.1. U-Pb dating

The U-Th-Pb system involves the decay of radioactive U isotopes to radiogenic Pb isotopes, through the following sequences (Winter 2001).

$$^{238}\mathrm{U} \rightarrow {}^{234}\mathrm{U} \rightarrow {}^{206}\mathrm{Pb}\ (\lambda = 1.5512 \times 10^{-10}\ \mathrm{a}^{-1})$$

$$^{238}\mathrm{U} \rightarrow {}^{235}\mathrm{U} \rightarrow {}^{207}\mathrm{Pb}\ (\lambda = 9.8485 \times 10^{-10}\ \mathrm{a}^{-1})$$

$$^{238}\mathrm{U} \rightarrow {}^{232}\mathrm{Th} \rightarrow {}^{208}\mathrm{Pb}\ (\lambda = 4.9475 \times 10^{-11}\ \mathrm{a}^{-1})$$

U, Th and Pb concentrations are recorded in zircons, which may either crystallise from the primary melt, or become incorporated into the igneous system through crustal contamination. Subsequent metamorphic events are also recorded, through the growth of metamorphic rims around the older zircon crystals.

The ratio of Th and U content within zircon may be used to determine whether zircon growth is magmatic or metamorphic in nature, with age corrections only required for samples with huge variations in U-Pb ages (Maas et al. 1992). Typical igneous zircons have been found to record Th/U ratios ranging from 0.2 to 1.0, while metamorphic zircons generally show much smaller Th/U ratios ranging from 0.1 to <0.05 (Williams and Claesson 1987, Schiøtte et al. 1988a, Schiøtte et al. 1988b, Schiøtte et al. 1989, Kinny et al. 1990).

The *in situ* sampling of U and Pb in zircon crystals by LA-ICP-MS allows the dating of petrogenetic events in igneous and metamorphic rocks, using the U-Pb dating method. The behaviour of U and Pb may be visually represented in Tera-Wasserburg diagrams, where $^{207}Pb/^{206}Pb$ is plotted against $^{238}U/^{206}Pb$ (Tera and Wasserburg 1972). Tera-Wasserburg diagrams were constructed using the Isoplot Ex v.2.6. program (Ludwig 1999). The alignment of data into an array allows the distinction to be made between common-Pb ($^{207}Pb/^{206}Pb$ at the upper intercept) and radiogenic Pb ($^{206}Pb^*/^{238}U$ at the lower intercept) (Parrish and Noble 2003).

The presence of an array in Tera-Wasserburg diagrams reflects the concordant nature of the data, as the $^{207}Pb^*/^{235}U$ and $^{206}Pb^*/^{238}U$ ages are consistent with each other. Concordant data is considered reliable, as it records the various stages of zircon growth and recrystallisation through time, without any evidence of significant alteration.

Data points which do not display a linear relationship when plotted in Tera-Wasserburg diagrams suggest discordance within the data set. Discordance within geochemical data may develop through extracrystalline diffusion, through the removal and addition of elements such as U, Th and Pb during alteration. U-Pb ages become affected by this style of diffusion, as the removal of such elements does not involve radioactive decay, and Pb isotopes become depleted with respect to their concentration in the rock (Wayne and Sinha 1988, Ashwal et al. 1999, Winter 2001). It is due to this decrease in Pb isotopes that discordant ages may be attributed to Pb-loss through diffusion by some authors (Cherniak and Watson 2003, Parrish and Noble 2003), however, the slow diffusion rates of Pb in *crystalline* zircon makes Pb-loss by volume diffusion unlikely (Cherniak and Watson 2000). Pb-loss by diffusion is more likely to develop in *metamict* zircon grains that have experienced damage to the crystal lattice associated with U and Th radioactive decay, allowing the recrystallisation and/or mobilisation of Pb to occur (Silver 1963, Pidgeon et al. 1968, Whitehouse et al. 1999, Cherniak and Watson 2000, Bowring and Schmitz 2003).

Connelly (2000) discusses the relationship between intracrystalline deformation and the degree of preservation of primary growth zoning within individual igneous zircon grains. Connelly suggests that variations in the preservation of growth zoning may be used as a proxy for the amount of intracrystalline diffusion that has taken place within individual grains. Intracrystalline diffusion and recrystallisation of zircon results in concordance within the geochemical data, as changes to the chemistry of individual grains takes place within closed systems.

Sampling of sections with poorly preserved growth zoning patterns have been shown to produce discordant data, however, this relationship must not be assumed to be the

case for all zircons. CL imaging prior to geochemical sampling clearly becomes an invaluable tool, as any grains that appear to have experienced alteration may be avoided to reduce chances of discordance within samples (Connelly 2000).

The four samples from the Paparoa Metamorphic Core Complex (UC05592, UC08368, PCC06-01 and RNZ119) were analysed with the LA-ICP-MS technique, for the concentrations of U, Th and Pb (Tables 4.9a, 4.9b, 4.9c and 4.9d).

Tera-Wasserburg concordia diagrams and probability density distribution-histogram plots were constructed to visually represent U-Pb behaviour for each sample. The imaging of zircon grains from each sample by CL allowed any anomalous features to be avoided during sampling (Figures 3.1a, 3.1b, 3.1c and 3.1d). Zircon analysis involved both xenocrystic core and rim sampling, in attempt to illustrate chemical variations between inherited and metamorphic crystallisation histories.

UC05592

The probability density distribution-histogram plot for UC05592, with all analyses included, shows inheritance of zircon grains up to c. 1000 Ma old. Two main peaks are noted at c. 300 and c. 100 Ma (Figure 4.5a). Data points around c. 300 Ma are illustrated in a separate probability density distribution-histogram plot, which shows three main peaks within the limited data set at c. 250, c. 300 and c. 330 Ma (Figure 4.5b). Data plotted in the Tera-Wasserburg concordia diagram do not display a strong linear relationship, and are considered to be discordant (Figure 4.5c).

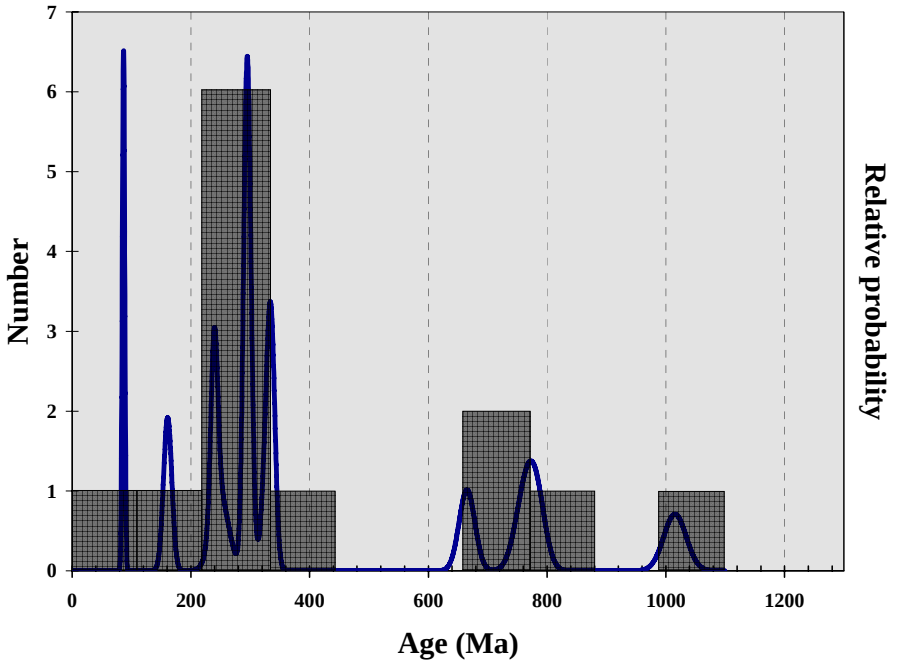

Figure 4.5a: Probability density distribution-histogram plot of all data for sample UC05592.

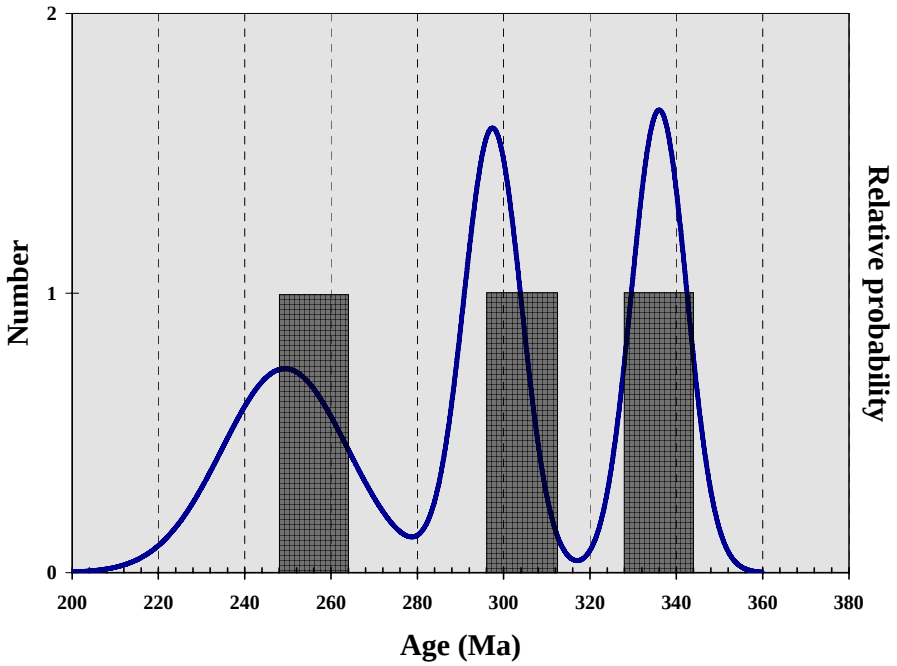

Figure 4.5b: Probability density distribution-histogram plot of inherited c. 300 Ma zircons for sample UC05592.

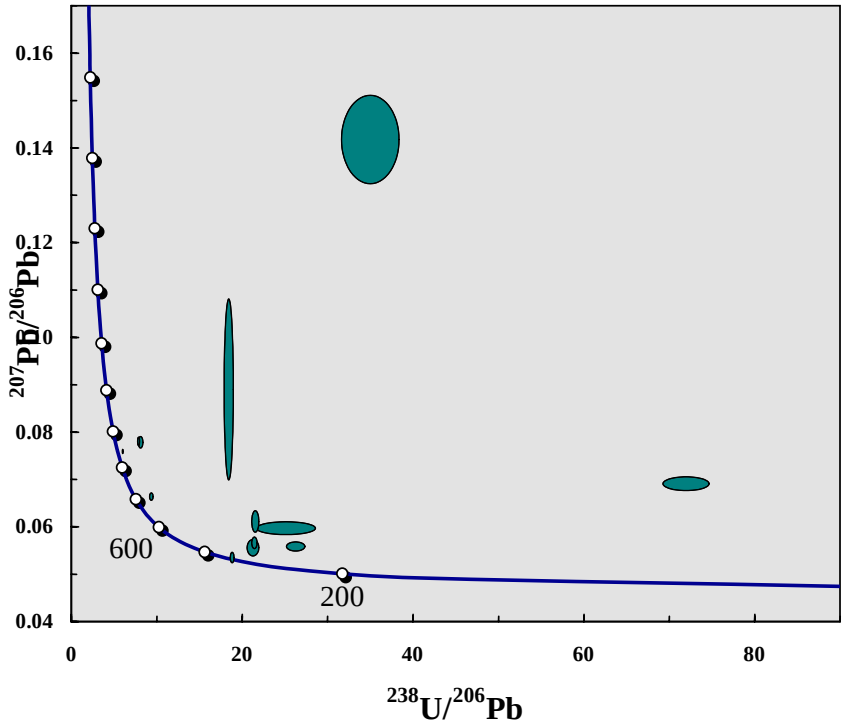

Figure 4.5c: Tera-Wasserburg concordia diagram of sample UC05592. Data-point error ellipses are 2σ.

UC08368

The probability density distribution-histogram plot for UC08368, with all analyses included, has inherited zircon up to c. 1400 Ma in age. Two main peaks exist at c. 1000 and c. 300 Ma (Figure 4.6a). The probability density distribution-histogram plot for UC08368, with the exclusion of inherited grains, ranges between c. 410 and 330 Ma with three peaks at c. 400, c. 360 and c. 335 Ma (Figure 4.6b). Data plotted in the Tera-Wasserburg concordia diagram follows a linear relationship, with low error values. The data is therefore considered to be concordant in nature (Figure 4.6c).

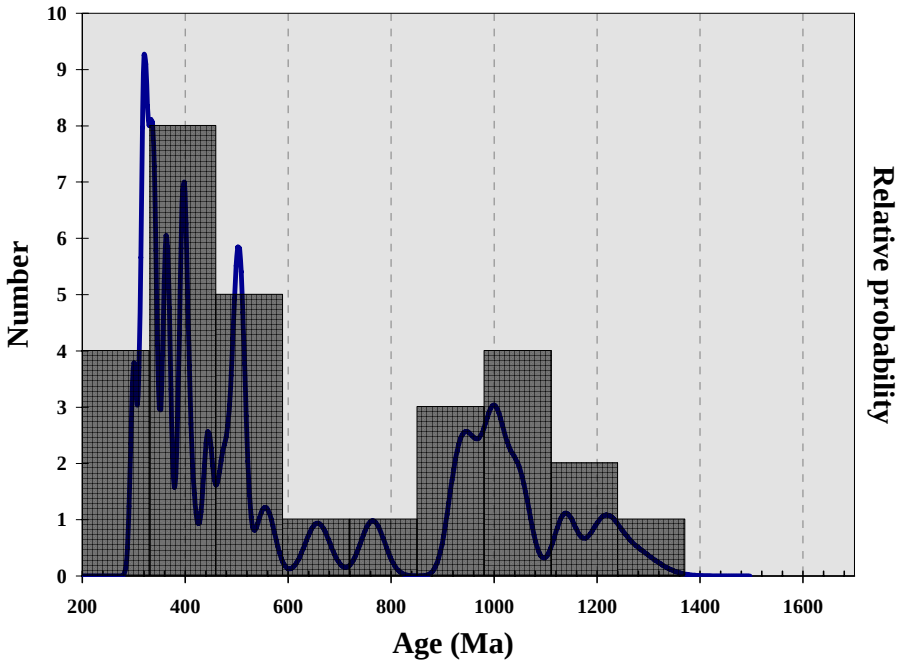

Figure 4.6a: Probability density distribution-histogram plot of all data for sample UC08368.

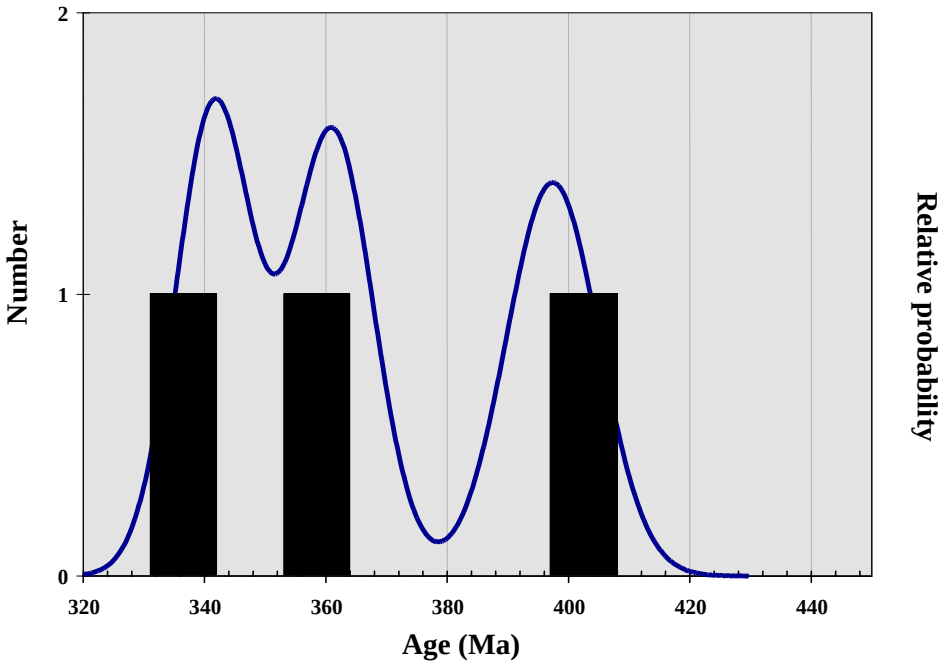

Figure 4.6b: Probability density distribution-histogram plot of inherited c. 300 to c. 400 Ma zircons for sample UC08368.

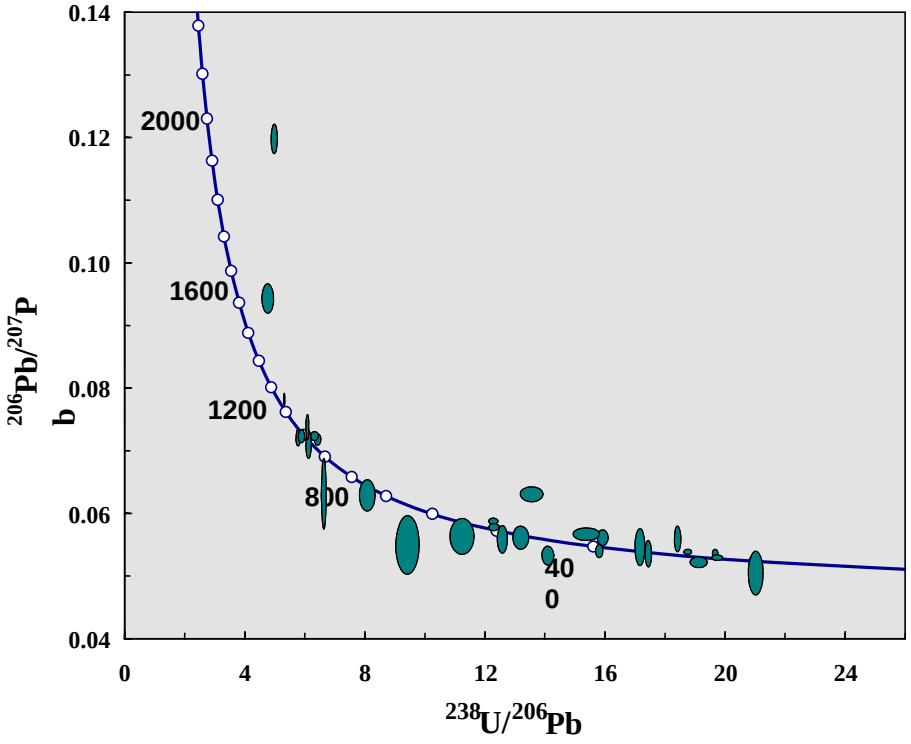

Figure 4.6c: Tera-Wasserburg concordia diagram of sample UC08368. Data-point error ellipses are 2σ.

PCC06-01

The probability density distribution-histogram plot for PCC06-01, with all analyses included, shows the presence of up to c. 2000 Ma inherited zircon within the mylonite. Two main peaks are present within this data set, at c. 600 and c. 300 Ma (Figure 4.7a). The probability density distribution-histogram plot for PCC06-01, with the exclusion of inherited grains, ranges from c. 700 to c. 300 Ma, with two main peaks at c. 550 and c. 350 Ma (Figure 4.7b).

Data plotted in the Tera-Wasserburg concordia diagram follows a linear relationship, with the data considered to be concordant in nature (Figure 4.7c).

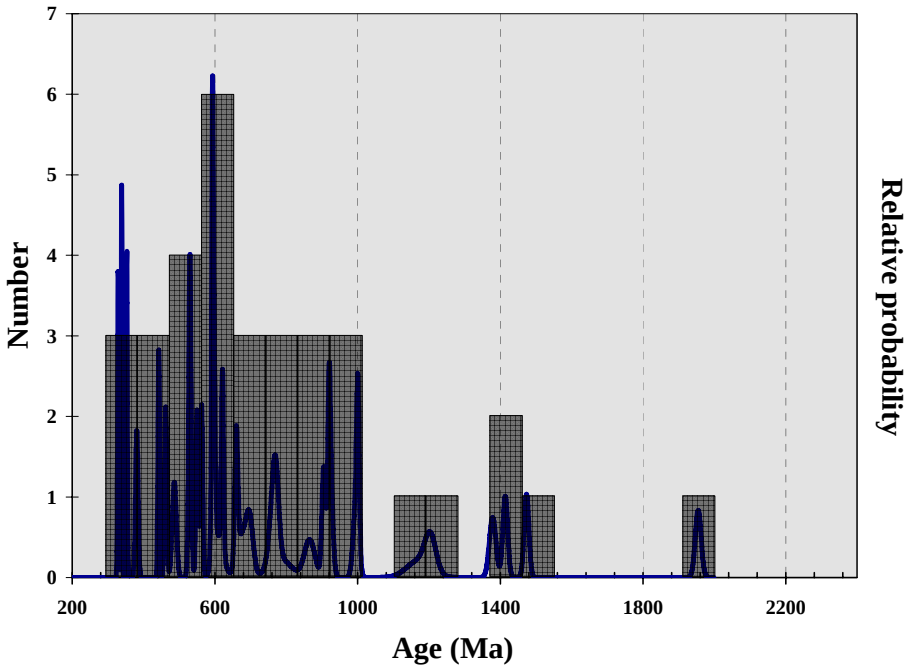

Figure 4.7a: Probability density distribution-histogram plot of all data for sample PCC06-01.

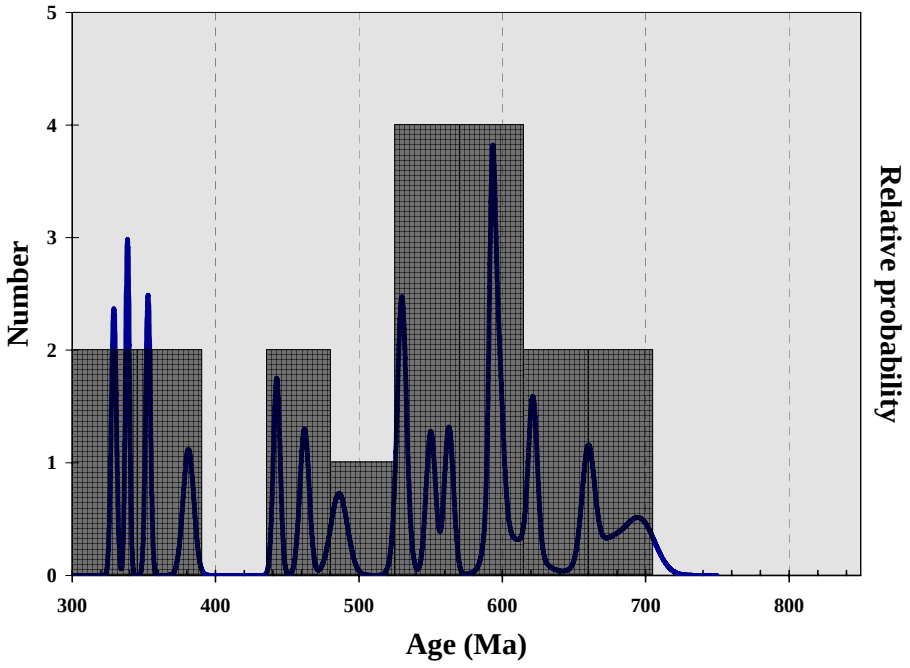

Figure 4.7b: Probability density distribution-histogram plot of data <700 Ma for sample PCC06-01.

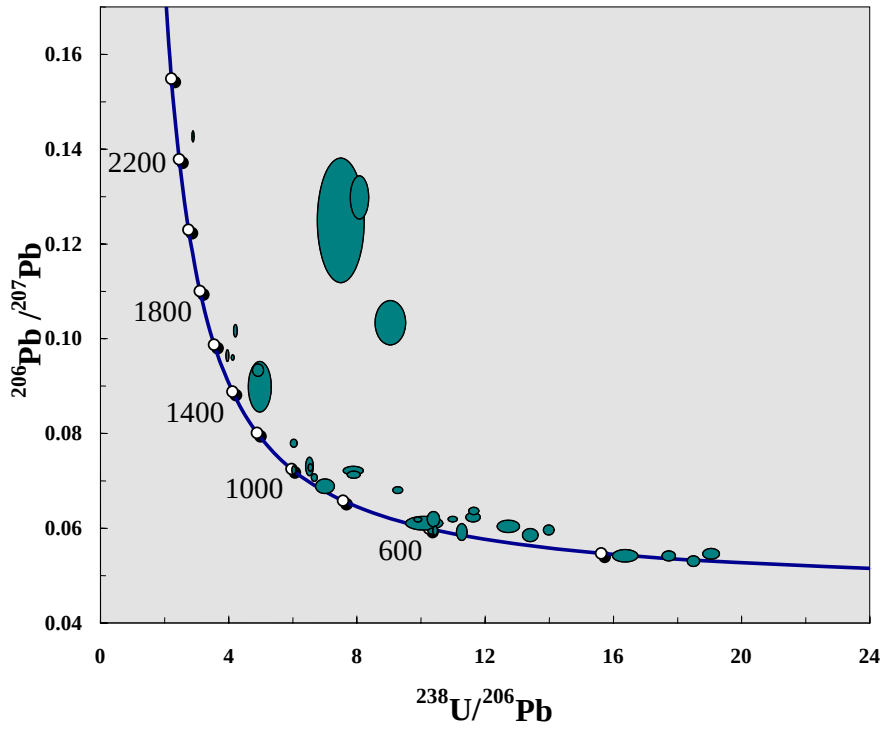

Figure 4.7c: Tera-Wasserburg concordia diagram of all data from sample PCC06-01. Data-point error ellipses are 2σ.

RNZ119

U-Pb dating of the Buckland Granite has been carried out by Muir and co workers (1994), through the *in situ* analysis of zircon grains using the Sensitive High Resolution Ion Micro Probe (SHRIMP) technique. Concordant U/Pb ages from Muir and co workers (1994) are listed in Table 4.10, and have been plotted in probability density distribution-histogram diagrams. All SHRIMP data points are plotted in Figure 4.8a, with the inheritance of zircon up to c. 1000 Ma and a main peak at c. 110 Ma. The probability density distribution-histogram plot of SHRIMP data, with the exclusion of inherited grains, records two main peaks at c. 118 and c. 109 Ma (Figure 4.8b).

Concordant $^{238}U/^{206}Pb$ Age	±1se	Concordant $^{238}U/^{206}Pb$ Age	±1se
120	2.6	105.1	2.5
492.9	10.9	880.3	19.8
117.8	2.6	107.9	2.5
538.1	11.9	117.1	3.2
463.8	10.2	116.1	2.7
111.8	2.5	110.9	2.4
112.5	2.5	105.5	2.8
824.2	18.2	112.1	2.9
106.8	2.4	106.8	2.8
559.8	12.4	924.9	23.5
690	15.2	117.6	3
299.7	6.6	492.1	12.4
107.9	2.5	117.8	3
360.8	7.9	113.5	2.9
599	13.4	114	3.2
645.3	14.3	111.2	3

Table 4.10: SHRIMP data for the Buckland Granite (sample RNZ119) by Muir et al. (1994).

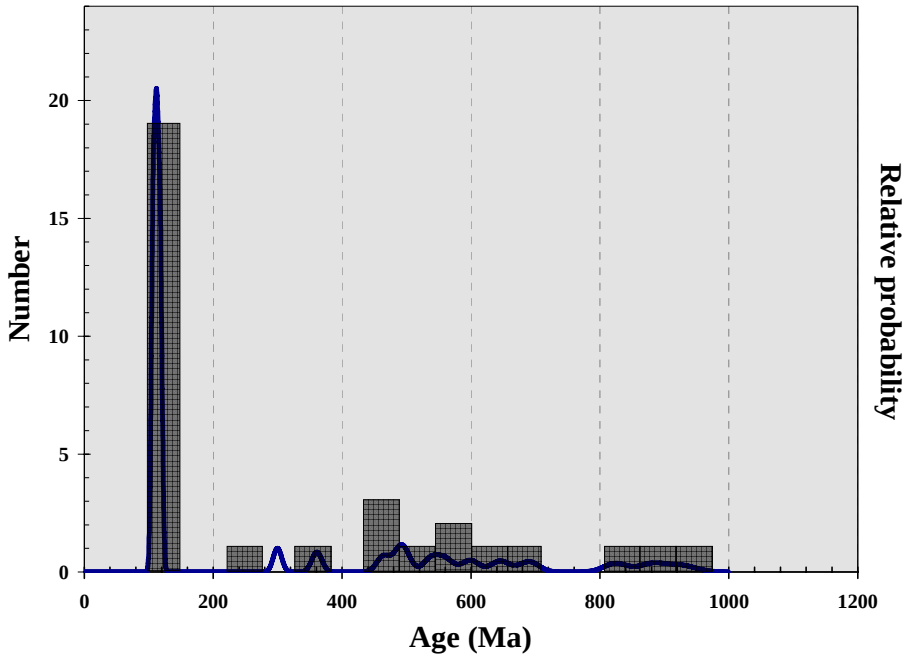

Figure 4.8a: Probability density distribution-histogram plot of all SHRIMP data for sample RNZ119 (Muir et al. 1994).

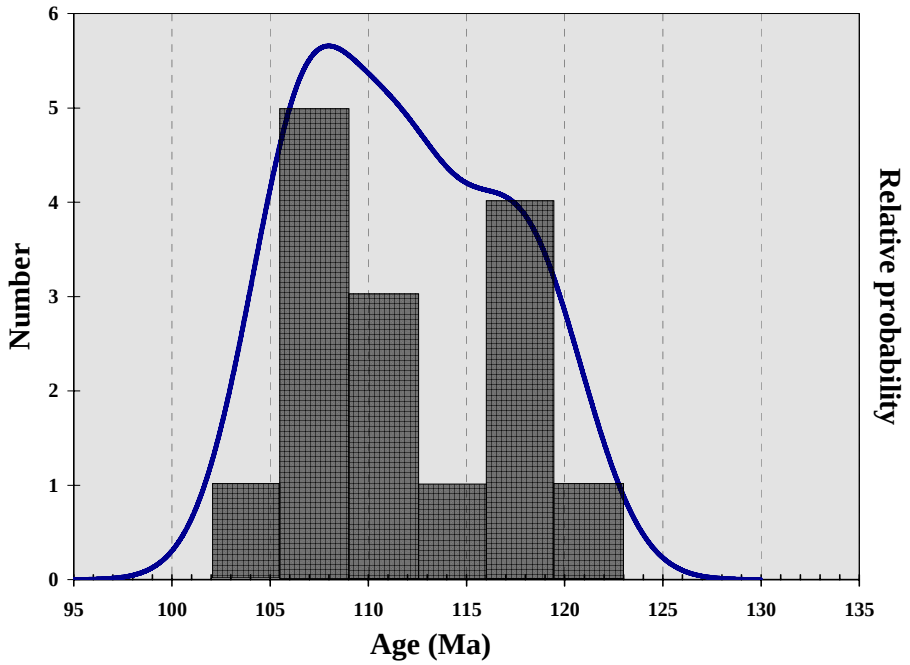

Figure 4.8b: Probability density distribution-histogram plot of SHRIMP data excluding inherited zircons for sample RNZ119 (Muir et al. 1994).

The analysis of RNZ119 was carried out using the LA-ICP-MS technique for this thesis, with the *in situ* systematic sampling of both zircon xenocrystic cores and rims (Table 3.2a). The probability density distribution-histogram plot for RNZ119, with all analyses included, shows the incorporation of zircon up to c. 1600 Ma, with a peak at c. 100 Ma (Figure 4.9a). The probability density distribution-histogram plot for RNZ119, with the exclusion of inherited grains, reflects two main peaks at 102.4 ± 0.7 and 110.3 ± 0.9 Ma (Figure 4.9b).

Data plotted in the Tera-Wasserburg concordia diagram highlights the two distinct age peaks at 102.4 ± 0.7 and 110.3 ± 0.9 Ma, with the data considered to be concordant due to the distinct linear relationship (Figure 4.9c).

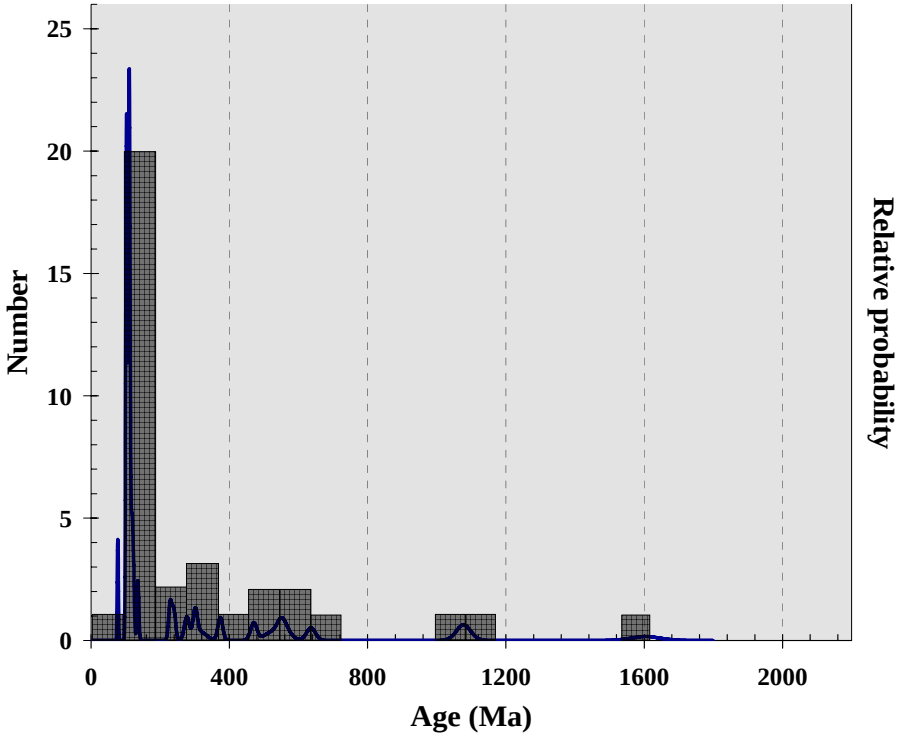

Figure 4.9a: Probability density distribution-histogram plot of all data for sample RNZ119.

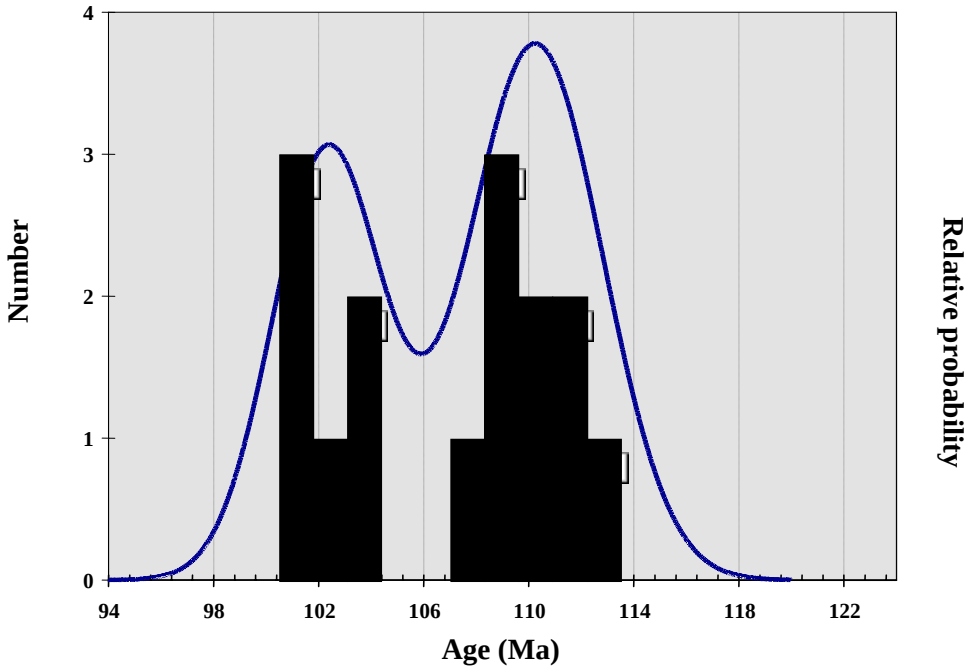

Figure 4.9b: Probability density distribution-histogram plot excluding inherited zircons for sample RNZ119.

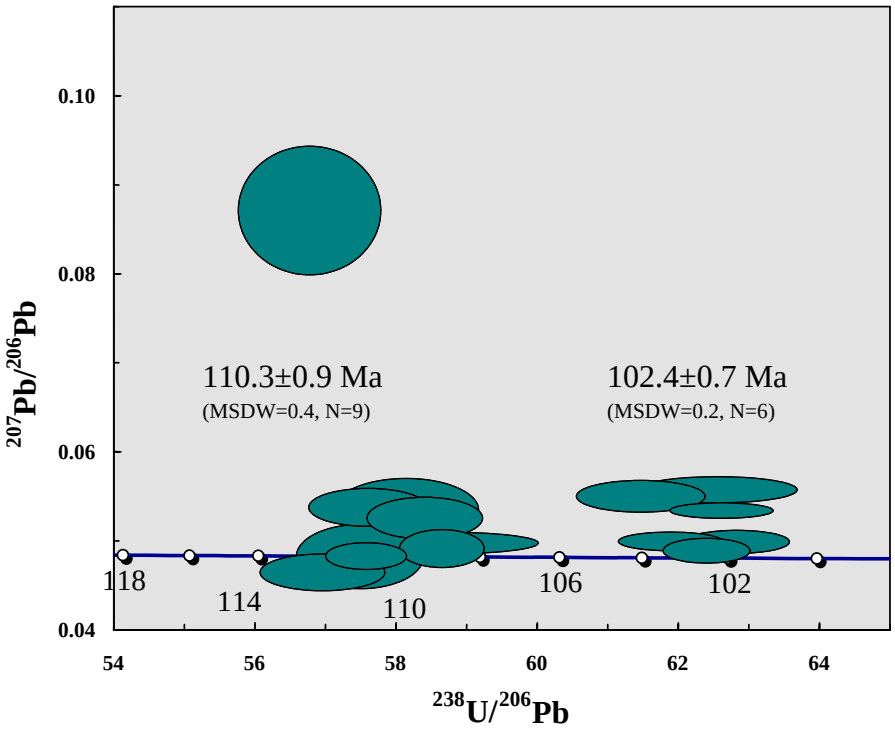

Figure 4.9c: Tera-Wasserburg concordia diagram of all data from sample PCC06-01. Data-point error ellipses are 2σ.

4.3. Combined geochemistry and geochronology

The combining of geochemical and geochronological data allows the observation of chemical changes during the evolution of a melt to be made, through the tracking of changes from zircon cores to rims in individual grains. The behaviour of O, Hf isotope ratios and Ti concentrations during crystallisation is constrained by U-Pb zircon ages, allowing petrogenetic interpretations to be made.

Zircons from the Buckland Granite are investigated in this section, due to the presence of igneous zircons which crystallised at the timing of emplacement during regional-scale extension in the Cretaceous.

Some of the following diagrams used to reflect changes during the evolution of the Buckland Granite have arrows linking individual zircon xenocrystic cores and rims

where appropriate. Diagrams tracking oxygen isotope behaviour have the average $\delta^{18}O$ mantle value of 5.3 ± 0.3‰ represented by the stippled area, with values greater than 5.3 ± 0.3‰ indicative of the incorporation of a sedimentary component into the melt (Eiler 2001, Valley 2003, Valley et al. 2005, Kemp et al. 2006, Kemp et al. 2007). $\delta^{18}O$ values greater than 5.3 ± 0.3‰ are consistent with S-type granites, which develop through the incorporation of crustal material into a once primitive magma.

The behaviour of oxygen isotopes during the crystallisation of zircons within the Buckland Granite is illustrated in Figure 4.10, where $\delta^{18}O$ ‰ [SMOW] is plotted against U-Pb zircon ages. All zircon grains sampled from the Buckland Granite display a strong sedimentary signature, as expected for the S-type pluton. All grains show a distinct increase in $\delta^{18}O$ as the granite evolved, from core to rim. Outliers within this figure include analyses B2-1 [C], B2-3 [C] and [R], B2-4 [C] and B2-5 [C], due to their variation from the overall trend. The xenocrystic cores (B2-1 [C], B2-3 [C] and B2-5 [C]) are considered to be inherited due to their U-Pb zircon ages, while the zircon rim (B2-3 [R]) has an older U-Pb zircon age than its corresponding xenocrystic core due to the analysis of an unexpectedly shallow xenocrystic core. The presence of inherited grains limits the ability to link the older cores with the igneous zircon rims which grew within the Buckland Granite during its emplacement and crystallisation.

Comparison between zircon xenocrystic core and rim $\delta^{18}O$ ‰ [SMOW] values from the Buckland Granite are shown in Figure 4.11. All data points plot above the average $\delta^{18}O$ mantle value, indicating a strong sedimentary component within the melt.

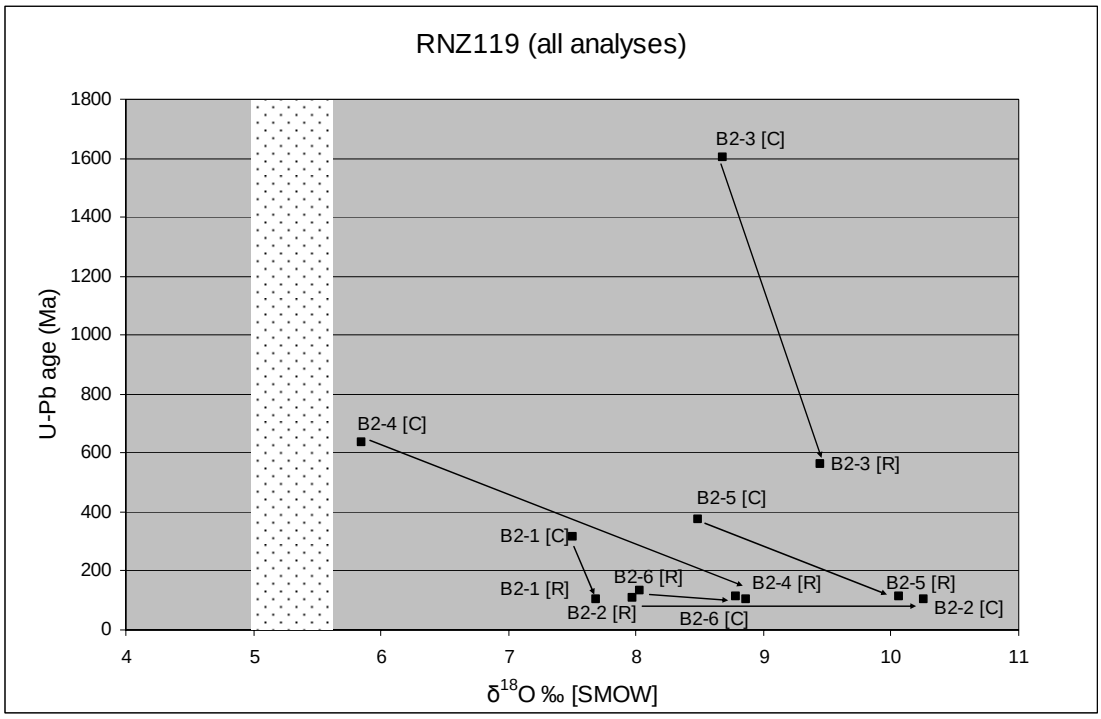

Figure 4.10: $\delta^{18}O$ ‰ [SMOW] vs. U-Pb age (Ma) for sample RNZ119. Arrows link cores and rims from individual zircon grains. Average $\delta^{18}O$ mantle value of 5.3 ± 0.3 ‰ shown as the stippled area.

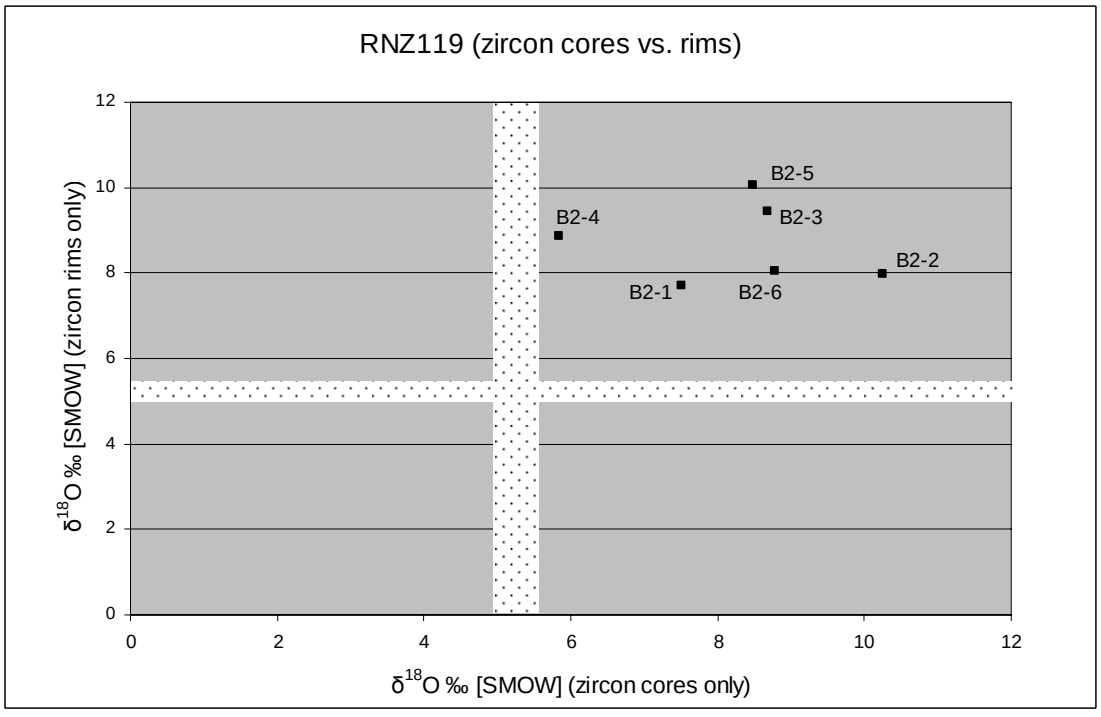

Figure 4.11: $\delta^{18}O$ ‰ [SMOW] (zircon cores only) vs. $\delta^{18}O$ ‰ [SMOW] (zircon rims only) for sample RNZ119. Average $\delta^{18}O$ mantle value of 5.3 ± 0.3 ‰ shown as the stippled area.

Histograms for samples UC08368, RNZ119, PCC06-01 and UC05592 are shown in Figures 4.12a, 4.12b, 4.12c and 4.12d, with xenocrystic cores and rims shown separately.

Crystallisation temperatures calculated for the Buckland Granite are plotted as Ti-in-zircon T (˚C) against U-Pb zircon ages, to illustrate changes in temperature during the crystallisation of the pluton (Figure 4.13). Outliers present include analyses B2-1 [C], B2-4 [C] and B2-5 [C], which are considered to be inherited xenocrystic cores and thus may not be directly correlated with the associated igneous zircon rims. Most zircon grains show the expected decrease in temperature as the melt evolved towards complete crystallisation of the pluton. The analyses [C] and [R], however, show an unexpected increase in temperature from 800˚C to 850˚C as the melt evolved. An increase in temperature during the crystallisation of a pluton suggests hotter, presumably more mafic melts entered the system.

Crystallisation temperatures are compared with $\delta^{18}O$ values for all analyses in Figure 4.14, with all data points plotting above the average $\delta^{18}O$ mantle value as expected for S-type granites. Most grains show an expected decrease in temperature as zircons crystallised from core to rim. An unexpected increase in temperature is observed from core to rim in analyses [C] and [R]. Zircon grain B2-6 appears to have a slightly older rim compared to the core which may be due to the analysis of an unexpectedly shallow xenocrystic core. An alternative explanation involves the replacement of dissolving zircon by newly forming zircon in the melt, which inherits the U-Pb zircon age of the previous grain. Crystallisation temperatures of both zircon xenocrystic cores and rims are plotted against εHf in Figure 4.15, with εHf acting as a proxy for

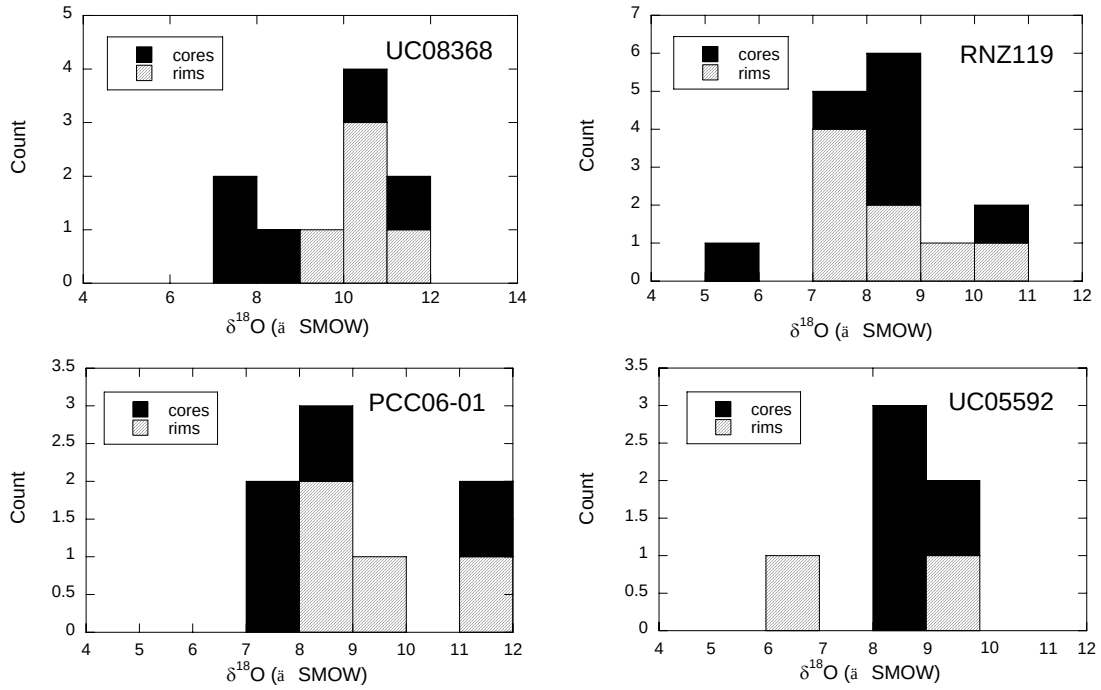

Figures 4.12a, b, c and d: Histograms of zircon xenocrystic cores and rims from samples UC08368, RNZ119, PCC06-01 and UC05592, respectively.

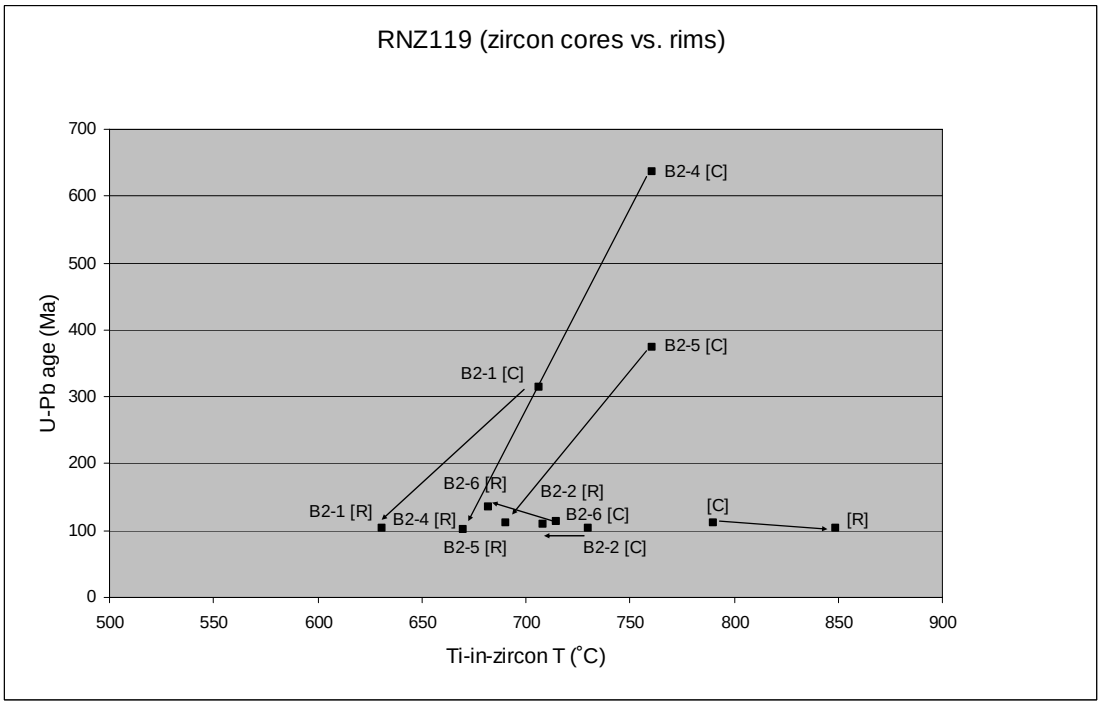

Figure 4.13: Ti-in-zircon T (˚C) vs. U-Pb age (Ma) for sample RNZ119. Arrows link cores and rims from individual zircon grains.

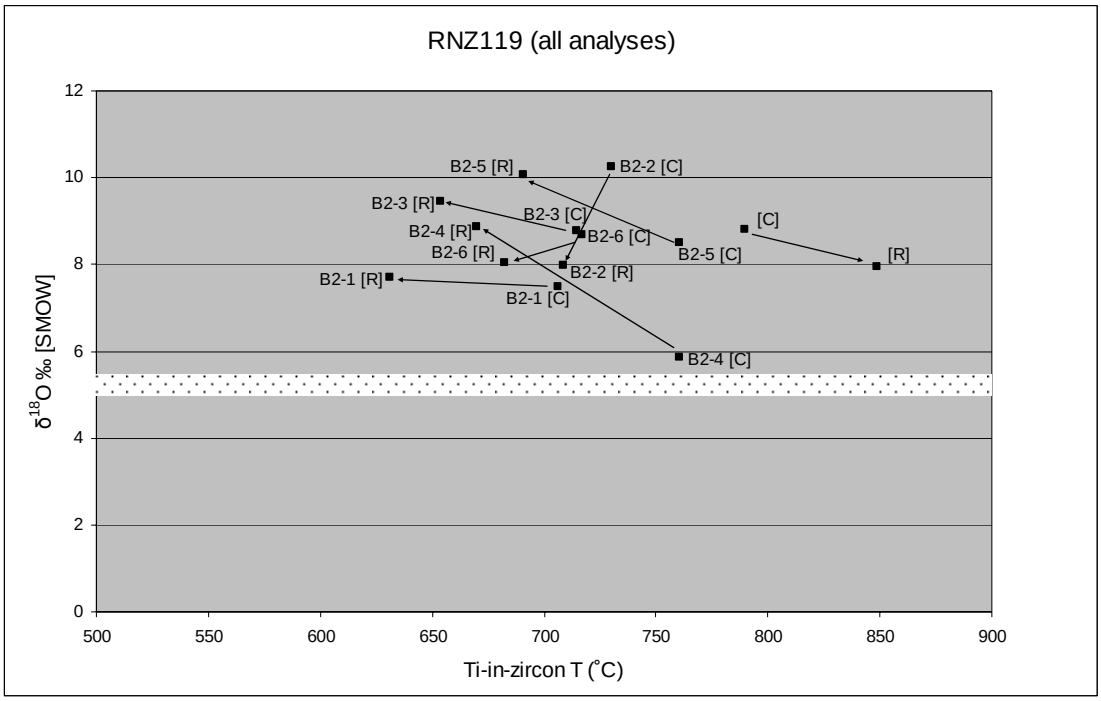

Figure 4.14: Ti-in-zircon T (˚C) vs. δ^{18}O ‰ [SMOW] for sample RNZ119. Arrows link cores and rims from individual zircon grains. Average δ^{18}O mantle value of 5.3 ± 0.3 ‰ shown as the stippled area.

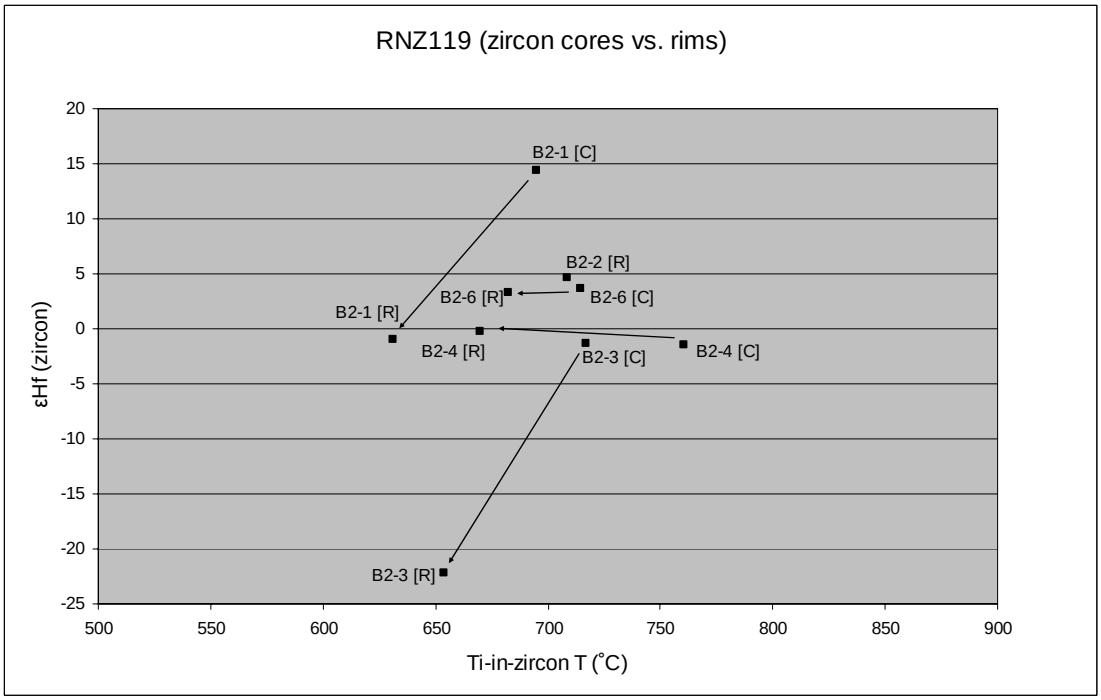

Figure 4.15: Ti-in-zircon T (˚C) vs. εHf (zircon) for sample RNZ119. Arrows link cores and rims from individual zircon grains.

the degree of evolution of a melt. The more evolved a granitic melt is, the more negative the εHf value will be. All grains show a consistent decrease in both εHf and temperature from core to rim, as expected for zircons crystallising in a cooling pluton.

εHf is plotted against U-Pb zircon age in Figure 4.16. The analysis HfB_03 from zircon grain B2-4 is an inherited core, with an age of c. 640 Ma. The analysis HfB_01 is an outlier, but is not considered to be inherited as it is a rim. The core appears to be younger, and is proposed to have resulted from the averaging out of ages by the sampling of an unexpectedly shallow core. A slight inversion in age is observed between the core (HfB_09) and rim (HfB_10) of zircon grain B2-6, with the rim appearing older and becoming more felsic as the melt evolved

εHf values for zircon xenocrystic cores and rims are directly compared in Figure 4.17, with the T_{DM} for the Buckland Granite being calculated using the 110.3 ± 0.9 Ma U-Pb zircon age from the LA-ICP-MS data set (Figure 4.9b). The 110.3 ± 0.9 Ma age is statistically identical to, albeit more precise than, the SHRIMP U-Pb zircon age of 109.6 ± 1.7 Ma calculated by Muir and co workers (1992), and is used as the crystallisation age of the pluton for this particular figure.

εHf and $\delta^{18}O$ values are compared for all analyses of the Buckland Granite in Figure 4.18. All analyses plot above average $\delta^{18}O$ mantle value indicative of a sedimentary influence, as expected for the S-type granite. Most grains show an obvious increase in εHf from core to rim, which suggests the incorporation of a mafic component in the later stages of crystallisation of the melt. Zircon grain B2-6 does not follow this trend, and becomes more felsic (decreasing εHf) as the melt evolved. The greatest change in εHf is observed in grain B2-1 from mafic to felsic εHf values of c. -1 to c. 14. No

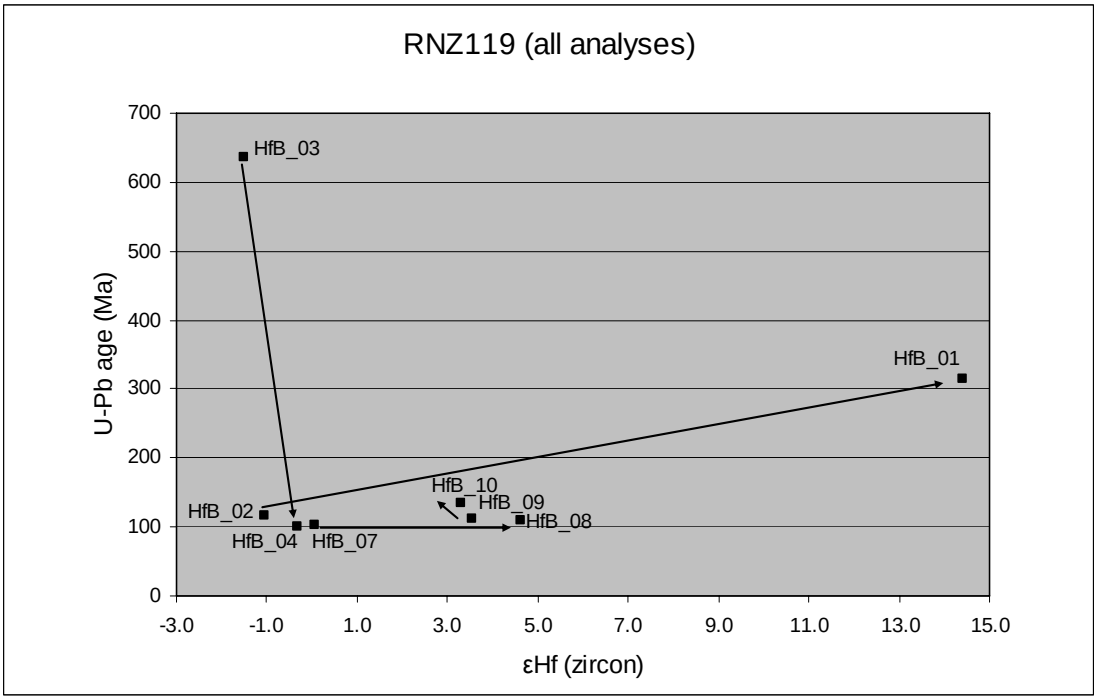

Figure 4.16: εHf vs. U-Pb age (Ma) for sample RNZ119. Arrows link cores and rims from individual zircon grains.

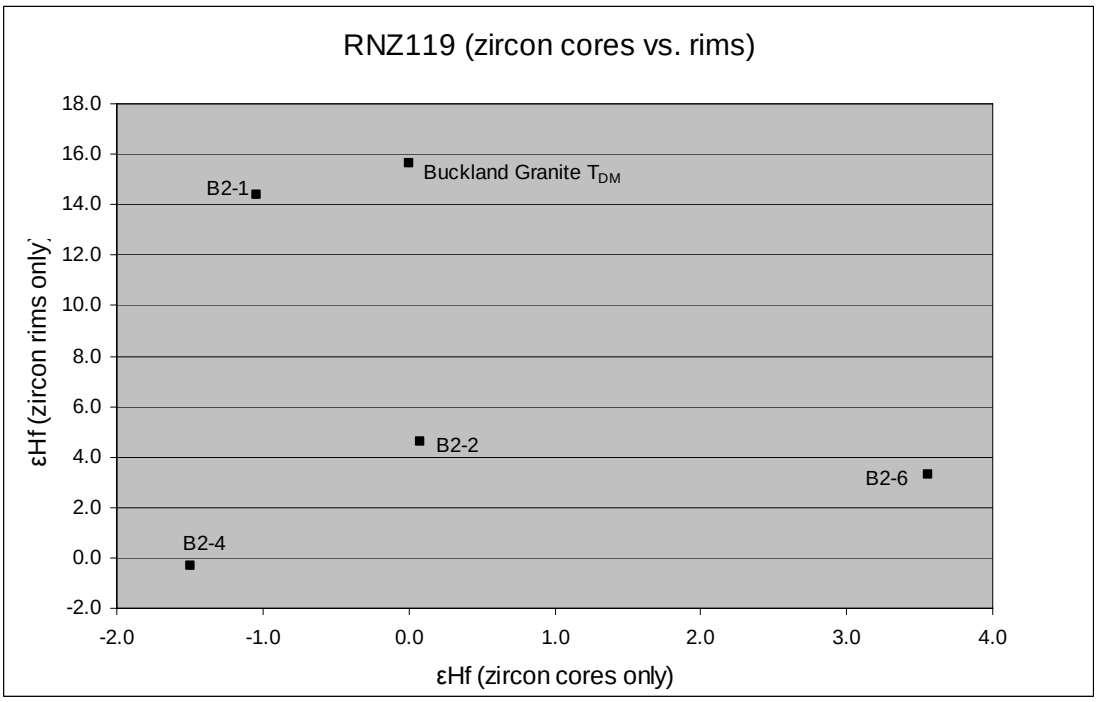

Figure 4.17: εHf (zircon cores only) vs. εHf (zircon rims only) for sample RNZ119. Buckland Granite T_{DM} calculated using the U-Pb zircon crystallisation age of 110.3 ± 0.9 Ma.

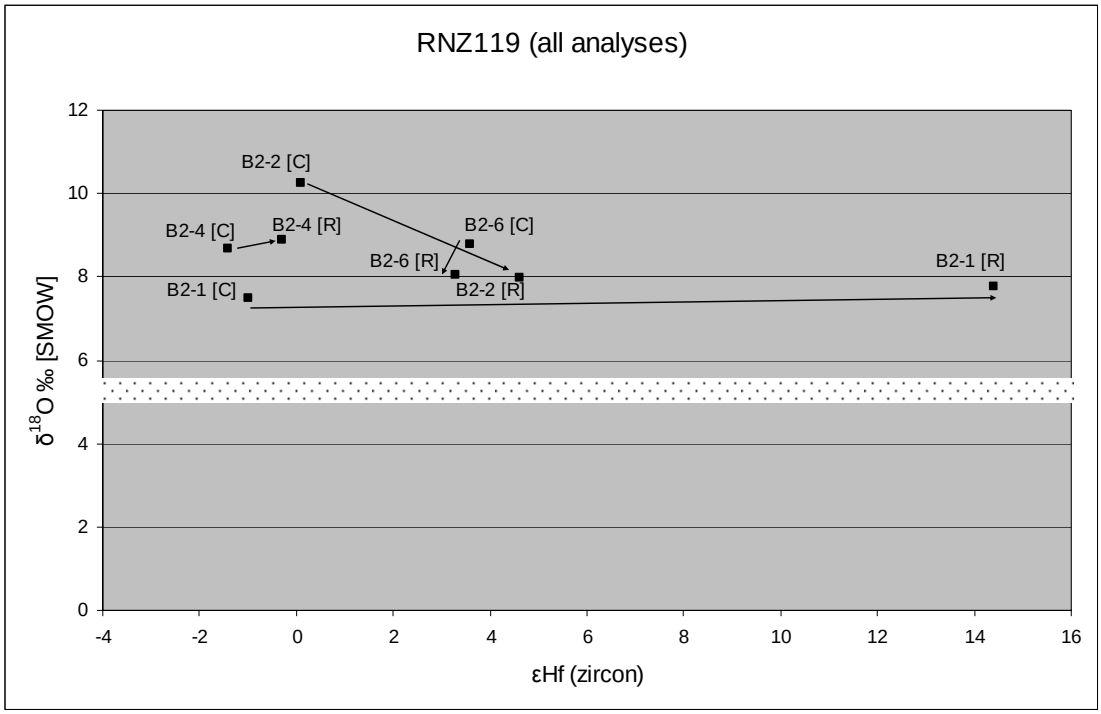

Figure 4.18: εHf (zircon) vs. $\delta^{18}O$ ‰ [SMOW] for sample RNZ119. Arrows link cores and rims from individual zircon grains. Average $\delta^{18}O$ mantle value of 5.3 ± 0.3 ‰ shown as the stippled area.

observable change is recorded in the $\delta^{18}O$ value during the crystallisation from core to rim in this particular zircon grain.

Zr/Hf values are plotted against U-Pb zircon ages for all analyses from the Buckland Granite in Figure 4.19. Most analyses show the expected decrease in age from core to rim, and decrease in the Zr/Hf ratio – with lower Zr/Hf values reflecting greater degrees of magma differentiation. Analysis B2-4 [C] is an inherited xenocrystic core, and therefore cannot be directly compared with the associated igneous zircon rim. εHf is plotted against Zr/Hf values for all analyses in Figure 4.20. A consistent move from felsic to mafic compositions (negative to positive εHf values) is observed in all grains, as Zr/Hf values decrease. This follows the pattern expected for the differentiation of a magma as the melt evolves. These patterns are suggestive of the

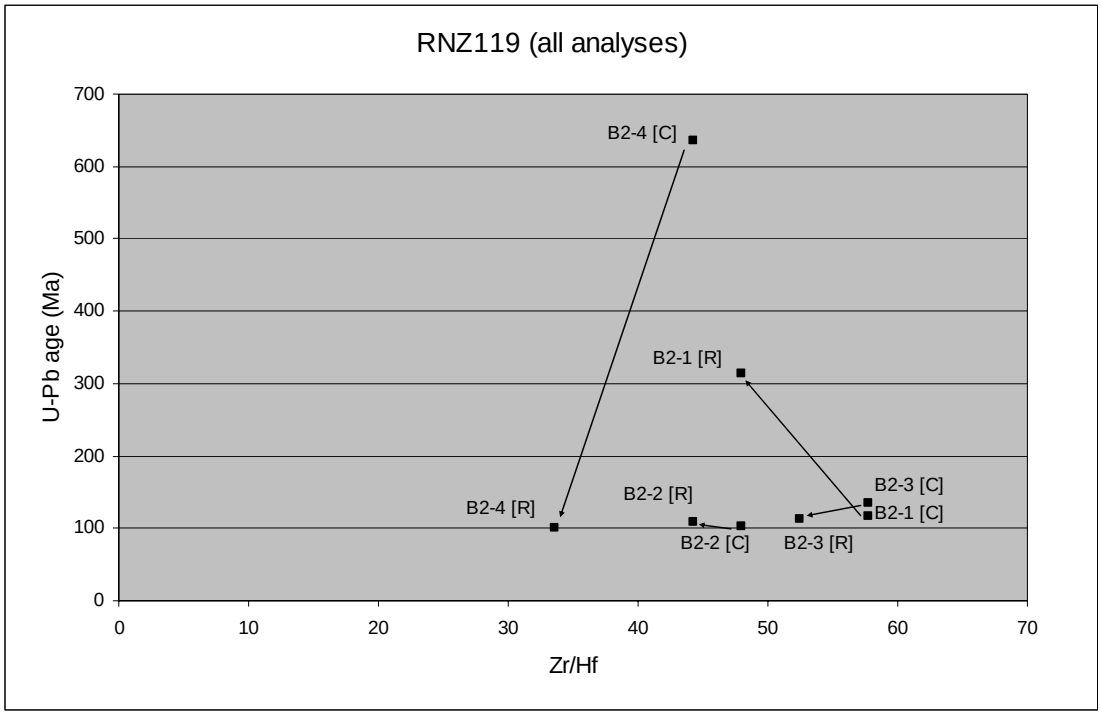

Figure 4.19: Zr/Hf vs. U-Pb age (Ma) for sample RNZ119. Arrows link cores and rims from individual zircon grains.

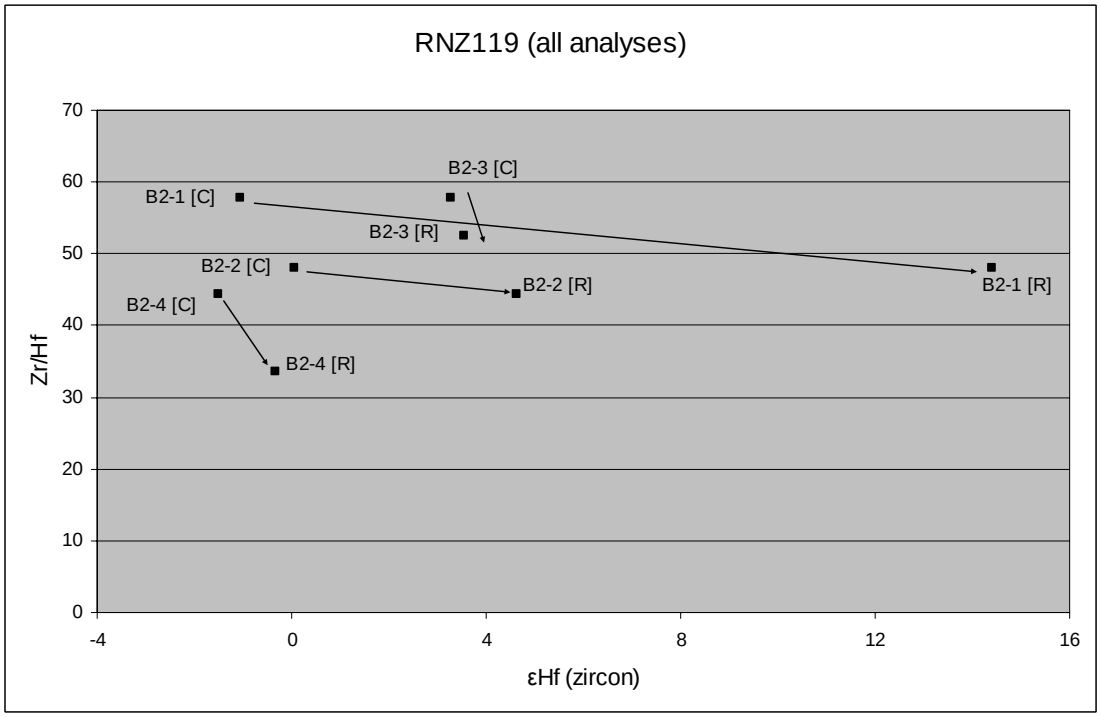

Figure 4.20: εHf (zircon) vs. Zr/Hf for sample RNZ119. Arrows link cores and rims from individual zircon grains.

incorporation of a mafic component into the initially felsic Buckland Granite at the later stages of crystallisation, as observed in Figure 4.13. The mafic imprint becomes more pronounced during the crystallisation of zircon rims.

Crystallisation temperatures and Zr/Hf values are compared for all analyses of the Buckland Granite in Figure 4.21. A consistent decrease in Zr/Hf is observed in all analyses from core to rim, as expected for an evolving melt. Zircon grains B2-2 and B2-4 show an expected decrease in temperature from core to rim, as the pluton cooled towards complete crystallisation. Zircon grains B2-1 and B2-3, however, show an unexpected increase in temperature with decreasing Zr/Hf, as the melt became more evolved. The inversion of U-Pb zircon ages in grain B2-1 (Figure 4.19) supports the inversion of temperatures, due to the analysis of an unexpectedly shallow core. Zircon grain B2-3, however, shows no reversal of U-Pb age (Figure 4.19), which supports the suggested heating of the system due to the influx of a hotter, presumably more mafic component into the Buckland Granite in the later stages of crystallisation.

εHf values are plotted against Th/U in Figure 4.22. The Th/U values are consistent within this figure, with values decreasing from core to rim as the melt crystallised. εHf values consistently increase from core to rim, further supporting the evidence of a mafic component in the late stages of crystallisation of the pluton. Th/U is used as an alternative proxy for the degree of evolution of a melt, but is not always reliable as the ratio is influenced strongly by accessory minerals such as zircon, apatite, allanite, monazite and xenotime as U is much more compatible than Th (Hoskin and Schaltegger 2003). The Zr/Hf ratio is considerably more reliable, as both elements are influenced by such accessory minerals (Lowery Claiborne et al. 2007). Zircons from

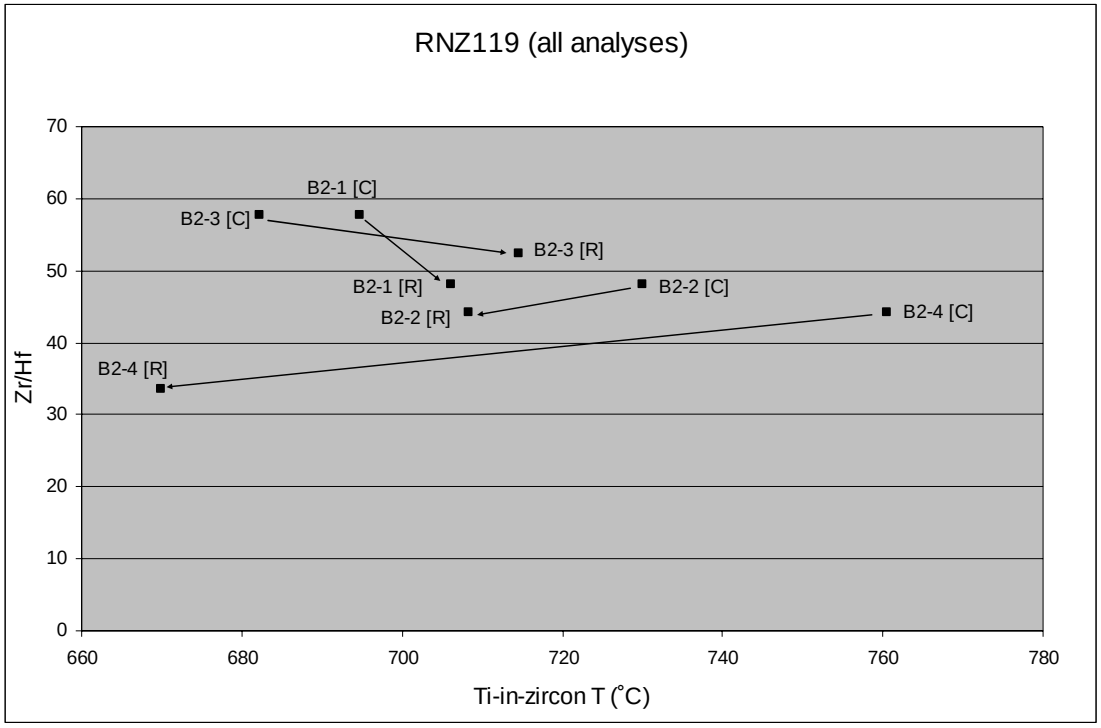

Figure 4.21: Ti-in-zircon T (˚C) vs. Zr/Hf for sample RNZ119. Arrows link cores and rims from individual zircon grains.

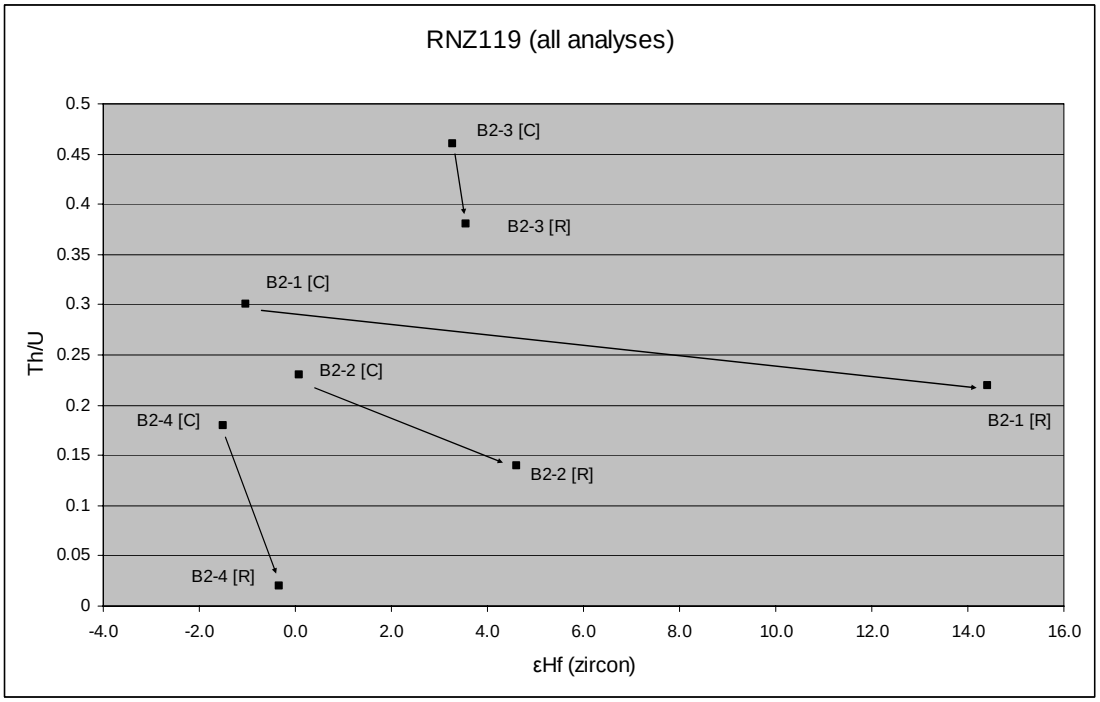

Figure 4.22: εHf (zircon) vs. Th/U for sample RNZ119. Arrows link cores and rims from individual zircon grains.

the Buckland Granite show similar distributions in both the Th/U and the Zr/Hf figures, which suggests the Th/U values are reliable in this particular study.

4.4. Provenance of zircon grains

The geochronology of a pluton may be established through the *in situ* U-Pb dating of individual zircon grains, for the timing of both primary crystallisation and subsequent metamorphism of a rock unit. Primary igneous zircons record temperature conditions (zircon saturation thermometry) and timing (U-Pb zircon dating) of a magma during crystallisation. The incorporation of pre-existing zircons into igneous rocks commonly takes place during the petrogenesis of a melt, with zircon grains often surviving the process due to their resilient nature.

The provenance of inherited and igneous zircon grains may be investigated through the combined approach of both geochemical and geochronological data (Hoskin and Ireland 2000, Hoskin and Schaltegger 2003), on the basis of identification through distinct chemical variability between potential source rocks. Analysis by LA-ICP-MS allows the rapid sampling of several grains, for high precision U-Pb zircon dating of events during the petrogenesis of igneous and metamorphic rocks. The comparison between the geochemistry and geochronology of a sample with that of known potential source rocks allows the provenance of inherited zircons to be interpreted (Fedo et al. 2003).

Geochemical data used for provenance studies may include oxygen isotopes, titanium and hafnium, along with the geochronological data provided by U-Pb dating. The use of REE's in determining the provenance of a rock unit is considered to be limited to rocks of 'extreme' composition such as kimberlites (Griffin et al. 2000, Fedo et al. 2003), and is therefore not considered further in this particular thesis.

4.4.1. Provenance of zircons from the PMCC

The presence of inherited zircons in the Paparoa Metamorphic Core Complex granitoids and mylonites allows the provenance of source rocks to be investigated. The Buckland Granite (sample RNZ119) has not been included in this section, as the geochemistry and geochronology of the pluton primarily provides information on the timing and nature of its crystallisation at 110.3 ± 0.9 Ma.

Geochemical and geochronological data from samples UC05592, UC08368 and PCC06-01 have been correlated with the known provenance of potential source rocks, including the Greenland Group metasediments and Paleozoic granitoid rocks (Figure 4.23). The Ordovician Greenland Group metasediments show two main U-Pb age peaks at c. 600-500 and c. 1200-1000 Ma (Ireland and Gibson 1998). Paleozoic granitoid rocks of the Western Province are dominated by the Karamea Batholith, with an overall crystallisation U-Pb age of c. 380-370 Ma. The Cape Foulwind and Windy Point plutons of the Karamea Batholith have younger crystallisation U-Pb ages, peaking at c. 330 Ma (Muir et al. 1994, Muir et al. 1996).

The geochemistry of samples UC05592, UC08368 and PCC06-01 have been established through the *in situ* sampling of O, Ti and Hf concentrations in individual zircon grains, by the LA-ICP-MS technique (Tables 4.9a, 4.9b, 4.9c and 4.9d).

The geochronology of rocks of the Paparoa Metamorphic Core Complex have been determined through the *in situ* U-Pb zircon dating of samples UC05592, UC08368 and PCC06-01, using the LA-ICP-MS technique. U-Pb data is visually represented in Tera-Wasserburg concordia diagrams and probability density distribution-histogram plots, constructed using the Isoplot Ex v.2.6. program (Tera and Wasserburg 1972, Ludwig 1999).

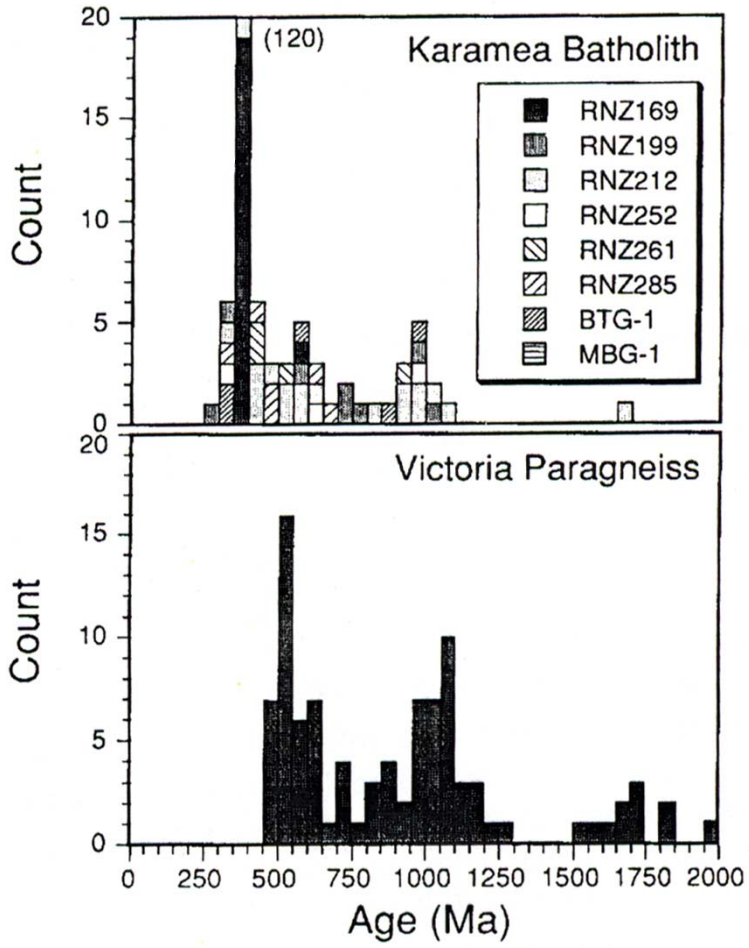

Figure 4.23: Probability-density distribution-histogram plots of the Karamea Batholith and Victoria Paragneiss (Greenland Group metasediments), Muir et al. (1996).

U-Pb zircon age peaks are observed at c. 1000, c. 600 and c. 300 Ma in samples UC05592, UC08368 and PCC06-01, characteristic of Paleozoic zircon-bearing sediments deposited along the eastern margin of Gondwana, and Mesozoic granitoid rocks of the Western Province (Ireland 1992, Muir et al. 1995).

Inherited zircons present in rocks of the Paparoa Metamorphic Core Complex are interpreted to have been sourced from heterogeneous local crust, including the Greenland Group metasediments and Karamea Batholith plutons.

CHAPTER 5: DISCUSSION

5.1. Geometry and nature of metamorphism of the PMCC

Deformation associated with the Ohika and Pike Detachment Faults illustrates that the two detachment faults had distinctly different histories. Rocks adjacent to the Ohika Detachment Fault display extensive cataclastic deformation, with limited recrystallisation of quartz in granitoid rocks of the Lower Plate. Thermal metamorphism of the Upper Plate Greenland Group metasediments in the Lower Buller Gorge resulted in the growth of andalusite, probably in response to the emplacement of the Buckland Granite. Offset along the Ohika Detachment Fault is suggested to be relatively limited, as the thermally altered Upper Plate rocks are still found adjacent to the Buckland Granite in the Lower Buller Gorge. Exhumation along the Ohika Detachment Fault is proposed to have taken place from depths of 1.5-5km, further supporting observations of the metamorphism of Upper Plate rocks adjacent to the Buckland Granite. The presence of cataclastic deformation indicates temperatures were less than c. 280˚C. Using the thermal gradient of 50-90˚C/km (White 1994), a maximum depth of 3-6km is calculated.

The dominance of cataclastic deformation in the Lower Buller Gorge reflects the low temperatures reached during extension, with temperatures proposed to have remained below c. 280˚C, probably at the c. 150-250˚C range. Temperature estimates are based on the presence of recrystallised quartz, the dominance of brittle deformation, and the lack of observable mylonitisation of rocks adjacent to the Ohika Detachment Fault.

Deformation is distinctly different in the southern section of the Paparoa Metamorphic Core Complex, with ductile deformation dominating the geology.

Cataclastic deformation is observed near the inferred Pike Detachment Fault, followed by the mylonites and ultramylonites of Morrisey Creek. The degree of deformation in the basement rocks increases to the north, in contrast to the pattern observed in the Lower Buller Gorge area, reflecting the heterogeneous nature of ductile deformation of the Lower Plate rocks.

The mylonites and ultramylonites exposed along the coastline reached upper-amphibolite facies metamorphic conditions during movement along the Pike Detachment Fault, with exhumation proposed to have taken place from depths of 12-18 km. The greater degree of exhumation, along with the presence of highly deformed rocks, supports the idea that the Pike Detachment Fault was the more dominant structure during the onset and continuation of the Paparoa Metamorphic Core Complex.

The onset of extension is proposed to have taken place at 116.2 ± 5.9 Ma along the Pike Detachment, based on the Rb/Sr date of ductile deformation of the ultramylonite (sample PCC06-02) at White Horse Creek (Ring et al. 2006). The inception of continental extension along the Pike Detachment conflicts with earlier authors who proposed extension initiated along the Ohika Detachment Fault to the north (Tulloch and Palmer 1990, Spell et al. 2000).

The emplacement of the Buckland Granite resulted in the thermal relaxation of the crust and subsequent cessation of the Ohika Detachment Fault. The dominance of movement shifted to the Pike Detachment fault, allowing greater exhumation to take place in the south.

The dip angle for the Pike Detachment Fault has been calculated using the exhumation rate of 0.6-1.0mm/yr and the slip rate of 4mm/yr, proposed by White (1994) and Spell and co workers (2000), respectively. The proposed dip angle for the Pike Detachment Fault is 15-30˚. The calculated 15-30˚ dip angle supports the notion that the Pike Detachment Fault is a regional-scale low angle structure. The presence of large-scale low angle faults within the continental crust conflicts with rock mechanics, as faults with dip angles of less than c. 30˚ are theoretically unable to slip within the brittle crust (Anderson 1942). Detachment faults of the Paparoa Metamorphic Core Complex are proposed to have been able to slip due to the significant weakening of the continental crust during regional-scale extension. Weakening of the crust may take place by the presence of high pore fluid pressure along a large-scale low angle fault, resulting in brittle fracturing and cataclasis of adjacent rock. Chloritization and sericitization may also take place through the replacement of micas and feldspar, as commonly observed in metamorphic core complexes (Coney 1980, Wernicke 1981a, Davis 1983).

An alternative mechanism for the existence of large-scale low angle detachment faults involves the exhumation of the brittle-ductile transition zone (Miller et al. 1983, Axen 2004). Low angle structures may develop within the ductile zone of the continental crust, due to the weak nature of the crust at depth. In the case of regional-scale extension, the crust becomes isostatically uplifted, and would result in the transportation of the low angle structure into the brittle zone of the continental crust. It has been suggested that faults which initially develop within the ductile lower crust are able to remain at a low angle, as the structure remains relatively weak during the transition (Miller et al. 1983, Axen 2004).

5.2. Geochemical and geochronological findings

The use of geochemistry and geochronology has allowed interpretations to be made on the petrogenesis of the Buckland Granite and the provenance of inherited zircons within the Paparoa Metamorphic Core Complex rocks. Correlation of data has been possible due to the method of sampling adopted for this thesis, with analysis numbers listed alongside the zircon grain numbers in Tables 5.1a, b, c and d.

Crystallisation temperatures of the Buckland Granite calculated using the zircon saturation thermometry technique averaged at 697°C (3sf), with a standard deviation of 54.6 (3sf). Xenocrystic cores and rims of zircons were calculated separately, with temperatures averaging at 723°C (3sf) and 730°C, respectively. The temperature difference between the xenocrystic cores and rims is considered to be negligible. The range in crystallisation temperatures for the Buckland Granite lie within the upper-amphibolite facies range, which is consistent with ductile deformation of rocks along the coastline north of the inferred Pike Detachment Fault (sample PCC06-02).

The majority of zircon grains show the expected decrease in temperature from core to rim, as the Buckland Granite evolved towards complete crystallisation (Figure 4.13). An unexpected increase in temperature is observed from core [C] to rim [R] in one grain, which is found to represent heating of the pluton through the incorporation of hotter, presumably more mafic melts in the later stages of crystallisation.

Alternatively, the temperature inversion may record inherited U-Pb ages of pre-existing grains which dissolved and were replaced by newly forming zircon in the melt. The replenishment of the Buckland Granite magma chamber is considered to be more likely, and is further supported by the Ti-in-zircon T (˚C) vs. Zr/Hf plot, in

Zircon grain	Ti analysis	C vs. R	Hf analysis	C vs. R	O analysis	C vs. R	^{208}Pb corrected ^{206}Pb/^{238}U age	±1s.e.
B2-5	**BUCK_01**	**C**	-	-	**3c**	**C**	**373.71906**	**1.88505**
B2-5	**BUCK_02**	**R**	-	-	**3r**	**R**	**111.1498235**	**0.45163**
B2-6	BUCK_03	C	HfB_09	C	2c	C	112.5138063	0.71869
B2-6	BUCK_04	R	HfB_10	R	2r	R	135.4818137	1.05859
-	**BUCK_05**	**C**	-	-	**1c**	**C**	**110.4814407**	**0.9017**
-	**BUCK_06**	**R**	-	-	**1r**	**R**	**103.4311859**	**0.63704**
B2-3	BUCK_07	R	HfB_06	R	6r	R	562.5694685	14.8549
B2-3	BUCK_08	C	HfB_05	C	6c	C	1604.237201	29.2793
B2-4	**BUCK_09**	**C**	**HfB_03**	**C**	**7c**	**C**	**636.0121967**	**5.85876**
B2-4	**BUCK_10**	**R**	**HfB_04**	**R**	**7r**	**R**	**101.3314408**	**0.47943**
B2-1	BUCK_11	C	HfB_01	R	5c	C	314.6349783	17.5711
B2-1	BUCK_12	C	HfB_02	C	5r	R	116.3241816	1.71268
B2-1	BUCK_13	R	-	-	5rr	R	103.2511763	0.51961
B2-2	**BUCK_14**	**C**	**HfB_07**	**C**	**4c**	**C**	**102.7025288**	**0.41536**
B2-2	**BUCK_15**	**R**	**HfB_08**	**R**	**4r**	**R**	**109.3607797**	**0.63347**
-	BUCK_16	C	-	-	-	-	109.4416091	0.4574
-	BUCK_17	R	-	-	-	-	110.6759035	0.67846
-	*BUCK_18*	*C*	-	-	-	-	*111.7369862*	*0.73542*
-	*BUCK_19*	*R*	-	-	-	-	*108.060718*	*0.95884*
-	*BUCK_20*	*R*	-	-	-	-	*122.695243*	*1.32172*
-	**BUCK_21**	**R**	-	-	-	-	**118.7945414**	**1.28069**
-	**BUCK_22**	**C**	-	-	-	-	**550.1788569**	**7.68848**
-	BUCK_23	C	-	-	-	-	470.4739599	3.9026
-	BUCK_24	R	-	-	-	-	108.9868464	1.03203
-	**BUCK_25**	**C**	-	-	-	-	**1071.627117**	**4.7526**
-	**BUCK_26**	**R**	-	-	-	-	**1083.140186**	**4.67917**
-	BUCK_27	R	-	-	-	-	101.7708905	0.49309
-	BUCK_28	C	-	-	-	-	276.8368327	5.1002
-	*BUCK_29*	*C*	-	-	-	-	*228.5945607*	*1.84829*
-	**BUCK_30**	**R**	-	-	-	-	**77.27770481**	**0.77064**
-	**BUCK_31**	**C**	-	-	-	-	**239.1498642**	**2.94558**
-	BUCK_32	R	-	-	-	-	301.3601198	2.97239
-	BUCK_33	C	-	-	-	-	520.7914135	18.4208
-	**BUCK_34**	**C**	-	-	-	-	**103.3208177**	**1.51073**
-	**BUCK_35**	**R**	-	-	-	-	**101.74642**	**0.74715**

Table 5.1a: Combined geochemical analysis details for sample RNZ119 (Buckland Granite), with zircon grain number, location of analysis (core vs. rim) and U-Pb zircon ages.

Zircon grain	Ti analysis	C vs. R	Hf analysis	C vs. R	O analysis	C vs. R	^{208}Pb corrected ^{206}Pb/^{238}U age	±1s.e.
68-1	**68_01**	**C**	**Hf68_01**	**C**	**5c**	**C**	**0.07608141**	**0.00129**
68-1	**68_02**	**R**	**-**	**-**	**5r**	**R**	**0.06297728**	**0.00062**
68-5	68_03	C	Hf68_02	C	1c	C	0.17666481	0.00173
68-5	68_04	R	Hf68_03	R	1r	R	0.16617933	0.0019
68-2	**68_05**	**C**	**Hf68_04**	**C**	**2c**	**C**	**0.0798396**	**0.0009**
68-2	**68_06**	**R**	**Hf68_05**	**R**	**2r**	**R**	**0.07119915**	**0.00077**
68-3	68_07	R	-	-	3c	C	0.2062262	0.00349
68-3	68_08	R	-	-	3r	R	0.0741271	0.00169
68-4	**68_09**	**C**	**Hf68_06**	**C**	**4c**	**C**	**0.12545889**	**0.00327**
68-4	**68_10**	**R**	**Hf68_07**	**R**	**4r**	**R**	**0.05230716**	**0.00064**
-	68_11	C	-	-	-	-	0.17352587	0.00284
-	68_12	R	-	-	-	-	0.15833916	0.00196
-	*68_13*	*C*	-	-	-	-	*0.05740094*	*0.00028*
-	*68_14*	*?*	-	-	-	-	*0.06517195*	*0.00157*
-	*68_15*	*?*	-	-	-	-	*0.081862*	*0.00089*
-	*68_16*	*?*	-	-	-	-	*0.04756201*	*0.00047*
-	**68_17**	**C**	-	-	-	-	**0.19215437**	**0.00105**
-	**68_18**	**R**	-	-	-	-	**0.16091985**	**0.00299**
-	68_19	C	-	-	-	-	0.21546371	0.00773
-	68_20	R	-	-	-	-	0.05335202	0.00034
-	**68_21**	**C**	-	-	-	-	**0.10709415**	**0.00365**
-	**68_22**	**R**	-	-	-	-	**0.15350531**	**0.0015**
-	*68_23*	*?*	-	-	-	-	*0.16727636*	*0.00121*
-	68_24	?	-	-	-	-	*0.08179109*	*0.00091*
-	*68_25*	*?*	-	-	-	-	*0.05836476*	*0.00047*
-	*68_26*	*?*	-	-	-	-	*0.05435531*	*0.00025*
-	*68_27*	*?*	-	-	-	-	*0.06342026*	*0.00041*
-	68_28	?	-	-	-	-	*0.0508367*	*0.00019*
-	*68_29*	*?*	-	-	-	-	*0.08962102*	*0.00267*
-	*68_30*	*?*	-	-	-	-	*0.05067122*	*0.0004*

Table 5.1b: Combined geochemical analysis details for sample UC08368, with zircon grain number, location of analysis (core vs. rim) and U-Pb zircon ages.

Zircon grain	Ti analysis	C vs. R	Hf analysis	C vs. R	O analysis	C vs. R	^{208}Pb corrected ^{206}Pb/^{238}U age	±1s.e.
S-9	**S_01**	**C**	**HfS_03**	**C**	**1c**	**C**	**1473.462613**	**6.62742**
S-9	**S_02**	**R**	**HfS_04**	**R**	**1r**	**R**	**1413.899969**	**6.78041**
S-7	S_03	C	HfS_06	C	2c	C	1378.486856	9.21934
S-7	S_04	R	HfS_05	R	2r	R	1203.748023	15.5701
S-11	**S_05**	**C**	**HfS_07**	**C**	**3c**	**C**	**596.4776804**	**3.50282**
S-11	**S_06**	**R**	**HfS_08**	**R**	**3r**	**R**	**592.8904502**	**1.98352**
-	S_07	R	-	-	-	-	352.904914	1.68762
-	*S_08*	*R*	-	-	-	-	*610.3007943*	*13.4772*
S-3	**S_09**	**R**	-	-	-	-	**338.6017125**	**1.40453**
S-3	**S_10**	**C**	-	-	-	-	**1000.848893**	**3.72275**
-	S_11	C	-	-	-	-	1170.802297	33.134
S-10	**S_12**	**C**	-	-	**4c**	**C**	**995.0984611**	**7.52417**
S-10	**S_13**	**R**	-	-	**4r**	**R**	**659.88117**	**4.27246**
-	*S_15*		*HfS_01*	*R*	-	-	-	-
-	-	-	*HfS_02*	*C*	-	-	*762.1101741*	*10.9642*
-	S_16	C	-	-	-	-	905.0466005	5.03104
-	S_17	R	-	-	-	-	529.705269	4.20434
S-2	**S_18**	**R**	-	-	-	-	**782.9927549**	**30.0136**
S-2	**S_19**	**C**	-	-	-	-	**697.1386036**	**9.95564**
S-1	S_20	R	-	-	-	-	462.0378448	3.2312
S-1	S_21	C	-	-	-	-	529.9996739	2.83876
S-4	**S_22**	**C**	-	-	-	-	**865.339485**	**14.6921**
S-4	**S_23**	**R**	-	-	-	-	**562.758152**	**3.19464**
-	S_24	C	-	-	-	-	595.0140087	4.86137
-	S_25	R	-	-	-	-	381.0645092	3.74929
-	**S_26**	**C**	-	-	-	-	**919.9552513**	**3.79129**
-	**S_27**	**R**	-	-	-	-	**442.6680036**	**2.40194**
-	S_28	C	-	-	-	-	621.3486368	3.07765
-	S_29	R	-	-	-	-	486.1675665	5.77762
S-5	**S_30**	**C**	-	-	-	-	**1954.576378**	**8.22202**
S-5	**S_31**	**R**	-	-	-	-	**674.4936096**	**13.8623**
S-6	S_32	C	-	-	-	-	550.1452145	3.28984
S-6	S_33	R	-	-	-	-	329.0483789	1.77143
S-8	**S_34**	**C**	-	-	-	-	**924.6954943**	**6.20485**
S-8	**S_35**	**R**	-	-	-	-	**770.8304771**	**8.30041**

Table 5.1c: Combined geochemical analysis details for sample PCC06-01, with zircon grain number, location of analysis (core vs. rim) and U-Pb zircon ages.

Zircon grain	Ti analysis	C vs. R	Hf analysis	C vs. R	O analysis	C vs. R	^{208}Pb corrected ^{206}Pb/^{238}U age	±1s.e.
-	*92_01*	*?*	-	-	-	-	*297.4303486*	*3.99189*
-	*92_02*	*?*	-	-	-	-	*239.5477162*	*3.8867*
92-2	**92_03**	**C**	-	-	-	-	**336.0306656**	**2.08048**
-	*92_04*	*?*	-	-	-	-	*761.1094961*	*9.2472*
92-3	92_05	C	Hf92_04	C	1c	C	1015.456051	4.46141
-	**92_06**	**R**	-	-	-	-	**160.9600057**	**6.35517**
-	**92_07**	**R**	-	-	-	-	**249.3183688**	**13.8649**
-	**92_08**	**C**	-	-	-	-	**665.0654357**	**5.52218**
92-3	92_09	R	Hf92_03	R	-	-	781.3093172	6.24777
92-2	**92_10**	**R**	-	-	-	-	**293.3765261**	**1.78448**
-	*92_11*	*C*	-	-	-	-	*295.2686703*	*2.53716*
92-1	92_12	R	Hf92_02	R	3r	R	329.0550824	5.36499
92-1	92_13	C	Hf92_01	C	3c	C	86.64086097	1.31266
92-4	-	-	**Hf92_05**	**R**	**4c**	**C**	-	-
92-4	-	-	**Hf92_06**	**C**	**4r**	**R**	-	-

Table 5.1d: Combined geochemical analysis details for sample UC05592, with zircon grain number, location of analysis (core vs. rim) and U-Pb zircon ages.

which temperatures increase from core to rim in two of the grains analysed (Figure 4.21).

The timing of emplacement of the Buckland Granite has been further constrained from the previous date of 109.6 ± 1.7 Ma from Muir and co workers (1992). Two distinct U-Pb zircon age peaks are observed in the LA-ICP-MS data for the Buckland Granite (sample RNZ119), at 102.4 ± 0.7 and 110.3 ± 0.9 Ma. The presence of two distinct peaks in the U-Pb zircon age data may have resulted from the systematic sampling approach undertaken for this particular thesis, where xenocrystic cores and rims from individual zircons were analysed separately. The careful analysis of xenocrystic cores and rims allows tracking of chemical changes within the Buckland

Granite as the melt evolved to complete crystallisation. This thesis is one of few studies which presently involves the analysis of similar growth zones across a number of grains, allowing correlations between O and Hf isotope ratios, REE, Hf, U-Pb zircon ages and Ti-in-zircon temperatures to be made between samples.

The 110.3 ± 0.9 Ma U-Pb zircon age peak is statistically identical to, albeit more precise than, the SHRIMP U-Pb zircon age of 109.6 ± 1.7 Ma calculated by Muir and co workers (1992), and is interpreted as the timing of crystallisation of the Buckland Granite. The 102.4 ± 0.7 Ma U-Pb zircon age is more difficult to interpret, but may have resulted from three main options.

The first option is the potential influence of Pb-loss at a later stage, causing the 110.3 ± 0.9 Ma crystallisation age of damaged zircons to shift to the younger age of 102.4 ± 0.7 Ma. The second option is the remobilisation and precipitation of zircon grains at 102.4 ± 0.7 Ma in response to a thermal event (subsolidus crystallisation), to then become incorporated into the Buckland Granite. The third option is that the 102.4 ± 0.7 and 110.3 ± 0.9 Ma U-Pb zircon ages represent two distinct magma pulses during the emplacement of the Buckland Granite into the Lower Plate of the Paparoa Metamorphic Core Complex.

Pb-loss is considered to be unlikely, as analyses were carried out in grains/growth zones showing no observable metamictization, and differences in trace element concentrations are too great to be accounted by Pb-loss alone.

U and Th/U content, along with Ti-in-zircon crystallisation temperatures, are averaged for the 102 Ma and 110 Ma grains from the Buckland Granite (sample RNZ119) in Table 5.2. The 102 Ma zircons have greater U content, and lower average

Zircon grain	LA-ICP-MS analysis	C vs. R	^{208}Pb corr'd $^{206}Pb/^{238}U$ age	U (ppm)	Th/U	Ti-in-zircon T (°C)
B2-5	BUCK_02	R	*111.1498235*	*542.3*	*0.13*	*690.4989309*
B2-6	BUCK_03	C	*112.5138063*	*314.1*	*0.38*	*714.5328101*
-	BUCK_05	C	*110.4814407*	*248.7*	*1.07*	*789.8182829*
-	BUCK_06	R	**103.4311859**	**1486.1**	**0.15**	**849.0018538**
B2-4	BUCK_10	R	**101.3314408**	**3492.2**	**0.02**	**669.902422**
B2-1	BUCK_13	R	**103.2511763**	**2117.3**	**0.07**	**631.165597**
B2-2	BUCK_14	C	**102.7025288**	**976.9**	**0.23**	**730.101364**
B2-2	BUCK_15	R	*109.3607797*	*696.4*	*0.14*	*708.375387*
-	-	-	**102 Ma zircons (av)**	**2018.1**	**0.17**	**720.042808**
-	-	-	*110 Ma zircons (av)*	*450.4*	*0.41*	*725.806353*

Table 5.2: 102 vs. 110 Ma zircons from the Buckland Granite (sample RNZ119), with averages for U, Th/U and Ti-in-zircon T (˚C).

Th/U ratios than the 110 Ma zircons, while crystallisation temperatures show little variation. Zircons grown under subsolidus conditions characteristically show high LREE concentrations (Cavosie et al. 2006). The 102 Ma zircons from the Buckland Granite lack high LREE concentrations, and therefore cannot be interpreted to have resulted from subsolidus growth. A magmatic origin is considered to be more likely, as primary oscillatory (igneous) zoning is preserved in the 102 Ma zircons (Cavosie et al. 2006).

If the Buckland Granite 102 Ma zircons represent a magmatic pulse associated with extension, the upper crust should display associated extensional features (e.g. grabens) of the same age. The crystallisation age of c. 110-109 Ma for the Buckland Granite may only represent a small event, perhaps in response to extension along the Pike Detachment Fault. I speculate that there was a significant magmatic pulse at c. 102 Ma (Figure 5.1).

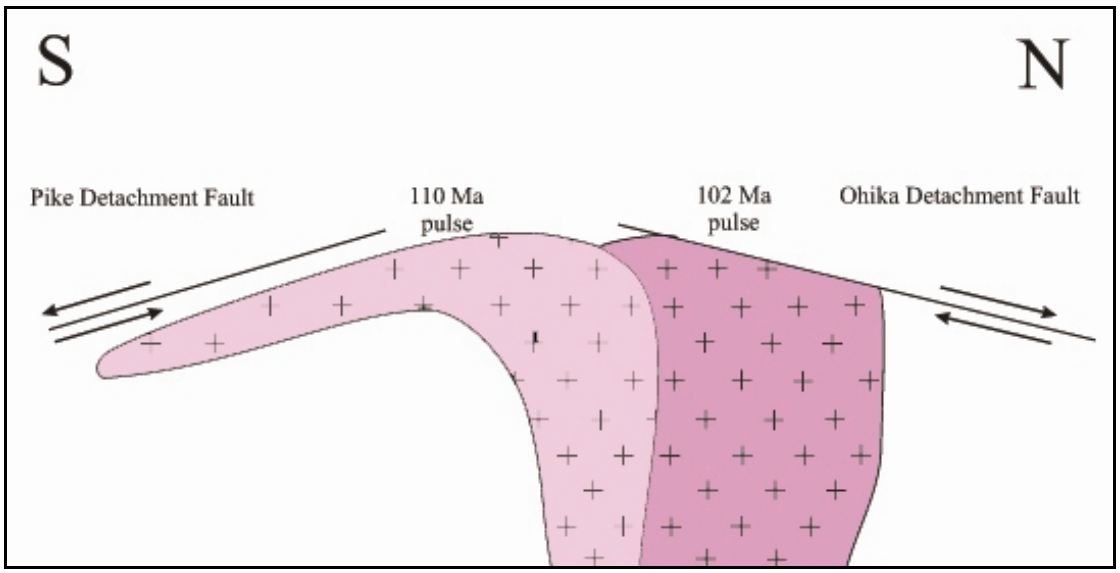

Figure 5.1: Schematic crosssection of the Paparoa Metamorphic Core Complex, with the Ohika and Pike Detachment Faults to the north and south, respectively. The proposed 102 and 110 Ma magmatic pulses are illustrated, with the 110 Ma pulse being dragged to the south in response to movement along the Pike Detachment Fault from c. 116 Ma (Ring et al. 2006).

Two samples of the Stitts Tuff provide crystallisation ages of 101 ± 2 and 102 ± 3 Ma (2σ error), with U, Th, Th/U and U-Pb data listed for 'Stitts Tuff I' and 'Stitts Tuff II' in Table 5.3 (Muir et al. 1997). Sample 'Stitts Tuff I' has a range of U content from 150-720ppm, and 0.47-1.29ppm for Th/U. Sample 'Stitts Tuff II' ranges in U content from 200-600ppm, and 0.55-0.78 for Th/U (Muir et al. 1997).

The U content and Th/U ratios for the 102 Ma Buckland Granite zircons have been compared with the 101-102 Ma zircons from the Stitts Tuff, with higher U contents and lower Th/U ratios in the Buckland Granite 102 Ma zircons. A regional thermal (magmatic?) event is proposed to have taken place at c. 102 Ma, in association with the Stitts Tuff volcanism at 101-102 Ma.

Hafnium is a useful indicator of crustal vs. mantle influences on a magma system, with ε_{Hf} values being calculated for the Buckland Granite following the method

Grain	U (ppm)	Th (ppm)	Th/U	$^{207}Pb/^{206}Pb$	$^{238}U/^{206}Pb$	$f^{206}Pb$† (%)	Age‡ (Ma)
Stitts Tuff I							
1.1	724	492	0.68	0.0511 ± 0.0015	64.74 ± 1.33	0.34 ± 0.17	98.5 ± 2.0
2.1	648	589	0.91	0.0518 ± 0.0017	63.48 ± 1.17	0.41 ± 0.19	100.3 ± 1.8
3.1	393	205	0.52	0.0535 ± 0.0013	16.93 ± 0.29	–0.05 ± 0.14	370.2 ± 6.2•
4.1	358	460	1.29	0.0541 ± 0.0019	60.43 ± 1.34	0.65 ± 0.21	105.1 ± 2.3
5.1	448	289	0.65	0.0496 ± 0.0015	64.95 ± 2.41	0.18 ± 0.16	98.3 ± 3.6
6.1	575	334	0.58	0.0482 ± 0.0016	64.72 ± 1.36	0.02 ± 0.18	98.8 ± 2.1
7.1	372	175	0.47	0.0535 ± 0.0026	65.87 ± 1.52	0.61 ± 0.28	96.6 ± 2.2
8.1	516	427	0.83	0.0516 ± 0.0016	64.45 ± 1.26	0.39 ± 0.18	98.9 ± 1.9
9.1	399	281	0.71	0.0531 ± 0.0026	63.70 ± 1.42	0.56 ± 0.29	99.9 ± 2.2
10.1	573	146	0.26	0.0551 ± 0.0020	55.21 ± 1.02	0.74 ± 0.22	114.9 ± 2.1•
11.1	559	489	0.87	0.0513 ± 0.0012	60.58 ± 1.11	0.35 ± 0.13	105.2 ± 2.1
12.1	379	383	1.01	0.0523 ± 0.0000	59.94 ± 0.96	0.45 ± 0.00	106.2 ± 2.1
13.1	280	178	0.63	0.0549 ± 0.0026	62.28 ± 1.47	0.75 ± 0.28	101.9 ± 2.4
14.1	235	297	1.26	0.0747 ± 0.0045	62.03 ± 2.08	2.92 ± 0.50	100.1 ± 3.4
15.1	379	57	0.15	0.0551 ± 0.0011	16.44 ± 0.34	0.09 ± 0.12	380.4 ± 7.6•
17.1	151	158	1.04	0.0564 ± 0.0031	63.64 ± 1.42	0.91 ± 0.34	99.6 ± 2.2
Stitts Tuff II							
1.1	514	375	0.73	0.0771 ± 0.0089	59.41 ± 1.73	3.18 ± 0.97	104.2 ± 3.2
1.2	580	451	0.78	0.0935 ± 0.0089	56.34 ± 2.36	4.98 ± 0.98	107.8 ± 4.6
2.1	557	401	0.72	0.0782 ± 0.0148	61.48 ± 1.28	3.30 ± 1.62	100.6 ± 2.7
2.2	590	461	0.78	0.0831 ± 0.0058	60.08 ± 1.60	3.84 ± 0.64	102.4 ± 2.8
3.1	419	281	0.67	0.0729 ± 0.0043	16.54 ± 0.34	2.08 ± 0.47	370.8 ± 7.7•
4.1	461	254	0.55	0.1045 ± 0.0110	57.01 ± 1.19	6.18 ± 1.21	105.2 ± 2.6
6.1	368	180	0.49	0.1139 ± 0.0099	27.77 ± 0.70	6.89 ± 1.09	212.6 ± 5.8•
7.1	481	121	0.25	0.0668 ± 0.0030	15.95 ± 0.53	1.41 ± 0.33	386.6 ± 12.6•
8.1	595	388	0.65	0.0639 ± 0.0039	64.11 ± 1.32	1.74 ± 0.42	98.1 ± 2.0
9.1	445	167	0.37	0.0703 ± 0.0050	16.90 ± 0.44	1.80 ± 0.55	364.1 ± 9.5•
10.1	202	124	0.61	0.2278 ± 0.0123	48.14 ± 4.00	19.67 ± 1.35	106.7 ± 9.0

† $f^{206}Pb$ is the fraction of common Pb of the total measured Pb in the analysis.
‡ $^{238}U/^{206}Pb^{*}$ age corrected for common Pb.
• Points omitted from the age calculation.
All errors are 1σ.

Table 5.3: U, Th, Th/U and U-Pb data for samples ‘Stitts Tuff I’ and Stitts Tuff II’ (Muir et al. 1997).

outlined in the paper by Nebel and co workers (2007). Both negative and positive ε_{Hf} values were calculated for sample RNZ119, with an average negative value of -1.7 indicative of crustal involvement in the melt (Table 4.7).

The observed increase in εHf from core to rim in most zircon grains is proposed to record the incorporation of a mafic component in the later stages of crystallisation of the melt, with the mafic imprint becoming more pronounced during crystallisation of zircon rims (Figures 4.18 and 4.20). The maximum (T_{DM} mafic) and minimum (T_{DM} felsic) model ages for the Buckland Granite were found to be 3410 Ma and 2969 Ma, respectively. The maximum model age of 3410 Ma coincides with the major crustal formation event for the Gondwana supercontinent at c. 3.4-3.5 Ga (Kemp et al. 2006), which records the timing and location at which the inherited zircons initially grew.

The provenance of zircon grains within the Paparoa Metamorphic Core Complex is investigated using the LA-ICP-MS U-Pb zircon data analysed for samples UC05592, UC08368, PCC06-01 and RNZ119. Probability density distribution-histogram plots and Tera-Wasserburg diagrams illustrate peaks at c. 1000, 600 and 300 Ma, which suggest the involvement of a local, heterogeneous crustal component (including the Greenland Group and the Karamea Batholith plutons). Inherited zircon grains in the Stitts Tuff show a distinct age peak at c. 300-400 Ma, characteristic of the nearby Karamea Batholith (Muir et al. 1996, Muir et al. 1997). This inheritance, also observed in the Buckland Granite, illustrates that the two rock units were influenced by the same local source.

5.3. Potential future work

Future work on the Paparoa Metamorphic Core Complex may involve the following suggestions:

1. Link the silicified material in the Pike Stream area to the nearby White Knight Stream area (resilicified Greenland Group at the inferred detachment fault, observed during field work for this particular thesis).
2. Access drill core PRDH12 (in the core store at Greymouth) to observe the sequence from the Upper Plate to Lower Plate (at depth), through the Pike Detachment Fault in the Pike Stream area.
3. Try and find evidence for the suggested gravitational reversal of shear sense in the Lower Buller Gorge associated with the switch in dominance from the

Ohika to Pike Detachment Fault (should see an older sense of shear to the south, overprinted by movement to the north).

4. Systematic U-Pb zircon dating of the Buckland Granite to determine the importance of the 102 and 110 Ma age peaks found in this study.
5. Look for any evidence of extension at 102 Ma in the upper crust adjacent to the Buckland Granite pluton in the Buller area.

CHAPTER 6: CONCLUSION

The Paparoa Metamorphic Core Complex was first proposed by Tulloch and Kimbrough in 1989 to explain the juxtaposition of high grade (Lower Plate) against low grade (Upper Plate) rocks on the West Coast of the South Island, New Zealand. Continental extension during the Cretaceous, through the development of the Paparoa Metamorphic Core Complex, led to the eventual separation of the New Zealand section from the Gondwana supercontinent, and the later formation of the Tasman Sea Basin at c. 84 Ma (Laird 1981, Grindley and Davey 1982, Bradshaw 1989, Tulloch and Kimbrough 1989, Muir et al. 1992, Laird 1993, Waight et al. 1998b, Spell et al. 2000, Laird and Bradshaw 2004).

The Paparoa Metamorphic Core Complex was suggested to be symmetric in nature (Spell et al. 2000), with the Ohika and Pike Detachment Faults thought to have experienced similar histories. The nature of ductile deformation of Lower Plate rocks was investigated, with deformation found to be distinctly different in rocks adjacent to the Ohika and Pike Detachment Faults. The presence of mylonites and ultramylonites adjacent to the Pike Detachment Fault illustrates the greater degree of exhumation in the south. Deformation of Lower Plate rocks to the north is predominantly cataclastic in nature, with limited offset along the Ohika Detachment Fault during extension.

The onset of extension is proposed to have taken place at 116.2 ± 5.9 Ma along the Pike Detachment, based on the Rb/Sr date of ductile deformation of the ultramylonite (sample PCC06-02) at White Horse Creek (Ring et al. 2006). The inception of continental extension along the Pike Detachment conflicts with earlier authors who

proposed extension initiated along the Ohika Detachment Fault to the north (Tulloch and Palmer 1990, Spell et al. 2000).

Geochemical and geochronological investigations involved the *in situ* analysis of zircon grains from a variety of Lower Plate rocks of the Paparoa Metamorphic Core Complex. Both internal and external morphological features were investigated, in combination with Hf and O isotope ratios, trace metals (Ti, REE's) and U-Pb data. The use of cathodoluminescence images (CL) allowed any altered or damaged grains to be avoided during sampling, thus reducing the potential incorporation of zircon grains which have experienced Pb-loss.

Zircons from the Buckland Granite (sample RNZ119) all displayed $\delta^{18}O$ values greater than the average $\delta^{18}O$ mantle value of 5.3 ± 0.3‰, as expected for the S-type granite. The average crystallisation temperature of the Buckland Granite (RNZ119) was found to be 697°C. Zircon xenocrystic cores and rims of the Buckland Granite were analysed separately, with crystallisation temperatures of 723°C and 730°C, respectively. The difference in average temperatures between xenocrystic cores and rims of sample RNZ119 is considered to be negligible, with the crystallisation temperatures lying within the upper-amphibolite facies range. Recrystallisation of feldspars within the Lower Plate mylonite at White Horse Creek (sample PCC06-02) indicates that deformation was well within the amphibolite facies range at 116.2 ± 5.9 Ma – further supporting the upper-amphibolite facies metamorphism of the Buckland Granite during the Cretaceous.

Crystallisation temperatures of the Buckland Granite (sample RNZ119) generally show the expected decrease as the melt evolved (from zircon core to rim). One grain, however, shows an unexpected increase in temperature from 800˚C to 850˚C as the

melt evolved. An increase in temperature during the crystallisation of the pluton suggests hotter, presumably more mafic melts entered the system. The incorporation of a mafic component into the initially felsic Buckland Granite is observed at the later stages of crystallisation, with the mafic imprint becoming more pronounced during the crystallisation of zircon rims. Mafic replenishment of the Buckland Granite in the later stages of crystallisation is proposed.

ε_{Hf} values of zircons from the Buckland Granite (sample RNZ119) are both negative and positive, with an average negative value of -1.7. The presence of negative ε_{Hf} values indicates crustal involvement during the crystallisation of zircon, as expected for the S-type nature of the Buckland Granite.

T_{DM} mafic (maximum) and T_{DM} felsic (minimum) values for the Buckland Granite (sample RNZ119) average at 3410 Ma and 2969 Ma, respectively, with the mafic T_{DM} value of 3410 Ma coinciding with the proposed major crustal formation event of the Gondwana supercontinent at c. 3.4-3.5 Ga (Kemp et al. 2006).

The REE patterns for the Lower Plate rocks UC05592, UC08368, RNZ119 (Buckland Granite) and PCC06-01 all show positive trends with a relative enrichment of HREE's and depletion of LREE's, as expected for zircon-bearing rocks which have not suffered extensive alteration.

Two distinct U-Pb zircon age peaks are observed in the LA-ICP-MS data for the Buckland Granite (sample RNZ119), at 102.4 ± 0.7 and 110.3 ± 0.9 Ma. The 110.3 ± 0.9 Ma age is statistically identical to, albeit more precise than, the SHRIMP U-Pb zircon age of 109.6 ± 1.7 Ma (Muir et al. 1992) and is interpreted as the timing of crystallisation of the Buckland Granite. The 102.4 ± 0.7 Ma U-Pb zircon age is proposed to represent a younger thermal (magmatic?) event, based on the U and Th/U

contents, and the presence of primary oscillatory (igneous) zoning in the 102 Ma zircons of the Buckland Granite.

The U content and Th/U ratios for the 102 Ma Buckland Granite zircons have been compared with the 101-102 Ma zircons from the Stitts Tuff (Muir et al. 1997), with higher U contents and lower Th/U ratios observed in the 102 Ma Buckland Granite zircons. The suggested thermal (magmatic?) activity at 102 Ma is proposed to be a regional event associated with the 101-102 Ma Stitts Tuff volcanic activity.

The inheritance of zircons in the Lower Plate rocks (samples UC05592, UC08368 and PCC06-01) is addressed, with three main age peaks observed at 1000, 600 and 300 Ma. These age peaks correspond with zircons of the Greenland Group metasediments and the Karamea Batholith (Muir et al. 1994, Muir et al. 1996, Ireland and Gibson 1998), and records the incorporation of heterogeneous local crust during petrogenesis. Inherited zircon grains in the Stitts Tuff show a distinct age peak at c. 300-400 Ma, characteristic of the Karamea Batholith (Muir et al. 1996, Muir et al. 1997). This inheritance, also observed in the Buckland Granite, illustrates that the two rock units were influenced by the same local source.

Future work on the Paparoa Metamorphic Core Complex may include the systematic sampling of the Buckland Granite for U-Pb zircon LA-ICP-MS analysis, to establish the importance of the 102 and 110 Ma age peaks observed in the data set of this thesis. The relationship between the 102 Ma zircons of the Buckland Granite and zircons of the 101-102 Ma Stitts Tuff is also considered to be of interest for future work on the Paparoa Metamorphic Core Complex.

REFERENCES:

Adams CJD 1975. Discovery of Precambrian rocks in New Zealand: Age relations of the Greenland Group and Constant Gneiss, Westland. *Earth and Planetary Science Letters* 28: 98-104.

Amelin Y, Lee DC, Halliday AN 2000. Early-middle Archaean crustal evolution deduced from Lu-Hf and U-Pb isotopic studies of single zircon grains. *Geochimica et Cosmochimica Acta* 64: 4205-4225.

Amelin Y, Lee DC, Halliday AN, Pidgeon RT 1999. Nature of the Earth's earliest crust from hafnium isotopes in single detrital zircons. *Nature* 399: 252-255.

Anderson EM 1942. The Dynamics of Faulting and Dike Formation with Application to Britain. Edinburgh, Oliver and Boyd. 191p.

Armstrong RL 1972. Low angle (denudation) faults, hinterland of the Sevier orogenic belt, eastern Nevada and western Utah. *Geological Society of America Bulletin* 83: 1729-1754.

Ashwal LD, Tucker RD, Zinner EK 1999. Slow cooling of deep crustal granulites and Pb-loss in zircon. *Geochimica et Cosmochimica Acta* 63: 2839-2851.

Axen GJ 2004. *Mechanisms of Low-Angle Normal Faults.* In: Karner GD, Taylor B, Driscoll NW, Kohlstedt DL ed. Rheology and Deformation of the Lithosphere at Continental Margins (Margins Theoretical and Experimental Earth Science Series): 46-91.

Ballard JR, Palin JM, Williams IS, Campbell IH 2001. Two ages of porphyry intrusion resolved for the super-giant Chuquicamata copper deposit in northern Chile by ELA-ICP-MS and SHRIMP. *Geology* 29: 383-386.

Belousova EA, Griffin WL, O'Reilly SY 2006. Zircon crystal morphology, trace element signatures and Hf isotope composition as a tool for petrogenetic modelling: Examples from eastern Australian granitoids. *Journal of Petrology* 47: 329-353.

Bertotti G, Podladchikov Y, Daehler A 2000. Dynamic link between the level of ductile crustal flow and style of normal faulting of brittle crust. *Tectonophysics* 320: 195-218.

Black LP, Kamo SL, Allen CM, Aleinikoff JN, Davis DW, Korsch RJ, Foudoulis C 2003. TEMORA 1: A new zircon standard for Phanerozoic U-Pb geochronology. *Chemical Geology* 200: 155-170.

Black LP, Williams IS, Compston W 1986. Four zircon ages from one rock: The history of a 3930 Ma-old granulite from Mount Sones, Enderby Land, Antarctica. *Contributions to Mineralogy and Petrology* 94: 427-437.

Blichert-Toft J, Albarède F 1997. The Lu-Hf isotope geochemistry of chondrites and the evolution of the mantle-crust system. *Earth and Planetary Science Letters* 148: 243-258.

Block L, Royden LH 1990. Core complex geometries and regional scale flow in the lower crust. *Tectonics* 9: 557-567.

Bowen FE 1964. *Sheet 15 – Buller*. Geological map of New Zealand 1:250 000. Wellington, New Zealand, Department of Scientific and Industrial Research.

Bowring SA, Schmitz MD 2003. High-precision U-Pb zircon geochronology and the stratigraphic record. In: Hanchar JM, Hoskin PWO ed. *Reviews in Mineralogy and Geochemistry* 53 – *Zircon*: 305-326.

Bradshaw JD 1989. Cretaceous geotectonic patterns in the New Zealand region. *Tectonics* 8: 803-820.

Bradshaw JD 1993. A review of the Median Tectonic Zone: Terrane boundaries and terrane amalgamation near the Median Tectonic Line. *New Zealand Journal of Geology and Geophysics* 36: 117-125.

Brun J-P, Sokoutis D, van den Driessche J 1994. Analogue modelling of detachment fault systems and core complexes. *Geology* 22: 319-322.

Buck W 1988. Flexural rotation of normal faults. *Tectonics* 7: 959-973.

Cavosie AJ, Valley, JW, Wilde S, E.I.M.F 2006. Correlated microanalysis of zircon: Trace element, $\delta^{18}O$, and U-Th-Pb isotopic constraints on the igneous origin of complex >3900 Ma detrital grains. *Geochimica et Cosmochimica Acta* 70: 5601-5616.

Chappell BW, White AJR 1974. Two constraining granite types. *Pacific Geology* 8: 173-174.

Chappell BW, White AJR 1992. I- and S-type granites in the Lachlan Fold Belt. *Transactions of the Royal Society of Edinburgh: Earth Sciences* 83: 1-26.

Chappell BW, White AJR, Williams IS, Wyborn D 2004. Low- and high-temperature granites. *Transactions of the Royal Society of Edinburgh: Earth Sciences* 95: 125-140.

Cherniak DJ, Lanford WA, Ryerson FJ 1991. Lead diffusion in apatite and zircon using ion implantation and Rutherford Backscattering techniques. *Geochimica et Cosmochimica Acta* 55: 1663-1673.

Cherniak DJ, Watson EB 2000. Pb diffusion in zircon. *Chemical Geology* 172: 5-24.

Cherniak DJ, Watson EB 2003. Diffusion in zircon. In: Hanchar JM, Hoskin PWO ed. *Reviews in Mineralogy and Geochemistry* 53 – *Zircon*: 113-143.

Christie AB, Brathwaite RL, Tulloch AJ 1998. Mineral commodity report 17 – rare earths and related elements. *New Zealand Mining* 24: 7-19.

Claiborne LL, Miller CF, Walker BA, Wodden JL, Mazdab FK and Bea F 2006. Tracking magmatic processes through Zr/Hf ratios in rocks and Hf and Ti zoning in zircons: An example from the Sprit Mountain batholith, Nevada. *Mineralogical Magazine* 70: 517-543.

Clemens JD 2003. S-type granitic magmas – petrogenetic issues, models and evidence. *Earth Science Reviews* 61: 1-18.

Compston W, Pidgeon RT 1986. Jack Hills, evidence of more very old detrital zircons in Western Australia. *Nature* 321: 766-769.

Compston W, Williams IS and Meyer C 1984. U-Pb geochronology of zircons from lunar breccia 73217 using a sensitive high mass-resolution ion microprobe. *Journal of Geophysical Research* 89: Supplement B525-B524.

Coney PJ 1980. Cordilleran metamorphic core complexes: An overview. *Geological Society of America Memoir 153*: 7-31.

Coney PJ, Harms TA 1984. Cordilleran metamorphic core complexes: Cenozoic extensional relics of Mesozoic compression. *Geology* 12: 550-554.

Connelly JN 2000. Degree of preservation of igneous zonation in zircon as a sign-post for concordancy in U/Pb geochronology. *Chemical Geology* 172: 25-39.

Corfu F, Hanchar JM, Hoskin PWO, Kinny P 2003. Atlas of zircon textures. In: Hanchar JM, Hoskin PWO ed. *Reviews in Mineralogy and Geochemistry* 53 – *Zircon*: 468-500.

Craig H 1961. Isotopic variations in meteoric waters. *Science* 133: 1702-1703.

Davis GH 1983. Shear-zone model for the origin of metamorphic core complexes. *Geology* 11: 342-347.

Davis GA, Anderson JL, Frost EG, Shakelford TJ 1980. Mylonitisation and detachment faulting in the Whipple-Buckskin-Rawhide Mountains terrane, southeastern California, and western Arizona. *Geological Society of America Memoir 153*: 79-130.

Davis GA, Lister GS, Reynolds SJ 1983. Interpretation of Cordilleran core complexes as evolving shear zones in an extending orogen. *Geological Society of America Abstracts* 15: 311.

Davis GA, Lister GS, Reynolds SJ 1986. Structural evolution of the Whipple and South Mountains shear zones, southwestern United States. *Geology* 14: 7-10.

Dickin AP 2005. *Radiogenic Isotope Geology – Second Edition.* Cambridge University Press. 492p.

Eiler JM 2001. Oxygen isotope variations of basaltic lavas and upper mantle rocks. In: Valley JW, Cole DR ed. *Stable isotope geochemistry. Reviews in Mineralogy and Geochemistry,* Mineralogical Society of America and Geochemical Society 43: 319-364.

Eskola P 1949. The problem of mantled gneiss domes. *Geological Society of London Quarterly Journal* 104: 461-476.

Falvey DA, Mutter JC 1981. Regional plate tectonics and evolution of Australia's passive continental margins. *Journal of Australian Geology and Geophysics* 6: 1-29.

Faure G 1986. *Principles of Isotope Geology - Second Edition.* New York, Wiley. 464p.

Fedo CM, Sircombe KN, Rainbird RH 2003. Detrital zircon analysis of the sedimentary record. In: Hanchar JM, Hoskin PWO ed. *Reviews in Mineralogy and Geochemistry* 53 – *Zircon*: 277-303.

Finch RJ, Hanchar JM 2003. Structure and chemistry of zircon and zircon-group minerals. In: Hanchar JM, Hoskin PWO ed. *Reviews in Mineralogy and Geochemistry* 53 – *Zircon*: 1-25.

Gans PB 1987. An open system, two-layer crustal stretching model for the eastern Great Basin. *Tectonics* 6: 1-12.

Goode ADT 1978. High temperature, high strain rate deformation in the Lower Crustal Kalk Intrusion, Central Australia. *Contributions to Mineralogy and Petrology* 66: 137-148.

Graham IJ, White PJ 1990. Rb-Sr dating of Rahu Suite granitoids from the Paparoa Range, North Westland, New Zealand. *New Zealand Journal of Geology and Geophysics* 33: 11-22.

Griffin WL, Pearson NJ, Belousova E, Jackson SE, van Achterbergh E, O'Reilly SYO, Shee SR 2000. The Hf isotope composition of cratonic mantle: LAM-MC-ICPMS analysis of zircon megacrysts in kimberlites. *Geochimica et Cosmochimica Acta* 64: 133-147.

Grindley GW, Davey FJ 1982. The reconstruction of New Zealand, Australia and Antarctica. In: Craddock C ed. *Antarctic Geoscience*: 15-29.

Hanchar JM, Watson EB 2003. Zircon saturation thermometry. In: Hanchar JM, Hoskin PWO ed. *Reviews in Mineralogy and Geochemistry* 53 – *Zircon*: 89-112.

Harrison TM, Blichert-Toft J, Müller W, Albarede F, Holden P, Mojzsis SJ 2005. Heterogeneous Hadean hafnium: Evidence of continental crust at 4.4 to 4.5 Ga. *Science* 310: 1947-1950.

Harvey PK, Taylor DM, Hendry RD, Bancroft F 1973. An accurate method for the analysis of rocks and chemically related minerals by X-ray fluorescence spectrometry. *X-ray Spectrometry* 2: 33-44.

Hawkesworth CJ, Kemp AIS 2006. Using hafnium and oxygen isotopes in zircons to unravel the record of crustal evolution. *Chemical Geology* 226: 144-162.

Hayden LA, Watson EB 2007. Rutile saturation in hydrous siliceous melts and its bearing on Ti-thermometry of quartz and zircon. *Earth and Planetary Science Letters*, doi: 10.1016/j.epsl.2007.04.020

Henderson P 1996. The rare earth elements: Introduction and review. In: Jones AP, Wall F, Williams CT ed. *Rare Earth Minerals.* The Mineralogical Society Series 7: 1-19.

Hoskin PWO, Black LP 2000. Metamorphic zircon formation by solid state recrystallisation of protolith igneous zircon. *Journal of Metamorphic Geology* 18: 423-439.

Hoskin PWO, Ireland TR 2000. Rare earth element chemistry of zircon and its use as a provenance indicator. *Geology* 28: 627-630.

Hoskin PWO, Schaltegger U 2003. The composition of zircon and igneous metamorphic petrogenesis. In: Hanchar JM, Hoskin PWO ed. *Reviews in Mineralogy and Geochemistry* 53 – *Zircon*: 27-62.

Hume BJ 1977. The relationship between the Charleston Metamorphic Group and the Greenland Group in the central Paparoa Range, South Island, New Zealand. *Journal of the Royal Society of New Zealand* 7: 379-392.

Hutton DWH, Dempster TJ, Brown PE, Becker SD 1990. A new mechanism of granite emplacement: Intrusion into active extensional shear zones. *Nature* 343: 452-455.

Ireland TR 1992. Crustal evolution of New Zealand: Evidence from age distributions of detrital zircon in Western Province paragneiss and Torlesse Greywacke. *Geochimica et Cosmochimica Acta* 56: 911-920.

Ireland TR, Gibson GM 1998. SHRIMP monazite and zircon geochronology of high-grade metamorphism in New Zealand. *Journal of Metamorphic Geology* 16: 149-167.

Kemp AIS, Hawkesworth CJ, Foster GL, Paterson BA, Woodhead JD, Hergt JM, Gray CM, Whitehouse MJ 2007. Magmatic and crustal differentiation history of granitic rocks from Hf-O isotopes in zircon. *Science* 315: 980-983.

Kemp AIS, Hawkesworth CJ, Paterson BA, Kinny PD 2006. Episodic growth of the Gondwana supercontinent from hafnium and oxygen isotopes in zircon. *Nature* 439: 580-583.

Kemp AIS, Whitehouse MJ, Hawkesworth CJ, Alarcon MK 2005a. A zircon U-Pb study of metaluminous (I-type) granites of the Lachlan Fold Belt, southeastern Australia: Implications for the high/low temperature classification and magma differentiation processes. *Contributions to Mineralogy and Petrology* 150: 230-249.

Kemp AIS, Wormald RJ, Whitehouse MJ, Price RC 2005b. Hf isotopes in zircon reveal contrasting sources and crystallisation histories for alkaline to peralkaline granites of Temora, southeastern Australia. *Geology* 33: 797-800.

Kinny PD, Maas R 2003. Lu-Hf and Sm-Nd isotope systems in zircon. In: Hanchar JM, Hoskin PWO ed. *Reviews in Mineralogy and Geochemistry* 53 – *Zircon*: 327-341.

Kinny PD, Wijbrans JR, Froude DO, Williams IS, Compston W 1990. Age constraints on the geological evolution of the Narryer Gneiss Complex, Western Australia. *Australian Journal of Earth Sciences* 37: 51-69.

Kimbrough DL, Tulloch AJ 1989. Early Cretaceous age of orthogneiss from the Charleston Metamorphic Group, New Zealand. *Earth and Planetary Science Letters* 95: 130-140.

Kimbrough DL, Tulloch AJ, Geary E, Coombs DS, Landis CA 1993. Isotopic ages from the Nelson region of the South Island, New Zealand: Crustal structure and deformation of the Median Tectonic Zone. *Tectonophysics* 225: 433-448.

Köppel V, Sommerauer J 1974. Trace elements and the behaviour of the U-Pb system in inherited and newly formed zircons. *Contributions to Mineralogy and Petrology* 43: 71-82.

Laird MG 1967. Field relations of the Constant Gneiss and Greenland Group in the Central Paparoa Range, West Coast, South Island. *New Zealand Journal of Geology and Geophysics* 10: 247-256.

Laird MG 1981. The late Mesozoic fragmentation of the New Zealand segment of Gondwana. In: Cresswell MM, Vella P ed. Gondwana Five – *selected papers and abstracts of papers presented at the Fifth International Gondwana Symposium*: 339.

Laird MG 1993. Cretaceous continental rifts: New Zealand region. In: Ballance PF ed. *South Pacific Sedimentary Basins: Sedimentary Basins of the World* 2: 37-49.

Laird MG, Bradshaw JD 2004. The break-up of a long-term relationship: The Cretaceous separation of New Zealand from Gondwana. *Gondwana Research* 7: 273-286.

Landis CA, Coombs DS 1967. Metamorphic belts and orogenesis in southern New Zealand. *Tectonophysics* 4: 501-518.

Ledlie I/CRA Exploration Co Ltd 1989-1990. *Progress report on EL 33-445 Ohika, Buller, New Zealand.* Ministry of Economic Development New Zealand. Unpublished Mineral Report MR2921.

Lister GS, Davis GA 1989. The origin of metamorphic core complexes and detachment faults formed during Tertiary continental extension in the northern Colorado River region, USA. *Journal of Structural Geology* 11: 65-94.

Lister GS, Davis GA, McClelland WC, Marcott DT 1984. Complexities in the evolution of low-angle crustal shear zones during continental extension. *Geological Society of America Abstracts* 16: 577.

Lister GS, Etheridge MA, Symonds PA 1991. Detachment models for the formation of passive continental margins. *Tectonics* 10: 1038-1064.

Lister GS, Snoke AW 1984. S-C mylonites. *Journal of Structural Geology* 6: 617-638.

Lowery Claiborne L, Miller CF, Walker N, Wooden JL, Mazdab FK, Bea F 2007. Tracking magmatic processes through Zr/Hf ratios in rocks and Hf and Ti zoning in zircons: An example from the Spirit Mountain Batholith, Nevada. *Mineralogical Magazine* 70: 517-543.

Ludwig KR 1999. Isoplot Ex v.2.6. Berkeley Geochronology Centre Special Publication 1a. 47p.

Maas R, Kinny PD, Williams IS, Froude DO, Compston W 1992. The Earth's oldest known crust: A geochronological and geochemical study of 3900-4200 Ma old detrital zircons from Mt. Narryer and Jack Hills, Western Australia. *Geochimica et Cosmochimica Acta* 56: 1281-1300.

Mattinson JM, Graubard CM, Parkinson DL, McLelland WC 1996. U-Pb reverse discordance in zircons: The role of fine-scale oscillatory zoning and sub-microscopic transport of Pb. *American Geophysical Union, Geophysical Monogram* 95: 355-370.

Mezger K, Krogstad EJ 1997. Interpretation of discordant U-Pb zircon ages: An evaluation. *Journal of Metamorphic Geology* 15: 127-140.

Miller CF, McDowell SM, Mapes RW 2003. Hot and cold granites? Implications of zircon saturation temperatures and preservation of inheritance. *Geology* 31: 529-532.

Miller EL, Gans PB, Garing J 1983. The Snake range decollement: An exhumed mid-Tertiary brittle-ductile transition. *Tectonics* 2: 239-263.

Misch P 1960. Regional structural reconnaissance in Central-northeast Nevada and some adjacent areas: Observations and interpretations. *Intermountain Association of Petroleum Geologists Guidebook for the 11th Annual Field Conference:* 17-42.

Mortimer N, Gans P, Calvert A, Walker N 1999. Geology and thermochronometry of the east edge of the Median Batholith (Median Tectonic Zone): A new perspective on Permian to Cretaceous crustal growth of New Zealand. *Island Arc* 8: 404-425.

Muir RJ, Bradshaw JD, Weaver SD 1992. Crustal extension prior to the opening of the Tasman Sea Basin: Evidence from New Zealand granites. In: van der Lingen GL, Swanson KM, Muir RJ ed. *Evolution of the Tasman Basin*. Proceedings of the Tasman Sea Conference, Christchurch, New Zealand, 27-30 November 1992: 55-64.

Muir RJ, Ireland TR, Weaver SD, Bradshaw JD 1994. Ion microprobe U-Pb zircon geochronology of granitic magmatism in the Western Province of the South Island, New Zealand. *Chemical Geology* 113: 171-189.

Muir RJ, Weaver SD, Bradshaw JD, Eby GN, Evans JA 1995. The Cretaceous Separation Point Batholith, New Zealand – Granitoid magmas formed by the melting of mafic lithosphere. *Journal of the Geological Society, London* 152: 689-701.

Muir RJ, Ireland TR, Weaver SD, Bradshaw JD 1996. Ion microprobe dating of Paleozoic granitoids: Devonian magmatism in New Zealand and correlations with Australia and Antarctica. *Chemical Geology* 127: 191-210.

Muir RJ, Ireland TR, Weaver SD, Bradshaw JD, Evans JA, Eby GN, Shelley D 1998. Geochronology and geochemistry of a Mesozoic magmatic arc system, Fiordland, New Zealand. *Journal of the Geological Society, London* 155: 1037-1052.

Muir RJ, Ireland TR, Weaver SD, Bradshaw JD, Waight TE, Jongens R, Eby GN 1997. SHRIMP U-Pb geochronology of Cretaceous magmatism in north Nelson-Westland, South Island, New Zealand. *New Zealand Journal of Geology and Geophysics* 40: 453-464.

Nathan S 1975. *Sheets S23 and S30 – Foulwind and Charleston.* Geological map of New Zealand 1:63,360. Wellington, New Zealand, Department of Scientific and Industrial Research.

Nathan S 1978. *Sheets S31 and S32 – Buller-Lyell.* Geological map of New Zealand 1:63,360. Wellington, New Zealand, Department of Scientific and Industrial Research.

Nebel O, Nebel-Jacobsen Y, Mezger K, Berndt J 2007. Initial Hf isotope compositions in magmatic zircon from early Proterozoic rocks from the Gawler Craton, Australia: A test for zircon model ages. *Chemical Geology* doi:10.1016/j.chemgeo.2007.02.008

Nebel-Jacobsen Y, Scherer EE, Münker C, Mezger K 2005. Separation of U, Pb, Lu, and Hf from single zircons for combined U-Pb dating and Hf isotope measurements by TIMS and MC-ICPMS. *Chemical Geology* 220: 105-120.

Nemchin AA, Pidgeon RT, Whitehouse MJ 2006a. Re-evaluation of the origin and evolution of >4.2 Ga zircons from the Jack Hills metasedimentary rocks. *Earth and Planetary Science Letters* 244: 218-233.

Nemchin AA, Whitehouse MJ, Pidgeon RT, Meyer C 2006b. Oxygen isotopic signature of 4.4-3.9 Ga zircons as a monitor of differentiation processes on the Moon. *Geochimica et Cosmochimica Acta* 70: 1864-1872.

Neves JMC, Nunes JEL, Sahama ThG 1974. High hafnium members of the zircon-hafnon series from the granite pegmatites of Zambézia, Mozambique. *Contributions to Mineralogy and Petrology* 48: 73-80.

Norrish K, Chappell B 1977. X-ray fluorescence spectrometry. In: Zussman J ed. *Physical methods in determinative mineralogy*: 201-272.

Norrish K, Hutton JT 1969. An accurate X-ray spectrographic method for the analysis of a wide range of geological samples. *Geochimica et Cosmochimica Acta* 33: 431-453.

Parrish RR, Noble SR 2003. Zircon U-Th-Pb geochronology by isotope dilution – thermal ionisation mass spectrometry (ID-TIMS). In: Hanchar JM, Hoskin PWO ed. *Reviews in Mineralogy and Geochemistry* 53 – *Zircon*: 183-213.

Passchier CW, Trouw RAJ 1996. *Microtectonics*. Berlin Heidelburg, Springer-Verlag. 289p.

Pearce NJC, Perkins WT, Westgate JA, Gorton MP, Jackson SE, Neal CR, Chenery SP 1997. A compilation of new and published major and trace element data for NIST SRM 610 and NIST SRM 612 glass reference materials. *Geostandards Newsletter* 21: 115-144.

Pidgeon RT, O'Neill JR, Silver LT 1968. Uranium and lead isotope stability in a metamict zircon under experimental hydrothermal conditions. *Science* 154: 1538-1540.

Price RA, Mountjoy EW 1970. Geologic structure of the Canadian Rocky Mountains between Bow and Athabasca Rivers – A progress report. *Geological Association of Canada, Special Paper 6:* 7-25.

Ranalli G, Murphy DC 1987. Rheological stratification of the lithosphere. *Tectonophysics* 132: 281-295.

Reynolds SJ, Lister GS 1990. Folding of mylonitic zones in Cordilleran metamorphic core complexes: Evidence from near the mylonitic front. *Geology* 18: 216-219.

Reynolds SJ, Spencer JE 1985. Evidence for large-scale transport on the Bullard detachment fault, west-central Arizona. *Geology* 13: 353-356.

Ring U, Herd M, Bohlar R, Glodny J, Palin M 2006. *Dating mylonitisation in the Paparoa Core Complex, Westland.* Abstract for the Geological Society of New Zealand Conference, Palmerston North, 4-7 December.

Ring U, Will T, Glodny J, Kumerics C, Gessner K, Thompson S, Güngör T, Monié P, Okrusch M, Drüppel K 2007. Early exhumation of high-pressure rocks in extrusion wedges: Cycladic blueschist unit in the eastern Aegean, Greece, and Turkey. Tectonics 26, TC2001, doi:10.1029/2005TC001872.

Rosenbaum G, Regenauer-Lieb K, Weinberg R 2005. Continental extension: From core complexes to rigid block faulting. *Geology* 33: 609-612.

Scherer E, Münker C, Mezger K 2001. Calibration of the lutetium-hafnium clock. *Science* 293: 683-687.

Schiøtte L, Compston W, Bridgwater D 1988a. U-Th-Pb ages of single zircons in Archean supracrusts from Nain Province, Labrador, Canada. *Canadian Journal of Earth Sciences* 26: 2636-2644.

Schiøtte L, Compston W, Bridgwater D 1988b. Late Archean ages for the deposition of clastic sediments belonging to the Malene supracrustals, southern West Greenland: Evidence from an ion microprobe U-Pb zircon study. *Earth and Planetary Science Letters* 87: 45-58.

Schiøtte L, Compston W, Bridgwater D 1989. Ion microprobe U-Th-Pb zircon dating of polymetamorphic orthogneisses from northern Labrador, Canada. *Canadian Journal of Earth Sciences* 26: 1533-1556.

Schuhmacher M, de Chambost E, McKeegan KD, Harrison TM, Migeon H 1994. In situ dating of zircon with the CAMECA ims 1270. In: Benninghoven A, Nihei Y, Shimizu R, Werner HW ed. *Secondary Ion Mass Spectrometry SIMS IX*: 919-922.

Silver LT 1963. The relation between radioactivity and discordance in zircons. *National Academy of Scientific Publications* 1075: 34-39.

Sinha AK, Glover IIIL 1978. U/Pb systematics during dynamic metamorphism, a study from the Brevard fault zone. *Contributions to Mineralogy and Petrology* 66: 305-310.

Spell TL, McDougall I, Tulloch AJ 2000. Thermochronologic constraints on the breakup of the Pacific Gondwana margin: The Paparoa metamorphic core complex, South Island, New Zealand. *Tectonics* 19: 433-451.

Spencer JE 1984. The role of tectonic denudation in the warping and uplift of low-angle normal faults. *Geology* 12: 95-98.

Taylor SR, McLennan SM 1985. *The Continental Crust: Its Composition and Evolution.* Oxford, UK, Blackwell Scientific Publications. 312p.

Tera F, Wasserburg G 1972. U-Th-Pb systematics in three Apollo 14 basalts and the problem of initial Pb in lunar rocks. *Earth and Planetary Science Letters* 14: 281-304.

Tulloch AJ 1988. Batholiths, plutons and suites: Nomenclature for the granitoid rocks of Westland-Nelson. *New Zealand Journal of Geology and Geophysics* 31: 505-509.

Tulloch AJ 1995. *Precious metal mineralization associated with the Cretaceous Paparoa Metamorphic Core Complex, New Zealand.* Proceedings of the 1995 PACRIM Congress: 575-580.

Tulloch AJ, Christie AB 2000. *Reconnaissance rare earth element (REE) geochemistry of Ohika Detachment Fault (Buller) and Mandamus Intrusives (north Canterbury), New Zealand. Institute of Geological and Nuclear Sciences Science Report 2000/10,* Institute of Geological and Nuclear Science Ltd, Lower Hutt, New Zealand: 1-26.

Tulloch AJ, Kimbrough DL 1989. The Paparoa Metamorphic Core Complex, New Zealand: Cretaceous extension associated with fragmentation of the Pacific margin of Gondwana. *Tectonics* 8: 1217-1234.

Tulloch AJ, Kimbrough DL, Waight TE 1994. The French Creek Granite, north Westland, New Zealand – Late Cretaceous A-type plutonism on the Tasman passive margin (extended abstract). In: van der Lingen GJ, Swanson KM, Muir RJ ed. *Evolution of the Tasman Basin*. Proceedings of the Tasman Sea Conference, Christchurch, New Zealand, 27-30 November 1992: 65-67.

Tulloch AJ, Palmer K 1990. Tectonic implications of granite cobbles from the mid-Cretaceous Pororari Group, southwest Nelson, New Zealand. *New Zealand Journal of Geology and Geophysics* 33: 205-217.

Valley JW 2003. Oxygen isotopes in zircon. In: Hanchar JM, Hoskin PWO ed. *Reviews in Mineralogy and Geochemistry* 53 – *Zircon*: 343-385.

Valley JW, Lackey JS, Cavosie AJ, Clechenko CC, Spicuzza MJ, Basei MAS, Bindeman IN, Ferreira VP, Sial AN, King EM, Peck WH, Sinha AK, Wei CS 2005. 4.4 billion years of crustal maturation: Oxygen isotope ratios of magmatic zircon. *Contributions to Mineralogy and Petrology* 150: 561-580.

Vavra G 1990. On the kinematics of zircon growth and its petrogenetic significance: A cathodoluminescence study. *Contributions to Mineralogy and Petrology* 106: 90-99.

Vervoort JD, Blichert-Toft J 1999. Evolution of the depleted mantle: Hf isotope evidence from juvenile rocks through time. *Geochimica et Cosmochimica Acta* 63: 533-556.

Waight TE 1994. The Hohonu Dike Swarm: Late Cretaceous crustal extension in the Buller Terrane. *Geological Society of New Zealand – Miscellaneous Publication 80A*: 183.

Waight TE 1995. The geology and geochemistry of the Hohonu Batholith and adjacent rocks, North Westland, New Zealand. *Unpublished Ph.D thesis*, University of Canterbury, Christchurch, New Zealand.

Waight TE, Weaver SD, Ireland TR, Maas R, Muir RJ, Shelley D 1997. Field characteristics, petrography, and geochronology of the Hohonu Batholith and the adjacent Granite Hill Complex, North Westland, New Zealand. N*ew Zealand Journal of Geology and Geophysics* 40: 1-17.

Waight TE, Weaver SD, Maas R, Eby GN 1998a. French Creek Granite and Hohonu dike swarm, South Island, New Zealand: Late Cretaceous alkaline magmatism and the opening of the Tasman Sea. *Australian Journal of Earth Sciences* 45: 823-835.

Waight TE, Weaver SD, Muir RJ 1998b. Mid-Cretaceous granitic magmatism during the transition from subduction to extension in southern New Zealand: A chemical and tectonic synthesis. *Lithos* 45: 469-482.

Wark DA, Miller CF 1993. Accessory mineral behaviour during differentiation of a granite suite: Monazite, xenotime, and zircon in the Sweetwater wash pluton, southeastern California, U.S.A. *Chemical Geology* 110: 49-67.

Watson EB, Harrison TM 1983. Zircon saturation revisited: Temperature and composition effects in a variety of crustal magma types. *Earth and Planetary Science Letters* 64: 295-304.

Watson EB, Harrison TM 2005. Zircon thermometer reveals minimum melting conditions on earliest Earth. *Science* 308: 841-844.

Watson EB, Wark DA, Thomas JB 2006. Crystallisation thermometers for zircon and rutile. *Contributions to Mineralogy and Petrology* 151: 413-433.

Watt GR, Harley SL 1993. Accessory phase controls on the geochemistry of crustal melts and restites produced during water-undersaturated partial melting. *Contributions to Mineralogy and Petrology* 114: 550-566.

Wayne DM, Sinha AK 1988. Physical and chemical response of zircons to deformation. *Contributions to Mineralogy and Petrology* 98: 109-121.

Wernicke B 1981a. Low-angle normal faults in the Basin and Range Province: Nappe tectonics in an extending orogen. *Nature* 291: 645-647.

Wernicke B 1981b. Insights from Basin and Range surface geology for the process of large-scale divergence of continental lithosphere (abstract). In: *Papers presented to the conference on processes of planetary rifting*, Lunar and Planetary Institute, Houston: 90-92.

Wernicke B 1983. Evidence for large-scale simple shear of the continental lithosphere during extension, Arizona and Utah. *Geological Society of America Abstracts* 15: 310-311.

Wernicke B 1985. Uniform-sense normal simple shear of the continental lithosphere. *Canadian Journal of Earth Sciences* 22: 108-126.

Wernicke B, Axen, GJ 1988. On the role of isostasy in the evolution of normal fault systems. *Geology* 16: 848–851.

White PJ 1994. Thermobarometry of the Charleston Metamorphic Group and implications for the evolution of the Paparoa Metamorphic Core Complex, New Zealand. *New Zealand Journal of Geology and Geophysics* 37: 201-209.

White SH, Burrows SE, Carreras J, Shaw ND, Humphreys FJ 1980. On mylonites in ductile shear zones. *Journal of Structural Geology* 2: 175-187.

Whitehouse MJ, Kamber BS, Moorbath S 1999. Age significance of U-Th-Pb zircon data from early Archean rocks of west Greenland – a reassessment based on combined ion-microprobe and imaging studies. *Chemical Geology* 160: 201-224.

Wiedenbeck M, Allé P, Corfu F, Griffin WL, Meier M, Oberli F, von Quadt A, Roddick JC, Spiegel W 1995. Three natural zircon standards for U-Th-Pb, Lu-Hf, trace element and REE analyses. *Geostandards Newsletter* 19: 1-23.

Williams IS, Claesson S 1987. Isotopic evidence for the Precambrian provenance and Caledonian metamorphism of high grade paragneisses from the Seve Nappes, Scandinavian Caledonides, II. Ion microprobe zircon U-Th-Pb. *Contributions to Mineralogy and Petrology* 97: 205-217.

Winter JD 2001. *An Introduction to Igneous and Metamorphic Petrology.* Upper Saddle River, NJ, Prentice-Hall Inc. 697p.

Wjins C, Weinberg R, Gessner K, Moresi L 2005. Mode of crustal extension determined by rheological layering. *Earth and Planetary Science Letters* 236: 120-134.

Woodhead J, Hergt J, Shelley M, Eggins S, Kemp R 2004. Zircon Hf-isotope analysis with an excimer laser, depth profiling, ablation of complex geometries, and concomitant age estimation. *Chemical Geology* 209: 121-135.

Woodhead JA, Rossman GR, Silver LT 1991. The metamictization of zircon: Radiation dose-dependent structural characteristics. *American Mineralogist* 76: 74-82.

Yang J-H, Wu F-Y, Wilde SA, Xie L-W, Yang Y-H, Liu X-M 2007. Tracing magma mixing in granite genesis: In situ U-Pb dating and Hf-isotope analysis of zircons. *Contributions to Mineralogy and Petrology* 153: 177-190.